UNIVERSITAT POLITÈCNICA DE VALÈNCIA

DEPARTAMENTO DE INGENIERÍA ELECTRÓNICA

Grupo de Sistemas Electrónicos Industriales

Tesis Doctoral

GESTIÓN EFICIENTE DE LOS CONVERTIDORES DE POTENCIA CONECTADOS AL BUS DC DE UNA MICRORRED HÍBRIDA DE GENERACIÓN DISTRIBUIDA.

Presentada por:

D. Robert Antonio Salas Puente

Dirigida por:

Dr. Gabriel Garcerá Sanfelíu

Dr. Emilio Figueres Amorós

Valencia, Diciembre de 2018

Página en blanco

Al amor de mi vida

Yulynel Gallado

Página en blanco

AGRADECIMIENTOS

En primer lugar quiero agradecer a todos los integrantes del Grupo de Sistemas Electrónicos Industriales (GSEI) de la UPV, por permitirme ser parte de esta comunidad y aprender de su gran profesionalidad.

A mis directores de tesis, los Profesores Gabriel Garcerá y Emilio Figueres, gracias por la paciencia y por todas las recomendaciones siempre acertadas, ha sido un gran honor trabajar con ustedes.

A mi esposa Yuly, por su valentía de acompañarme en este viaje, ha sido maravilloso y llegado a buen puerto gracias a su amor, sacrificio y esfuerzo, lo hemos logrado mi amor.

A mis padres Ana y José, a mis hermanas Karem y Ruth, por brindarme todo su amor y apoyo incondicional, gracias por ser los promotores de todas mis metas y sueños.

A mi gran amigo Jimer, por su ayuda incondicional y por ser siempre un gran soporte a largo de toda mi carrera, gracias amigo mío.

A mis compañeros de laboratorio (Silvia, Raúl, Iván, Marian, Jesús, Javier y Juanjo), gracias por toda la colaboración que me brindaron y por el intercambio de ideas que fueron de gran provecho y ahora son parte de esta tesis.

A la ilustre Universidad de Los Andes de Venezuela, por haberme brindado la oportunidad de prepararme académicamente para asumir este gran reto.

Finalmente, quiero agradecer a toda mi familia, amigos y personas que han contribuido directa e indirectamente para la realización de esta tesis, gracias a todos.

Página en blanco

RESUMEN

Dos aspectos críticos en la operación de una microrred son las estrategias de control y gestión de potencia implementadas, las cuales son esenciales para proporcionar su buen funcionamiento. La aplicación adecuada de dichas estrategias permite compensar los desequilibrios de potencia causados por la discontinuidad de la generación y de la demanda de energía en las microrredes. En este sentido, el objetivo global de estas estrategias de gestión es equilibrar adecuadamente el flujo de potencia en la microrred, mediante la aplicación de diferentes algoritmos que permiten cumplir con los criterios de estabilidad, protección, balance de potencia, transiciones, sincronización con la red y gestión adecuada de la microrred. En el caso de microrredes de pequeña escala de potencia con bajo número de generadores y sistemas de almacenamiento distribuidos, las estrategias de control centralizado ofrecen un alto nivel de flexibilidad para lograr funcionalidades avanzadas en la microrred y una adecuada distribución de la potencia entre los convertidores que la conforman. Esta tesis se ha enmarcado en el contexto de algoritmos de gestión centralizada de potencia de una microrred de generación distribuida en modo conectado a red. Los algoritmos presentados se pueden aplicar a los convertidores de potencia conectados al bus DC de una microrred AC/DC híbrida o en una microrred de DC, donde el despacho de potencia es observado y gestionado por un controlador central. Este último adquiere datos del sistema mediante una infraestructura de comunicaciones y estima la potencia que gestionará cada uno de los convertidores de potencia, sistemas de almacenamiento y cargas en funcionamiento.

En este estudio se muestra la validación experimental de las estrategias de gestión aplicadas en la microrred desde el enfoque del comportamiento de los convertidores de potencia, de las baterías y las cargas ante dicha gestión. Se verifica la estabilidad de la microrred sometiendo a los convertidores a diferentes escenarios de funcionamiento. Estos escenarios pueden ser fluctuaciones en la irradiación, la demanda, el estado de carga de las baterías, los límites máximos de exportación/importación de potencia desde/hacia la microrred hacia/desde la red principal y de la tarifa eléctrica. Adicionalmente, se propone un sistema de almacenamiento de energía en baterías encargado de mantener el equilibrio de potencia en el bus de DC de la microrred que permite aprovechar las fuentes de generación renovables presentes en la microrred y maximizar el tiempo de

servicio de las baterías mediante la aplicación de un algoritmo de carga de las baterías. Este último se ajusta al procedimiento de carga especificado por el fabricante, estableciendo las tasas de carga en función de los escenarios en que la microrred se encuentre. El procedimiento de carga en las baterías es fundamental para garantizar las condiciones adecuadas de operación de las mismas, ya que toman en consideración los parámetros establecidos por el fabricante, como son: tasas de carga/descarga, tensión máxima de carga, temperaturas de operación, etc…

RESUM

Dos dels aspectes crítics en l'operació d'una micro-xarxa són les estratègies de control i gestió de potència implementades, les quals són essencials per proporcionar el seu bon funcionament. L'aplicació adequada de dites estratègies permet compensar els desequilibris de potència causats per la discontinuïtat de la generació i demanda d'energia en les micro-xarxes. En aquest sentit, l'objectiu global de les nomenades estratègies de gestió és equilibrar adequadament el flux de potència en la micro-xarxa mitjançant l'aplicació de diferents algoritmes que permeten complir amb els criteris d'estabilitat, protecció, balanç de potència, transicions, sincronització amb la xarxa i gestió adequada de la micro-xarxa. En el cas de micro-xarxes de potència a petita escala i amb baix nombre de generadors i sistemes d'emmagatzematge distribuïts, les estratègies de control centralitzades ofereixen un alt nivell de flexibilitat per aconseguir funcionalitats avançades en la micro-xarxa i una adequada distribució de la potència entre els convertidors que la conformen. Aquesta tesi s'ha emmarcat al context d'algoritmes de gestió centralitzada de potència d'una micro-xarxa de generació distribuïda en mode de connexió a xarxa. Els algoritmes presentats es poden aplicar als convertidors de potència connectats al bus DC d'una micro-xarxa AC/DC hibrida o en una micro-xarxa de DC, on el despatx de potència és observat i gestionat per un controlador central. Aquest últim adquireix dades del sistema mitjançant una infraestructura de comunicacions i estima la potència que gestionarà cadascun dels convertidors de potència, sistemes d'emmagatzematge i càrregues en funcionament.

En aquest estudi es mostren la validació experimental de les estratègies de gestió aplicades en la micro-xarxa des d'un enfocament dels convertidors de potència, de les bateries i les càrregues davant d'aquesta gestió. Es verifica l'estabilitat de la micro-xarxa exposant als convertidors a diferents escenaris de funcionament. Aquest escenaris poden ser fluctuants en la irradiació, la demanda, l'estat de càrrega de les bateries, els límits màxims d'exportació/importació de potència des de/cap a la micro-xarxa cap a/des de la xarxa principal i de la tarifa elèctrica. Addicionalment, es proposa un sistema d'emmagatzematge d'energia en bateries encarregats de mantindre l'equilibri de potència al bus DC de la micro-xarxa i que permet aprofitar les fonts de generació renovables presents en la micro-xarxa i maximitzar el temps de servei de les bateries mitjançant l'aplicació

d'un algoritme de càrrega de bateries. Aquest últim s'ajusta al procediment de càrrega especificat pel fabricant, establint les taxes de càrrega en funció dels escenaris en que la micro-xarxa es trobe. El procediment de càrrega a les bateries es fonamental per garantir les condicions adequades d'operació de les mateixes, ja que prenen en consideració els paràmetres establerts pel fabricant, com ara són: taxes de càrrega/descàrrega, tensió màxima de càrrega, temperatures d'operació, etc.

ABSTRACT

Two critical aspects in microgrids operation are the control and power management strategies, which are essential for their efficient operation. The adequate application of these strategies allows compensating the power imbalance caused by the discontinuity in the energy generation or changes in the power demand of the microgrid. In this sense, the overall objective of these power management strategies is to keep the power balance between the generation and the demand in the microgrid through the application of different algorithms that fulfill the criteria of stability, protection, smooth transitions and synchronization with the main grid. In the case of small-scale microgrids with a low number of distributed generators and energy storage systems, the centralized control strategies offer a higher level of flexibility to achieve advanced features in the microgrid and for the suitable power sharing between the converters that compose it. This thesis has been focused on centralized power management algorithms of a microgrid working in grid connected mode. These algorithms can be applied to the power converters connected to the DC bus of both hybrid AC/DC and DC microgrids, where the power dispatch is controlled by a central controller which acquires system data through a communication infrastructure and sets the power to be managed by each of the converters under operation.

In this thesis the experimental validation of the power management strategies of the microgrid are presented, from the point of view of the behavior of the power converters, batteries and loads. It is provided a realistic evaluation under different microgrid operation scenarios. These scenarios were sudden changes of the irradiation, load, state of charge, the maximum power to be exported/imported from/to the microgrid to/from the grid, and the electricity tariff. Additionally, it is proposed a battery energy storage system that keeps the power balance at the DC bus of the microgrid, taking advantage from the renewable energy sources and adjusting the battery energy storage through a suitable charging procedure specified by the manufacturer. The proposed procedure changes the charging parameters of the batteries depending on the microgrid states. Its goal is to extend the service time of batteries and to allow a proper energy management in the system.

ÍNDICE

1

1. INTRODUCCIÓN

La presente tesis se ha escrito en forma de compendio de artículos, basado en 3 publicaciones en revista de investigación, que muestran los aspectos más relevantes.

En este capítulo se expone el estado de la técnica, la motivación y los objetivos principales de la tesis doctoral. Asimismo, se presenta la estructura del documento y las principales publicaciones realizadas durante el desarrollo de la tesis.

1.1. Estado de la técnica

Las tecnologías habilitadoras de las energías renovables son de gran interés a nivel mundial debido a que son una posible solución de algunos problemas importantes de la población. Uno de ellos es el agotamiento de las reservas de combustibles fósiles debido a la gran demanda global de energía por parte de los sectores industriales y de transporte, con una alta dependencia de estos combustibles. Por otro lado, su excesiva utilización produce daños medioambientales por el continuo incremento en las emisiones de CO_2 a la atmosfera.

La integración de las fuentes de energías renovables (FEERR) en la red eléctrica es realizada mediante microrredes de generación distribuida. Las FEERR permiten mitigar los efectos medioambientales y obtener beneficios socioeconómicos para el desarrollo sostenible de la población. En la Figura 1.1 se muestra la potencia instalada de las energías renovables en el mundo, que tuvo su mayor aumento en 2016, con una estimación de 161 GW de capacidad agregada [1]. La capacidad global de potencia de origen renovable instalada subió casi el 9% respecto 2015, alcanzando aproximadamente 2.017 GW al final del año. La generación solar representó alrededor del 47% de la capacidad de la energía renovable recién instalada en 2016. La energía eólica y la hidroeléctrica fueron las siguientes más importantes instaladas ese año, habiendo representado el 34% y el 15.5%, respectivamente [1].

1.1.1. Microrredes

Una microrred es un sistema de distribución de potencia de baja escala respecto la red principal. Esta última es considerada como un bus con capacidad infinita de generación vista desde el punto de vista de la microrred. Una microrred está conformada por: generadores distribuidos, sistemas de almacenamiento de energía y diferentes tipos de cargas [1-3]. En las microrredes la generación y distribución de la energía es realizada de forma local, con el objetivo de obtener tarifas privilegiadas para los consumidores [4]. La mayoría de las microrredes poseen la capacidad necesaria para operar como un único sistema de alimentación, con la flexibilidad de abastecer de forma fiable y segura ciertos niveles de potencia [5]. En algunas ocasiones las microrredes pueden proporcionar un menor coste de la inversión inicial, mejorar la calidad de la energía y reducir las pérdidas en la red de distribución. Conceptualmente, una microrred puede trabajar en conexión a red o de forma aislada. En ambos casos es necesaria la continua sincronización entre la red principal y la microrred [3].

Cuando la microrred opera conectada a la red, la variación del voltaje y la frecuencia son ajustadas por la red principal, mientras que los generadores distribuidos de la microrred se conectan generalmente como fuentes de corriente funcionando en su punto de máxima potencia. Si existe excedente de energía generada en la microrred, éste se inyecta a la red principal. Un escenario diferente es la microrred operando en modo aislado, que es habitual en redes rurales o cuando ocurre un fallo de la red principal. En este caso el voltaje y la frecuencia dependen de los algoritmos locales, distribuidos o centralizados, de los generadores distribuidos conectados a la microrred [6].

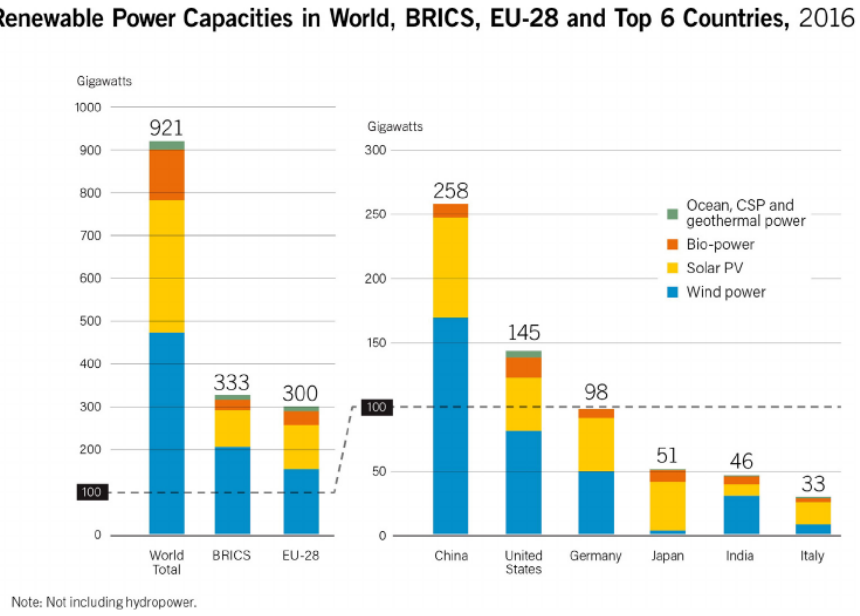

Figura 1.1. Capacidad instalada de las fuentes de energía renovables en el mundo (2016). Tomado de [1].

1.1.2. Tipos de Microrredes

Las microrredes se pueden clasificar en tres grupos, dependiendo de la manera en que los buses de AC y DC son conectados: microrred de AC, microrred de DC y microrred AC/DC [7].

La microrred de AC es una topología donde el bus de potencia es de corriente alterna y se puede conectar/desconectar al punto de conexión común de la red eléctrica e intercambiar energía con éste [8]. Estas

microrredes son compatibles con la red eléctrica actual y están más adaptadas a la mayoría de cargas del mercado [9]. Adicionalmente pueden transformar fácilmente los voltajes de AC a diferentes valores mediante transformadores, lo que aumenta la capacidad de estas microrredes para transmitir energía a largas distancias. Sin embargo, en estas microrredes la eficiencia se ve comprometida, debido a las pérdidas en la etapas de conversión de energía cuando se conectan al bus de AC, las FEERR, los sistemas de almacenamiento de energía y las cargas de DC [10].

La microrred de DC [11], es una topología en la que el bus de potencia es de corriente continua y se conecta al punto de conexión común de la red eléctrica, mediante un inversor de interconexión, el cual permite un flujo bidireccional de potencia entre el bus DC y la red. Estas microrredes se clasifican en tres tipos y según la estructura del bus DC: monopolar [12], bipolar [13] y homopolar [14]. En la Figura 1.2 se muestra la clasificación de las microrredes de DC.

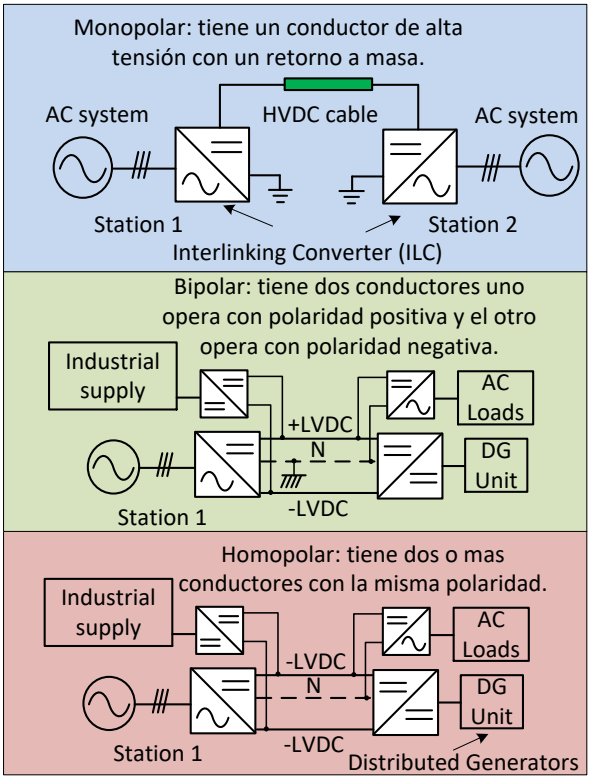

Figura 1.2. Microrredes de DC: monopolar, bipolar y homopolar. Tomado de [15].

Las microrredes DC presentan una alta calidad, fiabilidad y estabilidad en el bus de DC, debido a la ausencia de la potencia reactiva [11]. Adicionalmente, las microrredes de DC tienen las siguientes ventajas con respecto a las microrredes de AC: (i) son más compatibles para la integración de las FEERR y sistemas de almacenamiento de energía en baterías, ya que ofrecen mayor facilidad en la conexión de los convertidores de potencia al bus de DC, (ii) poseen menores pérdidas en la etapa de conversión de energía, debido a que sólo es necesaria una etapa para conectar las FEERR de origen fotovoltaico al bus de DC, y (iii) las microrredes DC presentan menor tamaño en el dimensionamiento del sistema y menores costes de implementación [15].

La microrred AC/DC híbrida [6] es la combinación de las microrredes de AC y DC en la misma red de distribución. La microrred AC/DC híbrida se puede observar en la Figura 1.3. Las principales ventajas de estas microrredes son: (i) coexistencia de ambos tipos de buses AC y DC, que permiten la fácil adaptación y conexión de los diferentes tipos de sistemas de generación y almacenamiento de energía, y (ii) alta capacidad de integración de diferentes tipos de cargas y sistemas de potencia. No obstante, en modo isla las microrredes AC/DC hibridas tienen una alta complejidad de su control, a causa de la difícil sincronización, protección y gestión de potencia entre los dispositivos que conforman la microrred [16,17].

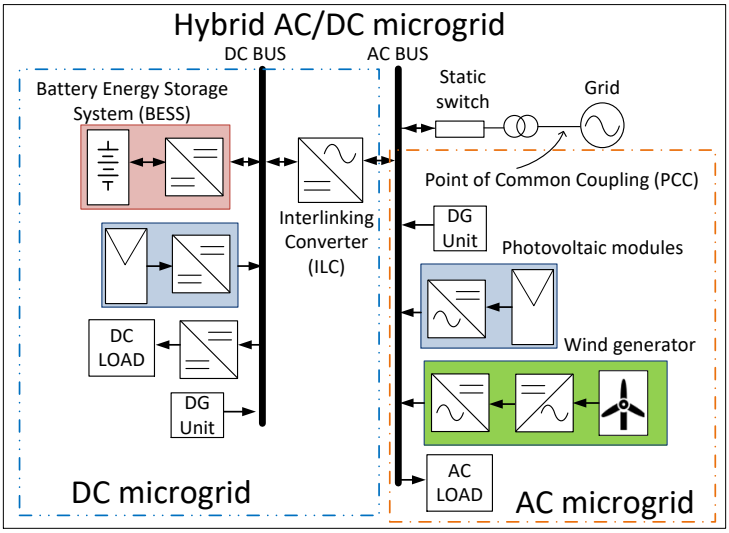

Figura 1.3. Microrred AC/DC híbrida [7].

1.1.3. Comunicaciones en microrredes

Las comunicaciones son una característica clave en la gestión y optimización de potencia en las microrredes [18]. Las tecnologías de comunicación que se elijan han de ser económicas, proporcionar un buen alcance de transmisión, tener buenas características de seguridad y ancho de banda [19]. Se pueden clasificar en dos categorías: tecnologías cableadas y tecnologías inalámbricas.

Las tecnologías cableadas tienen mayor tasa de transmisión de datos y fiabilidad, pero con un alto costo de instalación. Las principales tecnologías cableadas son: (*Power line communication*, PLC), (*Digital Subscriber Lines*, DSL) y fibra óptica.

Las tecnologías inalámbricas como Zigbee, Z-wave, GSM y wifi, etc., se pueden implementar fácilmente con un menor costo de instalación, por lo tanto, son mejores candidatos para áreas remotas, pese a que tienen baja tasa de transmisión de datos y problemas de interferencia de señal [20]. La Figura 1.4, tomada de [18], representa un resumen de los valores habituales de la tasa de transmisión de datos de las diferentes tecnologías de comunicación y el área que pueden cubrir cada una de estas.

1.1.4. Protección de microrredes

La protección en las microrredes es uno de los desafíos más importantes, ya que no es fácil diseñar un sistema de protección adecuado que responda a los fallos de la red principal y de la propia microrred. Esto se debe a que las magnitudes de corriente de fallo en el sistema dependen del modo de operación de la microrred, y pueden variar significativamente entre el modo conectado a red y el modo isla [21, 22]. Los sistemas de potencia tradicionales han sido diseñados y construidos con un flujo de corriente de fallo unidireccional. Sin embargo, la integración de las microrredes en la red principal cambia el flujo de corrientes de fallo de unidireccional a bidireccional.

Las microrredes se conectan al sistema de potencia principal mediante un interruptor estático de rápida desconexión, esto con el fin de proteger la microrred en ambos modos de operación y contra todo tipo de fallos [23, 24]. Además, las reglas de interconexión entre la microrred y la red principal están diseñadas para normalizar el proceso y gestionar los impactos de la integración de los generadores distribuidos, sin alterar la funcionalidad y la seguridad de la red principal [25]. Estas reglas establecen

que las microrredes deben desconectarse inmediatamente de la red en caso de fallos [21], apagones, etc…

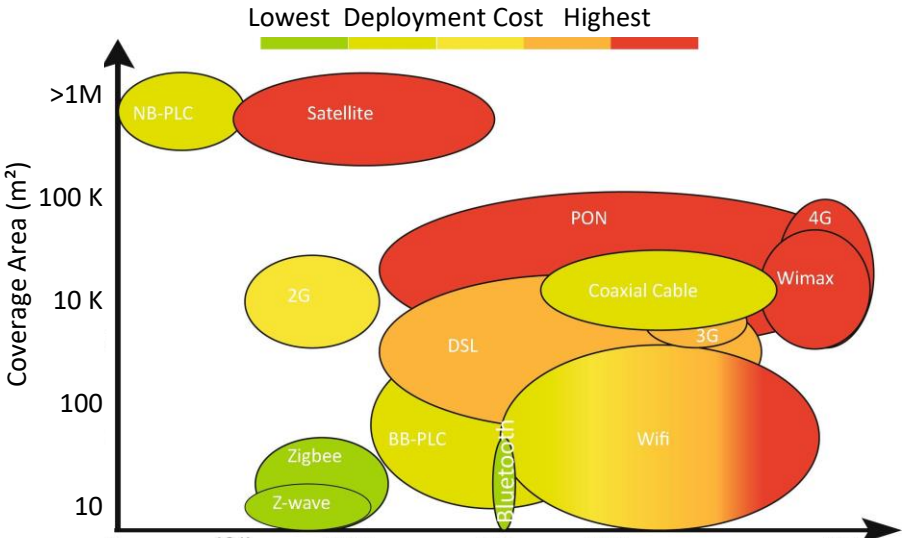

Figura 1.4. Tecnologias de comunicación en microrredes. Tomada de [18].

1.1.5. Estandarización en microrredes

En las últimas décadas, se han desarrollado múltiples tipos de convertidores y diferentes estrategias de control para integrar de manera adecuada los FEERR en la red principal. Por lo tanto, se pueden encontrar una gran variedad de controles, interconexiones e interfaces electrónicas, que dificultan el diseño de un único estándar para conectar las FEERR en la red. Por esta razón, se ha desarrollado una serie de estándares, uno de los más importantes es el Estándar IEEE *"Standard for interconnecting distributed resources with electric power systems 1547"* [26]. Este estándar establece criterios y requisitos para la interconexión de generadores distribuidos con la red eléctrica. Sin embargo, no se ha desarrollado un estándar específico para tratar con microrredes y algunos de los estándares existentes para FEERR pueden adaptarse a ellas. En Europa, algunos de los

estándares existentes, como EN 50160 y IEC 61000, pueden ser también adaptados a las microrredes [27]

1.1.6. Clasificación de las estrategias de control en microrredes

En la actualidad se han desarrollado diferentes estrategias de control adecuadas para la gestión de potencia en microrredes, que dependen de los objetivos de control planteados y del tipo de microrred implementada. Ahora bien, de manera general, estas estrategias de control se pueden clasificar en función del nivel de jerárquico en el que se apliquen [6]. Cada nivel supervisa y proporciona un control sobre los sistemas de nivel inferior. En este sentido, es necesario garantizar que el control y las señales de referencia, enviadas desde el nivel superior a los niveles inferiores, tengan un bajo impacto en el rendimiento, estabilidad y robustez. Por lo tanto, el ancho de banda debe disminuir con un aumento en el nivel de control. Estos niveles de control terciario, segundario y primario se muestran en la Figura 1.5 y se describen a continuación:

Nivel terciario: está encargado de la producción y gestión de la energía, controlando el flujo de potencia entre la microrred y la red, coordinando también el flujo de potencia entre varias microrredes [28]. Adicionalmente, en este nivel se puede tomar en cuenta para la optimización de la energía: la participación en el mercado, factores humanos, costos de mantenimiento, producción, emisiones de los generadores, penalizaciones, etc…

Las estrategias de control terciario se pueden aplicar de forma distribuida o centralizada. En las estrategias distribuidas las comunicaciones y el control se implementan de manera coordinada entre los dispositivos de la microrred, sin necesidad de un controlador central [6]. Su principal limitación se encuentra en entornos no ideales caracterizados por retrasos en la comunicación y errores de medición de las variables [12]. Los cuales causan problemas en la velocidad de convergencia y márgenes de estabilidad de sus controladores [11, 18]. Por otra parte, el control centralizado ofrece la optimización del flujo de potencia en la microrred mediante la coordinación de los dispositivos de la microrred con un sistema centralizado inteligente [29]. El controlador central de la microrred (*Microgrid Central Controller*, MGCC) adquiere datos del sistema y establece la potencia que gestionará cada uno de los convertidores en funcionamiento, transmitiendo referencias de potencia a todos los dispositivos de potencia de la microrred, como generadores distribuidos,

cargas, sistemas de almacenamiento de energía, etc... No obstante, la inclusión de un MGCC puede aumentar el coste inicial del sistema, ya que las estrategias de control y los requisitos de comunicación se vuelven extremadamente complejos cuando aumenta el número de dispositivos conectados en la microrred [6, 30]. Por esta razón, el control centralizado es recomendado en la literatura para la gestión de microrredes de pequeña escala, en las que hay un pequeño número de fuentes de energía distribuida. En este caso, el control centralizado puede proporcionar una gran capacidad de conexión plug and play [29]. En las tablas 1.1 y 1.2, se describen algunas de las estrategias de nivel terciario centralizadas y distribuidas, respectivamente.

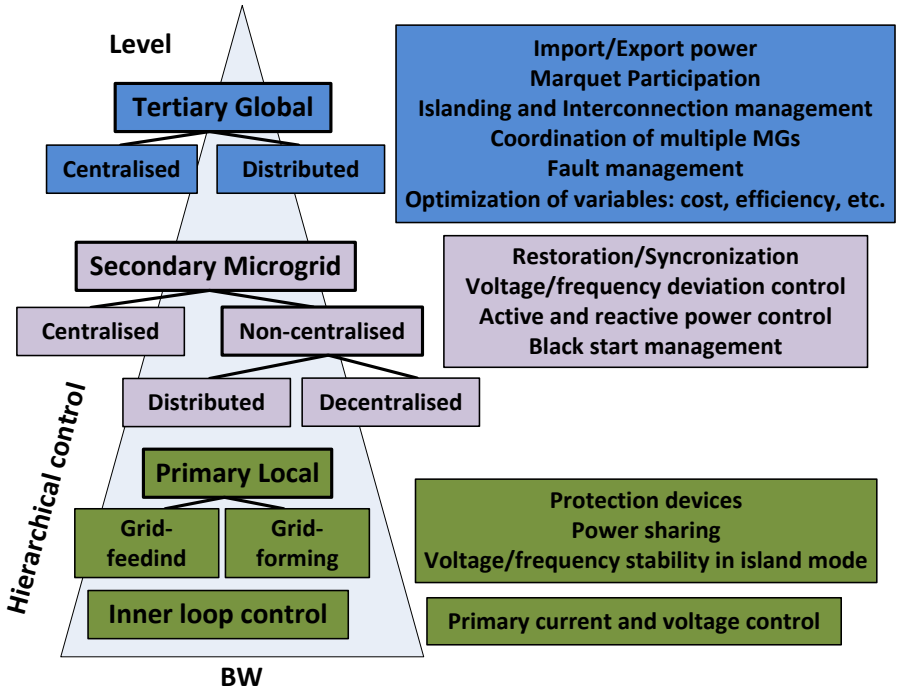

Figura 1.5. Estructura jerárquica de control de las microrredes. Tomado de [6].

Nivel segundario: se asegura de que los niveles eléctricos de la microrred estén dentro de los valores requeridos. Puede incluir un circuito de control de sincronización para conectar/desconectar la microrred a/de la red de distribución principal [28]. Las estrategias de control de este nivel se pueden aplicar de forma centralizada o descentralizada, tal como se describen en las tablas 1.3 y 1.4, respectivamente. En las estrategias de control descentralizadas, las responsabilidades de gestión y control de potencia se integran en los controladores locales de los dispositivos de

generación y almacenamiento, por lo que en caso de un fallo el resto de la microrred puede funcionar normalmente después de desconectar la unidad defectuosa. De acuerdo con [11], algunas estrategias de control descentralizado no necesitan implementar un sistema de comunicación, ya que realizan mediciones locales de los parámetros de interés y permiten garantizar la conexión *plug and play* de las futuras unidades [31]. De esta manera, se puede realizar un control encargado de compensar las variaciones de voltaje y frecuencia de los niveles de control primario. Sin embargo, debido a la falta de monitorización y del canal de comunicaciones, no es posible la optimización del despacho de potencia en la microrred y se crea cierta incertidumbre del estado en que se encuentra cada dispositivo [6].

Nivel primario: a este nivel corresponden los bucles de control interno de cada convertidor electrónico de potencia conectado a la microrred. Incluye los lazos de control de corriente y voltaje, tanto de realimentación como de prealimentación, que permiten regular la tensión de salida y la corriente mientras se mantiene estable el sistema [28]. Así, este control primario se enfoca principalmente a resolver problemas de control locales que tienen un requisito de respuesta muy rápida, tales como el control de transitorios de voltaje/corriente y el intercambio instantáneo de energía [32, 33, 34]. Este nivel está diseñado para satisfacer los siguientes requisitos:

- Después de un evento isla, estabilizar el voltaje y la frecuencia en las fuentes de energía distribuida. Ya que, la microrred puede perder dicha estabilidad en la tensión y la frecuencia debido a la falta de correspondencia entre la potencia generada y la potencia consumida [35].
- Ofrecer la capacidad *plug and play* para las fuentes de energía distribuida y compartir adecuadamente la potencia activa y reactiva entre ellas.

Las estrategias de nivel primario se pueden simplificar en dos tipos: *Grid-following* y *Grid-forming*. La primera es utilizada principalmente cuando la microrred está en modo conectado a la red, donde la tensión y la frecuencia de la microrred son establecidas por ésta [36]. Los controladores locales de los generadores distribuidos usualmente operan como fuentes de corriente controlada que inyectan energía a la red. Esta estrategia es utilizada para optimizar el reparto de potencia entre la microrred y la red principal [9]. Por otra parte, cuando la microrred se encuentra en modo isla,

se utiliza generalmente *Grid-forming*. En este caso, la estabilidad del voltaje y la frecuencia de la microrred tienen que ser aseguradas por los generadores distribuidos del sistema. El método de control *Droop* se usa a menudo en este caso [37], dado que emula el comportamiento físico de los generadores síncronos. También se puede incluir un bucle de control de impedancia virtual para emular la impedancia física de salida de los generadores distribuidos [38].

Tabla 1.1. Estrategias centralizadas de nivel terciario aplicadas a microrredes

Estrategias centralizadas de nivel terciario
[39,40] *Mixed integer linear programming* (MILP). En [40], se presenta un modelo de minimización de operación para la gestión energética óptima de una microrred de tipo residencial. Incorpora el costo del gasto de la energía, de la multa por el desprendimiento o deslastre de carga y el costo de uso de las baterías en vehículos eléctricos, además del factor de temor de agotamiento de la energía en el vehículo eléctrico antes de llegar al destino. Se consideran tres tipos de carga: carga crítica, ajustable y variable. Desventaja: No se discuten los efectos de la gestión en la estabilidad de la microrred [41] *Nonlinear programming.* En [41], se proponen dos políticas de mercado con el fin de determinar las ofertas de precios para la participación de la microrred en el mercado de la energía. El objetivo de la primera política es la minimización del costo operativo de la microrred, mientras que la segunda política tiene como objetivo maximizar su beneficio teniendo en cuenta las transacciones de energía con la red principal. Ambas políticas se resuelven utilizando el método de programación cuadrática secuencial. Desventaja: no se considera el sistema de almacenamiento de energía. [42] Dynamic programming. En [42], se presenta un modelo de gestión para optimizar el funcionamiento de una microrred conectada a la red. El objetivo es minimizar los costes de funcionamiento; que incluyen el costo de comercialización de energía, el costo de envejecimiento de la red principal y la batería. Se estudian dos casos de energía constante y precios de energía dinámicos. Desventaja: no se considera la descarga profunda de las baterías (DOD) y los efectos de la gestión pueden causar un ciclo de vida reducido de las baterías y una mayor inversión por costos de reemplazo. [43] *Rule-based approach*. En [43], se propuso un concepto de prosumers (*producer/consumer*) en la gestión de la microrred, la microrred consiste en prosumers y una microturbina. Siendo el prosumer un anglicismo que se refiere a un consumidor que no se conforma con sólo consumir. Un prosumer se compone del sistema fotovoltaico, batería y ultracondensador. Se consideran dos modelos de gestión para la operación de la microrred. El control central que utiliza un método de optimización basado en reglas para controlar la operación de energía en la microrred, mientras que un control de prosumer administra el equilibrio de energía y la regulación de frecuencia primaria en el sistema. Desventaja: no se toman en consideración el costo de la degradación de la batería y el costo de emisión de los generadores convencionales. [44] *Genetic Algorithm*. En [44], se desarrolló un método de optimización de la microrred, basado en los objetivos de minimización tanto del costo operación como de emisión de gases por parte de los generadores y maximización del beneficio del comercio de la energía producida. Las desventajas son: no se consideran la respuesta de la demanda, de las descargas profundas, ni la complejidad del tiempo computacional del enfoque propuesto. [45] *Meta-heuristic methods*. En [45], se propone un modelo de gestión de dos capas, basado en la optimización de colonias de hormigas para una microrred en modo isla, a fin de minimizar su costo operacional. Incluye el costo de licitación de las FEERR, la batería y el costo de penalización en el desprendimiento de carga. Se estudian tres escenarios de funcionamiento con validación experimental: Funcionamiento normal, exigencia repentina de alta demanda y capacidad plug and play. Desventaja: no se toman en consideración el costo de la degradación de la batería, ni el costo de emisión de los generadores convencionales. [46] *Fuzzy logic*. En [46], se propuso un control basado en lógica difusa para una microrred aislada, que minimiza el costo neto junto con el costo de penalización del estado de carga de la batería (*State of Charge*, SOC), del almacenamiento de hidrógeno y del agua. Las demandas de carga se dividen

en tres categorías: carga eléctrica, carga de agua y carga de transporte. Las entradas de decisión para el sistema de lógica difusa son SOC de batería, agua y frecuencia del sistema. Desventaja: no se discute la complejidad del tiempo de cálculo del enfoque propuesto

[47] *Neural Network*. En [47], se presentó un enfoque de redes neuronales con programación de Lagrange para minimizar el costo total de una microrred. El método incluye el costo del combustible, los costos de operación y mantenimiento, y el costo de emisión de las unidades de generación. Se pronostica la generación de energía de los FEERR y la demanda de la carga. Para considerar la respuesta en la demanda, la carga se divide en cuatro categorías: carga crítica, controlable, sensible al precio y térmica. Desventaja: No se discute la complejidad del tiempo computacional. No se considera el costo operacional de la batería.

Tabla 1.2. Estrategias distribuidas de nivel terciario aplicadas a microrredes

Estrategias descentralizadas de nivel terciario
[48] *Multi-agent system*. En [48], se propone un control basado en multi-agente jerárquico y multi-objetivo en una microrred conectada a la red, para minimizar su costo operativo, costo de emisión y pérdidas en la línea. El multi-agente jerárquico está dividido en tres niveles. El agente de nivel superior se ocupa de la optimización energética de la microrred. Los agentes de nivel medio se encargan de la coordinación entre los agentes de control para cambiar los modos de operación usando el modelo de Petri-net para la regulación de voltaje. Los agentes de nivel inferior definen las estrategias de control basadas en variación de frecuencia/tensión y potencia reactiva, para gestionar el funcionamiento de las FEERR en tiempo real. Desventaja: formulación de la optimización muy compleja, no se discute el tiempo de cálculo del enfoque propuesto.
[49] *Game theory*. En [49], se propuso el enfoque de la teoría del juego de Stackelberg, basada en los prosumers para la gestión óptima de la energía en una microrred conectada a la red. Funciona según el principio del modelo de líder-seguidor, donde microrred actúa como líder y todos los prosumers (Generadores fotovoltaicos) son seguidores. En el modelo propuesto, las incertidumbres de la energía solar y la demanda de carga se abordan mediante un enfoque de mecanismo de facturación. En este enfoque, la desviación horaria entre potencia programada y la real se compensa regulando los ingresos o costos de los usuarios de fotovoltaica con respecto a sus contribuciones en las ganancias de la microrred. El objetivo del líder, es la maximización de los beneficios globales, mientras que los objetivos del seguidor son la máxima utilización de los recursos energéticos a nivel de los prosumers. Sin embargo, un prosumer con un parámetro de preferencia más alto en el consumo de su energía, tiene un nivel de utilización más alto que, a su vez, disminuye los beneficios. Por lo tanto, existe una compensación entre el nivel de utilización y el beneficio, en referencia al parámetro de preferencia. Desventaja: formulación de la optimización compleja. No toma en cuenta el sistema de almacenamiento de energía, lo que puede provocar una pérdida de la carga conectada en caso de perturbación en la red principal.
[50] *Robust optimization.* En [50], se propuso un método para una microrred conectada a la red, que utiliza un modelo basado en agentes y un enfoque de optimización robusta para mejorar su rendimiento y fiabilidad. El rendimiento de la microrred se determina en términos del costo de desequilibrio asociado con las incertidumbres de la producción de potencia de los FEERR, la demanda de carga y el precio de la electricidad. Además, la confiabilidad de microrred mejora al considerar la pérdida de energía esperada y la pérdida de los parámetros de expectativa de carga. También maximiza los ingresos de la unidad de energía eólica a nivel individual. Desventaja: formulación de la optimización compleja.

Tabla 1.3. Estrategias centralizadas de nivel segundario aplicadas a microrredes

Centralizadas
[29] *Linear and mixer integer linear programming.* En [29], se propone un método que realiza el reparto de potencia y optimiza el funcionamiento de la microrred dependiendo del estado de la conexión con la red principal, aplicando dos modos de funcionamiento en los sistemas de almacenamiento de energía. Estos modos son: funcionamiento a modo ejecución continua (la celda de combustible está obligada a funcionar de manera permanente) y funcionamiento a modo mixto basado en el encendido/apagado de las celda de combustible.
[35], [51] *Droop-based*. En [35] se realiza un control encargado de compensar las variaciones de voltaje y frecuencia en los niveles de control primario, basado en referencias establecidas por el nivel superior de control, cuando opera en modo conectado a red. Alternativamente, estas referencias son internamente generadas cuando la microrred pasa a modo isla. En [51], se propone un controlador que recopila la información de las unidades generadores distribuidos y genera las referencias de potencia activa y reactiva para cada dispositivo. Este método proporciona una distribución de potencia activa y reactiva equilibrada entre los dispositivos controlados, mejorando las características de las técnicas basadas en droop. Desventaja: los efectos de la gestión pueden causar un ciclo de vida reducido de las baterías y una mayor inversión por costos de reemplazo
[52] *Mixed integer nonlinear.* En [52], se ha propuesto un modelo de control no lineal para la operación óptima de una microrred en modo isla. El modelo desarrollado incluye el costo operativo de generadores como una función objetiva. El funcionamiento de las unidades de desalinización del agua, también se incluyen como una restricción en el modelo propuesto. Además, el envío de potencia activa y reactiva es controlada por lazos de control droop del lado de AC. Desventaja: no se consideran el costo de las emisiones de los generadores convencionales, ni el funcionamiento de los sistemas de almacenamiento de energía.
[53] *Nonlinear programming.* En [53], desarrolla un modelo encargado de minimizar el costo de funcionamiento de una microrred conectada a la red. El algoritmo utilizado es restringido por una ventana de operación de voltaje y determina la solución de flujo de potencia en la microrred. Considera tres escenarios en la función objetivo; los beneficios para el cliente, pérdidas de red y niveles de carga conectada. Desventaja: no se considera el costo operacional de los FEERR, ni en las descargas profunda de las baterías. Los efectos de la gestión pueden causar un ciclo de vida reducido de las baterías y una mayor inversión por costos de reemplazo.
[54] *Rule-based approach.* En [54], se propone un modelo de gestión de energía basado en reglas centralizadas, para los modos de operación de la microrred: modo isla y modo conectado a la red. Este modelo garantiza una transición suave entre estos dos modos con respecto al voltaje y la estabilidad de frecuencia del sistema. En el modo isla, la celda de combustible funciona solo si el SOC de la batería está por debajo del 80%. Mientras que, en modo conectado a la red, el SOC de la batería debe permanecer más del 60% para tener una operación confiable en modo isla. Desventaja: el modelo no toma en consideración la demanda de la carga y la disponibilidad futura de las FEERR.
[55], [56] *Battery SOC rule-based approach.* En [55], se presentó una estructura jerárquica basada en el SOC de batería para la microrred y propuso ultracondensadores para la regulación de la potencia. El SOC y el nivel de energía de los ultracondensadores determinan la selección de cuatro modos de funcionamiento diferentes para una gestión energética eficiente de la microrred. Estos modos son: modo normal, modo de limitación de generación fotovoltaica, modo de recuperación y modo de desconexión. Desventaja: no se discuten los efectos de ocasionados en la estabilidad de la

microrred por cambios en la demanda de energía. En [56], se utiliza un método basado en el SOC para la gestión de una microrred residencial conectada a la red. Utiliza un método para reducir los picos y las fluctuaciones dentro del intercambio de energía de la microrred con la red principal, a través de la administración del SOC. La desventaja es que selecciona un alto valor de descarga que conduce a una degradación rápida de la batería.
[57] *Fuzzy logic*. En [57], se presentó un método basado en lógica difusa para lograr un flujo de potencia suave de una microrred residencial conectado a la red. El modelo propuesto minimiza las fluctuaciones y los picos de potencia en el intercambio de energía con la red principal. También mantiene el nivel del SOC cerca del 75% de su capacidad nominal para mejorar su vida útil. Desventaja: no es considerado la regulación de voltaje y frecuencia
[58] *Stochastic method*. En [58], se presenta un control estocástico para una microrred aislada, controlada por control droop. Minimiza las desviaciones de frecuencia durante la operación diaria de la microrred y limita los costos operacionales y de emisión de la microrred a un nivel razonable. El costo operacional de microrred incluye el costo operativo de los generadores convencionales, FEERR y reservas, costo de desprendimiento de carga e incentivos. Desventaja: no se discute la complejidad del tiempo computacional del enfoque propuesto.

Tabla 1.4. Estrategias descentralizadas de nivel segundario aplicadas a microrredes

Descentralizadas
[59] *Multi-agent system.* En [59] se presenta un enfoque descentralizado basado en multi-agentes para el funcionamiento óptimo de una microrred conectada a la red. Todos los consumidores, unidades de almacenamiento, unidades de generación y red se consideran agentes. En la toma de decisiones, se ha considerado como un factor importante la preferencia de consumo del consumidor. El algoritmo multi-agente reduce el costo del desequilibrio de energía al mismo tiempo que considera la preferencia de consumo del consumidor, como un factor importante en el proceso de toma de decisiones. Desventaja: no se consideran los efectos de los ciclos de carga ni descarga en la vida útil de la batería.
[60][61] *Fuzzy interference.* En [60] se ha propuesto una estrategia de control secundaria que usa variables locales para realizar el control de las unidades de almacenamiento. El método se basa en la inferencia difusa, para equilibrar adecuadamente el estado de carga del sistema de almacenamiento de energía mientras se proporciona una compensación de la desviación de voltaje. Esta técnica también es usada en [61] para restaurar la desviación de frecuencia producida en los controles primarios droop. Desventaja: no se consideran los efectos de los ciclos de carga ni descarga en la vida útil de la batería.
[62] *Virtual impedance*: La estrategia propuesta en [62] realiza la regulación de voltaje mediante un bucle de impedancia adaptativa virtual y realiza la regulación de frecuencia mediante un bucle de impedancia de frecuencia virtual. Desventaja: no se considera los sistemas de almacenamiento de energía en la regulación.

1.1.7. Microrredes conectados a Red

El objetivo principal de la microrred en modo conectado a red es optimizar el flujo de potencia entre la microrred y la red, así como también reducir la factura de electricidad mientras se satisface las necesidades y preferencias de la cargas. Para ello, en la literatura se han aplicado diversas técnicas de optimización y estrategias de control para garantizar una programación adecuada del consumo y de la generación de energía, con un costo mínimo de electricidad y sin perder capacidades de funcionamiento [6,29,37], [63-66]. Para una gestión adecuada de la generación y el consumo de energía se utilizan datos como las tarifas eléctricas, el pronóstico del tiempo o la demanda de energía [66]. Recientemente, los esquemas de precios han sido utilizados en la literatura para optimizar los beneficios económicos de los productores y consumidores de energía [66-71]. Una aplicación industrial con una óptima estrategia se presentó en [70] y se consideró una factura mensual para realizar la optimización de varios días. En [67] se presentó un modelo de gestión para instalaciones residenciales con sistemas de vehículo eléctrico que se conectan a la red. En [67 y 70] se consideraron los costos de desgaste de la batería y el precio de la tarifa eléctrica. En [68] se propuso un sistema de gestión de energía en el hogar para minimizar el coste de la electricidad mientras se mantiene la comodidad del usuario. El algoritmo que se presenta en [71] encuentra un momento apropiado para cargar vehículos eléctricos con bajo coste en la tarifa eléctrica, basado en la predicción de los precios de la energía durante el período de carga.

1.1.8. Sistemas de almacenamiento de energía en microrredes

Los sistemas de almacenamiento de energía son parte fundamental de una microrred ya que permiten un mejor aprovechamiento de las FEERRs y contribuyen a mejorar el balance de potencia, la estabilidad y fiabilidad de la microrred [11,16]. Los sistemas de almacenamiento de energía se clasifican en tres categorías: sistemas electroquímicos (baterías y baterías de flujo [72]), sistemas de almacenamiento de energía cinética (volante de inercia [73]) y almacenamiento de energía potencial (hidro-bombas [74] y almacenamiento de aire comprimido [75]).

Las baterías son el mejor y más utilizado dispositivo de almacenamiento de energía, gracias a la rápida evolución de la tecnología en *smart grids* y vehículos eléctricos [76]. Las baterías están hechas de células apiladas donde la energía química se convierte en energía eléctrica y viceversa. Las características más importantes de una batería son la eficiencia, vida útil (expresada en términos de número de ciclos), temperatura de funcionamiento

y la profundidad de descarga (*depth of discharge*, DOD). Hay que tener en cuenta que las baterías, generalmente, no se descargan completamente y la profundidad de descarga se refiere a la medida en que se descargan.

Los grandes aumentos en la escala de fabricación, las mejoras en la capacidad de almacenamiento, la densidad y las reducciones en los costes del material están ayudando a minimizar los costes de las baterías y de otras tecnologías de almacenamiento [11]. Las baterías utilizadas en aplicaciones de almacenamiento de energía en microrredes son: ácido-plomo (LA) o de ácido-plomo regulada por válvula (VRLA), níquel-cadmio (Ni-Cd), níquel-metal hidruro (NiMh) y de ión de litio (Li-ion). Sin embargo, debido a su bajo coste, las baterías más prominentes y utilizadas en microrredes son: ácido-plomo y de ión de litio. En [77] se muestra un estudio de las características más importantes de las baterías.

En la Tabla 1.5 se muestran las características más relevantes de las baterías de ácido-plomo y de ión de litio. Las ácido-plomo han experimentado un aumento en la vida útil gracias a la integración de carbono, este avance ha reducido los costes de fabricación de estas baterías dramáticamente. Las baterías ácido-plomo tienen costes de implementación más bajos que otras tecnologías [78-79] y presentan un rendimiento relativamente alto y gran robustez. Su principal desventaja con respecto a la batería de litio sigue siendo su corto ciclo de vida (1500-9000 ciclos) y su menor densidad energética. Por otra parte, las baterías de litio tienen un ciclo de vida muy alto (>10000 ciclos) y su eficiencia es superior al 95%. Entre 2010 y 2015, el precio promedio de las baterías de litio utilizadas en los vehículos eléctricos disminuyó un 65%, aproximadamente hasta los 350 USD por kW·h. A finales de 2016, los precios de la tecnología de litio desarrollados a gran escala fueron entre 1600 USD a 1900 USD por kW instalado (un ejemplo comparable con una planta de energía a gas natural de 100 MW) [1]. No obstante, comparando las baterías de litio con las de ácido-plomo sus obstáculos principales son: el alto costo (> USD 350/kW·h) [80], la falta de una tecnología para su reciclaje [78] y la complejidad del sistema de gestión de la batería, debida a los circuitos internos de protección [81-84], [85].

1.1.9. Sistema de gestión de las baterías (BMS)

El BMS es un sistema que implementa funciones que aseguran el uso óptimo de la batería. Para el diseño apropiado del BMS, se debe tener en consideración algunos factores que permitan una operación adecuada de las baterías, así como también prolongar el tiempo de servicio de las mismas. Estos parámetros son: (i) operar las baterías en sus niveles de carga/descarga

adecuados, monitorizando el estado de carga [29]; y (ii) evitar las descargas profundas con el fin de aumentar la vida útil de las baterías [76-77]. Vale la pena destacar que la vida útil depende también de otros factores como son: las variaciones en la temperatura, la corrosión, etc...

Tabla 1.5. Principales caracteristicas de las baterías más utilizadas en microrredes. Tomado de [77]

Tipo de batería	Rango de potencia (MW)	Tiempo de descarga	Tiempo de vida (años)	Ciclo de vida (ciclos)	Eficiencia (%)	Precio (USD/kW·h)
Acido- Plomo	0-20	Segundos - horas	5-15	1500-9000	70-90%	180-300
Litio	0-0.1	Minutos-horas	5-15	>10000	Cerca del 100%	350-1100

En las microrredes los dispositivos encargados del almacenamiento de la energía en las baterías deben poseer un BMS con funcionalidades básicas [81-82], que debe implementar un algoritmo encargado de cargar las baterías con un procedimiento adecuado y dos modos de carga: carga a corriente controlada (CC) y carga a voltaje controlado (CV) [83-87]. Sin embargo, en las microrredes se pueden presentar altas fluctuaciones en la potencia generada por las FEERRs, que causan variaciones inesperadas en las corrientes de carga/descarga de las baterías. Estas variaciones aumentan la complejidad del BMS y exigen la utilización de técnicas de gestión de carga más avanzadas [85]. En [86] y [87], se presenta una revisión de los algoritmos utilizados para diferentes aplicaciones y sus limitaciones. Otros elementos que aumentan la complejidad del BMS son el tipo de baterías utilizadas y las técnicas de determinación del estado de carga (*state of charge,* SOC), el estado de salud (*state of health*, SOH) y el estado de vida (*state of life*) de las baterías [82].

El SOH y SOL son similares. No obstante, el SOH representa una estimación de la capacidad de la batería para almacenar o entregar energía comparada con una batería nueva [88], mientras que el SOL es el tiempo restante hasta que la batería debe ser reemplazada [82]. Es posible estimar el SOL, recopilando datos correspondientes a las descargas profundas y temperaturas a las que han sido expuestas las baterías [77].

El SOC es un indicador que representa la cantidad de carga almacenada en la batería comparada con la capacidad de carga completa (*full charge*) de la batería, y es usado para determinar la potencia que se puede extraer de las mismas. Debido a las reacciones químicas inherentes en las baterías y a diferentes factores, la capacidad máxima de las baterías va disminuyendo en el

tiempo. Además, el SOC no puede ser medido directamente en la batería. Por lo tanto, suele ser estimado en función de las medidas de tensión y corriente. En la literatura se presentan diferentes métodos de estimación del SOC, como son: método de la integral de amperios-hora o método de conteo de Coulomb [89], método de medición de la tensión de circuito abierto [90], método de medición de impedancia electroquímica [91], método basado en aprendizaje automático [92], método basado en los filtros Kalman [93], método de observación de ganancia adaptativa no lineal [94] y el método de observación en modo deslizamiento [95], entre otros. Los primeros cuatro métodos no necesitan establecer el modelo de la batería, por lo que generalmente se llaman "métodos no basados en modelos" (*non-model based methods*). Estos métodos no pueden corregir errores causados por una inicialización incorrecta del valor del SOC, por ruido de medida o por algunas perturbaciones externas. Sin embargo, en la practica el SOC puede ser calibrado refiriendo la calibración inicial al punto de carga completa y tomando en cuenta el envejecimiento de las baterías. Esto se logra mediante la comparación de los datos actuales de la batería con los datos almacenados en una tabla con información precisa de la capacidad de descarga y la tensión de circuito abierto [71].

En la tabla 1.6 se comparan algunos de los cargadores de baterías reportados en la literatura. Cada parámetro de comparación se describe a continuación:

- Monitorización: Se refiere a la medida y/o estimación de los parámetros de las baterías: tensión, corriente, temperatura e impedancia. Esta monitorización permite al BMS la estimación del SOC, del SOH y del modelo de la batería. Asimismo, permite almacenar los datos de las baterías, los cuales son utilizados para realizar calibraciones del sistema debido al envejecimiento de las baterías. Se puede almacenar los datos referidos al número de DOD realizados y las temperaturas a las que han sido expuestas las baterías. Se puede estimar cuándo las baterías deben ser reemplazadas [96].

- Protección: Se refiere a la protección y diagnóstico de las baterías, que se puede realizar en el *hardware* y en el *software*. Puede incluir: protección contra sobrecargas, sobrecorrientes, protección térmica, protección por fallos de la comunicación y alarmas de fallos [97].

- Control: Es la etapa del BMS que aplica el algoritmo encargado de ejecutar los procedimientos de carga de la batería. Su objetivo es prolongar la vida útil de las mismas. Asimismo, las baterías pueden ser

cargadas o descargadas en función del coste de la tarifa eléctrica y de la disponibilidad de energía presente en las FEERR de la microrred [112].

Tabla 1.6. Tabla comparativa de algunos de los cargadores de baterías reportados en la literatura

Sistema de gestión de baterias												
Monitorización			Proteción				Control			Aplicaciones		
	Estimación											
Modelo de la bateria	SOC	SOH	Temperatura	Sobrecarga	Sobrecorrientes	Perdidas de comunicacion	Gestion termica	Optimización	Sistema de comunicación		Reference
– [(1)]	•	–	–	–	–	–	–	–	•	Fuente de alimentación ininterrumpida	[98]
•	•	–	–	•	•	•	•	•	•	Microrred de DC	[99]
–	•	–	•	•	•	•	–	–	•	Fuente de alimentación ininterrumpida	[100]
–	•	–	•	•	•	–	•	•	–	Dispositivos portatiles	[101]
•	–	•	–	•	•	–	–	–	–	Motocicletas, carros y sillas de ruedas	[102]
–	–	–	•	•	•	–	–	–	•	Dispositivos portatiles	[103]
–	–	•	•	•	•	–	•	•	•	Dispositivos portatiles	[104]
–	•	•	•	•	•	–	•	•	–	Vehiculos eléctricos híbridos	[105]
–	–	–	•	•	•	–	•	•	•	Aplicaciones portatiles	[106]
–	•	–	•	•	•	–	–	–	–	Vehiculos eléctricos	[107]
–	•	–	•	•	•	–	•	•	–	Motocicletas, carros y sillas de ruedas	[108]
•	•	–	•	•	•	–	–	–	–	Sistema fotovoltaico	[109]
–	•	–	–	•	•	–	–	–	–	Vehiculos eléctricos y híbridos	[110]
–	•	–	•	•	•	–	–	–	–	Sistema fotovoltaico	[111]

[1] Un (•) indica que corresponde en la categoría especificada en el encabezado de la columna; un (-) indica que no lo hace.

- Sistema de comunicación: Este permite informar al usuario, a otros dispositivos o al controlador central los parámetros de las baterías, con el fin de optimizar el uso de la energía en la microrred. Las comunicaciones permiten agregar el interfaz con el usuario, que da protagonismo a la actuación del usuario con el despacho y gestión de la energía dentro de la microrred.

1.2. Motivación y Objetivos

1.2.1. Motivación

Los aspectos críticos en la operación de una microrred son las estrategias de control y gestión de potencia, esenciales para su buen funcionamiento. La aplicación adecuada de dichas estrategias permite compensar los desequilibrios de potencia causados por la discrepancia entre la generación y la demanda en las microrredes. En este sentido, el objetivo global de estas estrategias de gestión es equilibrar adecuadamente el flujo de potencia en la microrred mediante la aplicación de varios algoritmos que permiten cumplir con los criterios de estabilidad, protección, balance de potencia, respuesta transitoria, sincronización y gestión adecuada de los recursos de la microrred.

La tesis se enfoca en aplicar estrategias de control centralizado en la microrred, donde el despacho de potencia es observado y gestionado por un controlador central. Este último adquiere datos del sistema mediante una infraestructura de comunicaciones y estima la potencia que gestionará cada uno de los convertidores de potencia, sistemas de almacenamiento y cargas en funcionamiento.

En este estudio se muestra la validación experimental de las estrategias de gestión de potencia aplicadas a la microrred, desde el enfoque del comportamiento de los convertidores de potencia, de las baterías y de las cargas. Se verifica la estabilidad de la microrred sometiéndola a diferentes escenarios realistas de funcionamiento, como: fluctuaciones en la irradiación solar, en la demanda, en el estado de carga de las baterías, en la tarifa eléctrica, y en los límites máximos de exportación/importación de potencia desde/hacia la microrred hacia/desde la red principal.

Un parámetro importante de estas estrategias de gestión centralizadas es el tiempo de cómputo de los algoritmos de gestión, que ocasiona retardos en la aplicación de las consignas de potencia enviadas a los convertidores presentes en la microrred y, en consecuencia, puede causar cambios bruscos en el flujo de potencia y desestabilizarla. Por este motivo, en este estudio se implementan algoritmos de gestión de potencia que pueden ser ejecutados por microcontroladores. Adicionalmente, las comunicaciones implementadas permiten un adecuado flujo de potencia en la microrred, así como también integrar otros elementos en ésta si es necesario.

Debido a su naturaleza intermitente, las FEERRs pueden presentar fuertes desequilibrios de potencia en la microrred. Estos pueden ser compensados

mediante la gestión de la potencia de carga y descarga del sistema de almacenamiento de energía presente en la misma. Para ello, en este estudio se propone un sistema de almacenamiento en baterías (*Battery Energy Storage System*, BESS), encargado de mantener el equilibrio de potencia en el bus de DC, que permite aprovechar las fuentes de generación renovables presentes en la microrred y maximizar el tiempo de servicio de las baterías mediante la aplicación de un algoritmo BMS. Este último, aplica un procedimiento de carga especificado por el fabricante y ajusta las tasas de carga en función del estado de la microrred. El procedimiento de carga en las baterías es fundamental para garantizar las condiciones adecuadas de operación de las mismas, ya que toman en consideración los parámetros establecidos por el fabricante, como son: tasas de carga/descarga, tensión máxima de carga, temperatura de operación, etc... El BESS propuesto permite minimizar el coste de la energía importada de la red principal mediante la gestión conjunta con el controlador central.

En este trabajo la estrategia utilizada para reducir el coste de la factura eléctrica en la microrred conectada a red consiste en gestionar el funcionamiento del sistema de almacenamiento, cambiando el horario de aprovechamiento de la energía almacenada en baterías a partir de las opciones de generación que contenga la microrred. Esto permite cargar las baterías cuando la demanda y el precio de la electricidad son bajos, para posteriormente utilizar la energía almacenada cuando la demanda y el precio de la energía son altos, en lugar de importar electricidad a un alto precio.

1.2.2. Objetivos principales de la tesis.

- Desarrollo, implementación y validación de algoritmos de gestión centralizados para el despacho inteligente de potencia de los convertidores conectados al bus DC de una microrred AC/DC híbrida de generación distribuida en modo conectado a red. La estructura de la microrred se muestra en la Figura 1.6.

- Diseño e implementación de un sistema de almacenamiento de energía en baterías para la microrred, que permita maximizar el tiempo de vida de las baterías, mediante la aplicación de un procedimiento de carga recomendado por el fabricante [113-115].

1.2.3. Objetivos específicos de la tesis

- Estudio de los algoritmos de gestión y despacho de potencia en una microrred híbrida, hallando sus ventajas e inconvenientes.

- Estudio y validación por simulación de los algoritmos de gestión planteados, tomando como consideración principal el aprovechamiento máximo de la energía generada y almacenada en la microrred.

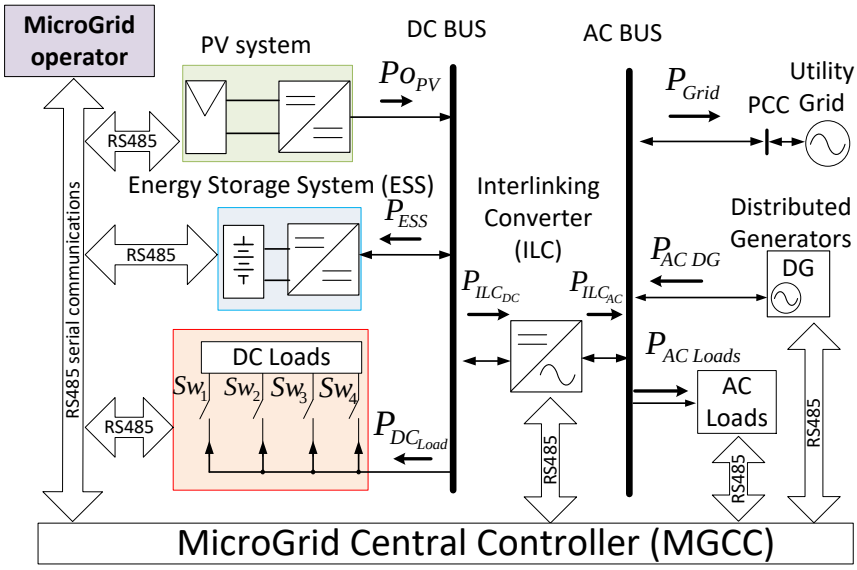

Figura 1.6. Estructura de la microrred AC/DC híbrida desarrollada en la tesis.

- Diseño e implementación de cada uno de los convertidores de potencia de la microrred híbrida, para la validación realista de los resultados de simulación.

- Diseño, implementación y evaluación experimental de los lazos de control de las etapas de potencia de los convertidores presentes en la microrred híbrida.

- Diseño e implementación experimental de una plataforma de monitorización y control de los convertidores presentes en la microrred estudiada.

- Estudio y comprobación experimental del comportamiento de los convertidores de potencia presentes en la microrred ante diferentes escenarios realistas de funcionamiento.

1.3 Estructura de la Tesis

El trabajo de investigación desarrollado durante la presente tesis doctoral ha sido realizado en la Universitat Politècnica de Valencia, en el Departamento de Ingeniería Electrónica, dentro del Grupo de Sistemas Electrónicos Industriales (GSEI).

Esta tesis se presenta como compendio de las publicaciones [i, ii, iii], consistente en 3 artículos en una revista internacional que presentan la parte más significativa de los estudios teórico-prácticos realizados entre Julio del 2015 y Agosto de 2018. Estas publicaciones se muestran íntegramente en los apartados 2-4. Por otro lado, durante la realización de esta tesis se han elaborado otras publicaciones no incluidas en este compendio [iv -ix].

La memoria de la tesis se divide en seis (6) capítulos:

- En el capítulo 1 se presenta la introducción, la motivación y los objetivos más relevantes de la tesis. Se introducen los aspectos fundamentales de las microrredes, incluyendo una clasificación de las estrategias de gestión de potencia de las mismas. Asimismo, se muestra una descripción de los parámetros principales de los sistemas de almacenamiento en baterías reportados en la literatura.

- En los capítulos 2, 3 y 4 se concentra el núcleo central de la tesis y se presentan tres artículos publicados en la revista internacional *Energies* (ISSN: 1996-1073), factor impacto para el 2017 de 2.676 y puesto 48/97 de la categoría "*Energy & Fuels*" del JCR, correspondiento al segundo cuartil (Q2). Los artículos muestran los diferentes algoritmos de gestión de potencia implementados y la validación experimental de las estrategias planteadas.

- Los análisis de los resultados obtenidos durante la realización de la tesis se muestran en el capítulo 5.

- Por último, en el capítulo 6 se presentan las conclusiones generales y las posibles líneas de investigación derivadas de los logros alcanzados en la tesis.

1.4 Publicaciones

En esta sección se presentan las publicaciones obtenidas durante el desarrollo de la tesis [116-124]. Las tres primeras (i), (ii) y (iii) corresponden a

los capítulos II, III y IV presentados en esta tesis como compendio de publicaciones.

(i) Salas-Puente, Robert; Marzal, Silvia; González-Medina, Raúl; Figueres, Emilio; Garcera, Gabriel. 2018. *"Power Management of the DC Bus Connected Converters in a Hybrid AC/DC Microgrid Tied to the Main Grid." Energies* 11, no. 4: 794. https://doi.org/10.3390/en11040794 [116].

(ii) Salas-Puente, Robert; Marzal, Silvia; González-Medina, Raúl; Figueres, Emilio; Garcera, Gabriel. 2017. *"Experimental Study of a Centralized Control Strategy of a DC Microgrid Working in Grid Connected Mode." Energies* 10, no. 10: 1627. https://doi.org/10.3390/en10101627 [117].

(iii) Salas-Puente, Robert; Marzal, Silvia; Gonzalez-Medina, Raul; Figueres, Emilio; Garcera, Gabriel. 2018. *"Practical Analysis and Design of a Battery Management System for a Grid-Connected DC Microgrid for the Reduction of the Tariff Cost and Battery Life Maximization." Energies* 11, no. 7: 1889. https://doi.org/10.3390/en11071889 [118].

(iv) Robert Salas-Puente, Silvia Marzal, Raúl González-Medina, Emilio Figueres and Gabriel Garcerá (2018) "*An Algorithm for the Efficient Management of the Power Converters Connected to the DC Bus of a Hybrid Microgrid Operating in Grid-connection Mode*", Electric Power Components and Systems, DOI: 10.1080/15325008.2018.1469177 [119].

(v) R. Salas-Puente, S. Marzal, R. González-Medina, E. Figueres and G. Garcerá, *"Efficient management strategy of the power converters connected to the DC bus in a hybrid microgrid of Distributed Generation,"* 2017 19th European Conference on Power Electronics and Applications (EPE'17 ECCE Europe), Warsaw, 2017, pp. P.1-P.10. DOI: 10.23919/EPE17ECCEEurope.2017.8098994 [120].

(vi) Silvia Marzal, Robert Salas, Raúl González-Medina, Gabriel Garcerá, Emilio Figueres, *"Current challenges and future trends in the field of communication architectures for microgrids," Renewable and Sustainable Energy Reviews*, Volume 82, Part 3, 2018, Pages 3610-3622, ISSN 1364-0321, https://doi.org/10.1016/j.rser.2017.10.101 [121].

(vii) S. Marzal, R. Salas-Puente, R. González-Medina, G. Garcerá and E. Figueres, *"Efficient Event Notification Middleware for Smart Microgrids over P2P Networks,"* in *IEEE Transactions on Smart Grid*. doi: 10.1109/TSG.2018.2865432 [122].

(viii) Marzal, Silvia; González-Medina, Raul; Salas-Puente, Robert; Figueres, Emilio; Garcerá, Gabriel.2017. *"A Novel Locality Algorithm and Peer-to-Peer Communication Infrastructure for Optimizing Network Performance in Smart Microgrids."* *Energies* 10, no. 9: 1275. https://doi.org/10.3390/en10091275 [123].

(ix) S. Marzal, R. Salas-Puente, R. González-Medina, E. Figueres and G. Garcerá, *"Peer-to-peer decentralized control structure for real time monitoring and control of microgrids,"* 2017 IEEE 26th International Symposium on Industrial Electronics (ISIE), Edinburgh, 2017, pp. 140-145. DOI: 10.1109/ISIE.2017.8001237 [124].

2

2. PUBLICACIÓN I

2.POWER MANAGEMENT OF THE DC BUS CONNECTED CONVERTERS IN A HYBRID AC/DC MICROGRID TIED TO THE MAIN GRID

Salas-Puente, Robert; Marzal, Silvia; González-Medina, Raúl; Figueres, Emilio; Garcera, Gabriel. 2018. "Power Management of the DC Bus Connected Converters in a Hybrid AC/DC Microgrid Tied to the Main Grid." Energies 11, no. 4: 794. DOI: 10.3390/en11040794.

Article

Power Management of the DC Bus Connected Converters in a Hybrid AC/DC Microgrid Tied to the Main Grid

Robert Salas-Puente *, Silvia Marzal, Raúl González-Medina, Emilio Figueres and Gabriel Garcera

Grupo de Sistemas Electrónicos Industriales del Departamento de Ingeniería Electrónica, Universitat Politècnica de València, Camino de Vera s/n, 46022 Valencia, Spain; silmarro@upv.es (S.M.); raugonme@upv.es (R.G.-M.); efiguere@eln.upv.es (E.F.); ggarcera@eln.upv.es (G.G.)

* Correspondence: rosapue1@posgrado.upv.es; Tel.: +34-(96)-3877007 (ext. 76021)

Received: 14 February 2018 / Accepted: 26 March 2018 / Published: 29 March 2018

Abstract: In this paper, a centralized control strategy for the efficient power management of power converters composing a hybrid AC/DC microgrid is explained. The study is focused on the converters connected to the DC bus. The proposed power management algorithm is implemented in a microgrid central processor which is based on assigning several operation functions to each of the generators, loads and energy storage systems in the microgrid. The power flows between the DC and AC buses are studied in several operational scenarios to verify the proposed control. Experimental and simulation results demonstrate that the algorithm allows control of the power dispatch inside the microgrid properly by performing the following tasks: communication among power converters, the grid operator and loads; connection and disconnection of loads; control of the power exchange between the distributed generators and the energy storage system and, finally, supervision of the power dispatch limit set by the grid operator.

Keywords: power management algorithm; microgrid; communication with power converters

2.1. Introduction

Most countries are dependent on fossil fuels and nuclear energy for electric power generation. However, due to the increasing energy demand and the proliferation of new forms of energy generation which are cheaper and environmentally-friendly, many distributed generation (DG) systems have been integrated into the power grid. Some DGs consist of Renewable Energy Sources (RES), such as Photovoltaic (PV), wind, biomass and geothermal [1]. The DGs are the basis of Microgrids (MGs), which can operate as a single power system that provides a safe and reliable operation at certain voltage and load levels. MGs may work in island-mode or in grid-connected mode, so that they can connect to DGs placed at various locations and inject their energy to the grid if it is needed [2]. The transition between these two operation modes is a process that can destabilize the voltage at the MG buses and damage the MG. In [3], a methodology to recover the MG operation during this transition was presented, along with the main technical problems which should be taken into account. There are three basic MG topologies that can be classified according to the nature of their voltage: DC microgrid (DC MG), AC microgrid (AC MG) and hybrid AC/DC microgrid [4], which is a microgrid with AC and DC buses. Hybrid AC/DC microgrids are currently of great interest to researchers and are considered the distribution and transmission systems of the future, because they enable the coexistence of both AC MGs and DC MGs. The main drawback of the hybrid AC/DC microgrid is the protection strategy because it is more complex than the traditional MG [5, 6]. The large amount of required power converters may complicate the control, management, communication and power dispatch among devices.

Early proposals for the control of a hybrid AC/DC microgrid were presented in [7-9]. In [10] a decentralized control of a MG was proposed, based on using an interlinking converter (ILC) in order to coordinate the power flows among the power converters connected to the AC and DC buses. Droop methods [11] were used to share power among converters. In [0], droop was applied to the power converters connected both to the DC and AC buses. This control concept was extended in [12-14] to implement power interchange among sub-grids comprising a hybrid AC/DC microgrid. Several studies about power management in hybrid AC/DC microgrids using droop strategies for power dispatch have been recently presented [15]. In [16], the droop concept was extended in combination with a cost function defined for the power sharing. Overall, the droop control has a drawback for MGs that result from their small scale. The voltage and the frequency of these systems can fluctuate significantly under load variations or system failures. In order to solve this problem, a communication system between the power converters through a

smart centralized system could be used [17-19]. Centralized systems allow optimization of power sharing and integrating different types of RES into the MG. The experimental results of an MG which integrates commercial generators to the distribution grid without any droop control was presented in [20]. In that work, power management of the MG was implemented through an energy management system (EMS). In [21] an EMS was proposed whose aim was to minimize the operational costs of an MG working in grid connected mode. However, local autonomous controllers are necessary in the case of communication failures with the central controller. Those local controllers have been explained in many previous works, such as [22, 23]. In [23], a distributed control scheme for the MG was proposed, in which the local controllers were linked to a central controller through a low bandwidth communication device. The central controller managed an optimal EMS.

In this paper a centralized power management algorithm of the DC bus connected DC/DC converters in a hybrid AC/DC microgrid is presented. As shown in Figure 1, the AC bus of the MG is connected to the grid, and the DC bus is connected to the AC bus through an ILC. The ILC is an AC/DC bidirectional converter which regulates the DC bus voltage, managing the power flow between the DC bus and the AC bus. If the microgrid is in island-mode, the distributed generators connected to the AC bus can regulate the AC bus voltage using droop methods. In that case, the ILC can keep regulating the DC bus voltage. The use of centralized communications among all the microgrid elements makes that task feasible [19]. A centralized control decides the status of the DGs, the loads and the energy storage system (ESS) in the MG by applying a set of predefined operation functions. The power exchange with the grid is calculated by an algorithm implemented in the microgrid central processor (MGCP). The algorithm uses the information of the PV available power, the load connected to the DC bus, the battery state of charge (*SOC*) and the power exchange limits provided by the grid operator. The goal of this algorithm is to import the needed power from the grid, keeping it below the limits established by the grid operator, feeding the loads and keeping the *SOC* inside a safe range. If a surplus of energy is available from the PV generation, power is injected to the grid below another limit imposed by the grid operator. It is worth pointing out that this work is focused on the centralized control of the power flow in the MG. It is assumed that each power converter in the MG has a local controller for operating in case of communications failure. The proposed system has a load shedding functionality at the DC bus. This function is performed when the power imported by the microgrid from the grid tends to surpass its pre-defined limits. If there is not enough energy in the distributed generators and batteries, the load shedding functionality will be activated. In

addition, in order to avoid the erratic connection/disconnection of loads, a hysteresis level is introduced through a set of power thresholds. The load shedding is used in industrial practice for preventing blackouts, cascading events and the collapse of the power system [24-26].

The main contributions of this manuscript are (i) the definition of twelve operation functions for the management of the DC bus connected converters of the hybrid AC/DC microgrid and (ii) the implementation of load-shedding hysteresis levels in cases where the aim is to keep the battery energy backup as high as possible without exceeding a certain power limit imported from the main grid. This strategy is usually the preferred one when the electricity tariff is low [27, 28]. Moreover, the experimental validation of the centralized power management algorithm in a hybrid AC/DC microgrid is shown. The power management algorithm has been implemented in a MGCP based on TMS320F28335 DSC. Both, the control and the communications of each power converter have been implemented by means of TMS320F28335 DSCs.

This paper consists of five sections. In Section 2, a description of the hybrid AC/DC microgrid under study is provided. In Section 3, several concepts of the power management algorithm are explained. In Section 4, simulation and experimental results at different scenarios of the MG are presented. Section 5 contains the conclusions of the study.

2.2. Description of the Hybrid AC/DC Microgrid under Study

The hybrid AC/DC microgrid is depicted in Figure 1. The parameters of the communication system inside the MG are shown in Table 1. The MG under study is based on a single DC bus and a single AC bus, connected to the Point of Common Coupling (PCC) of the public grid by means of a static switch. The connection between the DC and AC buses is performed by the ILC, allowing a bidirectional power flow. In grid connected mode, the ILC may work as a current source that injects power to the grid synchronously with the AC bus voltage. An anti-islanding protection, based on [29], has been performed on the DSP of the MGCP. In that case, the operation of the distributed generators connected to the AC bus changes to droop mode so that they can regulate the voltage at the AC bus. The ILC keeps controlling the voltage at the DC bus.

The MGCP sets the operation functions of the power converters, loads and the ESS, depending on the MG scenarios. These scenarios depend on the internal and external changes that affect the power dispatch, such as changes in the solar irradiation, the load, the ESS and the power limit established by the public grid operator.

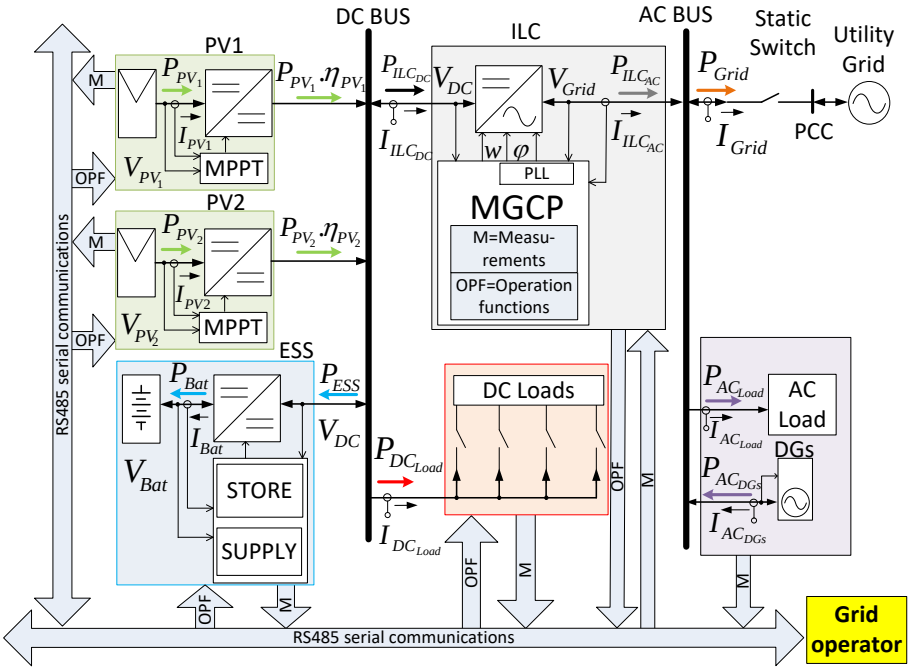

Figure 1. Conceptual scheme of the hybrid AC/DC microgrid under study.

Table 1. Communication parameters of the system.

Communication Parameters between the Devices of the microgrid (MG) and the microgrid central processor (MGCP)						
	DC MG				**AC MG**	
	ESS	**ILC**	**PV**	**DC Load**	**DGs**	**AC Load**
Operations functions	V_{DC_ref} I_{Dis_ref} I_{Ch_ref} VC	φ ω V_{DC_ref}	P_{PV_Lim}	Sw_1 Sw_2 Sw_3 Sw_4		
Measurements	I_{Bat} V_{DC} V_{Bat} SOC	I_{ILC_AC} V_{DC} V_{Grid}	I_{PV1} V_{PV1} I_{PV2} V_{PV2}	I_{DC_Load}	I_{AC_DGs} V_{Grid}	I_{AC_Load} V_{Grid}
Communication Parameters between the MGCP and the Grid Operator						
High-level control				EDL, $\widehat{P}_{Grid\text{-}to\text{-}MG}$, $\widehat{P}_{MG\text{-}to\text{-}Grid}$		

The MGCP optimizes power sharing by applying several control actions to the microgrid devices: (i) to connect/disconnect the loads as a function of the generated power and the available energy in the batteries; (ii) to share the available power between the priority loads [30] and the ESS; (iii) to adjust the hysteresis levels for avoiding oscillation in the DC bus due the connection-

disconnection of loads and (iv) to accomplish the power limits established by the grid operator. Note that the grid operator can establish different power exchange limits at any moment by means of serial communication. In fact, the power generated by the energy sources connected to the DC bus must be limited by the MGCP, in order to prevent an excessive power injection to the public grid beyond the limit set by the grid operator.

The MGCP defines the internal functionality depending on the possible scenarios of the MG. The communications allow control of the PV DGs, the ESS and the load connection/disconnection. In Figure 1, a 10 kW ILC, which connects the AC bus and the DC bus, can be observed. The AC bus is single phase and works in grid-connected mode with a grid voltage: V_{Grid} = 230 V_{rms} and F_{Grid} = 50 Hz ± 1 Hz. In the MG under study, two additional elements are connected to the AC bus: a 5 kW AC DG, and a 4 kW AC load. The nominal DC bus voltage is V_{DC} = 420 V, being regulated by the ILC. Three elements are connected to the DC bus: a 3 kW bidirectional DC/DC converter connected to a battery bank and two 5 kW DC/DC converters connected each one to one PV array. The voltage at the battery bank (V_{Bat}) ranges from 192 V to 252 V, whereas the voltages at the PV arrays (V_{PV1} and V_{PV2}) vary from 306 V to 378 V. Additionally four 'shed-able' 2 kW DC loads are connected to the DC bus. The loads can be connected or disconnected to/from the DC-bus by means of individual switches controlled by the MGCP (*Sw1* to *Sw4*).

2.3. Management and Control of the MG

2.3.1. Parameters of the Grid Operator

In this section, several concepts and parameters of the grid operator are explained in order to define the features and control functionalities of the proposed algorithm.

High-Level Control Limits

The grid operator establishes a tertiary high-level control strategy which controls the power flow between the MG and the main grid. That power flow imposes a limit of the power injected from the MG to the main grid or vice versa. The limits established from the high-level control are:

2.3.1.1. Energy Dispatch Limit (EDL)

The *EDL* is a digital flag that is inside the MGCP which indicates that there is an energy dispatch limit in the MG, set by the grid operator. The *EDL* allows the MGCP to set a suitable control strategy by taking into account the values of the maximum power extracted/injected from/to the grid to/from the MG. When

EDL = Off, there is no energy dispatch limit, and the MGCP can inject or extract unlimited power to/from the grid. In the opposite case (*EDL = On*), the MGCP establishes a set of power management criteria which depends on the load connected to the AC or DC buses, the power available in the MG and the *SOC* of the batteries.

2.3.1.2. Maximum Power Extracted from the Grid

The power flow scenarios between the grid and the MG are shown in Figure 2. Two general cases are possible: $P_{Grid} < 0$ and $P_{Grid} > 0$, being the power flow from the main grid to the microgrid or vice versa. Parameter $\widehat{P}_{Grid\text{-}to\text{-}MG}$ is established by the grid operator and represents the maximum power that can be extracted from the main grid to the MG, $|P_{Grid}| \leq \widehat{P}_{Grid\text{-}to\text{-}MG}$.

2.3.1.3. Maximum Power Injected to the Grid

Parameter $\widehat{P}_{MG\text{-}to\text{-}Grid}$ stands for the maximum power that can be injected from the MG to the main grid. This parameter is established by the grid operator, imposing the condition, $P_{Grid} \leq \widehat{P}_{MG\text{-}to\text{-}Grid}$.

2.3.2. Parameters of the MGCP

The MGCP establishes some parameters for the secondary control strategy, which is responsible for the power flow between the AC bus and the DC bus of the MG. The MGCP must limit the power generated by the RESs, if the available power is higher than that necessary at the MG buses.

2.3.2.1. Maximum Power Extracted from the AC Bus to the DC Bus Measured at the AC Side of the ILC

The power that flows from the grid to the MG is depicted in Figure 2a. In that case ($P_{Grid} < 0$ and $P_{ILC\_AC} < 0$), the value of P_{ILC_AC} can be calculated by Equation (1). The parameter $\widehat{P}_{ILC_{AC}}|_{Grid\text{-}to\text{-}MG}$ stands for the maximum power which can be extracted from the AC bus to the DC bus. This power is measured at the AC side of the ILC (2). The value of $\widehat{P}_{ILC_{AC}}|_{Grid\text{-}to\text{-}MG}$ depends on the MGCP, because the value of $\widehat{P}_{Grid\text{-}to\text{-}MG}$ is set by the MGCP. The absolute value of P_{ILC_AC} must meet the condition expressed by Equation (3) at any time, taking into account the rated power of the ILC.

$$P_{ILC_{AC}} = P_{AC_{DGs}} + |P_{Grid}| - P_{AC_{Load}} \quad (1)$$

$$\widehat{P}_{ILC_{AC}}|_{Grid\text{-}to\text{-}MG} = P_{AC_{DGs}} + \widehat{P}_{Grid\text{-}to\text{-}MG} - P_{AC_{Load}} \quad (2)$$

$$|P_{ILC_{AC}}| \leq MIN\left(P_{ILC_{Rated}}, \hat{P}_{ILC_{AC}}|_{Grid-to-MG}\right) \quad (3)$$

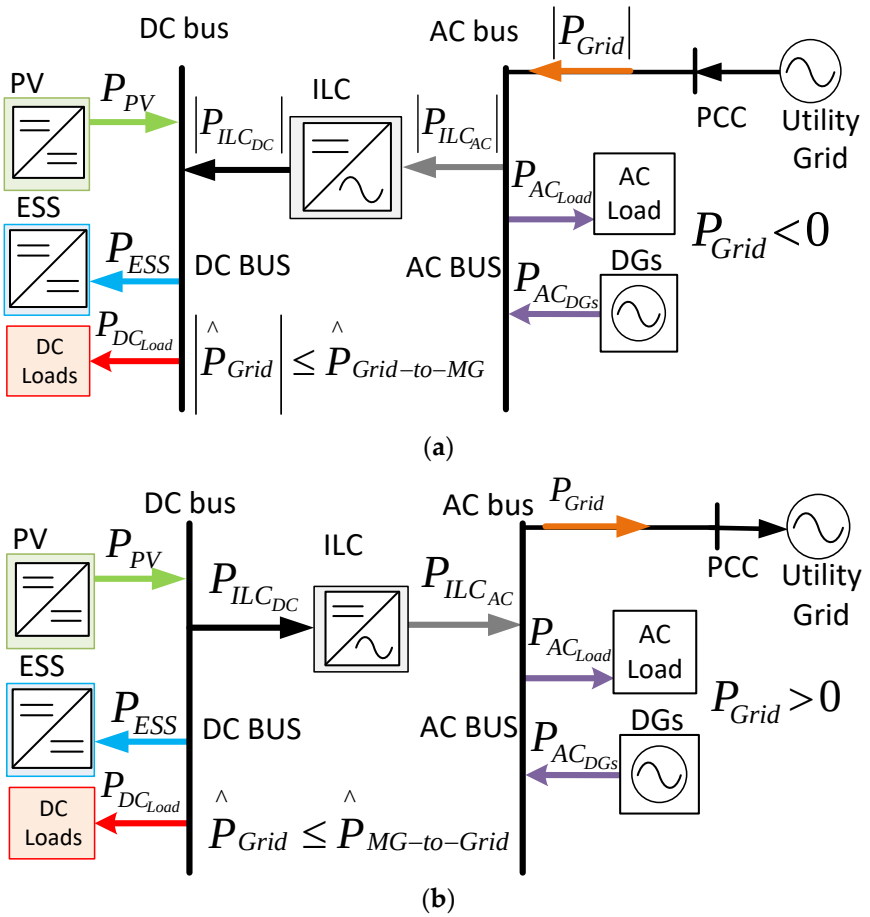

Figure 2. Power flow scenarios between the grid and the MG: (**a**) power flow from the grid to the MG, $P_{Grid} < 0$; (**b**) power flow from the MG to the grid, $P_{Grid} > 0$.

2.3.2.2. Maximum Power Injected from the DC Bus to the AC Bus Measured at the AC Side of the ILC

The power that flows from the MG to the grid is depicted in Figure 2b. In that case ($P_{Grid} > 0$ and $P_{ILC\_AC} > 0$), the value of P_{ILC_AC} can be calculated by Equation (4). Parameter $\widehat{P}_{ILC_{AC}}|_{MG\text{-}to\text{-}Grid}$ stands for the maximum power which can be injected from the DC bus to the AC bus, measured at the AC side of the ILC (5). The maximum power injected from the DC bus to the AC bus by the ILC must meet the conditions of Equation (6).

$$P_{ILC_{AC}} = P_{Grid} + P_{AC_{Load}} - P_{AC_{DGs}} \quad (4)$$

$$\widehat{P}_{ILC_{AC}}/_{MG\text{-}to\text{-}Grid} = \widehat{P}_{MG\text{-}to\text{-}Grid} + P_{AC_{Load}} - P_{AC_{DGs}} \quad (5)$$

$$\widehat{P}_{ILC_{AC}} \leq MIN\left(P_{ILC_{Rated}}, \widehat{P}_{ILC_{AC}}|_{MG-to-Grid}\right) \quad (6)$$

2.3.2.3. PV Power Generated in the DC Bus

The power outputs generated by the PV DGs connected to the DC bus are measured individually. Parameter P_{PV} is the overall PV power generated in the DC bus of the MG. The total power generated by two PV DC/DC converters connected to the DC bus is shown in Equation (7).

$$P_{PV} = P_{PV1} \cdot \eta_{PV1} + P_{PV2} \cdot \eta_{PV2} \quad (7)$$

2.3.2.4. Power Consumed by the Loads Connected to the DC and AC Buses

The power consumed by the loads connected to the DC bus is $P_{DC_{Load}} = I_{DC_{Load}} \cdot V_{DC}$ and to the AC bus is $P_{AC_{Load}} = I_{AC_{Load_{rms}}} \cdot V_{Grid_{rms}}$.

2.3.2.5. Maximum Power Consumed by the Loads Connected to the DC Bus

Parameter $\widehat{P}_{DC_{Load}}$ stands for the maximum overall power which the DC loads are allowed to consume. The load shedding functionality at the DC bus performed by the MGCP depends on this parameter. $\widehat{P}_{DC_{Load}} \leq P_{ILC_{Rated}}$ establishes an upper limit for the maximum power as a function of the ILC power rating.

2.3.2.6. PV Power Limit

Parameter P_{PV_Lim} is the maximum power that should be extracted from the PV sources at any time, so that it can be consumed by the DC loads and by the batteries ($P_{ESS} > 0$) and/or it injected into the grid. P_{PV_Lim} is represented by Equation (8), where $P_{ESS} = (V_{Bat} \cdot I_{Bat})/\eta_{ESS}$.

$$P_{PV_{Lim}} = \widehat{P}_{ILC_{AC}}/_{MG\text{-}to\text{-}Grid} + P_{DC_{Load}} + P_{ESS} \quad (8)$$

2.3.2.7. PV Generation Power Available in the DC Bus

Parameter $P_{AvailableDC\_MG}$ is the extra power available from the PV DGs of the DC bus after feeding the load connected in the DC bus. The available PV generation power is defined by Equation (9).

$$P_{Available_{DC\_MG}} = P_{PV} - P_{DC_{Load}} \quad (9)$$

2.3.2.8. DC Load Switch

The flag of DC load switch takes two possible states, Sw_{Load} = *On* and Sw_{Load} = *Off*, depending on the connection or disconnection of loads to the DC bus, respectively.

2.3.2.9. DC Load Hysteresis

Parameter DC_{Load_hyst} is calculated as 10% of the overall power consumed by the DC loads, $DC_{Load_{hyst}} = 0.1 \cdot P_{DC_{Load}}$. DC_{Load_hyst} is the hysteresis level which has been established for avoiding erratic connection/disconnection of the loads.

2.3.2.10. Power Consumed for the Batteries to C10

Parameter $PESS_{C10}$ is the maximum power consumption for the charge of the batteries of the ESS, $PESS_{C10} = (V_{Bat} \cdot I_{C10})/\eta_{ESS}$. It has been established that the batteries are charged with a current equal to $I_{C10} = C_{10}/10$, where *C10* the specified battery capacity (measured in A·h) for a discharge time of 10 h.

2.3.3. Power Management Algorithm

Several calculations and functions are necessary for the suitable power management of the MG control algorithm. These calculations and functions depend on the *SOC* of the battery, the availability of power in the buses, the limits set by the grid operator and the status of Sw_{Load}.

2.3.3.1. Operation Functions of the MGCP

The power management algorithm embedded in the MGCP executes 12 operation functions according to the various operating scenarios. The operation functions of the MGCP and their interactions with the power converters of the MG are described in the following paragraphs.

2.3.3.1.1. Operation Functions in DC Load Connection Mode (Sw_{Load} = On)

*Function 1 (**F1**):* All DC loads are fed. When $SOC \leq SOC_{Full}$ (SOC_{Full} = 100%), the DC/DC converter of the ESS charges the batteries from the DC bus with a current (I_{C10}). The PV DGs work at their maximum power point (MPP), so that *MPPT* = *On*. If there is not enough power available from the PV DGs connected to the DC bus, the ILC can extract the rest of the power from the AC bus with the only restriction being $\left|\widehat{P}_{ILC_{AC}}\right| \leq P_{ILC_{Rated}}$, taking into account that *EDL* = *Off*.

*Function 2 (**F2**):* All DC loads are fed. When $SOC \leq SOC_{Full}$; the DC/DC converter of the ESS charges the batteries from the DC bus with a current equal to I_{C10}. The PV DGs work at their MPP (*MPPT* = *On*). In this case, the PV DGs connected to the DC bus may produce excess power which can be injected into the AC bus by the ILC if necessary, with the only limitation being its rated power: $\widehat{P}_{ILC_{AC}} \leq P_{ILC_{Rated}}$.

*Function 3 (**F3**):* All DC loads are fed. When $SOC \leq SOC_{Full}$; the DC/DC converter of the ESS charges the batteries from the DC bus with a current equal to I_{C10}. The PV DGs do not work at their MPP (*MPPT* = *Off*). In this case the PV DGs connected to the DC bus produce a limited amount of power, because the power which can be injected to the AC bus by the ILC is limited by the grid operator. The power injected from the DC to AC bus by the ILC is given by: $P_{ILC_{AC}} \leq \widehat{P}_{ILC_{AC}}|_{MG\text{-}to\text{-}Grid}$. Figure 3 depicts the power dispatch inside the MG after applying the operation functions: *F3*, *F8*, *F10* and *F11*.

*Function 4 (**F4**):* All DC loads are disconnected. When $SOC \leq SOC_{MIN}$ (SOC_{MIN} = 20%), the ESS is in standby mode. The flag Sw_{Load} changes from *On* to *Off*, entering the DC load disconnection mode. The PV DGs work at their MPP (*MPPT* = *On*).

*Function 5 (**F5**):* All DC loads are fed. While $SOC \leq SOC_{Full}$, the DC/DC converter of the ESS charges the batteries from the DC bus with a current equal to I_{C10}. The PV DGs work at their maximum power point (*MPPT* = *On*). The ILC injects the excess power at the DC bus to the AC bus. The power injected to the AC bus must comply with the following conditions: $P_{ILC_{AC}} \leq \widehat{P}_{ILC_{AC}}|_{MG\text{-}to\text{-}Grid}$.

*Function 6 (**F6**):* All DC loads are fed. As the *SOC* has reached SOC_{FullI}, the DC/DC converter of the ESS stops charging the batteries, putting the ESS in standby mode. The PV DGs work at their MPP (*MPPT* = *On*), producing an excess of power which can be injected to the AC bus by the ILC.

*Function 7 (**F7**):* All DC loads are fed. While $SOC \leq SOC_{Full}$, the DC/DC converter of the ESS charges the batteries from the DC bus with a current whose value is shown by Equation (10) which is smaller than I_{C10}. The PV DGs work at their MPP (*MPPT* = *On*). If there is not enough power available from the PV DGs, the ILC can extract the rest of power from the AC bus subject to the following limit: $\left|P_{ILC_{AC}}\right| \leq \widehat{P}_{ILC_{AC}}|_{Grid\text{-}to\text{-}MG}$.

$$I_{Ch_{ref}} = MIN\left(I_{C10}, \frac{P_{Available_{DC\_MG}} + \widehat{P}_{ILC_{AC}}|_{Grid-to-MG}}{V_{DC}}\right) \quad (10)$$

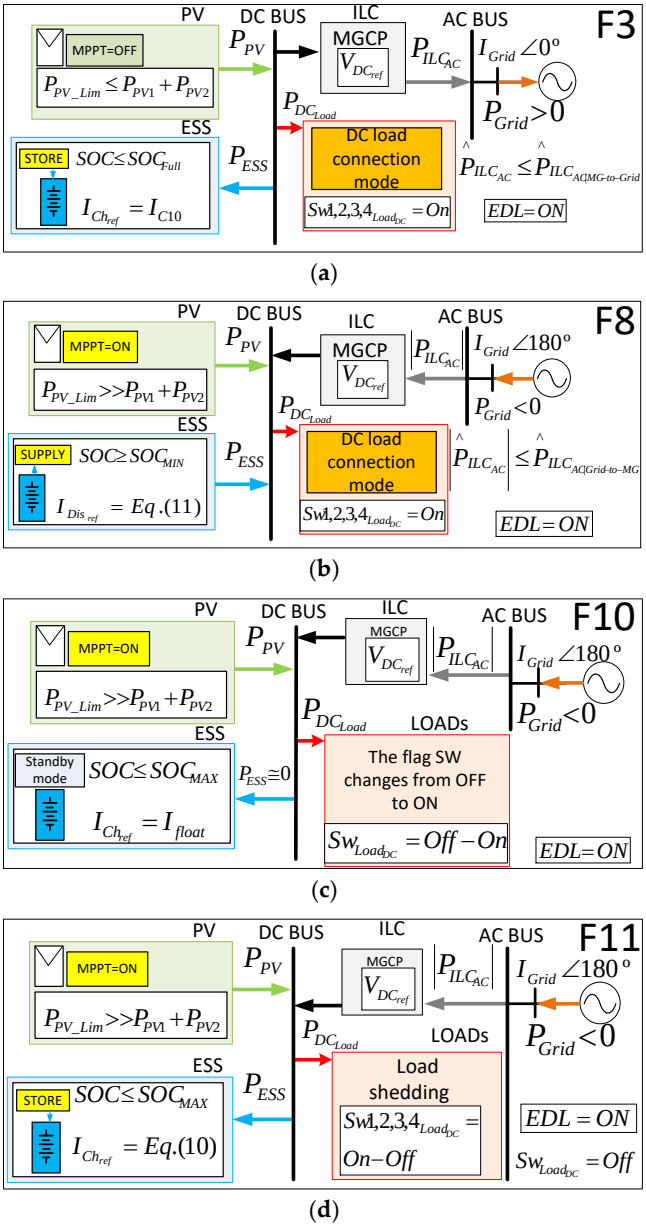

Figure 3. Power dispatch inside the MG after applying the operation functions: (**a**) *F3*; (**b**) *F8*; (**c**) *F10* and (**d**) *F11*.

*Function 8 (**F8**):* All DC loads are fed. When $SOC \geq SOC_{MIN}$, the DC/DC converter of the ESS operates as a controlled current source discharging the batteries to the DC bus. In *F8*, the PV DGs work at their MPP (*MPPT* = *On*). The

sum of the power coming from the ESS and from the PV DGs is not enough to energize the DC loads, so that the required extra power can be transferred from the AC bus to the DC bus through the ILC. That extra power is limited in order not to override the power which can be absorbed by the DC loads. Equation (11) shows the expression of the discharge current. In this case, the extra available power is negative ($P_{AvailableDC\_MG} < 0$), because the power coming from the PV DGs is not enough to energize the DC loads. The power flows in the MG when *F8* is active are shown in Figure 3b.

$$I_{Dis_{ref}} = MIN\left(I_{C10}, \left|\frac{P_{Available_{DC\_MG}} + \widehat{P}_{ILC_{AC}}|_{Grid\text{-}to\text{-}MG}}{V_{bat}}\right|\right) \quad (11)$$

*Function 9 (**F9**):* All DC loads are fed. As the *SOC* has reached SOC_{Full}, the DC/DC converter of the ESS stops charging the batteries and enters standby mode. The PV DGs do not work at their maximum power point (*MPPT* = *Off*), because the DC loads cannot absorb the sum of MPP powers. The ILC injects a limited amount of power from the DC to the AC bus which is the required extra power to feed the DC loads.

2.3.3.1.2. Operation Functions in DC Load Disconnection Mode (Sw_{Load} = Off)

*Function 10 (**F10**):* In *F10*, the flag Sw_{Load} switches from *Off* to *On*. All DC loads are fed. The ESS is in standby mode. The PV DGs work at their MPP (*MPPT* = *On*). The power flows in the MG when *F10* is active are shown in Figure 3c.

*Function 11 (**F11**):* Some DC loads are fed by the load shedding functionality, as is shown in Figure 4. This function each of the DC loads on and off automatically. While $SOC \leq SOC_{MAX}$ (SOC_{MAX} = 80%), the DC/DC converter of the ESS charges the batteries with a current smaller than I_{C10}, given by Equation (10). The power flows in the MG when *F11* is active are shown in Figure 3d. *Cal.0* is the calculation of the available PV power plus the maximum power that can be transferred from the AC bus to the DC bus by the ILC. This expression is shown in Equation (12). A decision tree can be observed in Figure 4, which depicts how 1 to 4 DC loads are connected–disconnected as a function of the value of *Cal.0*. If *Cal.0* is not enough to energize all the DC loads, *F11* begins their disconnection depending on the values of *Cal.0* and the state (1 or 0) of the logic variables, *Comp.1* to *Comp.3*, which are calculated as *AND* functions. Note that a 10% hysteresis band of the power of one DC load has been chosen for establishing the comparison: DC_{Load_hyst} = 0.1·2 kW = 0.2 kW.

$$Cal.0 = P_{PV} + \widehat{P}_{ILC_{AC}}/_{Grid\text{-}to\text{-}MG} \quad (12)$$

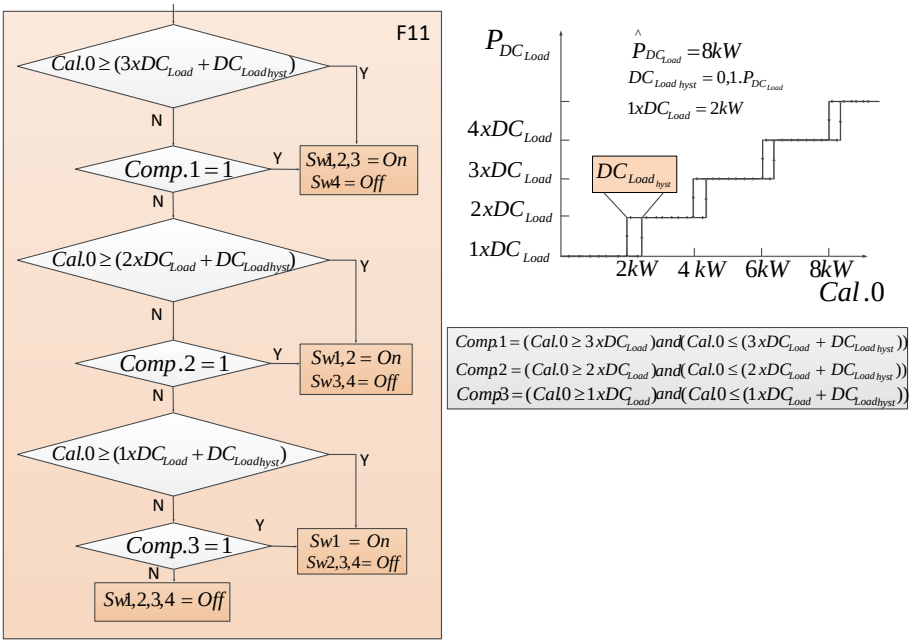

Figure 4. Load shedding functionality.

*Function 12 (**F12**):* All DC loads are fed. When $SOC \leq SOC_{MAX}$, the DC/DC converter of the ESS charges the batteries with a current smaller than I_{C10}, given by Equation (10). The PV DGs work at their MPP (*MPPT* = *On*). If the power coming from the PV DGs is not enough to energize the DC loads, the required extra power can be transferred from the AC to the DC bus through the ILC.

2.3.3.2. Power Management Algorithm of the MG

The flow diagram of the power management algorithm is shown in Figure 5. *Comp.4* is a logic variable calculated as an OR function. The flags, Sw_{Load} and *EDL*, are fundamental parameters for the power dispatch in the MG. When *EDL* = *Off*, there is no energy dispatch limit, so that functions *F1* or *F2* can be applied. When *EDL* = *On* and Sw_{Load} = *On*, the MGCP applies functions *F3* to *F9*. The flag Sw_{Load} can be turned *Off* by *F4*; after that, the MGCP can apply functions *F10* to *F12*. The functions are implemented so that the power transfer limits between both buses are not exceeded. The calculations performed by the power management algorithm, *Cal.0* to *Cal.4*, are shown in Equations (12)–(15) and allow the power availability of both buses to be checked, taking into account their power dispatch limits. Equation (13) stands for the power availability in the DC bus coming from DGs and batteries plus the maximum power which can be extracted from the AC bus to the DC bus.

$$Cal.1 = P_{Available_{DCMG}} + \hat{P}_{ILC_{AC}}/_{Grid\text{-}to\text{-}MG} \quad (13)$$

Equation (14) stands for the maximum power that can be injected from the DC to the AC bus plus the power consumed for charging the batteries at a current (I_{C10}).

$$Cal.2 = \hat{P}_{ILC_{AC}}/_{MG\text{-}to\text{-}Grid} + P_{ESS_{C10}} \quad (14)$$

Equation (15) stands for the power available in the DC bus plus the maximum power which can be extracted from the AC bus to the DC bus.

$$Cal.3 = P_{PV} + \hat{P}_{ILC_{AC}}/_{Grid\text{-}to\text{-}MG} - \hat{P}_{DC_{Load}} \quad (15)$$

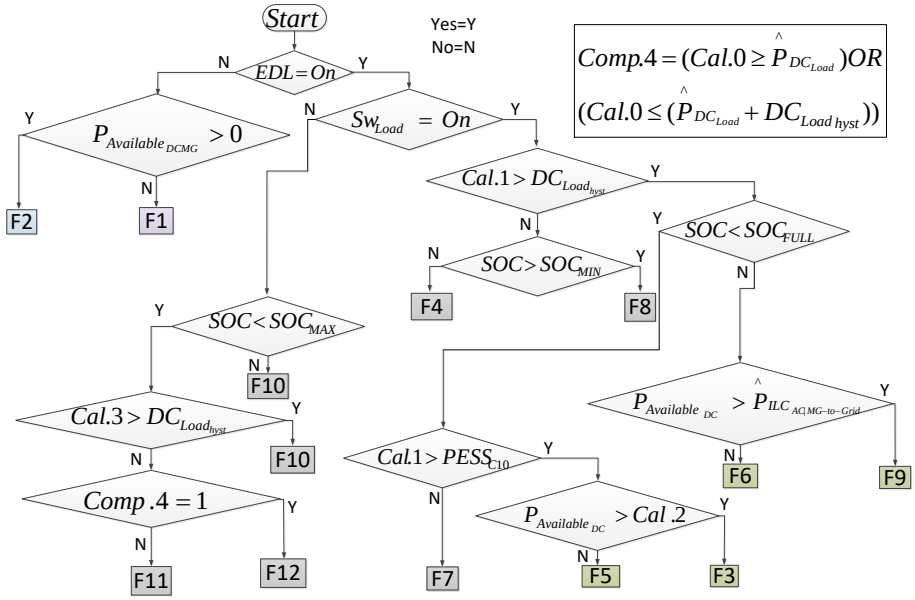

Figure 5. Power management algorithm of the MG.

2.4. Simulation and Experimental Results

2.4.1. Simulation Results

The proposed power management algorithm has been simulated by means of PSIM™ [31] under various scenarios. This study is focused on the particular case in which the MG is operating in grid connected mode. The characteristics of the power electronic converters comprising the MG are listed in Table 2. The simulation scenarios of the MG are explained in Table 3. It is worth pointing out that step changes of irradiation shown in Table 3 do not correspond to reality, but they allow us to study the behavior of the MG and the stability of the buses

in very extreme cases. In order to check of the proposed algorithm in different situations with a short simulation time, the algorithm was run in simulations at 25 Hz. The duration of the operation functions *F4* and *F10* is one clock cycle (40 ms), because their main function is to change the load shedding functionality. It is assumed that the ESS is initially discharged ($SOC \leq SOC_{MIN}$). A selected number of possible scenarios have been studied in order to demonstrate the suitable behavior of the MG in its most common and critical situations. In the scenarios under study, step changes of the irradiation, the DC load and the *EDL* were considered, as can be observed in Table 3. The behavior of the proposed algorithm and the application of particular functions *F1* to *F12* by the MGCP can be observed from the following graphs: Figure 6 depicts the behavior of the currents, I_{Bat}, $I_{PV} = I_{PV1} + I_{PV2}$, and of the *SOC* versus time. The evolution of the powers, P_{Bat}, P_{PV}, P_{DCLoad}, P_{ILC_AC} and P_{Grid}, can be observed in Figure 7. Figure 8 provides detail about the most sudden transients of I_{ILC_AC}, V_{DC} and P_{ILC_AC}, which take place throughout the whole simulation, corresponding to the time span, 34.8 s to 35.4 s.

Table 2. Characteristics of the power converters of the MG.

ILC	2 PV DC/DC Converters (DGs)	ESS
P_{ILC_Rated} = 10 kW V_{Grid} = 230 V F_{Grid} = 50 Hz V_{DC} = 420 V F_{swILC} = 12.8 kHz	$P_{PV1,2\_Boost}$ = 5 kW V_{PV} = 306 V F_{sw_PV} = 16 kHz PV Panel: Atersa A-250P GSE V_{PV_oc} = 37.61 V I_{PV_MAX} = 8.18 A V_{PV_MAX} = 30.58 V I_{PV_CC} = 8.71 A	P_{ESS_HB} = 3 kW V_{Bat} = 216 V F_{sw_ESS} = 16 kHz Battery Bank: 18 batteries type SUN POWER VRM 12V105 connected in series V_{Bat_Nom} = 216 V V_{Bat_MIN} = 185 V V_{Bat_MAX} = 259.2 V C_{10}≅105 A·h I_{C10} = 10.5 A

The analysis is performed according to the following time intervals:

<u>*Interval 1 (0 ≤ t < 1 s):*</u> This interval is divided into two subintervals.

0 ≤ t < 40 ms: At *t = 0* s, the ESS is initially discharged ($SOC \leq SOC_{MIN}$). The irradiation is 300 W/m² and the overall DC load absorbs 8 kW. Due to the fact that the PV available power, P_{PV}, at that low irradiation level is not enough to feed the loads, the MGCP applies function *F4*, internally activating flag Sw_{Load} = *Off*.

40 ms ≤ t < 1 s: After to *F4*, *F11* is applied to disconnect two DC loads (overall *DC load* = 4 kW), and the batteries are charged with a current given by Equation (10).

Table 3. The simulation scenarios of the MG.

SIMULATION Scenarios							
Time Intervals (s)							
Time interval number	1	2	3	4	5	6	7
Time span (s)	$0 < t < 1$	$1 < t < 10$	$10 < t < 18$	$18 < t < 20$	$20 < t < 28$	$28 < t < 35$	$35 < t < 40$
Irradiation (W/m²)	300	600	400	800	800	800	100
Load connected to the DC bus	4 loads (8 kW)	4 loads (8 kW)	4 loads (8 kW)	4 loads (8 kW)	2 loads (4 kW)	2 loads (4 kW)	2 loads (4 kW)
EDL[1]	*On*	*On*	*On*	*On*	*On*	*Off*	*Off*
ILC	The MG is operating in grid-connection mode						
ESS	The batteries of the ESS are initially discharged. $SOC \leq SOC_{MIN}$						
Power limits	$\hat{P}_{MG-to-Grid}$ = 4 kW, $\hat{P}_{Grid-to-MG}$ = 1kW, $\hat{P}_{DC_{Load}}$ = 8 kW						
AC bus	$P_{AC_{Load}}$ = 4 kW, $P_{AC_{DGs}}$ = 5 kW						

[1] Energy dispatch limit.

Interval 2 (1 s ≤ t < 10 s): At t = 1 s, the irradiation undergoes a change from 300 W/m² to 600 W/m², whereas the *SOC* keeps growing below SOC_{MAX}. The MGCP goes on applying *F11*. The PV generation is increased and *F11* connects an additional 2 kW DC load (overall *DC load* = 6 kW) to the DC bus. The MGCP makes both PV DC/DC converters operate at their MPP, whereas the DC bus voltage is regulated to 420 V by the ILC.

Interval 3 (10 s ≤ t ≤ 18 s): This interval is divided into five subintervals.

10 ≤ t < 10.2 s: At t = 10 s, the irradiation decreases from 600 W/m² to 400 W/m², whereas the *SOC* keeps growing below SOC_{MAX}. The MGCP maintains *F11*. The power generated by the panels, P_{PV}, with this irradiation is insufficient to feed three loads, and *F11* disconnects one load (*DC load* = 4 kW) in the DC bus.

10.2 s ≤ t <10.24 s: At t = 10.2 s the *SOC* surpasses SOC_{MAX}, whereas the irradiation stays at a constant value of 400 W/m². The MGCP applies *F10* after detection of SOC_{MAX}, which internally activates the flag, Sw_{Load} = *On*.

10.24 s ≤ t <15.4 s: At t = 10.24 s, the generated PV power at the current irradiation level is not enough to feed all the DC loads, so that the MGCP applies *F8* in order to get additional power from the ESS, and the battery bank is discharged at a current given by (11). *F8* connects all DC loads (8 kW) to the DC bus and extracts power from the AC bus taking into account the limit that the maximum power that can be extracted of the same ($|P_{ILC_{AC}}| \leq (\hat{P}_{ILC_{AC}}|_{Grid\text{-}to\text{-}MG}$), and the ESS injects the current required by the DC bus to feed the DC loads.

15.4 s ≤ t < 15.44 s: At t = 15.4 s the *SOC* goes below SOC_{MIN}, so that the MGCP applies *F4*, internally activating flag Sw_{Load} = *Off*.

15.44 s ≤ t < 18 s: At t = 15.44 s, the MGCP applies *F11*. *F11* disconnects two DC loads (overall *DC load* = 4 kW), so that the batteries are charged with a current given by (10).

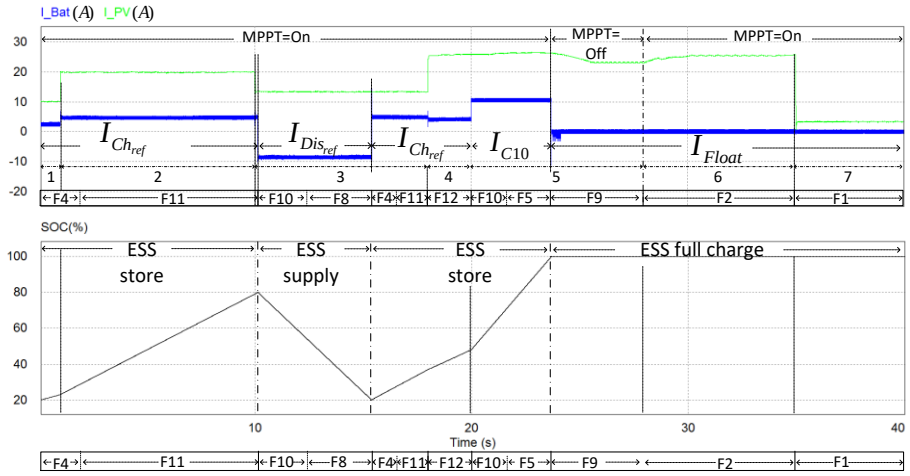

Figure 6. Simulation waveforms, I_{Bat}, $I_{PV} = I_{PV1} + I_{PV2}$ the *SOC* over time.

Interval 4 (18 s ≤ t < 20 s): At t = 18 s, the irradiation undergoes a linear change of 400 W/m² to 800 W/m², being $SOC < SOC_{MAX}$. The generated PV power and the extracted power from the AC bus are enough to feed all DC loads. Due to limitations on the amount of power that can be interchanged between the buses, the MGCP applies *F12*, and the batteries are charged with a current given by Equation (10). *F12* connects all the DC loads and also sets the PV sources at their MPP.

Interval 5 (20 s ≤ t < 28 s): This interval is divided into three subintervals.

20 ≤ t< 20.04 s: The irradiation keeps a constant 800 W/m² value, whereas *SOC* remains below SOC_{Full}. At t = 20 s, the load connected to the DC bus decreases from 8 kW to 4 kW. The PV-generated power (P_{PV}) at the current irradiation is enough to feed all DC loads. The MGCP applies *F10* which internally activates the flag, $Sw_{Load} = On$.

20.04 ≤ t< 23.7 s: At t = 20.04 s, MGCP applies *F5*. *F5* sets the charge the batteries with a current (I_{C10}). The PV sources work at their MPP. The ILC injects the power excess to the AC bus.

23.7 s ≤ t< 28 s: Both the irradiation (800 W/m²) and the DC load (4 kW) remain constant, whereas the *SOC* has reached 100%. The power generated by the panels is higher than that necessary for feeding the DC loads: $P_{PV} > 4$ kW. The MGCP applies *F9* to stop charging the batteries and to set the PV

generators outside their MPP (*MPPT* = *Off*). In this case, ($P_{ILC_{AC}} \leq \hat{P}_{ILC_{AC}}|_{MG\text{-}to\text{-}Grid}$).

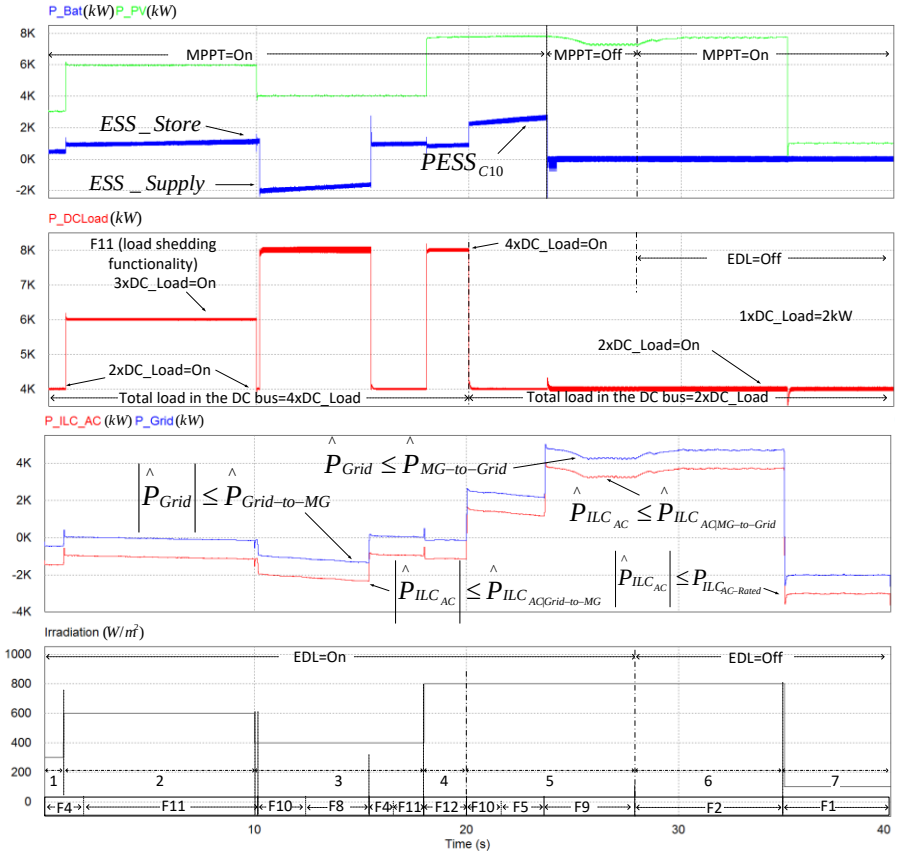

Figure 7. Simulation waveforms of the powers, P_{Bat}, P_{PV}, P_{DCLoad}, P_{ILC_AC} and P_{Grid}.

Interval 6 (28 s ≤ t < 35 s): The irradiation and the *SOC* remain constant: 800 W/m² and 100%, respectively. *EDL* switches from *On* to *Off*. The MGCP applies *F2*, and the ILC injects power into the grid to its rated power, if necessary ($P_{ILC_{AC}} \leq P_{ILC_{Rated}}$). At *t* = 30 s, MPPT switches from *Off* to *On*.

Interval 7 (35 s ≤ t < 40 s): The irradiation undergoes a change from 800 W/m² to 100 W/m². The MGCP applies *F1*, so that the ILC can extract power from the grid ($|P_{ILC_{AC}}| \leq P_{ILC_{Rated}}$) when *MPPT* = *On*.

2.4.2. Experimental Results

The experimental power electronic converters, whose characteristics are summarized in Table 2, were built to validate the proposed power management

algorithm. The following devices have been connected to the DC bus of the MG available in the lab: a 3 kW battery ESS, a 2.5 kW PV source and four electronic switches to connect/disconnect four DC loads of 0.6 kW ($\hat{P}_{DC_{Load}}$ = 2.4 kW). Figure 9 shows a picture of the experimental setup. The batteries were emulated by a bidirectional DC source/battery emulator, model TC.GSS-Bidirectional-DC-PSU, from Regatron. The PV array was emulated by means of a 10 kW PV array simulator, TerraSAS ETS1000/10, from Ametek (Berwyn, PA, USA). Three experiments were carried out. The experimental scenarios are summarized by Table 4. Figures 10 and 11 depict the waveforms of the currents, voltages and powers of the power converters that form the DC bus of the MG, with Figure 10 corresponding to Experiment 1 and Figure 11 corresponding to Experiment 2. Figure 12 corresponds to Experiment 3.

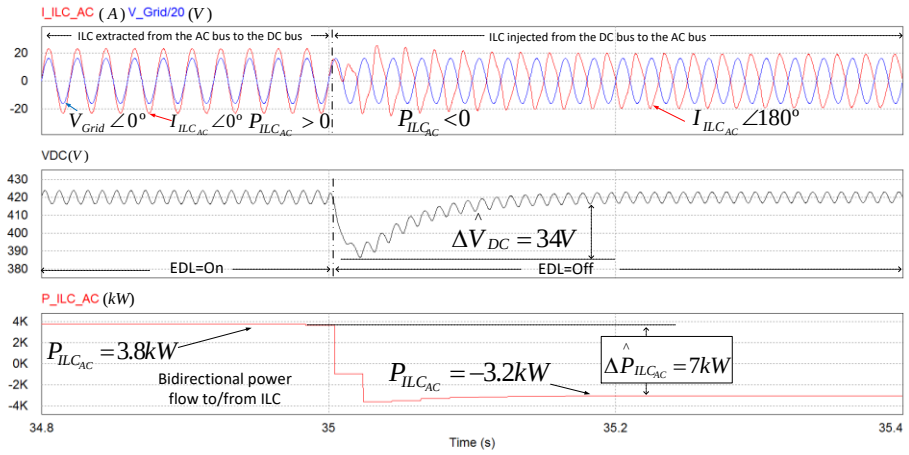

Figure 8. Simulation waveforms of the most sudden transients of I_{ILC_AC}, V_{DC} and P_{ILC_AC}.

Experiment 1 and Experiment 2 show the behavior of the system with the same change in the irradiation level at the PV source, but with a different *SOC* of the ESS. The available power injected from the AC bus to the DC bus by the ILC is P_{ILC_DC} = −1 kW.

2.4.2.1. Experiment 1

The ESS is initially at an *SOC* ≥ 80% (charged). The four loads remain connected throughout the whole experiment, as can be seen in Figure 10. (P_{DC_Load} = 2.4 kW). The hysteresis level for comparisons with power thresholds is DC_{Load_hyst} = 0.24 kW.

Interval1 1 (0 s < t < 8 s): The irradiation level is 100 W/m² and the PV source works at its maximum power point (MPP), providing P_{PV} = 0.14 kW to the DC

bus. That irradiation is not enough to feed all of the loads. Taking into account that the ESS is charged ($SOC \geq 80\%$), the MGCP transfers the maximum possible power from the AC bus ($P_{ILC\_DC} = -1$ kW) to the DC bus through the ILC and applies *F8*. This keeps all the DC loads connected and orders the ESS supplying all the power required by the DC bus, $P_{Bat} = -1.26$ kW.

Table 4. The experimental scenarios of the MG.

Experimental Scenarios [1]					
ESS	Experiment 1: The batteries of the ESS are initially charged. $SOC = SOC_{MAX}$				
Time span (s)	$0 < t < 8$	$8 < t < 11$	$11 < t < 41$	$41 < t < 44$	$44 < t < 50$
Irradiation (W/m²)	100	100–800	800	800–100	100
ESS	Experiment 2: The batteries of the ESS are initially discharged. $SOC \leq SOC_{MIN}$				
Time span (s)	$0 < t < 7$	$7 < t < 10$	$10 < t < 40$	$40 < t < 43$	$43 < t < 50$
Irradiation (W/m²)	100	100–800	800	800–100	100
Load connected to the DC bus	4 loads (2.4 kW)				
EDL	*On*				
ILC	The MG is operating in grid-connection mode				
Power limits	$\hat{P}_{MG-to-Grid} = 4$ kW, $\hat{P}_{Grid-to-MG} = 1$ kW, $\hat{P}_{DC_{Load}} = 2.4$ kW				
AC bus	$P_{AC_{Load}} = 4$ kW, $P_{AC_{DGs}} = 5$ kW				

[1] The algorithm is running in the experiments at 1 Hz.

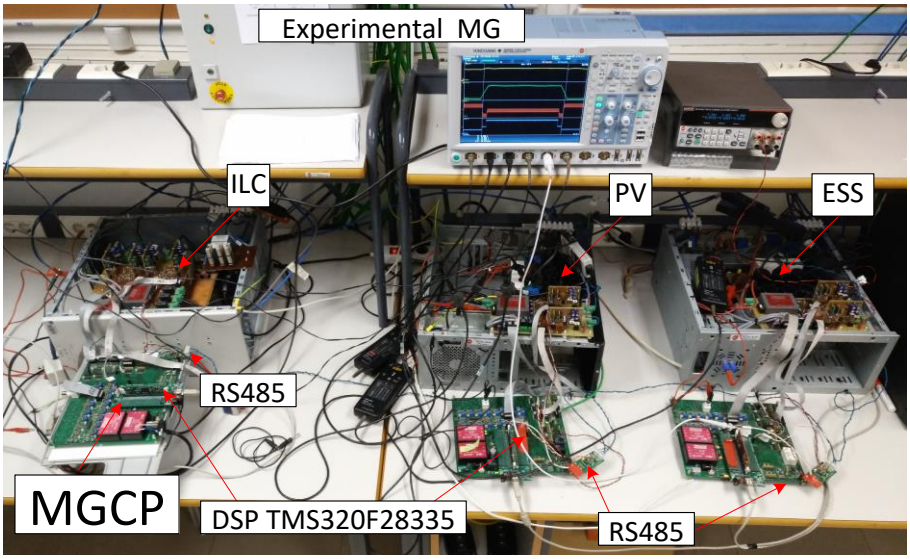

Figure 9. Experimental setup picture.

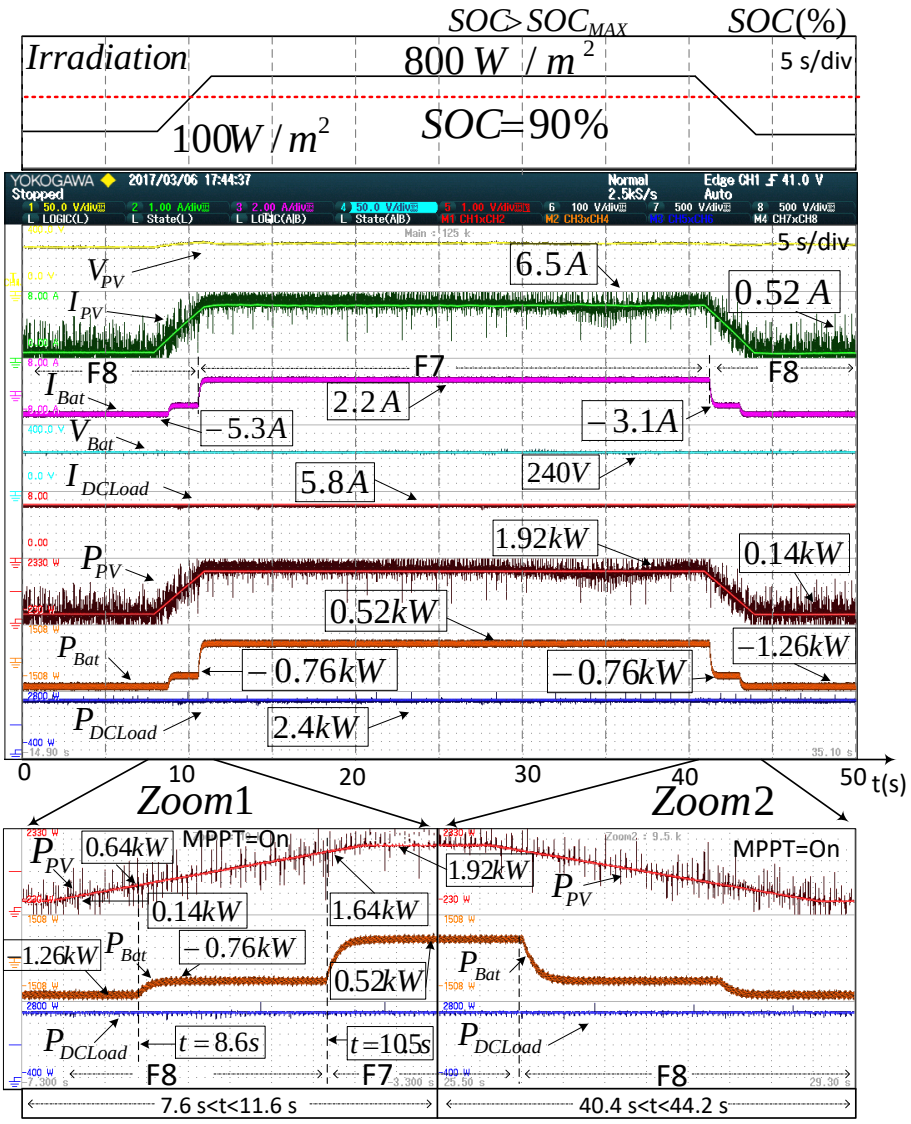

Figure 10. Experiment 1.

Interval 2 (8 s < t < 11 s): The irradiation increases from 100 W/m² to 800 W/m² in 3 s. The MGCP keeps *F8* activated and the power delivered by the ESS can be reduced.

At t = 8.6 s, MGCP detects increasing generation, and the PV source works at its MPP, delivering P_{PV} = 0.64 kW. The MGCP keeps *F8* activated and transfers the maximum possible power from the AC bus (P_{ILC_DC} = −1 kW) and

keeps all of the DC loads connected. The ESS supplies the power required by the DC bus; the power delivered by the ESS is reduced to P_{Bat} = −0.76 kW.

At t = 10.5 s, the PV source works at its MPP delivering P_{PV} = 1.64 kW, with P_{ILC_DC} = −1 kW. At this moment, the MGCP detects that the available power at the DC bus to fed all the DC loads is higher than the hysteresis level (*Cal.1* > DC_{Load_hyst}). The MGCP changes from *F8* to *F7*. *F7* forces the ESS to change its operation to energy storage mode; the batteries are charged with a current given by Equation (10). The MGCP changes the setpoint of the ESS charge current, I_{Ch_ref}, until the available power generation is stable (At t = 11.6 s, P_{Bat} = 0.5 kW). The power flows in the MG when the MGCP changes from *F8* to *F7* are shown in Zoom 1 of Figure 10.

Interval 3 (40.4 s < t < 44.2 s): The irradiation decreases from 800 W/m² to 100 W/m² in 3 s. The MGCP keeps *F8* activated and the power delivered by the ESS can be reduced. The power flows in the MG when *F8* is active are shown in Zoom 2 of Figure 10.

2.4.2.2. Experiment 2

The ESS is initially at an $SOC \leq 20\%$ (discharged).

Interval 1 (0 s < t <7 s): The irradiation level is 100 W/m², and the PV source works at its maximum power point (MPP), providing P_{PV} = 0.14 kW to the DC bus. That irradiation is not enough to feed all of the loads. Considering that the ESS is discharged (SOC < 20%), the MGCP transfers the maximum possible power from the AC bus (P_{ILC_DC} = −1 kW) to the DC bus through the ILC and applies the load shedding functionality, *F11*. Taking into account that the available power at the DC bus (1.14 kW) is not enough to feed two loads, *F11* connects only one DC load (0.6 kW). The rest of the available power is used for charging the batteries at P_{Bat} = 0.54 kW. The power flows in the MG when *F11* is active are shown in Zoom 1 of Figure 11.

Interval 2 (7 s < t < 10 s): The irradiation increases from 100 W/m² to 800 W/m² in 3 s. The MGCP keeps function *F11* activated.

At t = 8 s, the PV source works at its MPP, delivering P_{PV} = 0.6 kW, whereas P_{ILC_DC} = −1 kW. At this moment, the MGCP detects that the available power at the DC bus, taking into account the hysteresis level is enough to feed two of the loads. *F11* connects two loads and changes the setpoint I_{Ch_ref} of the ESS from 2.9 A to 0.78 A, where P_{Bat} = 0.15 kW. Note that at t = 8 s, after the connection of the two loads, only $|P_{ILC\_DC}| \leq 0.75$ kW is taken from the AC bus. This ensures a minimum level of power is available in the DC bus.

At t= 9.8 s, the PV source works at its MPP, delivering P_{PV} = 1.7 kW, where P_{ILC_DC} = −1 kW. At this moment, the MGCP detects that the available power at the DC bus to feed all the DC loads is greater than the hysteresis level

(DC_{Load_hyst}). The MGCP applies function *F10* which internally activates the flag, Sw_{Load} = *On*. After that, the MGCP starts a transition from *F10* to *F7*. *F7* connects all the DC loads and changes the setpoint of the ESS to I_{Ch_ref} = 1.82 A until the available power generation is stable at the instant t = 11.4 s, where P_{Bat} = 0.35 kW. At t = 9.8 s, the MGCP applies function *F10* during an execution cycle of the algorithm, i.e., for 73 ms. After that, function *F7* is applied.

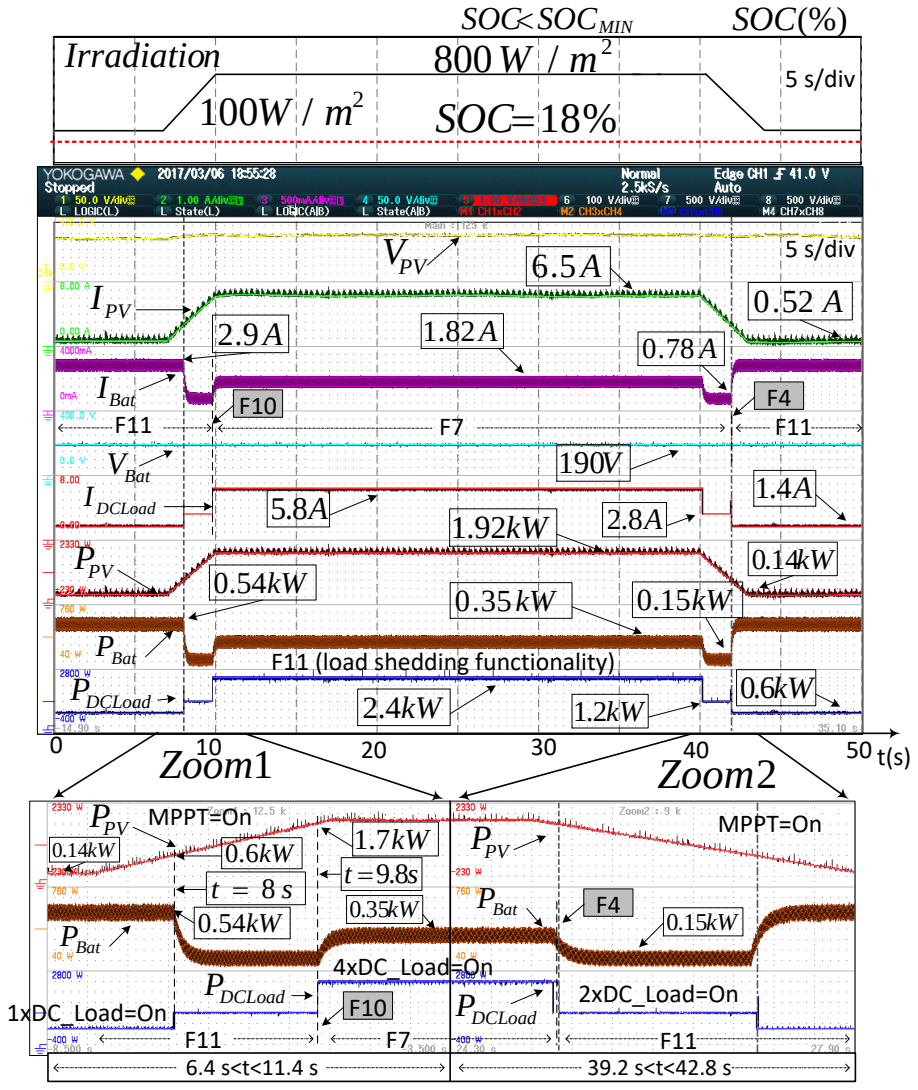

Figure 11. Experiment 2.

Interval 3 (39.2 s < t < 42.8 s): The irradiation decreases from 800 W/m² to 100 W/m² in 3 s. Note that at t = 40 s, the MGCP applies function *F4* which internally activates the flag, Sw_{Load} = *Off*. Then, the MGCP starts a transition from *F4* to *F11*. The MGCP keeps *F11* activated and the power delivered by the ESS can be reduced. The power flows in the MG when the MGCP starts a transition from *F4* to *F11* are shown in Zoom 2 of Figure 11.

2.4.2.3. Experiment 3

The operation functions broadcasted by the MGCP to the MG elements have a communication delay which depends on the RS485 communication system. In the experimental MG, the computing time of one operation function and its delay to be broadcasted and processed by one of the elements is lower than 74 ms, as can be observed in Figure 12.

2.4.3. Discussion

In Figure 7, the power exchange between devices of the MG is shown. In the first part of interval 5 (20 < t < 23.7 s), the MGCP causes the battery system to be charged to its maximum capacity, $PESS_{C10}$, using the power available from the PV DGs. In the second part of interval 5 (23.7 s ≤ t < 28 s), the MGCP limits the generation from the PV DGs, setting their operation points out of the MPP (*MPPT* = *Off*).

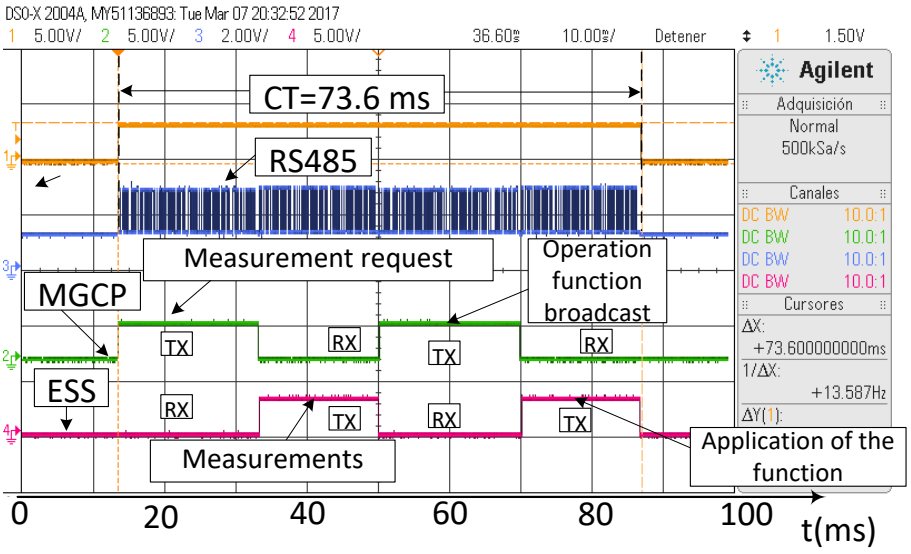

Figure 12. Experiment 3.

The ILC controls the DC bus voltage, because the AC bus works in grid connection mode. The ILC also carries out the synchronization of the AC bus with the grid, causing the current, I_{ILC_AC}, flowing through the ILC to/from the AC bus to have low distortion and to be synchronized with the grid voltage, V_{Grid}, when the MG exports/imports power to the grid. Figure 8 shows the waveforms of I_{ILC_AC} and of V_{Grid} in both situations, where a smooth transient, a good synchronization and a low distortion of I_{ILC_AC} can be observed in the transition from exporting to importing power to/from the AC bus. A smooth transient of the DC bus voltage, V_{DC}, is also observed in that transition at t = 35 s, which is the most sudden transient during the whole study, producing a transient undervoltage of $\Delta\hat{V}_{DC}$ = 34 V, i.e., less than 10% of the DC bus voltage. It should be considered that the power, P_{ILC_AC}, interchanged between the ILC and the AC bus, undergoes an abrupt change from 3.8 kW to −3.2 kW (7 kW step) at t = 35 s, provoked by a fast irradiation decrease.

Figure 10 shows the power exchange among the MG devices in Experiment 1. In time intervals 1 and 3, the MGCP applies the operation function *F8*. In this case, the demand of the DC bus is higher than the sum of the available PV power and the power import limit established by the grid operator. In that case, the MGCP requests the ESS to extract energy from the batteries to temporary feed the DC bus. This functionality reduces the cost of the electric bill.

The power flow in the MG after the application of the load shedding functionality can be observed in the zoom areas of Figure 11. No oscillations during those transients are observed.

In Experiment 3, the overall computing + transmission + processing delay of one operation function is 74 ms, where the ESS is at a distance of 2 m from the MGCP. According to the TIA/EIA-485-A standard, the maximum bandwidth at a 1.2 km distance is 100 kbps, which is much higher than the 9600 bps used in the experimental microgrid. The delay of a CAT5e twisted pair wire is less than 10 μs/km [32]. Therefore, if the distance between the ESS and the MGCP increases to 1 km, taking into account that the messages between the MGCP and the ESS run through the twisted pair four times (see the green and pink waveforms of Figure 12), the overall delay would increase to about 40 μs, i.e., about 0.05% of the total delays considered in the tests (73.6 ms). Further, the proposed algorithm is executed every second in the microgrid under study, so that the communication delays produced by moderate distances up to a few kilometers are not critical.

2.5. Conclusions

A new algorithm for the efficient management of the power converters of the hybrid AC/DC microgrid working in grid-connected mode has been presented. The algorithm is based on categorizing the devices according to their type: generation, storage, interlinking converter and load. Twelve operations functions have been defined and programmed in a Microgrid Central Processor for managing the power flow in the MG. The choice of the active operation function depends on the status of the distributed generators, the loads, the energy storage system and the energy dispatch limits between the AC and DC buses established by the grid operator. The MGCP broadcasts the set points of each converter through a RS485 communications system. The experimental and simulation results confirm that the proposed power management algorithm allows a suitable power balance among the MG devices when changes in PV generation, load demand and state of charge of the ESS occur. At any time, the power dispatch limits set by the public grid operator can be accomplished.

Acknowledgments: This work has been cofinanced by the Spanish Ministry of Economy and Competitiveness (MINECO) and by the European Regional Development Fund (ERDF) under Grant ENE2015-64087-C2-2.

Author Contributions: Robert Salas-Puente, Emilio Figueres and Gabriel Garcerá proposed the main idea, conceived and designed the experiments; Robert Salas-Puente and Raúl González-Medina performed the experiments; Silvia Marzal designed the communication; Silvia Marzal and Raúl González-Medina reviewed the article; Robert Salas-Puente, Emilio Figueres and Gabriel Garcerá wrote this paper.

Conflicts of Interest: The authors declare no conflict of interest.

2.6. Nomenclature

P_{PV1}, P_{PV2}	Power supplied by the PV arrays 1 and 2
P_{PV}	Total PV power generated by the DC MG
P_{DCLoad}	Total power consumed by the DC loads
P_{Grid}	Power injected from the hybrid AC/DC microgrid to the main grid
P_{ILC_AC}	Power injected from the DC bus to the AC bus by the ILC, measured at the AC side of the ILC
P_{ILC_DC}	Power injected from the DC bus to the AC bus by the ILC, measured at the DC side of the ILC
P_{ESS}	Power absorbed by ESS from the DC bus
P_{Bat}	Battery bank charge power
P_{ACLoad}	Total power consumed by the AC loads
P_{AC_DGs}	Power supplied by the AC DGs

η_{EES}	Efficiency of the ESS
η_{PV1}, η_{PV2}	Efficiency of the PV DC/DC converters 1 and 2
η_{ILC}	Efficiency of the ILC
I_{Grid}	RMS Current injected from the hybrid AC/DC microgrid to the main grid
V_{Grid}	RMS value of the grid voltage
ω	Grid angular frequency
φ	Grid phase
I_{ACLoad}	Total RMS current consumed by the AC loads
I_{DCLoad}	Total current consumed by the DC loads
V_{DC}	DC bus voltage
I_{ILC_AC}	RMS current injected from the ILC to the AC bus
SOC	State of charge of the battery bank
I_{Bat}	Charge current of the battery bank
V_{Bat}	Voltage of the battery bank
I_{Ch_ref}	Reference of the charge current of the battery bank
I_{Dis_ref}	Reference of the discharge current of the battery bank
I_{PV1}, I_{PV2}	Current supplied by the PV arrays 1 and 2
P_{PV_Lim}	Limit of the PV power generation
I_{DCLoad}	Total current consumed by the DC loads
$S_{W1,2,3,4DC\_Load}$	Switches of the DC loads (loads 1 to 4)
EDL	Energy dispatch limit
$\hat{P}_{Grid-to-MG}$	Maximum power drawn from the grid to the hybrid AC/DC microgrid
$\hat{P}_{MG-to-Grid}$	Maximum power injected to the grid from the hybrid AC/DC microgrid
$\hat{P}_{ILC_{AC}}\|_{Grid-to-MG}$	Maximum power drawn from the AC bus to the DC bus measured at the AC side of the ILC
$\hat{P}_{ILC_{AC}}\|_{MG-to-Grid}$	Maximum power injected from the DC bus to the AC bus, measured at the AC side of the ILC
$P_{ILC_{Rated}}$	Rated power of the ILC
$\hat{P}_{DC_{Load}}$	Maximum power consumed by the DC loads
$P_{AvailableDC\_MG}$	Power available at the DC bus of the MG
DC_{Load_hyst}	Power hysteresis level used by the load shedding functionality
$PESS_{C10}$	Power drawn by the ESS from the DC bus at a charge current of the battery bank equal to I_{C10}

2.7. References

1 Olivares, D.E.; Mehrizi-Sani, A.; Etemadi, A.H.; Cañizares, C.A.; Iravani, R.; Kazerani, M.; Hajimiragha, A.H.; Gomis-Bellmunt, O.; Saeedifard, M.; Palma-

Behnke, R.; et al. Trends in Microgrid Control. *IEEE Trans. Smart Grid* **2014**, *5*, 1905–1919.

2 Dragičević, T.; Lu, X.; Vasquez, J.C.; Guerrero, J.M. DC Microgrids—Part I: A Review of Control Strategies and Stabilization Techniques. *IEEE Trans. Power Electron*. **2016**, *31*, 4876–4891.

3 Cagnano, A.; de Tuglie, E.; Cicognani, L. Prince—Electrical Energy Systems Lab: A pilot project for smart microgrids. *Electr. Power Syst. Res.* **2017**, *148*, 10–17.

4 Unamuno, E.; Barrena, J.A. Hybrid AC/DC microgrids—Part II: Review and classification of control strategies. *Renew. Sustain. Energy Rev*. **2015**, *52*, 1123–1134.

5 Liu, X.; Wang, P.; Loh, P.C. A Hybrid AC/DC Microgrid and Coordination Control. *IEEE Trans. Smart Grid* **2013**, *2*, 278–286.

6 Nejabatkhah, F.; Li, Y.W. Overview of Power Management Strategies of Hybrid AC/DC Microgrid. *IEEE Trans. Power Electron.* **2015**, *30*, 7072–7089.

7 Liu, X.; Wang, P.; Loh, P.C. A hybrid AC/DC micro-grid. In Proceedings of the IPEC Conference Proceedings, Singapore, 27–29 October 2010; pp. 746–751.

8 Wang, P.; Liu, X.; Jin, C.; Loh, P.; Choo, F. A hybrid AC/DC micro-grid architecture, operation and control. In Proceedings of the IEEE Power and Energy Society General Meeting, Detroit, MI, USA, 24–29 July 2011; pp. 1–8.

9 Josep Guerrero, J.V. Hierarchical Control of Droop-Controlled AC and DC Microgrids. A General Approach toward Standardization. *IEEE Trans. Ind. Electron.* **2011**, *58*, 158–172.

10 Poh Chiang Loh, S.M. Autonomous Control of Interlinking Converter with Energy Storage in Hybrid AC–DC Microgrid. *IEEE Trans. Ind. Appl.* **2013**, *49*, 1374–1376.

11 De Brabandere, K.; Bolsens, B.; van den Keybus, J.; Woyte, A.; Driesen, J.; Belmans, R. A Voltage and Frequency Droop Control Method for Parallel Inverters. *IEEE Trans. Power Electron.* **2007**, *22*, 1107–1115.

12 Loh, P.C.; Li, D.; Chai, Y.K.; Blaabjerg, F. Autonomous Operation of Hybrid Microgrid with AC and DC Subgrids. *IEEE Trans. Power Electron.* **2013**, *28*, 2214–2223.

13 Aryani, D.R.; Kim, J.-S.; Song, H. Interlink Converter with Linear Quadratic Regulator Based Current Control for Hybrid AC/DC Microgrid. *Energies* **2017**, *10*, 1799.

14 Luo, F.; Loo, K.H.; Lai, Y.M. A hybrid AC/DC microgrid control scheme with voltage-source inverter-controlled interlinking converters. In Proceedings of the 2016 18th European Conference on Power Electronics and Applications (EPE'16 ECCE Europe), Karlsruhe, Germany, 5–8 September 2016; pp. 1–8.

15 Karimi, Y.; Guerrero, J.M.; Oraee, H. Decentralized method for load sharing and power management in a hybrid single/three-phase islanded microgrid consisting of hybrid source PV/battery units. In Proceedings of the 2016 IEEE Energy Conversion Congress and Exposition (ECCE), Milwaukee, WI, USA, 18–22 September 2016; pp. 1–8.

16 Hasan, M.A.; Vemula, N.K.; Parida, S.K. Cost based dynamic load dispatch for

an autonomous parallel converter hybrid AC-DC microgrid. In Proceedings of the National Power Systems Conference (NPSC), Bhubaneswar, India, 19–21 December 2016; pp. 1–5.

17 Yue, J.; Hu, Z.; Li, C.; Vasquez, J.C.; Guerrero, J.M. Economic Power Schedule and Transactive Energy through an Intelligent Centralized Energy Management System for a DC Residential Distribution System. *Energies* **2017**, *10*, 916.

18 Gao, L.; Liu, Y.; Ren, H.; Guerrero, J.M. A DC Microgrid Coordinated Control Strategy Based on Integrator Current-Sharing. *Energies* **2017**, *10*, 1116.

19 Kaur, A.; Kaushal, J.; Basak, P. A review on microgrid central controller. *Renew. Sustain. Energy Rev.* **2016**, *55*, 338–345.

20 Aluisio, B.; Cagnano, A.; de Tuglie, E.; Dicorato, M.; Forte, G.; Trovato, M. PrInCE lab microgrid: Early experimental results. In Proceedings of the 2016 AEIT International Annual Conference (AEIT), Capri, Italy, 5–7 October 2016; pp. 1–6

21 El-Hendawi, M.; Gabbar, H.A.; El-Saady, G.; Ibrahim, E.-N.A. Control and EMS of a Grid-Connected Microgrid with Economical Analysis. *Energie*s **2018**, *11*, 129.

22 Dou, C.; Zhang, Z.; Yue, D.; Zheng, Y. MAS-Based Hierarchical Distributed Coordinate Control Strategy of Virtual Power Source Voltage in Low-Voltage Microgrid. *IEEE Access* **2017**, *5*, 11381–11390.

23 Baek, J.; Choi, W.; Chae, S. Distributed Control Strategy for Autonomous Operation of Hybrid AC/DC Microgrid. *Energies* **2017**, *10*, 373.

24 Tofis, Y.; Timotheou, S.; Kyriakides, E. Minimal Load Shedding Using the Swing Equation. *IEEE Trans. Power Syst.* **2017**, *32*, 2466–2467.

25 Choi, Y.; Lim, Y.; Kim, H.-M. Optimal Load Shedding for Maximizing Satisfaction in an Islanded Microgrid. *Energies* **2017**, *10*, 45.

26 Zhou, H.; Qiu, Y.; Lin, Y.; Wang, Z.; Ma, J. Remote automatic switching and load shedding linkage control scheme. In Proceedings of the 2016 IEEE International Conference on Power and Renewable Energy (ICPRE), Shanghai, China, 21–23 October 2016; pp. 260–263.

27 Grantham, A.; Pudney, P.; Ward, L.A.; Whaley, D.; Boland, J. The viability of electrical energy storage for low-energy households. *Sol. Energy* **2017**, *155*, 1216–1224.

28 Leadbetter, J.; Swan, L. Battery storage system for residential electricity peak demand shaving. *Energy Build.* **2012**, *55*, 685–692.

29 Ciobotaru, M.; Agelidis, V.G.; Teodorescu, R.; Blaabjerg, F. Accurate and less-disturbing active antiislanding method based on PLL for gridconnected converters. *IEEE Trans. Power Electron*. **2010**, *25*, 1576–1584.

30 Faxas-Guzmán, J.; García-Valverde, R.; Serrano-Luján, L.; Urbina, A. Priority load control algorithm for optimal energy management in stand-alone photovoltaic systems. *Renew. Energy* **2014**, *68*, 156–162.

31 PowerSim. *PSIM10.0*; (Rockville, MD, USA) PowerSim 2016.

32 Patrao, I.; González-Medina, R.; Marzal, S.; Garcerá, G.; Figueres, E. Synchronization of Power Inverters in Islanded Microgrids Using an FM-

Modulated Signal. IEEE Trans. Smart Grid 2017, 8, 503–510.

3

3. PUBLICACIÓN II

3.EXPERIMENTAL STUDY OF A CENTRALIZED CONTROL STRATEGY OF A DC MICROGRID WORKING IN GRID CONNECTED MODE

Salas-Puente, Robert; Marzal, Silvia; González-Medina, Raúl; Figueres, Emilio; Garcera, Gabriel.2017. "Experimental Study of a Centralized Control Strategy of a DC Microgrid Working in Grid Connected Mode." Energies 10, no. 10: 1627. DOI:10.3390/en10101627.

Article

Experimental Study of a Centralized Control Strategy of a DC Microgrid Working in Grid Connected Mode

Robert Salas-Puente *, Silvia Marzal, Raúl González-Medina, Emilio Figueres and Gabriel Garcera

Grupo de Sistemas Electrónicos Industriales del Departamento de Ingeniería Electrónica, Universitat Politècnica de València, Camino de Vera s/n, 46022 Valencia, Spain; rosapue1@posgrado.upv.es (R.S.-P.); silmarro@upv.es (S.M.); raugonme@upv.es (R.G.-M.); efiguere@eln.upv.es (E.F.); ggarcera@eln.upv.es (G.G.)

* Correspondence: rosapue1@posgrado.upv.es; Tel.: +34-(96)-3877007 (ext. 76021)

Received: 18 September 2017; Accepted: 12 October 2017; Published: 17 October 2017

Abstract: The results concerning the integration of a set of power management strategies and serial communications for the efficient coordination of the power converters composing an experimental DC microgrid is presented. The DC microgrid operates in grid connected mode by means of an interlinking converter. The overall control is carried out by means of a centralized microgrid controller implemented on a Texas Instruments TMS320F28335 DSP. The main objectives of the applied control strategies are to ensure the extract/inject power limits established by the grid operator as well as the renewable generation limits if it is required; to devise a realistic charging procedure of the energy storage batteries as a function of the microgrid status; to manage sudden changes of the available power from the photovoltaic energy sources, of the load power demand and of the power references established by the central controller; and to implement a load shedding functionality. The experimental results demonstrate that the proposed power management methodology allows the control of the power dispatch inside the DC microgrid properly.

Keywords: DC microgrid; central controller; power management; power converters

3.1. Introduction

In the context of increasing demand for electric power, local energy production through the integration of microgrids (MGs) in the main grid is becoming an interesting research topic. MGs are formed by various distributed generators (DGs), energy storage systems (ESS) and controllable loads. Distributed Generators can include Renewable Energy Sources (RESs). There are several renewable generation technologies that can provide electricity in a distributed manner, including photovoltaic (PV) systems, micro hydropower, small-scale biomass facilities, small wind turbines, etc. MGs can operate either in grid-connected or in islanded mode, i.e., connected or disconnected from the Point of Common Coupling (PCC). An MG can be disconnected from the main grid in the case of faults [1, 2]. Once the fault has disappeared, it can be reconnected to the grid. In addition, a microgrid has its own control system to ensure the correct operation and coordination of the different devices.

Currently, MGs have several configurations: AC, DC or Hybrid AC/DC. However, in some applications DC microgrids have become more attractive than traditional AC microgrids [3, 4] because of their higher energy efficiency, their ability to easily connect DC/DC converters to the common DC bus, and their ability to directly couple DC power sources, like batteries and PV sources, with DC loads, which results in a reduction of power conversion losses and costs [4]. Moreover, the control system of DC/DC converters connected to DC microgrid does not have to deal with the problems caused by reactive power flow, synchronization and frequency regulation [5]. A DC microgrid can operate in grid-connected mode by means of an InterLinking Converter (ILC), which connects the DC bus to the PCC of the main grid [6, 7]. In this mode, the DC bus voltage is regulated by the ILC, being highly stable, even in the case of low quality distribution grids [8]. When the distribution grid fails, the microgrid must regulate the DC bus voltage without the ILC. Some control methods have been developed and proposed in the literature [9-11] for reaching this goal. The typical objectives of the DC microgrid in grid-connected mode are: to minimize the cost of the imported energy from the main grid, to optimize the power dispatch among the converters and the DC bus and to regulate the DC bus voltage [12]. For the optimization of the power dispatch, communications between the devices of the MG and the grid operator are necessary [13, 14].

Regarding the control system, one of the main challenges in MGs is how to maintain the generation and consumption energy balance [15]. Power imbalance is a common scenario in MGs, which is caused by the discontinuous power generation availability caused in turn by the intermittent nature of renewables and the variable power demand of the loads connected to the MG,

among other factors. These imbalances should be managed fast, safely and effectively by the MG control in order to avoid electrical transients, which can damage or destabilize the system [6-8]. Therefore, proper power management control strategies have been developed. These strategies are aimed mainly at: (i) controlling the connected DGs and energy storage system, (ii) regulating the DC bus voltage, (iii) optimizing the power dispatch between DC/DC converters and the DC bus voltage to minimize the cost of imported energy from the main grid, (iv) managing and optimizing the ESS operation, and (v) managing current sharing between parallel converters [16, 17]. At present, the major control strategies to maintain power balance in DC microgrids are the well-known droop control methods [14-18], which don't require any communication infrastructure, or other solutions using communications. The power management of MGs can be classified into three categories: centralized, decentralized and distributed control [17-21]. Centralized control systems offer a higher precision of the power sharing among the power converters in MGs [20, 21]. In those systems, the energy dispatch can be observed and managed by an intelligent centralized system [22, 23]. A Microgrid Central Controller (MGCC) acquires system data and takes decisions about the power to be managed by each of the power converters under operation, forecasting power references to all the power devices of the MG such as DGs, loads, ESS, etc. In the case of communication lost or even the failure of the MGCC, local autonomous controllers are necessary. These controls have been explained in many previous works [24-27], most of them being based on some droop strategies [14]. It is worth pointing out that this paper is focused on a centralized MGCC algorithm. A future work could deal with the coordinated operation of the centralized algorithm with local droop controllers in the case of system failures. However, that study is beyond the scope of this paper. Besides, some previous works [1], [20] recommend centralized solutions for small scale microgrids.

Up to the present different centralized control strategies of microgrids have been proposed in the literature [28-30]. In [28], a control strategy for a DC microgrid was proposed. The strategy was aimed at minimizing the daily total energy costs. In [29], an optimization algorithm was applied to a group of interconnected MGs with the main grid. The procedures under study were charging/discharging of the ESS, starting or stopping the DGs, and receiving/sending power from/to neighboring MGs. In this case, the charge and discharge of the ESS relies on the energy demand and production. A centralized system for a DC distribution system was presented in [30]. The main objective of that control method was cost minimization based on the real-time electrical price. In order to meet that goal, converter control was based on voltage droop,

which achieved the power sharing among the DGs and was responsible for tracking the DC bus voltage reference. In [31], a coordinated control strategy was addressed within a DC microgrid. In that case the converters were working as voltage sources. A virtual output resistance was implemented for each converter. However, no communications were implemented, which are necessary to optimize the power dispatch among the power converters and to restore the voltage deviations produced.

As it was described above, several centralized management and control strategies have been developed for DC microgrids. The strategies have been implemented by solving partial problems or using a particular control strategy. In this work, a centralized control technique for the efficient power management of an experimental DC microgrid is explained. The proposed DC microgrid is connected to the main grid through a bidirectional ILC (see Figure 1). The ILC is an AC/DC bidirectional converter which is responsible for managing the power flow between the DC bus and the main grid. The ILC regulates the DC bus voltage at a fixed value.

In this work, the MGCC does not account for the cost-effective operation of the system in terms of the energy tariffs. The MGCC receives information about the power exchange limits with the main grid from the grid operator. The power to be injected/extracted to/from the grid is calculated by an algorithm implemented in the MGCC starting from the knowledge of the PV available power, the load connected to the DC bus, the battery state and the power exchange limits provided by the grid operator. The goal of that algorithm is to import the needed power from the grid, keeping it below the established limits, feeding the loads and keeping the batteries *SoC* inside a safe range. If a surplus of energy is available from the PV generation, power is injected to the grid below the limit imposed by the grid operator. No energy price considerations are taken into account by the implemented algorithm.

As shown in Figure 1, the DC microgrid consists of: (a) an MGCC; (b) an ILC connected to the main grid which controls the DC bus voltage; (c) two DC/DC converters that operate as a current source interchanging their power with the DC bus; (d) four loads with their respective electronic switches; (e) an RS-485 serial communication system and (e) the grid operator.

The main contribution of this paper is the integration of conventional control strategies of all the power converters in the microgrid by means of a centralized algorithm implemented in a MGCC, taking into account real time serial communications for sending/receiving the necessary data. An additional contribution of this work is the use of a realistic battery ESS control algorithm in the context of DC microgrids, which follows the charging procedure DIN 41773 [32, 33]. Depending on their voltage, the batteries are charged either at a

constant current or at a constant voltage. Once the current absorbed by the batteries is smaller than a pre-specified value of tail current, the battery voltage is kept at a certain float voltage. The integration of a load management algorithm, compatible with the microgrid status, is also described. The integration of all those strategies through an MGCC has not been reported by previous studies, to the best authors' knowledge. It is worth pointing out that most of previous studies for this kind of MG are theoretical, having been validated by simulation results [4,28-31,34,35]. In this paper, the experimental validation of the MGCC centralized algorithm in a DC microgrid is shown. It provides a realistic evaluation under different MG operation scenarios. Moreover, this work shows the MGCC algorithm runtime as well as the communication delays in order to ensure the stability of the DC bus.

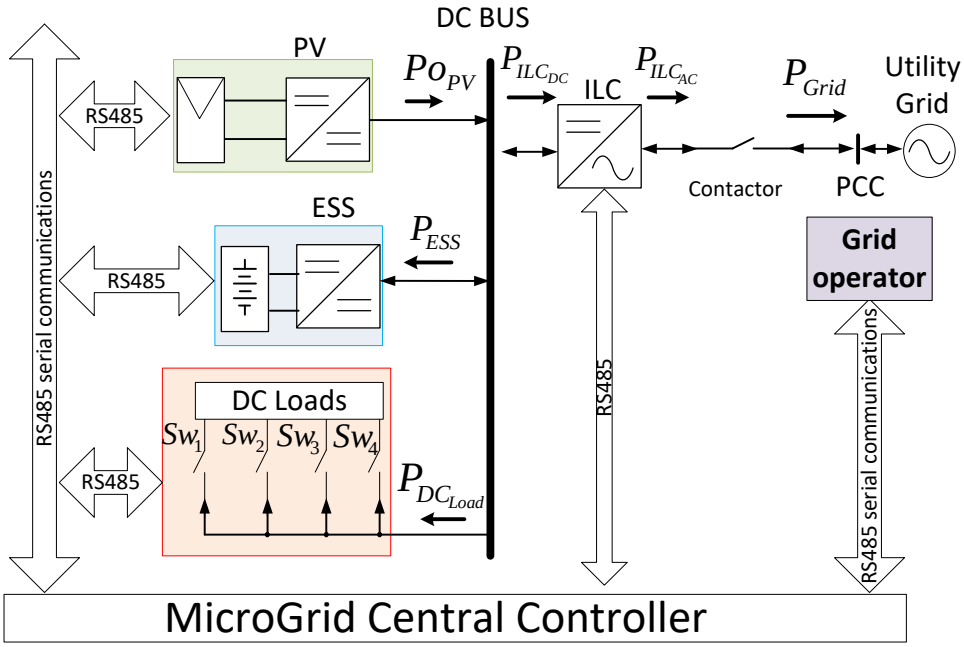

Figure 1. Conceptual scheme of the DC microgrid.

The main objectives of the control strategies applied to the DC microgrid are the following:

- To comply with the power flow limits from/to the DC microgrid to/from the main grid. These limits are established by the grid operator and are set according to the purchase or sale tariffs of generated or consumed energy. This study takes into account the limit value of the power

absorption/injection sent by the grid operator to the MGCC, as well as its effect on the general MG power management and on the power converters electrical behavior.

- To limit the photovoltaic power generation below the maximum available power if it is required. This limit depends on the power available in the DC bus and the power injection limit set by the grid operator.
- To develop the charging procedure DIN 41773 for Valve Regulated Lead-Acid (VRLA) [36] batteries of the ESS connected to the DC bus, in order to ensure the proper operation of the ESS and extend the life of its batteries.
- To manage the power demand of the devices connected to the DC bus by means of a load shedding functionality. This function, which is used only as a last resort, is applied according to the batteries status, the available power and a pre-established power threshold. The pre-established thresholds have a hysteresis level when connecting/disconnecting, avoiding destabilizing transients at the DC bus.
- To control in real time the power flow inside the MG through RS485 serial communication. The proposed power management algorithm provides the optimal reference values, which are transmitted to each converter to establish their operation.
- To obtain smooth transients in the voltages and currents of the power converters connected in the DC bus, during the sudden changes of the power set points in each converter.

This paper is organized as follows: Section 2 describes the primary controls of every power converter of the DC microgrid. In Section 3, concepts related to the power management algorithm are explained. In Section 4, experimental and discussion results are presented. Finally, the conclusions are presented in Section 5.

3.2. Description of the Power Electronic Converters Involved in the DC Microgrid

The proposed DC microgrid is depicted in Figure 1. The interconnection between the DC bus and the PCC of the public grid is performed by a 10 kW bidirectional IC, which works in grid-connected mode. The V_{Grid} = 230 V_{rms} and its frequency is F_{Grid} = 50 Hz ± 1 Hz. The nominal DC bus voltage is V_{DC} = 380 V, being regulated by the ILC [37]. In the MG under study, two converters are connected to the DC bus: the first one is a 3 kW bidirectional DC/DC converter connected to the batteries and the second one a 2.5 kW DC/DC converter connected to a PV array. The battery bank voltage (V_{Bat}) of the ESS ranges from 194 V to 254 V, whereas the voltages at the PV arrays (V_{PV}) vary from 300 V to 370 V. Additionally four 'shedable' 650 W DC loads are connected in the DC bus by means of individual electronic switches (S_{w1} to S_{w4}), that are controlled

by the MGCC. It is important to highlight that the primary controllers of every converter are designed for satisfying demands of the MG; maintaining the stability in the DC bus voltage, battery bank and PV arrays. These control loops have a high bandwidth to ensure a fast response to changes in the current/voltage references [6]. Each power converter runs their corresponding inner primary controllers in a TMS320F28335 DSP. MGCC allows an exchange of information among different devices connected to the MG by means of the RS485 serial communication bus as is depicted in Figure 1. The parameters broadcasted through this bus among the power converters of the DC microgrid and the MGCC are shown in Table 1.

Table 1. Parameters broadcasted between the power converters of the DC microgrid and the MGCC.

MGCC	**Power Converters**			
	ILC	**ESS**	**PV**	**DC Load**
Output setpoint*	V_{DC}*	P_{ESS}*	P_{PV_Lim}*	$S = \{S_{w1}^*, S_{w2}^*, S_{w3}^*, S_{w4}^*\}$
Input measurement	P_{ILC_AC}	P_{ESS}, SoC	Po_{PV}	P_{DC_Load}

* MGCC references

3.2.1. PV System

The PV system consists of the PV arrays and a Boost DC/DC converter that is controlled as current source providing a certain amount of power to the DC bus (1):

$$Po_{PV} = I_{PV} \cdot V_{PV} \cdot \eta_{PV} \quad (1)$$

The PV system is shown in Figure 2a. An ISO5500 driver provides the isolation required between the PWM module of the DSP TMS320F28335 (Delfino Microcontroller, Texas Instruments Incorporated, Dallas, TX, USA) and the IGBTs (VS-GT50TP60N, Vishay Electronic GmbH, Selb, Germany). The control of the PV array voltage (V_{PV}) has been implemented in cascade with the control of output current (I_{LPV}) [7]. Gi_{PV} and Gv_{PV} blocks represent current and voltage regulators of the Boost DC/DC converter, respectively. These regulators are implemented by means of PI controllers, which are initialized to obtain soft transients in the following scenarios: (i) at the time of initial connection of the PV system to the DC bus, (ii) at sudden changes of irradiation and (iii) at sudden changes in the set point of PV power limit established by the MGCC (P_{PV_Lim}*). Thus, transient over-currents and over-voltages at the DC bus are avoided.

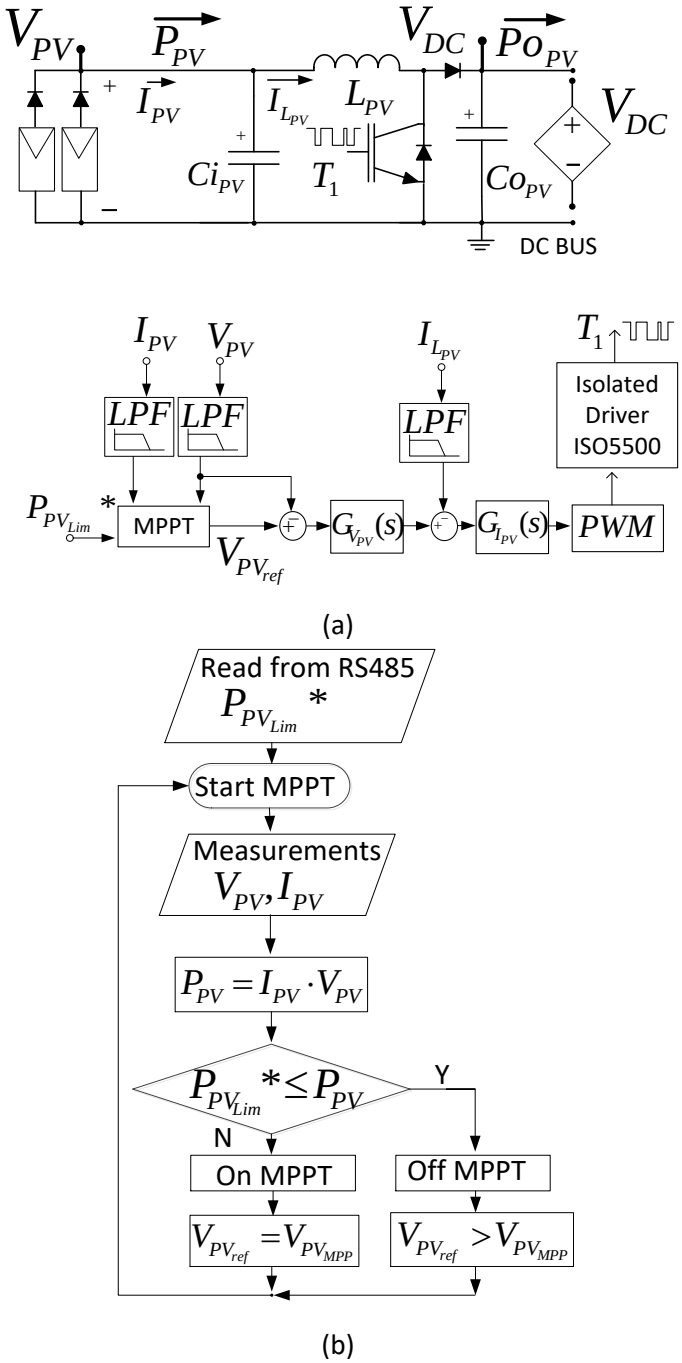

Figure 2. Topology and control of the PV system: (**a**) DC/DC converter, (**b**) Control strategy of the PV system.

The control strategy decision tree of the PV converter is depicted in Figure 2b. P_{PV_Lim}* is a reference power sent by the MGCC. The PV converter compares the available power in the PV array with the P_{PV_Lim}*. If the available power at the PV array is lower than P_{PV_Lim}*, the DC/DC will operate at the maximum power point (MPP) of the PV array, controlling V_{PV} at the corresponding level. The Maximum Power Point Tracking (MPPT) algorithm sets the reference voltage (V_{PV_ref}) to V_{PV_ref} = V_{PV_MPP} and the PV source works at its MPP (On MPPT). Otherwise, in order to limit the PV power injected to the DC bus to P_{PV_Lim}*, the MPPT sets V_{PV_ref} at a voltage higher than V_{PV_MPP}, so that the PV array can be operated outside its MPP (Off MPPT).

3.2.2. Energy Storage System (ESS)

The ESS keeps the power balance of the DC bus [38, 39] and consists of the battery bank and a 3 kW half-bridge DC/DC converter (see Figure 3). The ESS is controlled as current source, absorbing a certain amount of power from the DC bus. P_{ESS} is the power at which the battery ESS is charged, which is measured in real time. That power is calculated by Equation (2).

$$P_{ESS} = I_{Bat} \cdot V_{Bat} \cdot \eta_{ESS} \quad (2)$$

It is worth pointing out that P_{ESS} is negative if the power is injected to the DC bus from the ESS. The battery bank of the ESS is designed to deliver up to 3 kW. The battery bank it is composed of 18 batteries of 12 V connected in series, with a nominal voltage of V_{Bat} = 216V and a charging voltage of $V_{Bat(Ch)}$ = 254 V. VRLA model SUN POWER VRM 12V105 batteries (HOPPECKE, Brilon, Germany) for cyclic applications were selected,. The characteristics of the ESS are shown in Table 2. The control loops of the ESS are also represented in Figure 3. The control of the battery bank voltage (V_{Bat}) has been implemented in cascade with the output current controller (I_{LBat}). Gv_{Bat} and Gi_{Ilbat} blocks represent the voltage and current regulators of the DC/DC converter, respectively. These regulators are PI controllers, which are adjusted and initialized to obtain soft transients for any sudden change of the power reference P_{ESS}* sent by the MGCC.

The battery management algorithm is depicted in Figure 4. The setpoint P_{ESS}* is the power available at the DC bus for charging the batteries, which is calculated by the MGCC. P_{ESS}* is sent by the MGCC to the ESS. The ESS reads P_{ESS}* and changes the signal 'Mode' depending on P_{ESS}*. 'Mode' is a flag that takes two possible states.

If P_{ESS}* > 0, the signal 'Mode' takes a high value, 'Mode = 1' (supply mode). On the contrary, if P_{ESS}* < 0 the signal 'Mode' takes a low value, 'Mode = 0' (charge mode). The ESS performs soft power transitions to avoid fluctuations of

the DC bus voltage by means of avoiding abrupt bidirectional changes in the signal P_{ESS}*, see Figure 5a. P_{ESS_ref} is the power reference for the DC/DC control and it is changed progressively from an initial value $P_{ESS\_initial}$* to a final value P_{ESS}* according to a ramp function with a 100 ms duration. The ramp function produces a variation of P_{ESS_ref} between the values $P_{ESS\_initial}$* and P_{ESS}* in a time of 100 ms, with an update period of Δt_{RAMP} = 1 ms. The ramp function and P_{ESS_ref} are shown by Equations (3) and (4), respectively:

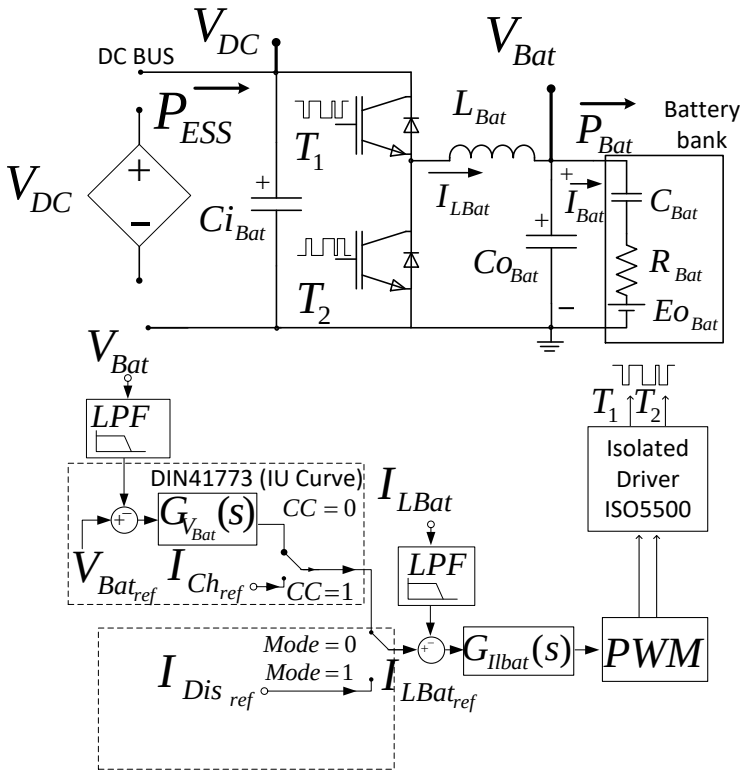

Figure 3. Topology and control of the ESS, Half-bridge DC/DC converter.

$$r(t) = \frac{t}{100 \cdot \Delta t_{RAMP}}, (0 \leq t \leq 100\ ms) \quad (3)$$

$$P_{ESS_{ref}} = P_{ESS_{initial}} + \left(P_{ESS} * - P_{ESS_{initial}}\right) \cdot r(t) \quad (4)$$

The battery management algorithm guarantees suitable voltage levels and charging/discharging currents. Thus, both the overheating and the damage of the batteries are avoided. The charging process follows the DIN 41773 (IU curve), see Figure 5b. Depending on their voltage, the batteries are charged

either at a constant current or at a constant voltage. Once the current absorbed by the batteries is smaller than a pre-specified value of tail current (I_{bat_tail}) or a charging time (t_{Ch}), the battery voltage is kept at a certain float voltage (V_{bat_float}). The signal '*CC*' is a flag that identifies the charge mode. If '*CC* = 1' it means that the batteries are being charged at a constant current (constant current mode), whereas if '*CC* = 0' the batteries are being charged at a constant voltage (constant voltage mode).

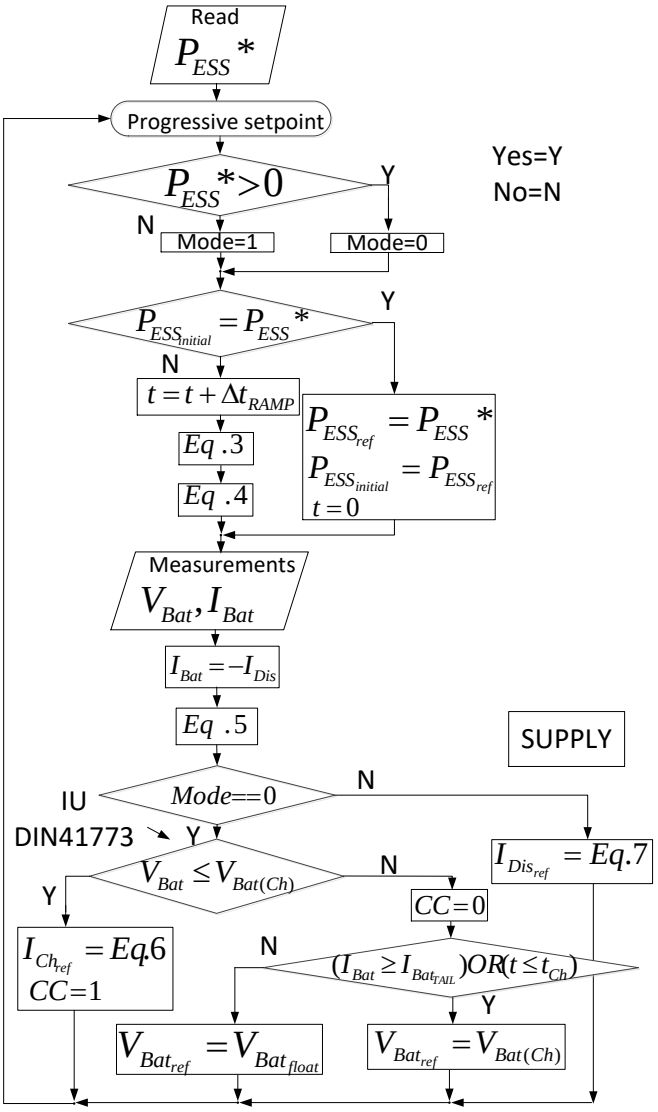

Figure 4. **Proposed battery charging/discharging control algorithm**

Table 2. Characteristics of the ESS.

DC/DC Converter	Battery Specifications	DIN 41773
	SUN POWER VRM 12V105	Battery Bank 18 Batteries Connected in Series
P_{ESS_HB} = 3 kW	V_{rated} = 12 V	V_{Bat_rated} = 216 V
F_{sw_ESS} = 16 kHz	V_{MIN} = 10.28 V	$V_{Bat(Ch)}$ = 254 V
C_{iBat} = 1 mF	C_T = 105 A·h	V_{Bat_float} = 243 V
C_{oBat} = 1 mF	C_{100} = 101 A·h	V_{Bat_MIN} = 194 V
L_{Bat} = 5.4 mH	C_{10} = 87 A·h	I_{C10} = 8.7 A
I_{Lbat_max} = 12 A	η_{C10} = 0.83	I_{Bat_tail} = 0.5 A
η_{ESS} = 0.97	η_{C100} = 0.96	t_{Ch} < 48 h

The ESS sends the state of charge (*SoC*) of the battery bank to the MGCC in order to obtain the highest possible performance [39-41]. In Figure 4, *SoC* is calculated from Equation (5) where: C_T is the total capacity of the battery bank (A·h), C_{Dis} is the discharge capacity in A·h, and η_{Dis} is the discharge efficiency. The reference of the battery charge current (I_{Ch_ref}) is calculated from Equation (6); whereas the discharge current ones (I_{Dis_ref}) is calculated from Equation (7). Parameter P_{ESSC10} is the maximum power for discharging the batteries of the ESS. It has been established that the batteries are charged with a current equal to $I_{C10} = C_{10}/10$ h, being C_{10} the specified battery capacity (measured in A·h) for a discharge time of 10 hours. $P_{ESSC10} = V_{Bat} \cdot I_{C10}/\eta_{ESS}$, where η_{ESS} is the ESS efficiency:

$$SoC(t) = SoC(0) - \eta \cdot \int_0^t \frac{I_{Dis}(t)}{C_T} \cdot dt$$
$$\eta_{Dis} = \frac{C_{Dis}}{C_T} \quad (5)$$

$$I_{Ch_{ref}} = MIN\left(\frac{P_{ESSC10}}{V_{Bat}}, \frac{P_{ESS_{ref}} \cdot \eta_{ESS}}{V_{Bat}}\right) \text{ where } P_{ESS_{ref}} > 0 \quad (6)$$

$$I_{Dis_{ref}} = -MIN\left(\frac{P_{ESSC10}}{V_{Bat}}, \left|\frac{P_{ESS_{ref}} \cdot \eta_{ESS}}{V_{Bat}}\right|\right) \text{ where } P_{ESS_{ref}} < 0 \quad (7)$$

3.2.3. Interlinking Converter

Figure 6 depicts the single-phase ILC implemented. The power stage is a full-bridge (bidirectional) inverter, which interconnects the DC bus and the grid. The ILC is controlled as a current source (I_{ILC_AC}) injecting/extracting a power to/from the main grid synchronously with the grid [42]. If the power flows from the grid to MG, it results: $P_{Grid} < 0$ and $|P_{ILC_{AC}}| = |P_{Grid}|$. Otherwise, when the power flows from the MG to the grid, it results: $P_{Grid} > 0$ and $P_{ILC\_AC} = P_{Grid}$. P_{ILC_AC} stands for the power injected by the ILC to the grid.

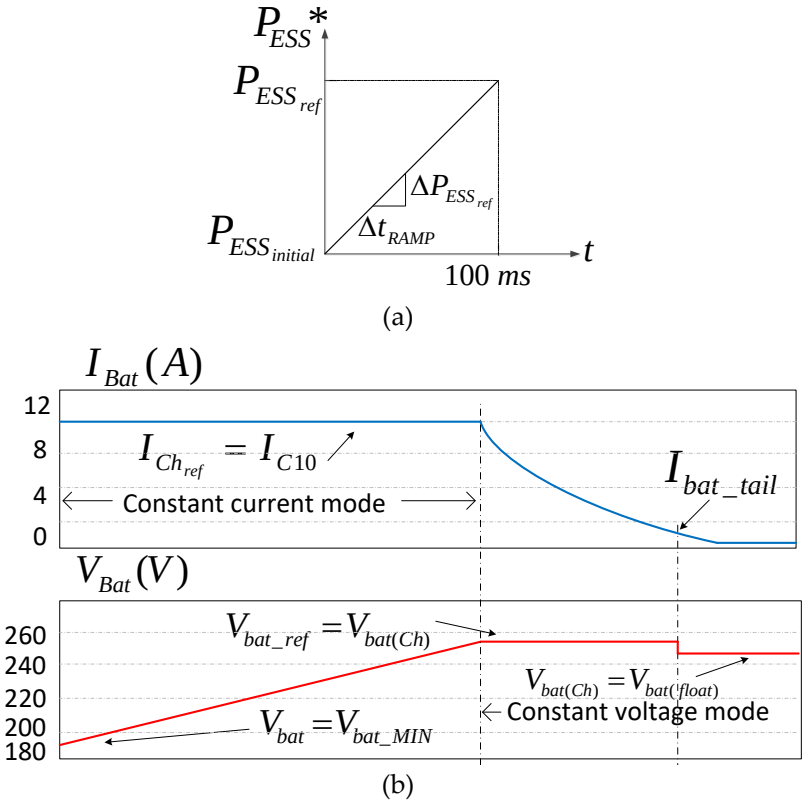

Figure 5. Control of the ESS: (**a**) Ramp function, (**b**) DIN 41773 (IU curve).

The DC bus voltage is controlled by the ILC, which is possible in grid-connected mode, as can be seen in Figure 6. The nominal DC bus voltage is 380 V, as it's the current trend in domestic and industrial DC microgrids [43]. The grid voltage (V_{Grid}) is measured by a PLL (Phase Locked Loop) [44] programmed inside the ILC DSP controller, which detects the grid phase (φ) and its frequency (ω). $Gi_{ILC}(s)$ and $Gv_{ILC}(s)$ blocks represent, respectively, the transfer functions of the current and voltage regulators of the ILC, having the following characteristics:

- $Gi_{ILC}(s)$ consists of a proportional regulator working in parallel with four resonant controllers tuned at frequencies: ω, 3 ω, 5 ω and 7 ω, being ω the grid angular frequency (Equation (8)). Those resonant controllers are known as SOGIs (Second Order Generalized Integrators) [42], which provide a high gain at the grid frequency and at some of its odd non-triplen multiples. If a variation of the frequency of the grid takes place, the SOGIs center frequencies vary correspondingly.

- $Gv_{ILC}(s)$ consists of a Notch filter operating in series with a PI controller (Equation (9)). The notch filter removes the second harmonic of the grid fundamental frequency present at the DC bus voltage from the reference signal of the current controller:

$$Gi_{ILC}(s) = 0.035 + \sum_{i=1,3,5,7} \frac{40}{i} \cdot \frac{0.001 \cdot (i \cdot \omega) \cdot s}{s^2 + 0.001 \cdot (i \cdot \omega) \cdot s + (i \cdot \omega)^2} \quad (8)$$

$$Gv_{ILC}(s) = -0.1178 \cdot \frac{1 + 0.46 \cdot s}{0.46 \cdot s} \cdot \frac{s^2 + (2 \cdot \omega)^2}{s^2 + (2 \cdot \omega) \cdot s + (2 \cdot \omega)^2} \quad (9)$$

The controllers of the ILC keep the Total Harmonic Distortion (THDi) of the current injected/absorbed to/from the grid within the limits of the IEEE1547 standard [45].

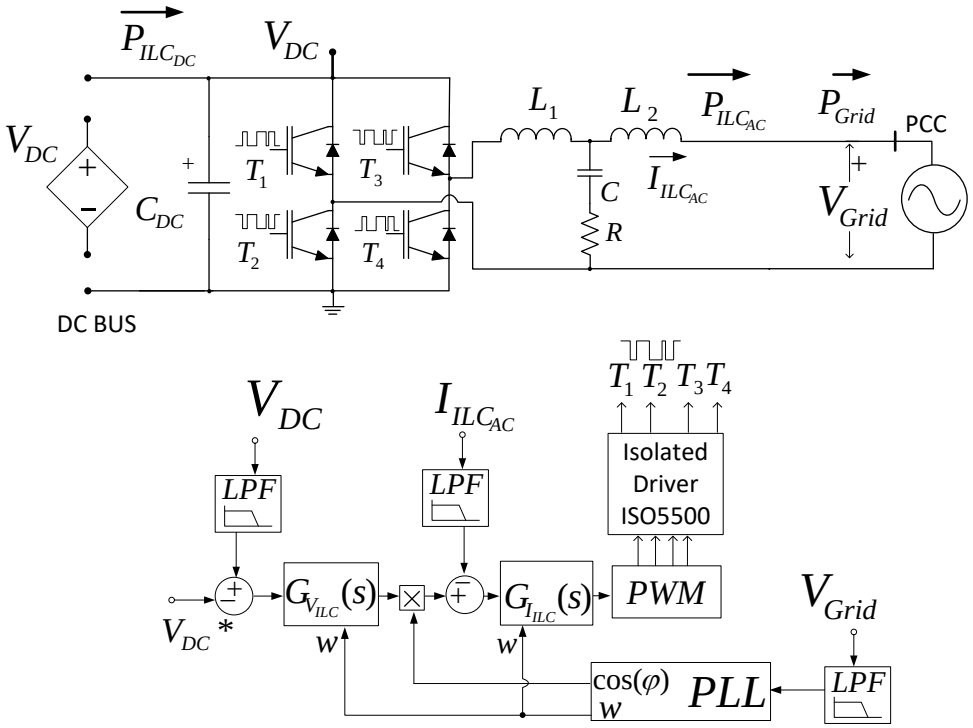

Figure 6. Topology and control diagram of the ILC.

3.2.4. Electronic Switches

The MGCC controls the load demand at the DC bus by connecting/disconnecting up to four loads to/from the DC-bus using of individual switches, as it can be observed in Figure 7. The sets of electronic

switches are S_{w1}, S_{w2}, S_{w3}, S_{w4}. The control signals sent by the MGCC are represented by $S_{w(i)}$* = {S_{w1}*, S_{w2}*, S_{w3}*, S_{w4}*}. S_w* is a vector where every of its elements are binary variables {0, 1}, indicating which loads are connected {1} or disconnected {0}. An ISO5500 driver provides the isolation required between the control circuitry implemented around a TMS320F28335 DSP and the IGBT-diodes bidirectional electronic switches. Four electronic switches control the shed-able DC loads remotely by means of RS485 communication implemented in the DSP. The DSP gets the measurements of the overall load current (I_{DCLoad}) and of the DC bus voltage and computes the overall DC load power consumption, P_{DC_Load}. P_{DC_Load} can be expressed by Equation (10):

$$P_{DC_{Load}} = V_{DC} \cdot \sum_{i=1}^{4} I_{DC_{Load(i)}} \cdot S_{w(i)}^{*} \quad (10)$$

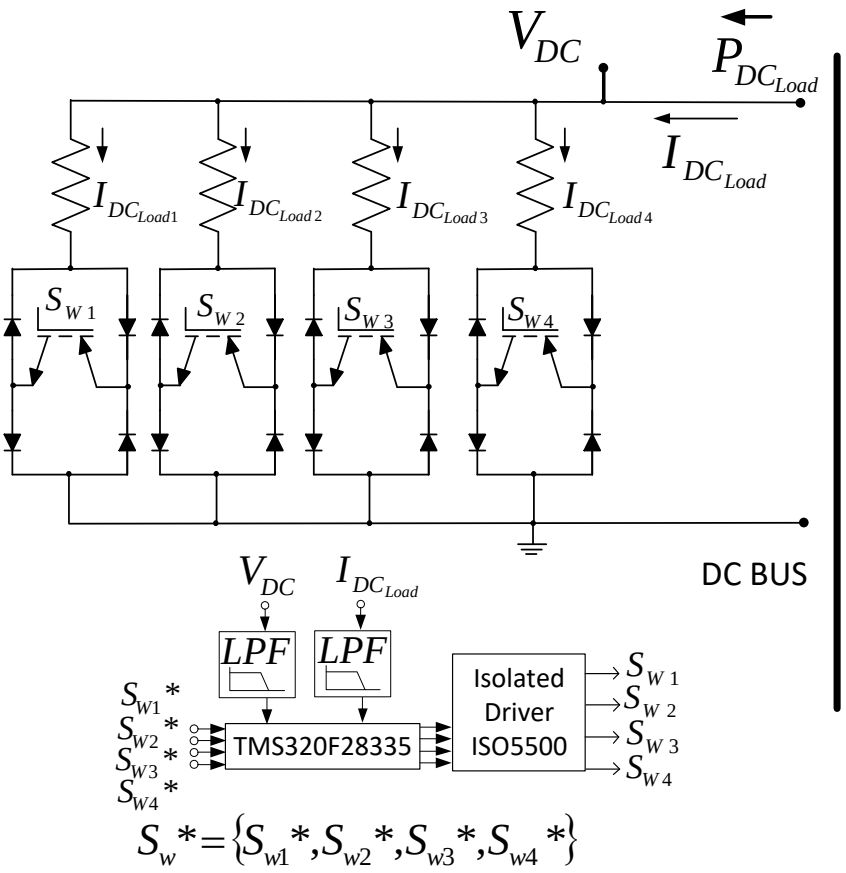

Figure 7. Topology of the electronics switches.

3.3. Management and Control of the DC Microgrid

In this section, several concepts and parameters of the MGCC are explained, in order to define the DC microgrid features, control and functionalities for the efficient application of the proposed algorithm.

3.3.1. Grid Operator Power Limits

The main grid operator establishes a tertiary high-level control strategy that manages the power flow between the DC microgrid and the grid. The grid operator imposes a limit of the power injected from the DC microgrid to the grid or vice versa. The power flow scenarios between the grid and the DC microgrid are shown in Figure 8. Two general cases are possible: $P_{Grid} < 0$ and $P_{Grid} > 0$.

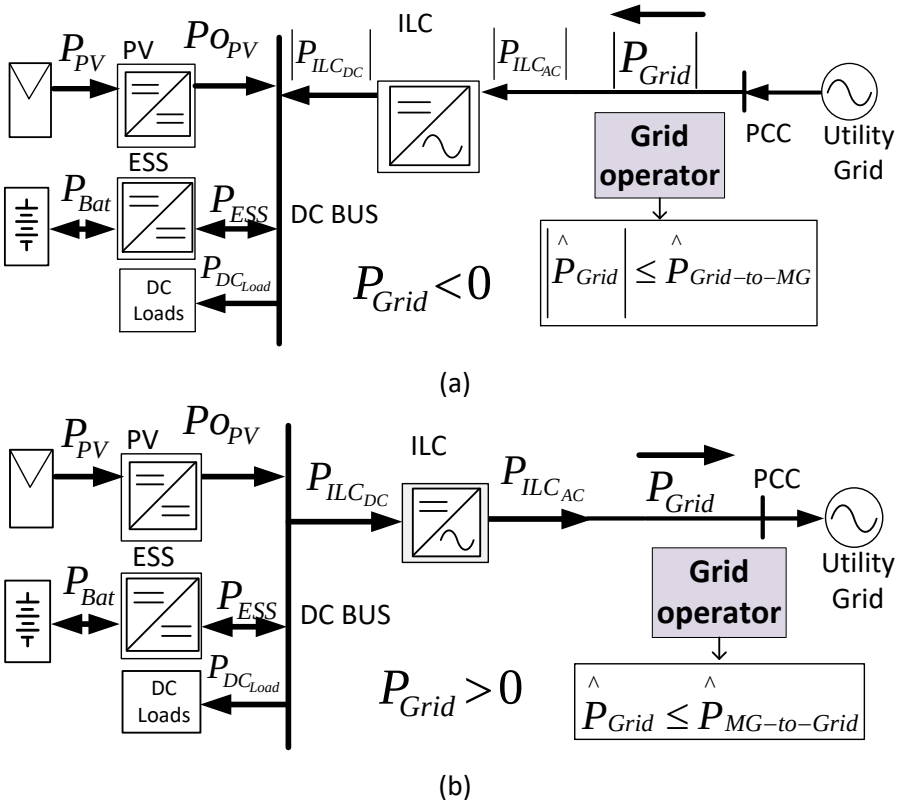

Figure 8. The power flow scenarios between the grid and the DC microgrid: (**a**) Power flow from the grid to the DC microgrid ($P_{Grid} < 0$); (**b**) Power flow from the DC microgrid to the grid ($P_{Grid} > 0$).

3.3.1.1. Maximum Power Extracted from the Grid

The power flow from the grid to the DC microgrid is shown in Figure 8a. Parameter $\hat{P}_{Grid-to-MG}$ is established by the grid operator, standing for the maximum power that can be extracted from the main grid to the DC microgrid, imposing Condition (11):

$$|P_{Grid}| \leq \hat{P}_{Grid-to-MG}. \quad (11)$$

3.3.1.2. Maximum Power Injected to the Grid

The power flow from the DC microgrid to the grid is shown in Figure 8b. Parameter $\hat{P}_{MG-to-Grid}$ stands for the maximum power that can be injected from the DC microgrid to the main grid. This parameter is established by the grid operator, imposing Condition (12):

$$P_{Grid} \leq \hat{P}_{MG-to-Grid}. \quad (12)$$

3.3.2. MG Central Controller

The MGCC establishes some parameters for the secondary control strategy, which is responsible for the power flow between the grid and the DC microgrid.

3.3.2.1. Power Flow Limits between the MG and the Grid

Equation (13) stands for the maximum power which can be extracted from the grid to the DC bus, measured at the AC side of the ILC. In (14) is represented the maximum absolute value of P_{ILC_AC} must meet condition at any time, taking into account the rated power of the ILC, $P_{ILC\ AC\text{-}Rated}$. In this study: $P_{ILC\ AC\text{-}Rated}$ = 10 kW:

$$\hat{P}_{ILC_{AC}}|_{Grid-to-MG} = \hat{P}_{Grid-to-MG} \quad (13)$$

$$\left|\hat{P}_{ILC_{AC}}\right| \leq MIN(\, P_{ILC_{AC-Rated}}, \hat{P}_{ILC_{AC}}|_{Grid-to-MG}\,) \quad (14)$$

Equation (15) stands for the maximum power which can be injected from the DC bus to the grid, measured at the AC side of the ILC. The maximum power injected from the DC bus to the grid by the ILC at any time is defined by (16):

$$\hat{P}_{ILC_{AC}}|_{MG-to-Grid} = \hat{P}_{MG-to-Grid} \quad (15)$$

$$\hat{P}_{ILC_{AC}} \leq MIN(\, P_{ILC_{AC-Rated}}, \hat{P}_{ILC_{AC}}|_{MG-to-Grid}\,) \quad (16)$$

3.3.2.2. Power Comparison Parameters

Equation (17) gives the available PV power plus the maximum power that can be transferred from the grid to the DC bus by the ILC, where η_{ILC} is the ILC efficiency:

$$P_{DC-BUS} = Po_{PV} + \frac{\hat{P}_{ILC_{AC}}|_{Grid-to-MG}}{\eta_{ILC}} \quad (17)$$

Equation (18) is the extra power available both from the PV DG connected to the DC bus and from the grid coming through the ILC, after feeding the load connected to the DC bus. The powers consumed by the loads connected to the DC bus is P_{DC_Load}. DC_{Load_hyst} is a hysteresis threshold used for performing the comparison between the available power level and the power required by the load. The comparison is performed with a certain hysteresis, so that erratic connections/disconnections of the load are avoided when the available power and the required power are very close each other. The value of DC_{Load_hyst} is 10% of the power consumed by the DC loads:

$$P_{Available_{DC}} = P_{DC-BUS} - P_{DC_{Load}} - DC_{Load_{hys}} \quad (18)$$

3.3.2.3. Power Control Parameters

Parameter P_{PV_Lim}* is the maximum power that should be extracted from the PV sources at any time, therefore it can be consumed by the DC loads and by the batteries and/or it can be injected to the grid. P_{PV_Lim}* is represented by (19). $\hat{P}_{DC_{Load}}$ stands for the maximum overall power consumed by the DC loads without applying the load shedding functionality:

$$P_{PV_{Lim}}{}^{*} = \frac{\hat{P}_{ILC_{AC}}|_{MG-to-Grid}}{\eta_{ILC}} + \hat{P}_{DC_{Load}} + P_{ESS} \quad (19)$$

The ESS has two possible modes, supply mode and charge mode, depending on the available power at the DC bus and the *SoC* of the battery bank. The *SoC* is kept between the following values: SoC_{MIN} = 20% and SoC_{Full} = 100%.

In charge mode, the ESS absorbs power from the DC bus to charge the battery bank. ESS gets the power reference from the MGCC, which it is calculated as in (20). ESS charges the batteries until $SoC_{Ready} \leq SoC \leq SoC_{Full}$, being SoC_{Ready} = 80%.

In supply mode, the ESS injects power from the battery bank to the DC bus and can be activated if $SoC \geq SoC_{Ready}$. The ESS gets the power reference from the MGCC, which it is calculated as in (21):

$$P_{ESS}{}^{*} = MIN(\ PESS_{C10}, P_{DC-BUS}\ -\ P_{DC_{Load}}\ ) \quad (20)$$

$$P_{ESS}{}^{*} = -MIN\left(PESS_{C10}, \left|P_{DC-BUS}\ -\ P_{DC_{Load}}\right|\right) \quad (21)$$

3.3.2.4. Power Management Algorithm of the DC Microgrid

Figure 9a depicts the flowchart of the proposed power management algorithm. The MGCC requests power information of all the MG elements and the *SoC* of the batteries, which is used to estimate the power references of each converter, that are broadcasted to establish the power flows required in the MG. The DC load switch (Sw) is a flag that takes two possible states *Sw* = On and *Sw* = Off, depending on the connection or disconnection of loads to the DC bus, respectively. The load shedding functionality can be observed in the Figure 9b, which depicts how one to four DC-loads are connected-disconnected as a function of the value of Equation (18). The load shedding functionality decides on their disconnection if Equation (18) is not enough to energize all the DC loads.

3.4. Experimental Results and Discussion

Several experimental power electronic converters have been built for validating the power management strategies devised in this study. The power converters and PV panel specifications are shown in the Table 3. The following devices have been connected to the DC bus of the MG available in the lab: a 3 kW battery ESS, a 2.5 kW PV source and four electronic switches to connect/disconnect four DC loads of 650 W each one. The connection of the DC bus and the grid is performed by a single-phase ILC of 10 kW that works in grid-connected mode. Figures 10a,b show the schematic diagram and a picture of the experimental DC microgrid, respectively.

The batteries have been emulated by a bidirectional DC source/battery emulator model TC.GSS-Bidirectional-DC-PSU from Regatron AG(Rorschach, Switzerland). The PV array has been emulated by means of a 10 kW PV array simulator TerraSAS ETS1000/10 from Ametek (San Diego, CA, USA). The LabView software (National Instruments Spain, Madrid, Spain) is used for emulated the grid operator, for the initializing/stopping sequence and the monitoring the power dispatch of the DC microgrid.

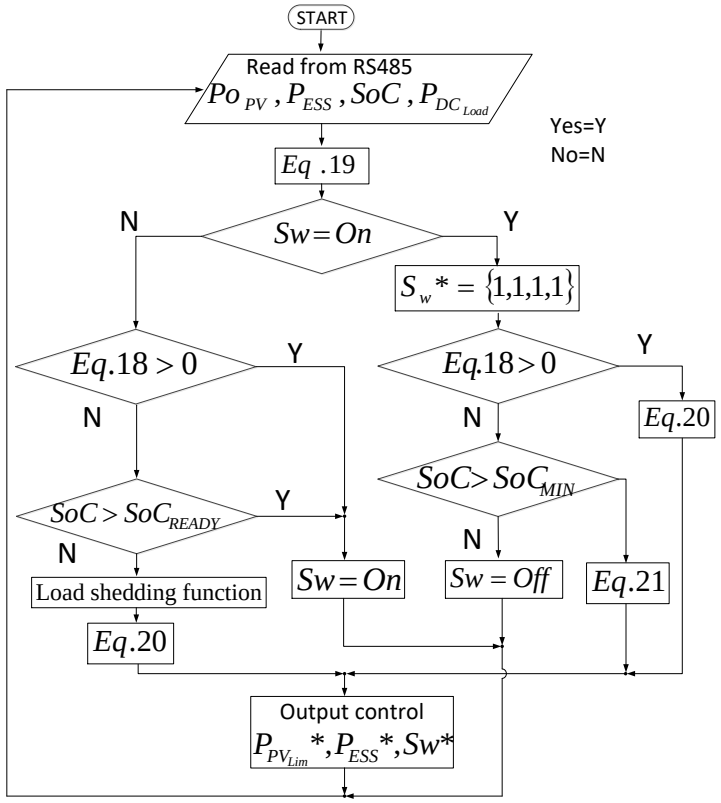

(a)

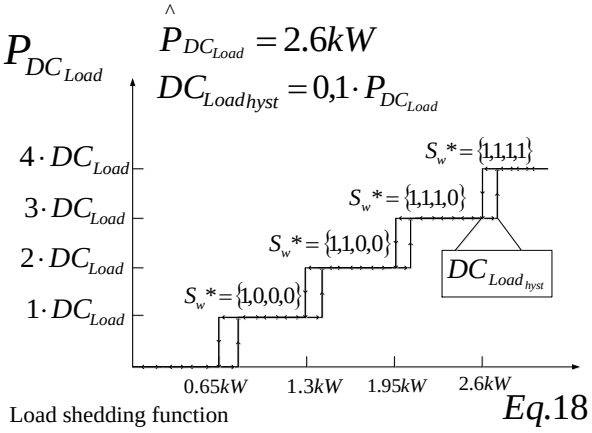

(b)

Figure 9. MGCC: (**a**) Power management algorithm of the DC microgrid; (**b**) Load shedding functionality.

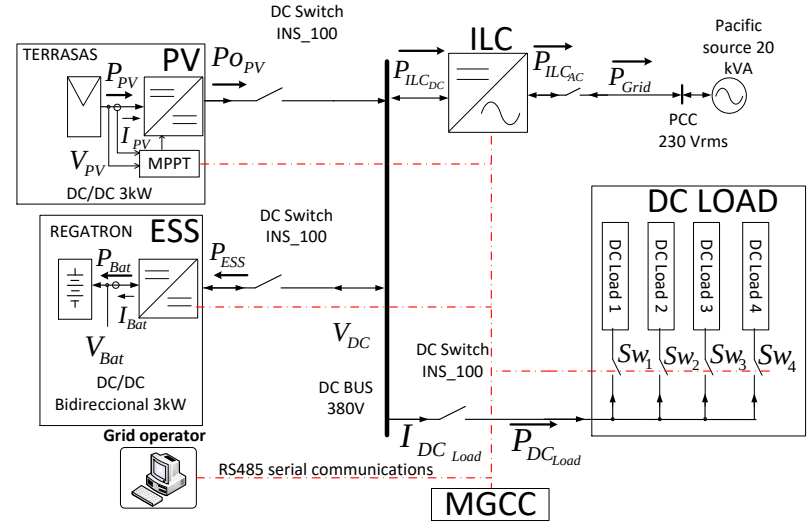

(a)

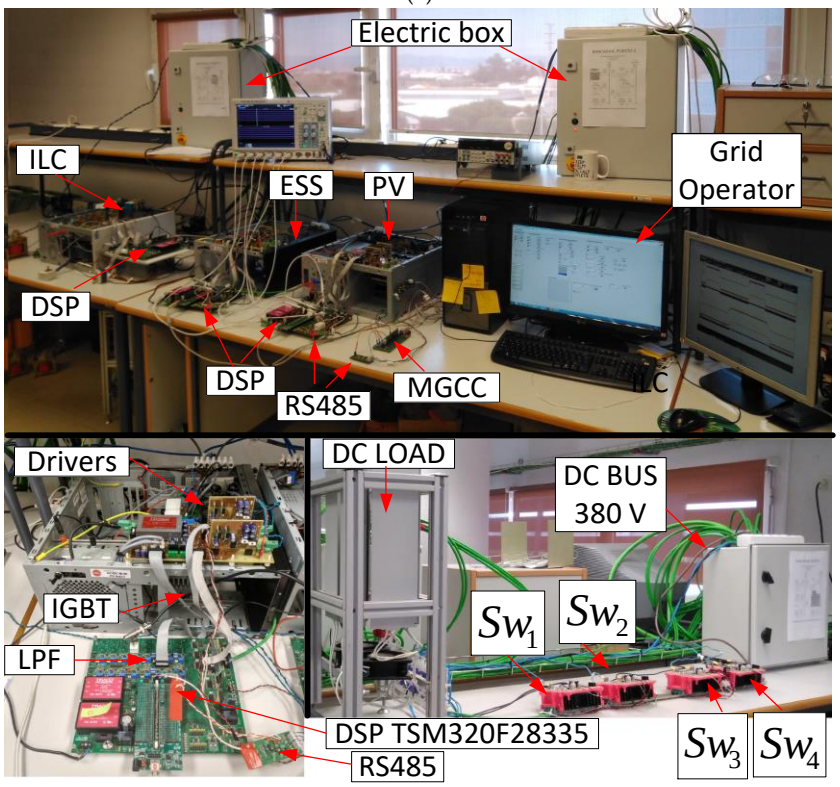

(b)

Figure 10. Experimental MG: (**a**) Schematic diagram of the experimental DC microgrid (**b**) Picture of the experimental DC microgrid.

Several scenarios have been studied in order to demonstrate the suitable behavior of the DC microgrid in its most common and critical situations. In the scenarios under study step changes of the irradiation, DC load, *SoC* and power limits have been considered, as it can be observed in the following graphics. Four experiments have been carried out. Figures 11–13 depict the waveforms of the currents, voltages and powers of the power converters composing the DC bus of the MG corresponding to experiments #1 to #3, respectively. Figure 14 corresponds to experiment #4 and depicts the waveforms and delays of the communication system of the MG. Experiments #1 to #3 show the behavior of the system with the same change of the irradiation level at the PV source, except with a different *SoC* of the ESS. The power dispatch limits established by the grid operator from the grid to the DC bus by the ILC is P_{ILC_DC} = −1 kW in all the experiments. The hysteresis level for comparisons is: DC_{Load_hyst} = 260 W.

Table 3. Characteristics of the power converters composing the DC microgrid.

ILC	ESS	PV
P_{ILC} = 10 kW	P_{ESS_HB} = 3 kW	P_{PV_Boost} = 2.5 kW
V_{Grid} = 230 V	V_{Bat} = 216 V	V_{PV} = 306 V
F_{Grid} = 50 Hz	F_{sw_ESS} = 16 kHz	F_{sw_PV} = 16 kHz
V_{DC} = 380 V	C_{iBat} = 1 mF	C_{oPV} = 1 mF
F_{sw_ILC} = 12.8 kHz	C_{oBat} = 1 mF	C_{iPV} = 1 mF
C_{DC} = 3.8 mF	L_{Bat} = 5.4 mH	L_{PV} = 5.4 mH
L_1 = 1.2 mH	Battery Bank: 18 batteries type SUN	PV Panel: Atersa A-250P E
L_2 = 0.4 mH	POWER VRM 12V105 connected in series	$V_{PV\ oc}$ = 37.01 V
C = 2 µF		I_{PV_MAX} = 8.18 A
C_{DC} = 3.8 mF		V_{PV_MAX} = 30.58 V
		$I_{PV\ CC}$ = 8.71 A
Power dispatch limits established by the grid operator		
$\hat{P}_{MG-to-Grid}$ = 4 kW	$\hat{P}_{Grid-to-MG}$ = 1 kW	

3.4.1. Experiment #1

The ESS is initially at a $SoC \geq SoC_{MIN}$. In Figure 11 can be observed that four loads keep connected during the whole experiment, (P_{DC_Load} = 2.6 kW). Two zoom images can be observed in the lower plot from Figure 11. In Zoom 1, it is shown the detection by the MGCC of an increase in PV system generation. In Zoom 2 it is shown the detection of a decrease in PV system generation. The analysis is performed according to the following time intervals:

Interval 1.1 (0 s < t < 38 s): The irradiation level is 100 W/m^2 and the PV source works at its MPP, providing P_{PV} = 230 W to the DC bus. That irradiation is not enough to feed all the DC loads. Taking into account that the ESS is charged ($SoC \geq 50\%$) the MGCC transfers the maximum possible power from the grid (P_{ILC_DC} = −1 kW) to the DC bus through the ILC. MGCC keeps all the

DC loads connected and orders the ESS deliveries all the power required by the DC bus, P_{Bat} = −1.4 kW. See Figure 11.

In Zoom 1 of the Figure 11, at t = 38.5 s; MGCC detects an increase of PV system generation, the PV source works at its MPP delivering P_{PV} = 0.4 kW. The MGCC transfers the maximum possible power from the grid (P_{ILC_DC} = −1 kW), and keeps all the DC loads connected (P_{DC_Load} = 2.6 kW). ESS supplies all the power required by the DC bus, the power delivered by the ESS is reduced to P_{Bat} = −1.2 kW.

Interval 1.2 (38 s < t < 41 s): The irradiation increases from 100 W/m² to 800 W/m² in 3 s.

At t = 39.9 s; MGCC detects increasing generation, the PV source works at its MPP delivering P_{PV} = 1.2 kW. The MGCC transfers the maximum possible power from the grid (P_{ILC_DC} = −1 kW), and keeps all the DC loads connected (P_{DC_Load} = 2.6 kW). ESS supplies all the power required by the DC bus, the power delivered by the ESS is reduced to P_{Bat} = −0.4 kW.

At t = 41 s the PV source works at its MPP delivering P_{PV} = 1.85 kW, being P_{ILC_DC} = −1 kW. At that instant the MGCC detects that the available power at the DC bus to feed all the DC loads is higher than the hysteresis level (Equation (18) ≥ 0).

Interval 1.3 (41 s < t < 70.5 s): The irradiation level is 800 W/m² and the PV source works at its MPP, providing P_{PV} = 1.85 kW to the DC bus. The MGCC forces the ESS to change its operation to energy storage mode, the batteries are charged with a current given by (6). The ESS changes the setpoint I_{Ch_ref}, until the available power is stable (At t = 42 s, P_{Bat} = 0.2 kW).

Interval 1.4 (70.5 s < t < 75.5 s): The irradiation decreases from 800 W/m² to 100 W/m² in 3 s. See Zoom 2 of the Figure 11.

At t = 72.8 s the PV source works at its MPP, providing P_{PV} = 0.82 kW to the DC bus. Taking into account that the ESS is charged (SoC > 50%). The MGCC forces the ESS to change its operation to supply mode, the batteries are discharged with a current given by Equation (7). The ESS changes the setpoint I_{Dis_ref}, until the available power generation is stable (At t > 74.5 s, P_{Bat} = −1.4 kW).

3.4.2. Experiment #2

The ESS is initially at a SoC ≤ 20% (discharged). MGCC applies the load shedding functionality; see Figure 12. Two zoom images can be observed in the lower plot from Figure 12. In Zoom 1 it is shown the detection by the MGCC of an increase in PV system generation. In Zoom 2 it is shown the detection of a decrease in PV system generation. The analysis is performed according to the following time intervals:

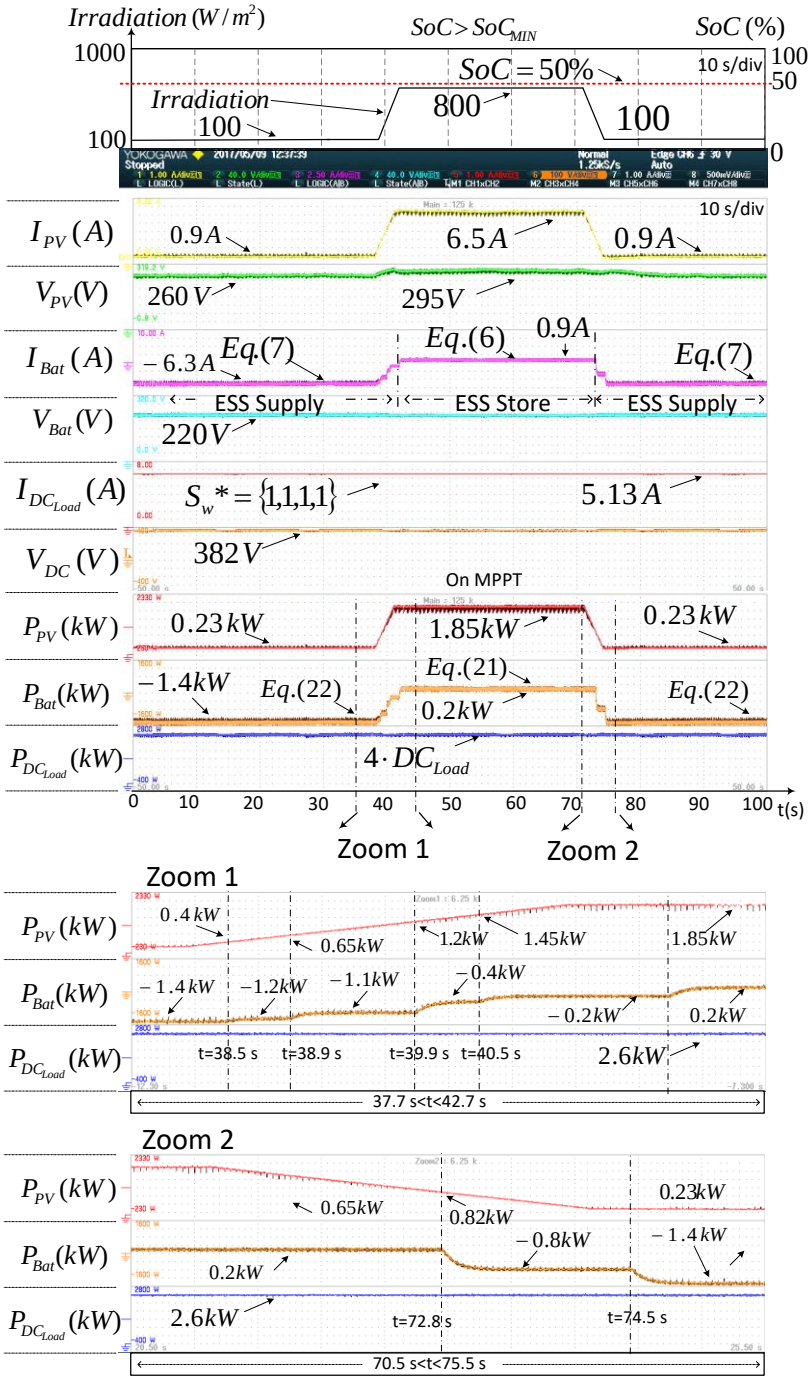

Figure 11. Experiment #1. Evolution of the currents, the power exchange and voltage in the DC microgrid for changes in the irradiation at a $SoC > SoC_{MIN}$.

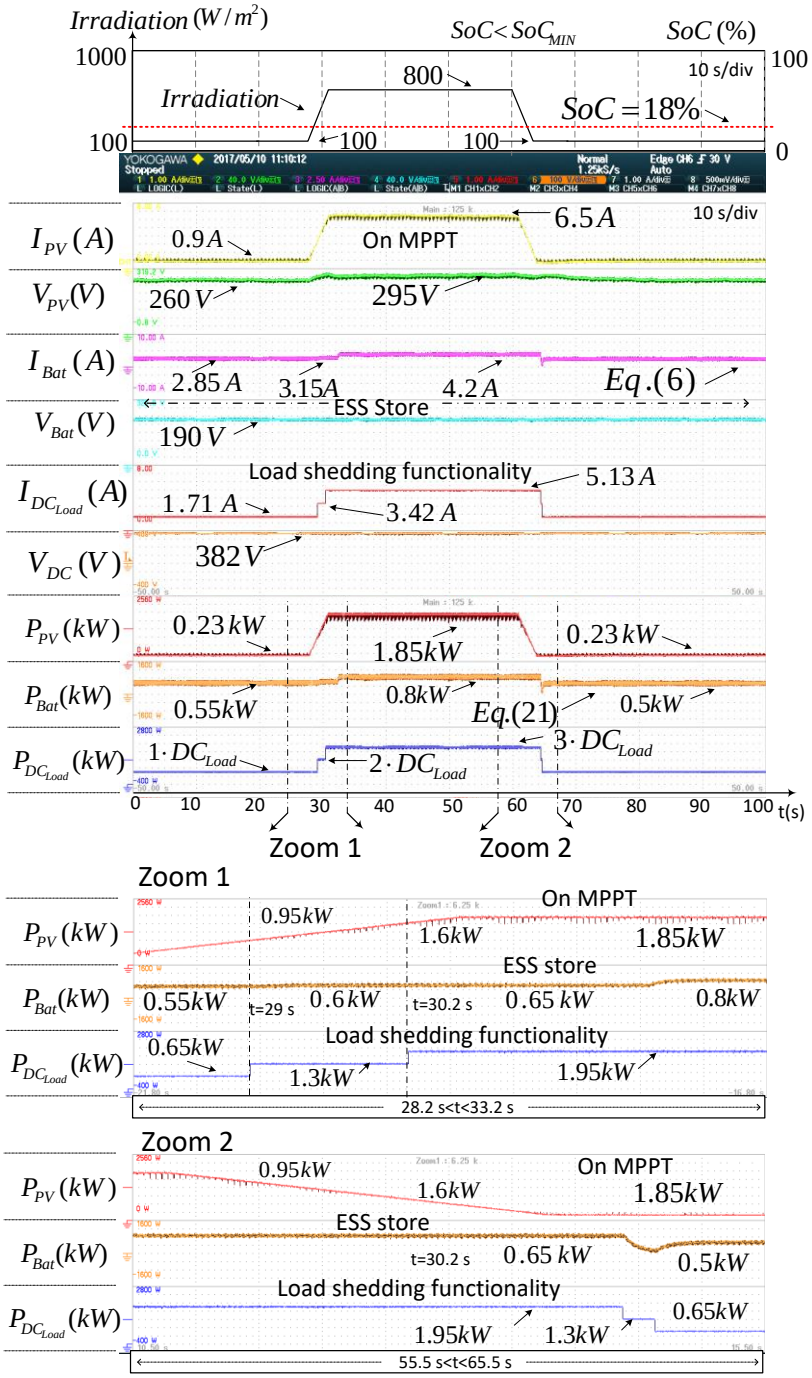

Figure 12. Experiment #2. Evolution of the currents, the power exchange and voltage in the DC microgrid for changes in the irradiation at a $SoC < SoC_{MIN}$.

Interval 2.1 (0 s < t < 28 s): The irradiation level is 100 W/m² and the PV source works at its MPP, providing P_{PV} = 230 W to the DC bus. That irradiation is not enough to feed all the loads. Considering that the ESS is discharged (SoC < 20%), the MGCC transfers the maximum possible power from the grid (P_{ILC_DC} = −1 kW) to the DC bus through the ILC, and applies the load shedding functionality. Taking into account that the available power at the DC bus (1.28 kW) is not enough to feed two loads, the MGCC connects only one DC load (P_{DC_Load} = 0.65 kW), using the rest of this power for charging the batteries at P_{Bat} = 0.55 kW.

Interval 2.2 (28 s < t < 31 s): The irradiation increases from 100 W/m² to 800 W/m² in 3 s, which makes the MGCC to apply the load shedding functionality. See Zoom 1 of Figure 12.

At t = 29 s the PV source works at its MPP delivering P_{PV} = 0.95 kW, whereas P_{ILC_DC} = −1 kW. At that instant the MGCC detects that the available power at the DC bus is enough to feed two of the loads (P_{DC_Load} = 1.3 kW). The MGCC takes into account the hysteresis level in that connection and changes the setpoint P_{ESS}* from 0.55 kW to 0.6 kW. Note that at t = 29 s, after the connection of the two loads, only $|P_{ILC\_DC}| \leq 1$ kW is taken from the grid. This ensures a minimum level of power available in the DC bus.

At t = 30.2 s, the PV source works at its MPP delivering P_{PV} = 1.6 kW, being P_{ILC_DC} = −1 kW. At that instant the MGCC detects that the available power at the DC bus, taking into account the hysteresis level, is enough to feed three of the loads (P_{DC_Load} = 1.95 kW). The MGCC connects three loads and changes the setpoint P_{ESS}* of the ESS from 0.6 kW to 0.65 kW.

Interval 2.3 (55.5 s < t < 65.5 s): The irradiation decreases from 800 W/m² to 100 W/m² in 3 s. The MGCC keeps the load shedding functionality activated. See Zoom 2 of Figure 12.

At t = 64.3 s the PV source works at its MPP delivering P_{PV} = 0.23 kW, whereas P_{ILC_DC} = −1 kW. At that instant the MGCC detects that the available power at the DC bus taking into account the hysteresis level is enough to feed two of the loads (P_{DC_Load} = 1.3 kW). MGCC connects two loads and changes the setpoint P_{ESS}* of the ESS from 0.65 kW to 0.5 kW. Note that at t = 64.3 s, after the connection of the two loads, only $|P_{ILC\_DC}| \leq 1$ kW is taken from the grid. This ensures a minimum level of power available in the DC bus.

3.4.3. Experiment #3

The ESS is initially at a $SoC \geq SoC_{MIN}$. At t = 21.2 s the SoC changes at a $SoC < SoC_{MIN}$, see Figure 13. Three zoom images can be observed in the lower plot from Figure 13. Zoom 1 shows the details of the power flows in the MG when the MGCC detects that $SoC < SoC_{MIN}$. In Zoom 2 it is shown the detection by the

MGCC of an increase in PV generation. In Zoom 3 it is shown the detection of a decrease in PV generation. The analysis is performed according to the following time intervals:

Interval 3.1 (0 s < t < 21.2 s): The irradiation level is 100 W/m² and the PV source works at its MPP, providing P_{PV} = 230 W to the DC bus. That irradiation is not enough to feed all the loads. Taking into account that the SoC > 20%, the MGCC transfers the maximum possible power from the grid (P_{ILC_DC} = −1 kW) to the DC bus through the ILC. MGCC keeps all the DC loads connected and orders the ESS supplying all the power required by the DC bus, P_{Bat} = −1.4 kW.

At t = 21.2 s; the PV source works at its MPP delivering P_{PV} = 230 W. That irradiation is not enough to feed all the loads. Considering that MGCC detects that the ESS is discharged, SoC < 20%. MGCC transfers the maximum possible power from the grid (P_{ILC_DC} = −1 kW) to the DC bus through the ILC. MGCC starts a transition from Sw = On to Sw = Off and applies the load shedding functionality. Taking into account that the available power at the DC bus (1.23 kW) is not enough to feed two loads, MGCC connects only one DC load (P_{DC_Load} = 0.65 kW). The rest of the available power is used for charging the batteries. MGCC changes the setpoint P_{ESS}* of the ESS from −1.4 kW to 0.55 kW.

Zoom 1 of Figure 13 depicts P_{Bat} and its behavior to sudden changes of P_{ESS}* from 1.4 kW to 0.55 kW. If P_{ESS}* is negative, the ESS is supplying power to the DC bus according to Equation (21), whereas if P_{ESS}* is positive, the batteries are charged according to Equation (20).

Interval 3.2 (36.6 s < t < 41.2 s): The irradiation increases from 100 W/m² to 800 W/m² in 3 s. See Zoom 2 of the Figure 13. The MGCC detects an increase in PV generation. The PV source works at its MPP. That irradiation is not enough to feed all the loads. Considering that the ESS is discharged (SoC < 20%), the batteries are charged according to Equation (20). MGCC transfers the maximum possible power from the grid (P_{ILC_DC} = −1 kW) to the DC bus through the ILC, and applies the load shedding functionality.

Interval 3.3 (68 s < t < 74.5 s): The irradiation decreases from 800 W/m² to 100 W/m² in 3 s. See Zoom 3 of Figure 13. The MGCC detects a decrease in PV generation. The PV source works at its MPP. That irradiation is not enough to feed all the loads. The ESS is still discharged (SoC < 20%). The MGCC transfers the maximum possible power from the grid (P_{ILC_DC} = −1 kW) to the DC bus through the ILC, and applies the load shedding functionality.

3.4.4. Experiment #4

The communication delays and the running time of the power management algorithm can be observed in Figure 14. The RS485

communication bus baud rate is 9600 bps. In the Figure 14 (full capture) the power management algorithm is executed every 250 ms (4 Hz) performing the following tasks: request the measurements of voltages and currents to all devices in the microgrid, calculation of instantaneous powers references of the devices and the transmission of the references to the devices. The MGCC processing time of these tasks are shown in Table 4.

Table 4. Processing time used by the algorithms on the MGCC.

MGCC Algorithm Tasks	Processing Time
Measurement and setpoint:	
Request and receive data Calculate of references Send power state refereces	70 ms
Message processing	
Get command and values Calculate the references Build the response message	200 μs

Three different zoom times about intervals of the RS485 communication of Figure 14 (full capture) are shown.

The Zoom 1 of Figure 14 corresponds to 500 ms, the Zoom 2 of Figure 14 corresponds to 75 ms and the Zoom 3 of Figure 14 corresponds to 2 ms. In Zoom 1 of the Figure 14 it can be observed that the previously described tasks performed every 250 ms by the MGCC are completed in 70 ms. In Zoom 2 of the Figure 14 it can be observed the detail of the receiving (RX) and transmitting (TX) signals of every microgrid component on the bus RS485: PV generator, ESS, MGCC.

In Zoom 3 of the Figure 14 it is shown the time required for the MGCC from the reception of information of the converters and the compute the reference signals to be sent to each element is 200 μs. The communication transmission delays of the request, response and send operation commands in the DC microgrid are shown in the Table 5.

The implemented RS485 communication allows the calculation of the power values at several points of the microgrid in a fast and accurate way (see Figure 14). The power management algorithm is executed every 250 ms which is time enough to: (i) measure and calculate the generated and demanded powers, (ii) calculate the power references for every converter on stream and (iii) establish the load which can be connected to the DC bus. The most

important computation and transmission times have been reported in the Tables 4 and 5.

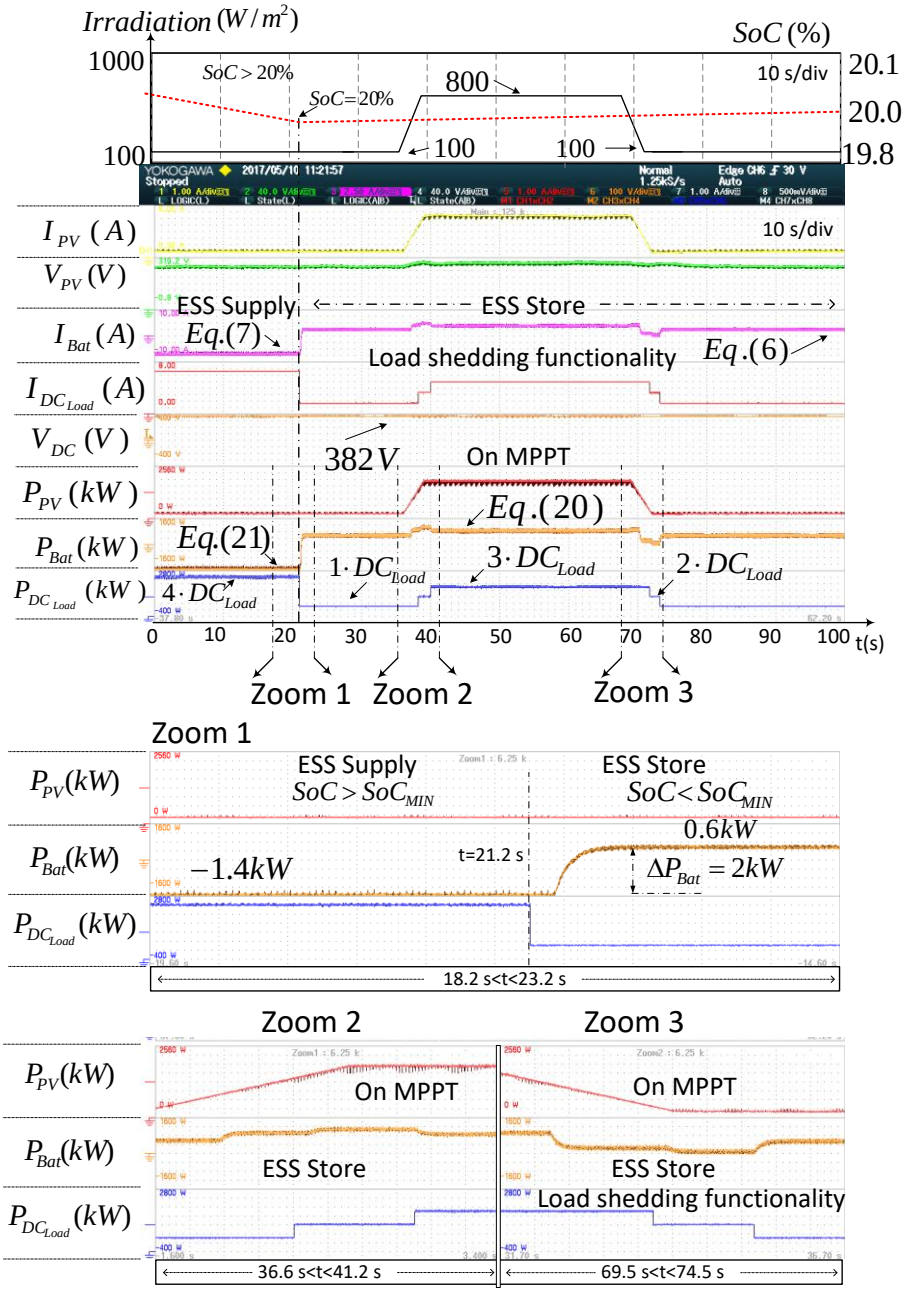

Figure 13. Experiment #3. Evolution of the currents, the power exchange and voltage in the DC microgrid for changes in the *SoC*.

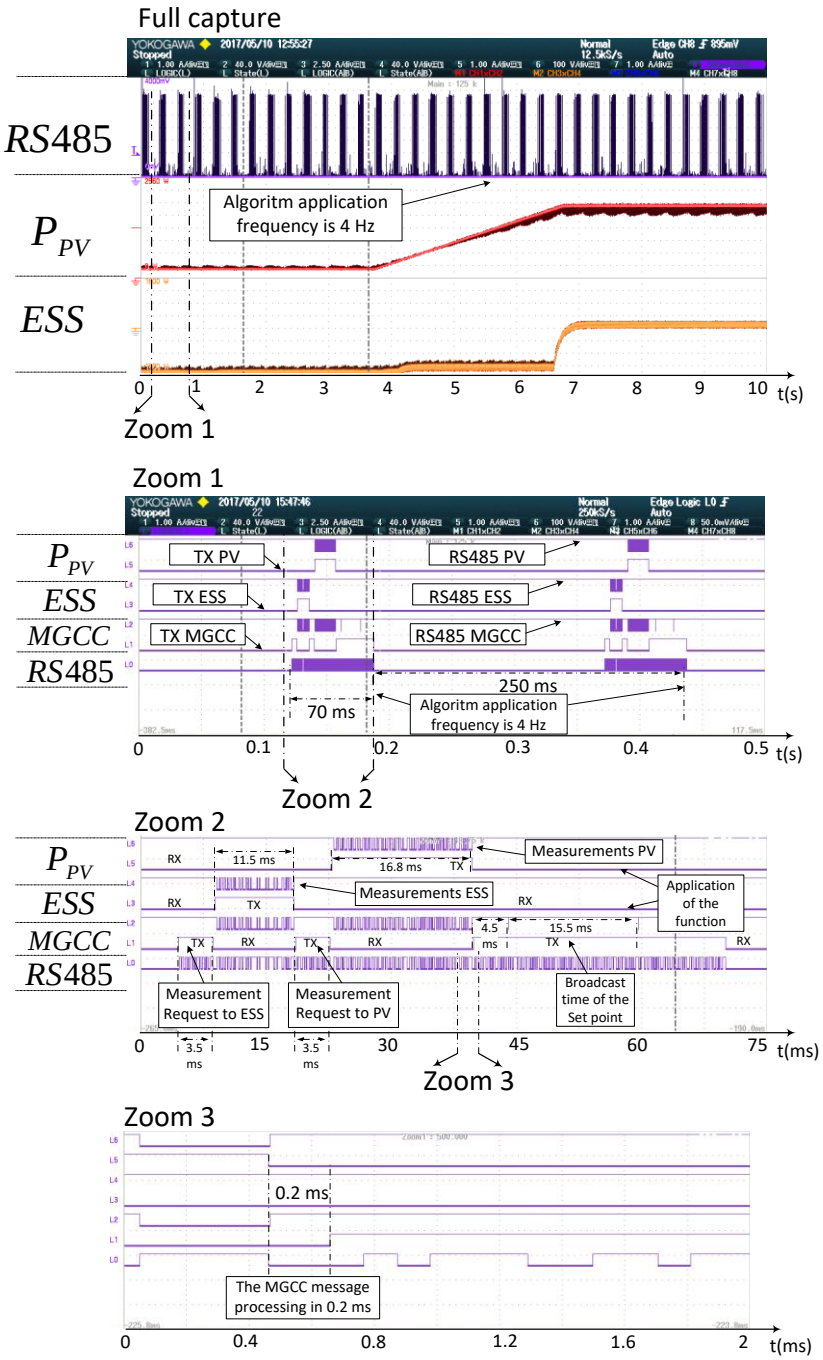

Figure 14. Experiment #4. Communications delay between the MGCC and two of the microgrid elements.

Power exchanges among the devices of the MG have been shown in the Figures 11–12. The load shedding functionality is applied when the battery bank is discharged. The batteries can be recharged with the excess available power after load connection/disconnection. The amount of load shedding depends on the available power at the DC bus taking into account a hysteresis level, which improves the reliability of the MG and ensures the safety and stability of the DC bus voltage. The main issue during the data processing is the disconnection/connection of an excessive load during a too long time, which can lead to strong transient disturbances. Therefore, the load demand is measured in real time and sent to the MGCC.

Table 5. Communication delays between the DC/DC power converters and the MGCC.

Communication Delays	MGCC	DC/DC Power Converters	
		ESS	PV
Request of the measurement	From MGCC to converter	3.5 ms	3.5 ms
Response of the measurement	From converter to MGCC	11.5 ms	16.8 ms
Send operation command (setpoint)	From MGCC to converter	15.5 ms	4.5 ms

3.5. Conclusions

This paper is focused on the centralized control of the power converters connected to a DC microgrid operating in grid-connected mode. The proposed strategy deals with different devices according to their type: generation, storage, interlinking converter and load. A coordinated power flow in the DC microgrid is achieved by means of a low-bandwidth RS485 serial communication system at 9600 bps. This kind of communication is a cost effective solution in MGs.

The secondary control level is performed by means of an MGCC that performs the calculations and communications. The MGCC calculates the suitable power references for every device in real time and broadcasts those values to the MG elements in order to set their status. The power reference of the ESS is determined by considering the additional power needed at the DC bus after having considered the power available at the PV DG and that coming from the ILC.

The power management system of the battery ESS follows the power command defined by the MGCC as a function of the batteries *SoC* and of the MG status, following the charging procedure to DIN 41773 for VRLA batteries

of the ESS. The ESS algorithm operates the batteries at a suitable power level, being compatible with the MG operation mode and the MG available power. The ESS has been chosen to keep the batteries at a relatively high charge level, so that enough energy can be extracted from the batteries when the power demand is higher than the sum of available PV power and maximum grid importable power. This feature allows to temporary feed a power higher than the maximum importable power defined in the electricity contract, thus reducing the electricity bill, which is higher the higher the maximum importable power established by the contract.

The experimental results demonstrate that the power strategies which have been integrated allow the control of the power dispatch inside the DC microgrid properly, respecting the established power limits. It has been demonstrated that smooth transients in the MG are obtained in some common and extreme scenarios, in spite of strong changes in the power flows inside the MG.

Acknowledgments: This work has been cofinanced by the Spanish Ministry of Economy and Competitiveness (MINECO) and by the European Regional Development Fund (ERDF) under Grant ENE2015-64087-C2-2.

Author Contributions: Robert Salas-Puente, Emilio Figueres and Gabriel Garcerá proposed the main idea, conceived and designed the experiments; Robert Salas-Puente and R. González-Medina performed the experiments; Silvia Marzal designed the communication; Silvia Marzal and Raúl González-Medina reviewed the article; Robert Salas-Puente, Emilio Figueres and Gabriel Garcerá wrote this paper.

Conflicts of Interest: The authors declare no conflict of interest.

3.6. Abbreviations

P_{PV}	Power supplied by the PV arrays
P_{OPV}	Power supplied by the PV arrays seen from the DC bus
P_{DCLoad}	Overall power consumed by the DC loads
P_{Grid}	Power injected from the DC microgrid to the grid
P_{ILC_AC}	Power injected from the DC bus to the grid by the ILC, measured at the AC side of the ILC
P_{ILC_DC}	Power injected from the DC bus to the grid by the ILC, measured at the DC side of the ILC
P_{ESS}	Battery charge power seen from the DC bus
P_{Bat}	Battery charge power
η_{EES}	Efficiency of the ESS
η_{PV}	Efficiency of the PV DC/DC converter
η_{ILC}	Efficiency of the ILC

I_{Grid}	RMS Current injected from the DC microgrid to the grid
V_{Grid}	RMS value of the grid voltage
ω	Grid angular frequency
φ	Grid phase
I_{DCLoad}	Overall current consumed by the DC loads
V_{DC}	DC bus voltage
I_{ILC_AC}	RMS current injected from the ILC to the grid
SoC	State of charge of the battery bank
I_{Bat}	Battery bank charge current
V_{Bat}	Battery bank voltage
I_{Ch_ref}	Reference of the battery charge current
I_{Dis_ref}	Reference of the battery discharge current
I_{PV}	Current supplied by the PV array
I_{DCLoad}	Overall current consumed by the DC loads
$S_{W1,2,3,4}$	DC load switches (load 1 to 4)
$\widehat{P}_{Grid-to-MG}$	Maximum power drawn from the grid to the DC microgrid
$\widehat{P}_{MG-to-Grid}$	Maximum power injected to the grid from the DC microgrod
$\widehat{P}_{ILC_{AC}\mid Grid-to-MG}$	Maximum power drawn from the grid to the DC bus measured at the AC side of the ILC
$\widehat{P}_{ILC_{AC}\mid MG-to-Grid}$	Maximum power injected from the DC bus to the grid measured at the AC side of the ILC
$P_{ILC_{AC-Rated}}$	Rated power of the ILC measured at its AC side
$P_{ILC_{DC-Rated}}$	Rated power of the ILC measured at its DC side
$\widehat{P}_{DC_{Load}}$	Maximum power consumed by the DC loads
$P_{DC\text{-}Bus}$	Power generated at the DC bus
$P_{Available\_DC}$	Power available at the DC bus
DC_{Load_hyst}	DC load hysteresis

3.7. References

1 Dragičević, T.; Lu, X.; Vasquez, J.C.; Guerrero, J.M. DC Microgrids—Part I: A Review of Control Strategies and Stabilization Techniques. *IEEE Trans. Power Electron*. **2016**, *31*, 4876–4891.

2 Baek, J.; Choi, W.; Chae, S. Distributed Control Strategy for Autonomous Operation of Hybrid AC/DC Microgrid. *Energies* **2017**, *10*, 373.

3 Patrao, I.; Figueres, E.; Garcerá, G. González-Medina, Microgrid architectures for low voltage distributed generation. *Renew. Sustain. Energy Rev*. **2015**, *43*, 415–424.

4 Ma, T.T.H.; Yahoui, H.; Vu, H.G.; Siauve, N.; Morel, H. A Control Strategy of DC Building Microgrid Connected to the Neighborhood and AC Power Network. *Buildings* **2017**, *7*, 42.

5 Lin, P.; Wang, P.; Xiao, J.; Wang, J.; Jin, C.; Tang, Y. An Integral Droop for

Transient Power Allocation and Output Impedance Shaping of Hybrid Energy Storage System in DC Microgrid. *IEEE Trans. Power Electron*. **2017**.

6 Liu, X.; Wang, P.; Loh, P.C. A hybrid AC/DC micro-grid. In Proceedings of the 2010 Conference IPEC, Singapore, 27–29 October 2010; pp. 746–751.

7 Wang, P.; Liu, X.; Jin, C.; Loh, P.; Choo, F. A hybrid AC/DC micro-grid architecture, operation and control. In Proceedings of the 2011 IEEE Power and Energy Society General Meeting, Detroit, MI, USA, 24–29 July 2011; pp. 1–8.

8 Kakigano, H.; Miura, Y.; Ise, T. Low-Voltage Bipolar-Type DC Microgrid for Super High Quality Distribution. *IEEE Trans. Power Electron.* **2010**, *25*, 3066–3075.

9 Zhang, L.; Wu, T.; Xing, Y.; Sun, K.; Gurrero, J.M. Power control of DC microgrid using DC bus signaling. In Proceedings of the 2011 Twenty-Sixth Annual IEEE Applied Power Electronics Conference and Exposition (APEC), Fort Worth, TX, USA, 6–11 March 2011; pp. 1926–1932.

10 Salomonsson, D.; Soder, L.; Sannino, A. An Adaptive Control System for a DC Microgrid for Data Centers. *IEEE Trans. Ind. Appl.* **2008**, *44*, 1910–1917.

11 Lie, X.; Dong, C. Control and Operation of a DC Microgrid with Variable Generation and Energy Storage. *IEEE Trans. Power Deliv.* **2011**, *26*, 2513–2522.

12 Liu, X.; Wang, P.; Loh, P.C. A Hybrid AC/DC Microgrid and Coordination Control. *IEEE Trans. Smart Grid* **2013**, *2*, 278–286.

13 Nejabatkhah, F.; Li, Y.W. Overview of Power Management Strategies of Hybrid AC/DC Microgrid. *IEEE Trans. Power Electron.* **2015**, *30*, 7072–7089.

14 Lu, X.; Guerrero, J.M.; Sun, K.; Vasquez, J.C. An improved droop control method for DC microgrids based on low bandwidth communication with DC bus voltage restoration and enhanced current sharing accuracy. *IEEE Trans. Power Electron*. **2014**, *29*, 1800–1812.

15 Chen, D.; Xu, L. Autonomous DC voltage control of a DC microgrid with multiple slack terminals. *IEEE Trans. Power Syst.* **2012**, *27*, 1897–1905.

16 Varghese, A.; Chandran, L.R.; Rajendran, A. Power flow control of solar PV based islanded low voltage DC microgrid with battery management system. In Proceedings of the 2016 IEEE 1st International Conference on Power Electronics, Intelligent Control and Energy Systems (ICPEICES), Delhi, India, 4–6 July 2016; pp. 1–6.

17 Josep Guerrero, J.V. Hierarchical Control of Droop-Controlled AC and DC Microgrids. A General Approach toward Standardization. *IEEE Trans. Ind. Electron.* **2011**, *58*, 158–172.

18 Vasquez, J.C.; Guerrero, J.M.; Miret, J.; Castilla, M.; de Vicuna, L.G. Hierarchical Control of Intelligent Microgrids. *IEEE Ind. Electron. Mag*. **2010**, *4*, 23–29.

19 Meng, L.; Savaghebi, M.; Andrade, F.; Vasquez, J.C.; Guerrero, J.M.; Graells, M. Microgrid central controller development and hierarchical control implementation in the intelligent microgrid lab of Aalborg University. In Proceedings of the Applied Power Electronics Conference and Exposition (APEC), Charlotte, NC, USA, 15–19 March 2015; pp. 2585–2592.

20 Unamuno, E.; Barrena, J.A. Hybrid AC/DC microgrids—Part II: Review and

classification of control strategies. *Renew. Sustain. Energy Rev*. **2015**, *52*, 1123–1134.

21 Feng, X.; Shekhar, A.; Yang, F.E.; Hebner, R.; Bauer, P. Comparison of Hierarchical Control and Distributed Control for Microgrid. *Electr. Power Compon. Syst*. **2017**, *45*, 1043–1056.

22 Marzal, S.; González-Medina, R.; Salas-Puente, R.; Figueres, E.; Garcerá, G. A Novel Locality Algorithm and Peer-to-Peer Communication Infrastructure for Optimizing Network Performance in Smart Microgrids. *Energies* **2017**, *10*, 1275.

23 Kaur, A.; Kaushal, J.; Basak, P. A review on microgrid central controller. *Renew. Sustain. Energy Rev.* **2016**, *55*, 338–345.

24 Begum, M.; Abuhilaleh, M.; Li, L.; Zhu, J. Distributed secondary voltage regulation for autonomous microgrid. In Proceedings of the 20th International Conference on Electrical Machines and Systems (ICEMS), Sydney, Australia, 11–14 August 2017; pp. 1–6.

25 Wu, D.; Tang, F.; Dragicevic, T.; Guerrero, J.M.; Vasquez, J.C. Coordinated Control Based on Bus-Signaling and Virtual Inertia for Islanded DC Microgrids. *IEEE Trans. Smart Grid* **2015**, *6*, 2627–2638.

26 Shi, D.; Chen, X.; Wang, Z.; Zhang, X.; Yu, Z.; Wang, X.; Bian, D. A Distributed Cooperative Control Framework for Synchronized Reconnection of a Multi-Bus Microgrid. *IEEE Trans. Smart Grid* **2017**, *PP*, 1–1.

27 Dou, C.; Zhang, Z.; Yue, D.; Zheng, Y. MAS-Based Hierarchical Distributed Coordinate Control Strategy of Virtual Power Source Voltage in Low-Voltage Microgrid. *IEEE Access* **2017**, *5*, 11381–11390.

28 Bracale, A.; Caramia, P.; Carpinelli, G.; Mancini, E.; Mottola, F. Optimal control strategy of a DC micro grid. *Int. J. Electr. Power Energy Syst.* **2015**, *67*, 25–38.

29 Hajar, K.; Hably, A.; Bacha, S.; Elrafhi, A.; Obeid, Z. Optimal centralized control application on microgrids. In Proceedings of the 2016 3rd International Conference on Renewable Energies for Developing Countries (REDEC), Zouk Mosbeh, Lebanon, 13–15 July 2016; pp. 1–6.

30 Yue, J.; Hu, Z.; Li, C.; Vasquez, J.C.; Guerrero, J.M. Economic Power Schedule and Transactive Energy through an Intelligent Centralized Energy Management System for a DC Residential Distribution System. *Energies* **2017**, *10*, 916.

31 Gao, L.; Liu, Y.; Ren, H.; Guerrero, J.M. A DC Microgrid Coordinated Control Strategy Based on Integrator Current-Sharing. *Energies* **2017**, *10*, 1116.

32 Hooppecke. Operating Instructions Valve Regulated Stationary Lead-Acid Batteries. Available online: http://www.hoppecke-us.com/tl_files/hoppecke/Documents/HO-US/Operating_Instructions_sealed_stationary_lead_acid_batteries_en1111.pdf (accessed on 13 October 2017).

33 TAB Batteries. Available online: http://www.tabspain.com/wp-content/uploads/informacion -tecnica/renovables/curvas-y-tablas/din-41773-y-din-41774-para-baterias-pzs.pdf (accessed on 13 October 2017).

34 Zhao, J.; Dörfler, F. Distributed control and optimization in DC microgrids. *Automatica* **2015**, *61*, 18–26.

35 Eghtedarpour, N.; Farjah, E. Power Control and Management in a Hybrid

AC/DC Microgrid. *IEEE Trans. Smart Grid* **2014**, *5*, 1494–1505.

36 Support, T. Installation, Commissioning and Operation Handbook for Gel-Vrla-Batteries. 2003. Available online: http://www.sonnenschein.org/PDF%20files/GelHandbookPart2.pdf (accessed on 13 October 2017).

37 AlLee, G.; Tschudi, W. Edison Redux: 380 Vdc Brings Reliability and Efficiency to Sustainable Data Centers. *IEEE Power Energy Mag*. **2012**, *10*, 50–59.

38 Joseph, A.; Shahidehpour, M. Battery storage systems in electric power systems. In Proceedings of the 2006 IEEE Power Engineering Society General Meeting, Montreal, QC, Canada 18–22 June 2006; p. 8.

39 Aryani, D.R.; Song, H. Coordination Control Strategy for AC/DC Hybrid Microgrids in Stand-Alone Mode. *Energies* **2016**, *9*, 469.

40 Dragičević, T.; Guerrero, J.M.; Vasquez, J.C.; Škrlec, D. Supervisory Control of an Adaptive-Droop Regulated DC Microgrid with Battery Management Capability. *IEEE Trans. Power Electron.* **2014**, *29*, 695–706.

41 Tian, Y.; Li, D.; Tian, J.; Xia, B. State of charge estimation of lithium-ion batteries using an optimal adaptive gain nonlinear observer. *Electrochim. Acta* **2017**, *225*, 225–234.

42 Golestan, S.; Monfared, M.; Guerrero, J. Second order generalized integrator based reference current generation method for single-phase shunt active power filters under adverse grid conditions. In Proceedings of the Power Electronics, Drive Systems and Technologies Conference (PEDSTC), Tehran, Iran, 13–14 February 2013; pp. 510–517.

43 Jianfang, X.; Peng, W. Multiple modes control of household DC microgrid with integration of various renewable energy sources. In Proceedings of the IECON 2013—39th Annual Conference of the IEEE Industrial Electronics Society, Vienna, Austria, 10–13 November 2013; pp. 1773–1778.

44 M. Ciobotaru, R. Teodorescu and F. Blaabjerg, "A new single-phase PLL structure based on second order generalized integrator," 2006 37th IEEE Power Electronics Specialists Conference, Jeju, South Korea,18-22 June 2006, pp. 1-6.

45 Standard for Interconnecting Distributed Resources with Electric Power Systems.

4

4. PUBLICACIÓN III

4.PRACTICAL ANALYSIS AND DESIGN OF A BATTERY MANAGEMENT SYSTEM FOR A GRID-CONNECTED DC MICROGRID FOR THE REDUCTION OF THE TARIFF COST AND BATTERY LIFE MAXIMIZATION

Salas-Puente, Robert; Marzal, Silvia; Gonzalez-Medina, Raul; Figueres, Emilio; Garcera, Gabriel. 2018. "Practical Analysis and Design of a Battery Management System for a Grid-Connected DC Microgrid for the Reduction of the Tariff Cost and Battery Life Maximization." Energies 11, no. 7: 1889. DOI: 10.3390/en11071889.

(Article)

Practical Analysis and Design of a Battery Management System for a grid-connected DC Microgrid for the reduction of the tariff cost and battery life maximization

Robert Salas-Puente *, Silvia Marzal, Raul Gonzalez-Medina, Emilio Figueres and Gabriel Garcera

Grupo de Sistemas Electrónicos Industriales del Departamento de Ingeniería Electrónica,

Universitat Politècnica de València, Camino de Vera s/n, 46022 Valencia, Spain; silmarro@upv.es (S.M.); raugonme@upv.es (R.G.-M.); efiguere@eln.upv.es (E.F.); ggarcera@eln.upv.es (G.G.).

*Correspondence: rosapue1@posgrado.upv.es; Tel.: +34-(96)-3877007 (ext. 76021)
Received: 5 June 2018 / Revised: 9 July 2018 / Accepted: 16 July 2018 / Published: 19 July 2018

Abstract: This study is focused on two areas: the design of a Battery Energy Storage System (BESS) for a grid-connected DC Microgrid and the power management of that microgrid. The power management is performed by a Microgrid Central Controller (MGCC). A Microgrid operator provides daily information to the MGCC about the photovoltaic generation profile, the load demand profile, and the real-time prices of the electricity in order to plan the power interchange between the BESS and the main grid, establishing the desired state of charge of the batteries at any time. The main goals of the power management strategy under study are to minimize the cost of the electricity imported from the grid and to maximize battery life by means of an adequate charging procedure, which sets the charging rate as a function of the MG state. Experimental and simulation results in many realistic scenarios demonstrate that the proposed methodology achieves a proper power management of the DC microgrid.

Keywords: DC Microgrid; Battery Energy Storage System; Battery Management System.

4.1. Introduction

Nowadays, the increasing demand for electricity has encouraged the production of local energy by means of the integration of Microgrids (MGs) into the main grid [1]. The MGs are low power distribution systems which have distributed generation (DG), energy storage systems (ESSs) and a variety of loads. The DG is mainly composed by Renewable Energy Sources (RESs) such as PV systems, wind turbines, biomass, etc., whose intermittent nature produces strong power imbalances in the MG that can be compensated by the main grid or by the ESSs operating in the MG. A MG example is shown in Figure 1a, where the term PCC stands for the Point of Common Coupling with the main grid.

ESSs are a fundamental part of MGs, because they allow for a better utilization of the RESs, contributing to the MGs stability and reliability [1,2]. The DC microgrid under study in this work is depicted in Figure 1b. The Battery Energy Storage System (BESS) is formed of: (i) a battery bank, (ii) a Battery Management System (BMS) [3] and (iii) a DC/DC converter. It is important to point out that batteries are considered among the best energy storage devices, due to their quick technological evolution in smart grids and electric vehicles [4]. The essential characteristics of a battery are: the energy storage capacity, the efficiency, the lifetime (expressed in the number of cycles) and the operation temperature. The kind of batteries that are most commonly used in MGs for energy storage applications are Lead Acid (LA) or Valve regulated lead acid (VRLA) and lithium-ion (Li-ion) batteries [5–8]. In [6], a study was carried out on the most relevant characteristics in the selection process of the suitable battery technology for different applications. The main characteristics of the most widely used battery technologies in MGs are described in Table 1. LA batteries are widely used in MGs, because their implementation cost is the lowest among all usual technologies. In addition, this kind of batteries provides an acceptable performance and a great robustness. Nevertheless, their main drawback is their relatively short cycle life (1500–9000 charge/discharge cycles). On the contrary, Li-ion batteries have a long cycle life (>10,000 cycles) and their efficiency is approximately 95%, but their implementation cost is high (> USD 350/kW·h) [9] Moreover, the BMS of Li-ion batteries is more complex than that of VRLA batteries, due to the need for inner cell protections against overcharges and cell voltage equalization circuits [7,10,11].

Regarding the power management in the MGs, one of the crucial challenges is to keep the power balance between the generation and the

demand. The power imbalance is a common scenario in MGs, being caused by the discontinuity in the energy generation or by the changes in the power demand. Nowadays, adequate strategies have been developed to manage the power dispatch in the MGs, which can be: centralized, decentralized or distributed [12–21].

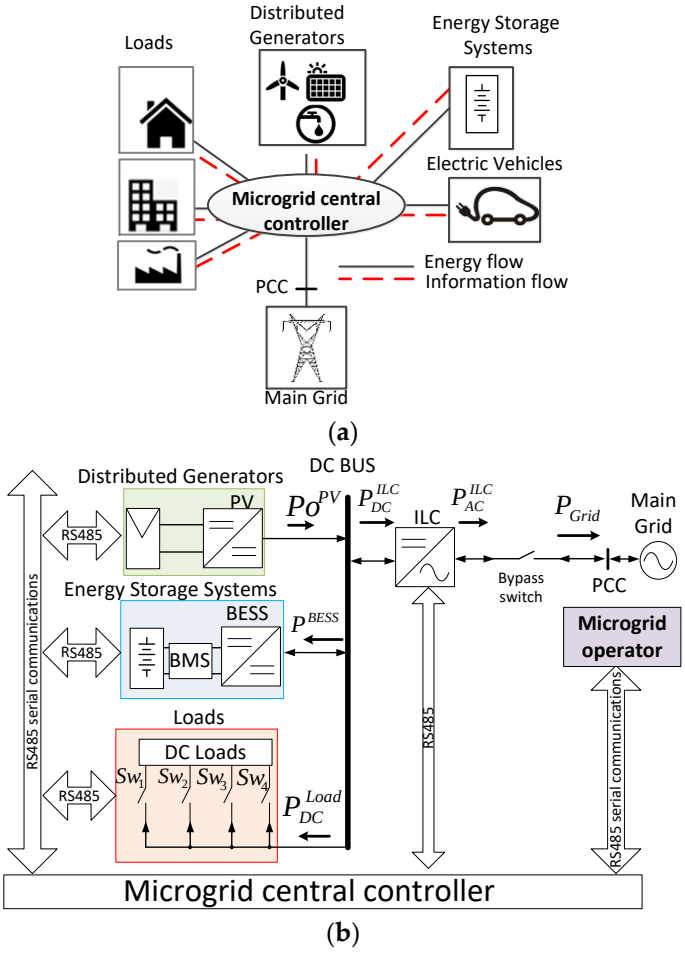

Figure 1. MG with central controller: (a) MG control system and intercommunication network; (b) DC Microgrid under study.

In the decentralized and distributed control strategies the power management and control are integrated in the local controllers of the DGs and ESSs, so that in the case of malfunction of any device, the MG can properly operate after the disconnection of the faulty unit. According to [1], some decentralized control strategies based on the droop method [20] do not need the implementation of a communications system and provide the plug and play

function of DG units. Nevertheless, a communication system is necessary for monitoring the power dispatch in the MG so that the power dispatch can be optimized and the status of each power unit can be known [17]. The main limitation of distributed control strategies takes place in environments with large communication delays and measurement errors, which brings about problems in the convergence speed and stability margins of the controls [1,17,18].

Table 1. Main characteristics of the most widely used battery technologies in MGs.

Battery Type	Power Rating (MW)	Discharge Time	Life Time (Years)	Cycle Life (Cycles)	Reliability and Efficiency (%)	Cost (USD/kW·h)
Flooded Lead Acid, VRLA	0–20	Seconds–hours	5–15	1500–9000	70–90%	180–300
Lithium ion	0–0.1	Minutes–hours	5–15	>10,000	Close to 100%	350–1100

Centralized control eases the optimization of the power distribution in the MG by coordinating the power devices by means of a smart centralized system operating through a communication system. A Microgrid Central Controller (MGCC) acquires system data and sets the power to be managed by each of the converters under operation, broadcasting power references to all the power devices in the MG, such as DGs, loads, ESSs, etc. [21].

Centralized control is suitable for small-scale microgrids with a low number of DGs an ESSs [1,21]. In this paper a MGCC performs the power management algorithms which can run on microcontrollers which provide simple communications [22].

This study is focused on two areas: the design of a Battery Energy Storage System (BESS) for a grid-connected DC microgrid and the power management of that MG. The goals of the grid connected MGs power management have been studied in previous works [16–23]. For optimizing the management of the energy generation and consumption, data like electricity tariffs, weather forecast or energy demand are used [23]. Recently, price schemes have been used in the literature to optimize the economic benefits of producers and consumers [24–28]. An industrial application of optimal operating strategies was presented in [27]. In [24], an optimal management model for residential facilities with Vehicle-to-grid (V2G) systems was presented. In those

management systems battery wear and energy costs were considered. In [25], a home power management system was proposed to minimize electricity cost and reduce high peak demand while maintaining user comfort. The algorithm that is presented in [28] finds an appropriate time of charging with low cost for electrical vehicles based on prediction of energy prices during the charging period. Most techniques optimize the power consumption over a single day, but in [27] a monthly bill was considered, for performing a multi-day optimization.

The main contribution of this work is the development of a power management strategy implemented in an MGCC for minimizing the cost of electricity in a grid connected DC microgrid and maximizing battery life. The MGCC receives from the MG operator the daily information about the prices of the electricity and the expected profiles of photovoltaic generation and load demand. The MGCC establishes the desired state of charge (SOC) in the BESS during the whole day. The proposed strategy takes advantage from the RESs and adjusts the battery energy storage through a suitable charging procedure. A BESS specially designed for DC microgrids is studied, whose BMS performs a charging procedure according to DIN 41773 [29,30] whenever it's possible. The BMS guarantees the proper operating conditions of the batteries, as specified by the manufacturer [29,30]. This approach maximizes the lifetime of the batteries and, consequently, minimizes the costs of their replacement [3,11]. The goal of the BMS is to charge the batteries with the excess of renewable generation and from the grid when the electricity tariff is low. If the SOC is below a certain minimum value and the renewable generation cannot charge the batteries alone, the extra power needed to charge the batteries will be imported from the grid with a value lower than or equal to the contracted power, no matter the electricity tariff. If the power which can be imported from the grid is enough to charge the batteries according to a DIN 41773 procedure, the batteries are charge accordingly. If not, the batteries are charged with a lower power.

This strategy allows to charge the batteries during off-peak hours, when kW·h is cheaper, and selling their energy to the main grid during peak hours. The charging rates and the available power for charging the batteries are adjusted based on a target SOC that is defined for several time intervals during a day, i.e., the BMS adjusts the charging rates based on the MG state. Furthermore, the modeling of the BESS by means of an accurate electrical second order model of the batteries is presented.

This paper consists of six sections. In Section 2 a brief overview of the Battery Management Systems is performed. Subsequently, a BESS specific design proposal for DC microgrids is described in Section 3. Then, all the concepts related to the proposed power management algorithm are explained

in Section 4. Simulations and experimental results are described in Section 5. Finally, Section 6 draws the conclusions of this paper.

4.2. Overview of Battery Management System in Microgrids

The main goals of a BMS that allow for an adequate operation of the batteries and to extend their service life are: (i) to operate the batteries according to an adequate SOC; (ii) to control the maximum charging/discharging current and voltage [3], as specified by the manufacturer; and (iii) to set a proper depth of discharge (DOD) of the batteries [3, 31]. In this work the maximum allowed value of the DOD is 65%, which is slightly smaller than the maximum recommended value for VLRA batteries (70%), which can be found in literature [8].

The BMS should implement an appropriate charge/discharge procedure of batteries that guarantees their operational conditions, as specified by the manufacturer. These procedures can be: charging batteries at constant current (CC) or constant voltage (CV). However, the RESs of the MGs may have power fluctuations that cause sudden variations in the available power for charging the batteries. Those sudden variations increase the BMS complexity and require the use of advanced techniques to manage the battery charging process [31–34]. In [32,33], some battery charging algorithms and their limitations have been reported. Other parameters that increase the BMS complexity are the kind of battery used and the estimation techniques of both the SOC and the state of life (SOL) [11]. Nevertheless, the battery life time is complex, because it depends on temperature variation, corrosion and maximum charge/discharge currents [4,6], etc. A comparative summary about some BMSs reported in the literature for diverse applications is shown in Table 2.

The SOC represents the available charge that is stored in the battery compared with the rated capacity charge of the battery. The SOC cannot be directly measured from the batteries and it is used to determine the power that can be extracted from them. In the literature, different methods to estimate the SOC are presented: the Ampere-hour integral or Coulomb counting method [35], the open-circuit voltage method [36], the electrochemical impedance spectroscopy method [37], machine learning-based methods [38], kalman-filter based methods [39], sliding mode observer methods [40], and the adaptive-gain nonlinear observer method [41], among others. The first four methods do not need to establish the battery model, so that they are called Non-model based methods. These methods cannot correct errors caused by the SOC incorrect initialization and the external perturbations [42]. The BMS proposed in this work has the following subsystems:

Table 2. Comparative table of some battery charging systems.

Battery Management System											
Monitoring			Protection				Control			Applications	
Battery Model	Estimation										
	SOC	SOH	Temperature	Overcharge	Overcurrent	Communication Loss	Thermal Management	Optimization	Communication System		Reference
– [1]	•	–	–	–	–	–	–	–	•	Uninterruptible power supplies	[45]
•	•	–	–	•	•	•	•	•	•	DC Microgrid	[46]
–	•	–	•	•	•	•	–	–	•	Uninterruptible power supplies	[47]
–	•	–	•	•	•	–	•	•	–	Portable electronic devices	[48]
•	–	•	–	•	•	–	–	–	–	Motorcycles, cars, wheelchairs, UPS	[49]
–	–	–	•	•	•	–	–	–	•	Portable electronics devices	[50]
–	–	•	•	•	•	–	•	•	•	Portable electronics devices	[51]
–	•	•	•	•	•	–	•	•	–	Hybrid electric vehicles	[52]
–	–	–	•	•	•	–	•	•	•	Portable applications	[53]
•	•	–	–	•	•	–	•	•	•	DC Microgrid	[54]
–	•	–	•	•	•	–	–	–	–	Electric vehicles	[55]
–	•	–	•	•	•	–	•	•	–	Motorcycles, cars, wheelchairs	[56]
•	•	–	•	•	•	–	–	–	–	Photovoltaic systems	[57]
–	•	–	–	•	•	–	–	–	–	Hybrid electric vehicles and Electric vehicles	[58]
–	•	–	•	•	•	–	–	–	–	Photovoltaic systems	[59]

[1] A (•) indicates that it falls in the category specified in the column heading; a (–) indicates that it does not.

- Battery monitoring: This subsystem includes voltage, current, impedance and temperature measurements. The monitoring allows for calculating the battery parameters: SOC, SOL, DOD and State of Health (SOH), yielding an estimation of the battery model. The SOH represents an estimation of the capacity of the battery to store and deliver energy, compared with a new battery [43]. The SOL is similar to the SOH. However, the SOL is defined in literature as the remaining time until the battery needs to be replaced [11]. It is possible to estimate the SOL, saving the data corresponding to the DOD values and the temperatures at which the batteries have been exposed [44]. The BMS of this paper uses the SOH concept. In order to estimate the SOH of the batteries, some studies [35]

consider the following expression: SOH (%) = (Q_{MAX}/Q_{Rated}) 100%; where Q_{Rated} is the rated capacity and Q_{MAX} is the maximum releasable capacity when the battery is fully charged, which will decline with the used time.

- Battery protection: Protection can be implemented in both the hardware and the software. This includes protection and diagnosis in the following situations: high temperature, overcharge, overcurrent and the communication loss with the system.
- Battery control: This subsystem is responsible for the battery charging procedure. Its goal is to extend the service time of batteries and to allow for a proper energy management in the system.
- Communication system: This subsystem informs a central controller about the parameters of the batteries in order to manage the power dispatch of the MG. These communications allow for an interface with the user and the interaction with the power management in the MG.

In this paper, the design of a BESS for a DC microgrid is presented. The BESS is based on a BMS that optimizes the energy storage and implements an adequate charge procedure, which changes the charging rate and plans the SOC of the battery depending on the MG scenarios. The BMS has all the elements summarized in Table 2 [45–59]. A battery electrical model is described, which allows for determining all the static and dynamic characteristics of the battery. This model is necessary to design the control loops of the power converter of the BESS taking into account all the involved variables. Overall, the batteries can be approximated to a voltage source in series with RC elements (Resistor-Capacitor), where each one represents a specific dynamics for every charging condition [41,60, 61].

4.3. Design of the Battery Energy Storage System

The BESS keeps the power balance at the DC bus of the MG. The BESS is composed by: (i) a battery bank, (ii) a BMS and (iii) a DC/DC converter. In this Section, all the power conversion processes have been modeled. The battery model, the BMS and a description of the converter control are shown in the following Subsections.

4.3.1. Selection of the Battery Bank.

The capacity of the battery bank is selected to fulfill the following criteria: (i) batteries can be discharged if the available power on the DC bus is lower than that necessary at the MG or when the electricity tariff is high; (ii) batteries must be charged during off-peak times with the surplus of energy which is available from the RES if there is such a surplus. If not, some power from the

main grid will be imported for charging the batteries; (iii) the batteries initial cost must be low. However, there's a trade-off between saving money from the electricity tariff, which requires a big battery bank, and obtaining a low cost of the battery system. In order to make both of the goals compatible, a low cost battery technology has been chosen. Furthermore, a value of the DOD (DOD = 65%) close to the maximum recommended [8,29] one has been aimed in the proposed BMS, in order to get a reasonable size of the battery bank. For this study, the power profile of the photovoltaic generation ($P^{PV}_{Profile}$), the power consumed by the loads ($P^{Load}_{DC\_Profile}$) and the tariff costs according to the time of use (TOU) of electricity are taken as reference. This is shown in Figure 2a.

$$P^{Bat}_{Available} = \frac{1}{\Delta t \cdot \mathrm{DOD}} \cdot \int_{t_o}^{t_o+\Delta t} \left(P^{PV}_{Profile} - P^{Load}_{DC\_Profile}\right) \cdot dt \quad (1)$$

$$Number^{Batteries} = \frac{\left|P^{Bat}_{Available}\right| \cdot \Delta t}{Q_{Rated} \cdot V^{Battery}_{Selected}} \quad (2)$$

The PV generation decreases from 16:00 h to 19:00 h, as can be seen in Figure 2a. At this time, the power demand is higher than PV generation and the TOU price is on peak. At this point, the batteries should have stored enough energy to fulfill the power demand of the MG. Equations (1) and (2) allow for determining the number of batteries that is needed to accomplish this last objective. In (1) and (2), $P^{Bat}_{Available}$ stands for the available power that the batteries should supply during a time interval Δt, supposing that they have been fully charged to a value SOC > 95% before. The time instant when the battery discharge interval starts is called t_o. $V^{Battery}_{Selected}$ is the rated voltage of the battery.

In this work, a VRLA battery has been selected, model: SUN POWER VRM 12V105 (HOPPECKE, Brilon, Germany). Its characteristics are shown in Table 3 [62]. As it can be seen in Figure 2a, the average power consumed by the load from 16:00 h to 24:00 h (t_o = 16 h, Δt = 8 h) is 2.7 kW and this average power should be provided by the batteries. $P^{Bat}_{Available} \cong$ 2.7 kW during that time interval, Δt. The number of batteries of the battery bank is obtained from Equation (2). It is composed of 18 batteries of 12 V connected in series, with a battery bank rated voltage of V^{Bat}_{Rated} = 216 V. The battery bank is charged/discharged from/to the DC bus of the MG by means of a 3 kW bidirectional half-bridge DC/DC converter, as shown in Figure 2b. The LC output filter of the DC/DC converter has an inductance value, L^{Bat}, which has been calculated taking into consideration: (i) the maximum ripple current allowed by the batteries, and (ii) the ripple current through L^{Bat}, ΔI^{Bat}_{L}, should guarantee the continuous current conduction mode if the current is higher than 10% of the maximum current. The

value of L^{Bat} is calculated from Equation (3), where V_{DC} is the DC bus voltage and F_{sw} is the switching frequency of the converter [49]. The values of the input and output capacitances, *Ci* and *Co*, can be calculated from (4) and (5), respectively.

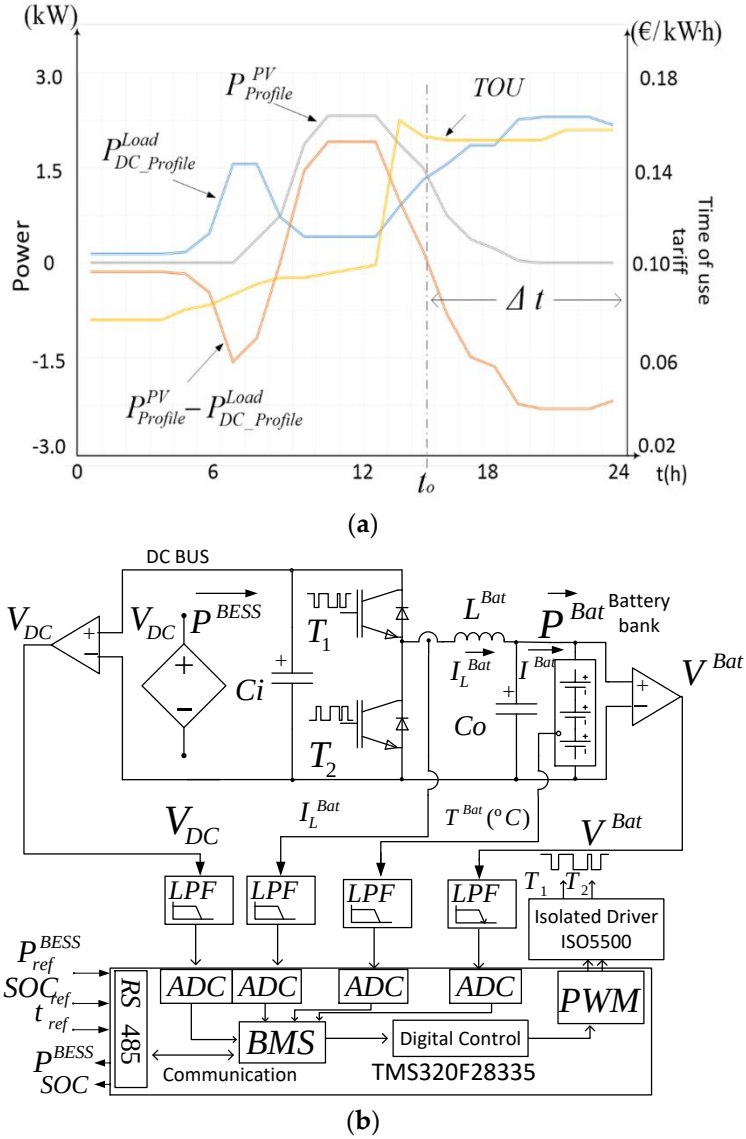

Figure 2. Battery Energy Storage System (BESS): (**a**) Reference profiles of PV generation ($P^{PV}_{Profile}$), power consumed by the loads ($P^{Load}_{DC\_Profile}$) and time of use (TOU) tariff of electricity in the MG; (**b**) Electrical diagram of the BESS.

$$L^{Bat} \geq \frac{V_{Rated}^{Bat}}{4 \cdot \Delta I_L^{Bat} \cdot F_{SW}} \quad (3)$$

$$Ci \geq \frac{P_{HB-Rated}^{BESS}}{2 \cdot V_{DC} \cdot \Delta V_{DC} \cdot F_{SW}} \quad (4)$$

$$Co \geq \frac{I_{Max}^{Bat}}{2 \cdot \Delta V_{Max}^{Bat} \cdot F_{SW}} \quad (5)$$

Table 3. BESS specifications.

DC/DC Converter	Battery Specifications	Battery Bank Parameters for Complying DIN 41773
	Sun Power VRM 12V105	
$P_{HB\_Rated}^{BESS}$ = 3 kW	$V_{Selected}^{Battery}$ = 12 V	−10 °C < T^{Bat} < 45 °C
F_{sw} = 16 kHz	I_{Max}^{Bat} = 20 A	V_{Min}^{Bat} = 194 V
C_i = 1 mF	V_{Rated}^{Bat} = 216 V	V_{Max}^{Bat} = 260 V
C_o = 1 mF	Q_{Rated} = 105 A·h	I_{tail}^{Bat} = 1 A
L^{Bat} = 5.4 mH	Q_{100} = 101 A·h	t_{Ch} < 48 h
η_{BESS} = 0.97	$\Delta V_{Max}^{Bat} = 0.02 \cdot V_{Rated}^{Bat}$	$I_{C5} \cong$ 20A
V_{DC} = 400 V ± ΔV_{DC}	$\Delta I_L^{Bat} = 0.1 \cdot I_{Max}^{Bat}$	$I_{C20} \cong$ 5A
ΔV_{DC} = 20 V	DOD = 65%	

4.3.2. Modeling of Battery Bank

The electric model of the battery bank used in this study is similar to that developed in [61], being shown in Figure 3. It has an open-circuit voltage source depending on the SOC, V_{OCV}^{Bat} (SOC), connected in series with a resistor and a second-order R-C circuit that represents the transient response of battery. The impedance of the battery bank is represented by Equation (6) and the battery voltage by Equation (7).

$$Z^{Bat}(s) = R_{Serie}^{Bat} + \frac{R_{Fast}^{Transient}}{s \cdot R_{Fast}^{Transient} \cdot C_{Fast}^{Transient} + 1} + \frac{R_{Slow}^{Transient}}{s \cdot R_{Slow}^{Transient} \cdot C_{Slow}^{Transient} + 1} \quad (6)$$

$$V^{Bat}(s) = V_{OCV}^{Bat}(SOC) - I^{Bat} \cdot Z^{Bat}(s) \quad (7)$$

The electric parameters of the chosen VRLA battery bank are shown by Equations (8) to (13) and have been obtained with an identical procedure to that shown in [60,61]. Those Equations are valid for SOC > 0.1. Taking into account that SOC in this work is kept higher or equal than 0.35, Equations (8) to (13) are valid in this study.

$$V_{OCV}^{Bat}(SOC) = 202.52 + 16.29 \cdot SOC - 6.36 \cdot SOC^2 + 24.19 \cdot SOC^3 - 55.67 \cdot e^{-35 \cdot SOC} \quad (8)$$

$$R_{Serie}^{Bat} = 8.4348 \cdot e^{-24.37 \cdot SOC} + 2.0208 \quad (9)$$

$$R_{Fast}^{Transient} = 17.3232 \cdot e^{-29.14 \cdot SOC} + 2.5212 \quad (10)$$

$$C_{Fast}^{Transient} = -14.1278 \cdot e^{-13.51 \cdot SOC} + 13.0296 \quad (11)$$

$$R_{Slow}^{Transient} = 356.562 \cdot e^{-155.2 \cdot SOC} + 2.6913 \quad (12)$$

$$C_{Slow}^{Transient} = -112.1481 \cdot e^{-13.51 \cdot SOC} + 82.8704 \quad (13)$$

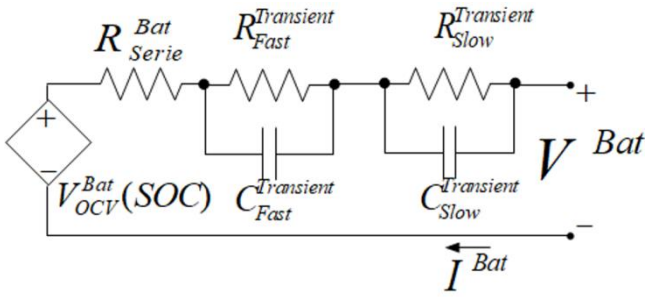

Figure 3. Second order model of the battery bank

4.3.3. Small-signal model of the BESS

The small-signal model of the bidirectional half-bridge DC/DC converter is shown in Figure 4. That model has been derived from an averaged model where any electrical value x has a static term at the operation point, X, and a small-signal dynamic term, $\tilde{x}$, being: $x = X + \tilde{x}$. When the batteries are being charged with a charge current $I_{L(Ch)}^{Bat}$, the converter works as a Buck converter, as depicted in Figure 4a. When the batteries are being discharged with a discharge current $I_{L(Dis)}^{Bat}$, the converter works as a Boost converter, see Figure 4b. The transfer functions in Equations (14) and (15) are obtained from Figure 4. They

are used to design the controllers in charge mode (Ch) or discharge mode (Dis) of the battery bank.

$$\left.\frac{\tilde{\imath}_{L(Ch/Dis)}^{Bat}}{\tilde{d}}(s)\right|_{\tilde{v}_{DC}=\tilde{v}_{OCV(SOC)}^{Bat}=0} = \frac{V_{DC}}{s\cdot L^{Bat}+\dfrac{1}{s\cdot Co+\dfrac{1}{Z^{Bat}(s)}}} \tag{14}$$

$$\left.\frac{\tilde{v}^{Bat}}{\tilde{\imath}_{L(Ch)}^{Bat}}(s)\right|_{\tilde{v}_{DC}=\tilde{v}_{OCV}^{Bat}(SOC)=0} = \frac{1}{s\cdot Co+\dfrac{1}{Z^{Bat}(s)}} \tag{15}$$

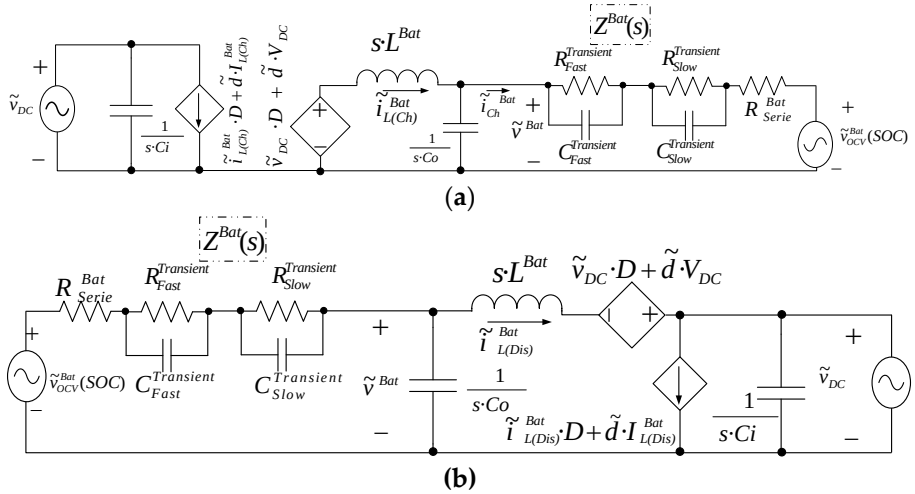

Figure 4. Small-signal model of the half-bridge DC/DC converter: (a) Buck small-signal model, charge mode (Ch); (b) Boost small-signal model, discharge mode (Dis).

4.3.4. Control loops design of the BESS

The BESS works from a BMS that sets either the charge of the batteries at constant current (CC) or constant voltage (CV), or the discharge of the batteries at a constant current. The block diagram of the current control loop and of the voltage control loop of the BESS are shown in Figure 5. $G_{IL}^{Bat}(s)$ and $G_{V}^{Bat}(s)$ blocks represent, respectively, the transfer functions of the current and voltage regulators. *Fm* is the gain of the PWM modulator. $T_{IL(Ch/Dis)}^{Bat}(s)$ is the transfer function of the open loop gain of the current loop, either in charge (Ch) or in discharge (Dis) mode. $T_{V}^{Bat}(s)$ is the transfer function of the open loop gain of the voltage loop in battery charge mode.

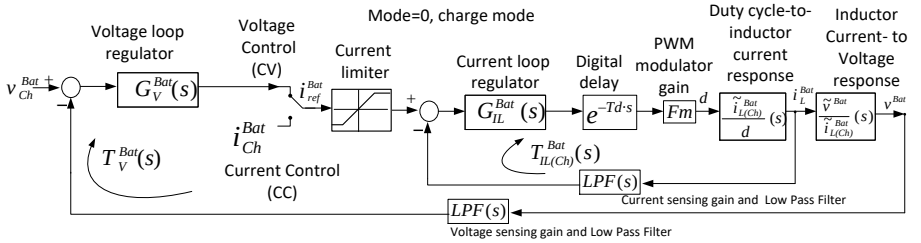

(**a**)

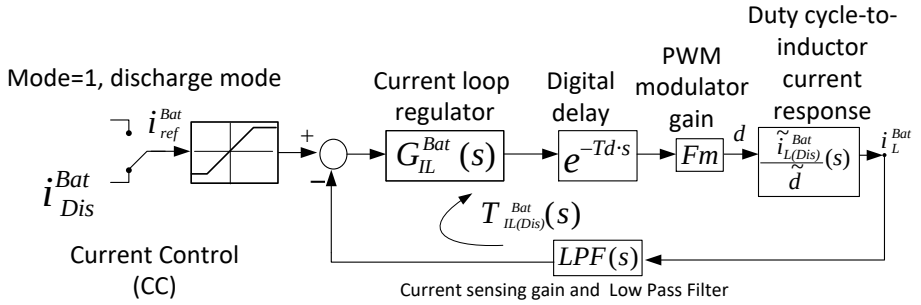

(**b**)

Figure 5. Control structure of the current control loop and of the voltage control loop of the batteries: (a) Charge Mode and (b) Discharge Mode.

Table 4. Transfer functions of the BESS controllers and loop gains.

Description	Transfer function
Low Pass Filter	$LPF(s) = \dfrac{1}{1.09 \cdot 10^{-9} \cdot s^2 + 9.91 \cdot 10^{-5} \cdot s + 1}$
PWM Modulator gain	$Fm = \dfrac{1}{\mathrm{V_{PP}}} = 1$
Battery Current-loop regulator	$G_{IL}^{Bat}(s) = \dfrac{0.0453 \cdot (1 + \mathrm{s} \cdot 0.018)}{\mathrm{s} \cdot 0.018}$
Battery Voltage-loop regulator	$G_{V}^{Bat}(s) = \dfrac{0.0806 \cdot (1 + \mathrm{s} \cdot 0.0041)}{\mathrm{s} \cdot 0.0041}$
Current Charge/Discharge-loop gain	$T_{IL(Ch/Dis)}^{Bat}(s) = G_{IL}^{Bat}(s) \cdot \mathrm{e}^{-\mathrm{Td} \cdot \mathrm{s}} \cdot Fm \cdot \dfrac{\tilde{\mathrm{i}}_{\mathrm{L(Ch/Dis)}}^{\mathrm{Bat}}}{\tilde{\mathrm{d}}}(\mathrm{s}) \cdot LPF(s)$
Voltage-loop gain	$T_{V}^{Bat}(s) = G_{V}^{Bat}(s) \cdot \dfrac{T_{IL(Ch/Dis)}^{Bat}(s)}{T_{IL(Ch/Dis)}^{Bat}(s) \cdot LPF(s) + 1} \cdot \dfrac{\tilde{v}^{Bat}}{\tilde{i}_{L(Ch)}^{Bat}}(\mathrm{s}) \cdot LPF(s)$

The Bode plots of the current loop $T_{IL(Ch/Dis)}^{Bat}(s)$ for different values of the DC-bus voltage, V_{DC}, are shown in Figure 6a. The controller was designed in the analog domain, taking into account a digital delay of a sampling period, $T_d = T_{samp}$, and discretized in the Z domain by using the Tustin transformation. The sampling frequency was F_{samp} = 16 kHz = $1/T_{samp,}$ which agrees with the switching frequency, F_{Sw}. The current regulator, $G_{IL}^{Bat}(s)$, is adjusted to get a crossover frequency of the current loop: F_{ci} = 500 Hz < $F_{Sw}/20$, with a phase margin around 60 deg. The Bode plots of the voltage loop, $T_V^{Bat}(s)$, for different values of the SOC are shown in Figure 6b. The voltage regulator $G_V^{Bat}(s)$ has been adjusted to get a crossover frequency of the voltage loop: F_{cv} = 12.6 Hz < $F_{ci}/20$, with a phase margin around 90 deg. The transfer functions of the regulators are summarized in Table 4. The BESS control loops are robust to any change in the battery charge/discharge currents, SOC, battery voltage and changes of the DC bus voltage, because the battery model is practically constant when the SOC is higher than 10%, which is a suitable working range for the batteries.

4.3.5. Design of the BMS

The BMS is designed to fulfill the following objectives: (i) To broadcast the SOC of the batteries to the MGCC (ii) To coordinate the charging/discharging of the batteries depending on the power management strategies that are established by the MGCC and (iii) To adjust the parameters of the battery charge procedure depending on the MG state. The proposed BMS structure for the DC microgrid is shown in Figure 7.

The BMS has the following subsystems:

- Battery Monitoring: It measures the battery parameters: current, voltage and temperature of the battery bank (I^{Bat}, V^{Bat} , T^{Bat}). The initial SOC, DOD and SOH are estimated. A data table is stored corresponding to the amount of charge/discharge cycles, the battery model and its initial impedance.
- Battery Protection: The batteries are protected against overcharge, overcurrent, high temperature, communication loss and connection loss. The BMS sets the maximum charging/discharging current, the advisable SOC, the battery voltage and the maximum temperature.
- Battery Communication: The communication allows for the optimization of the battery charging/discharging process. In charge mode, the MGCC sends to the BESS information about the available power to charge batteries (P_{ref}^{BESS}) and the time (t_{ref}) in which the BESS keeps this power. In addition, the MGCC sends the desired SOC (SOC_{ref}) of the batteries, to be reached in a time t_{ref}. The BESS informs the MGCC about the current SOC and the absorbed/injected power from/to the DC bus by the BESS.

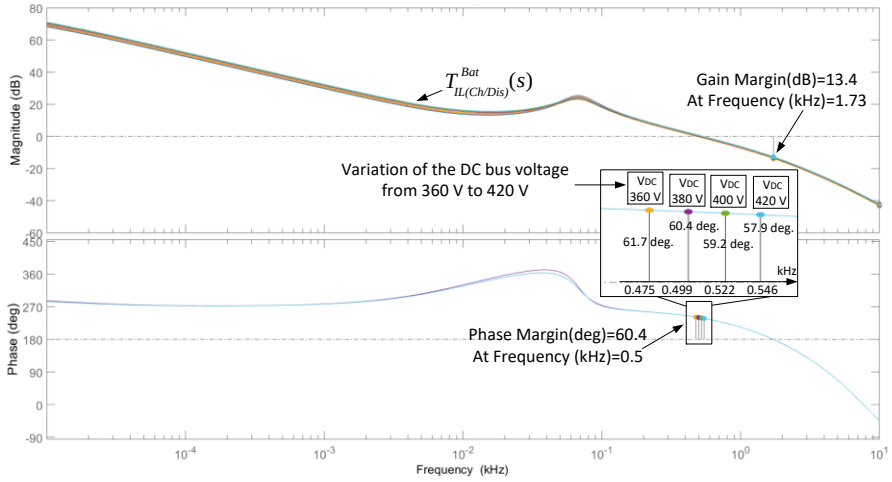

(**a**)

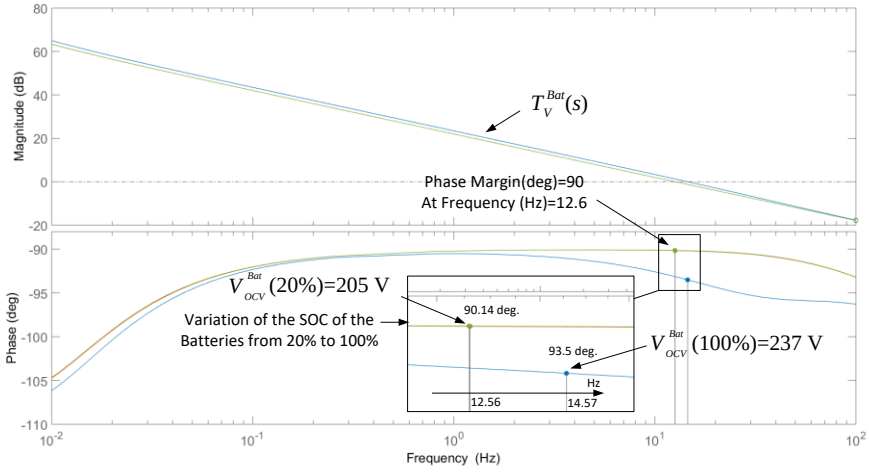

(**b**)

Figure 6. Bode plots of the loop gains: (a) Current loop for different values of the DC-bus voltage and (b) Voltage loop for different values of the SOC.

- Battery control: The current/voltage vs. time curves of the charge procedure of the battery bank are shown on the right side of Figure 7. First, the batteries are charged to a constant current (CC) until a maximum charging voltage is reached. At this point, the control is changed to constant voltage (CV) in the batteries. The procedure is based on adjusting the current and voltage charging parameters of the batteries as a function of the MG state and complying with the DIN 41773 specifications [29] at the same time. The charge procedure is done by adjusting the battery

current and voltage according to the temperature of the batteries and to the available power at the DC bus. In addition, the batteries can be charged or discharged depending on the cost of the electricity tariff and on the power availability at the RESs of the MG.

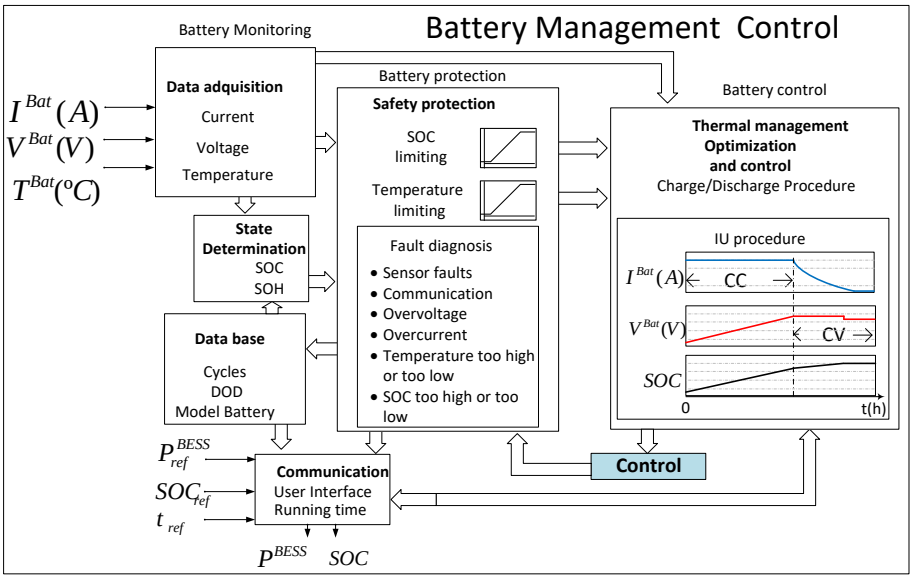

Figure 7. Proposed Battery Management System.

4.3.5.1. Battery management algorithm

The battery management algorithm implemented in the BMS is shown in Figure 8 and it is described in the following.

The BMS receives three control parameters from the MGCC through RS485 serial communications. These parameters are: (i) the target SOC (SOC_{ref}); (ii) the available/necessary power for discharging/charging the batteries (P_{ref}^{BESS}) to/from the DC bus; and (iii) the time interval t_{ref}, during which the BESS must reach SOC_{ref} with the available power at the DC bus.

The BMS has three inputs that are produced by sensors: the signals from the battery current sensor, from the battery voltage sensor and from the battery temperature sensor, corresponding to I^{Bat}, V^{Bat} and T^{Bat}, respectively.

The SOC of the batteries can be calculated from Equation (16), where a positive (negative) value of I^{Bat} represents a charging (discharging) current of the battery bank. Q_{Rated} stands for the rated battery bank capacity in A·h. $Q_{Dis(Ch)}$, expressed by Equation (17), is the expected dis (charge) capacity in A·h, which depends on the dis (charge) rate. $\eta_{Dis(Ch)}$ is the dis (charge) efficiency [10]. The

value of $Q_{Dis(Ch)}$ can be obtained by means of a linear interpolation of the curves of the battery capacity provided by the manufacturer [62].

$$SOC(t) = SOC(0) + \eta_{Dis} \cdot \int_0^t \frac{I^{Bat}(t)}{Q_{Rated}} \cdot dt \text{ where } \eta_{Dis} = \frac{Q_{Dis}}{Q_{Rated}} \quad (16)$$

$$Q_{Dis} = 104.6654 - 1.6456 \cdot |I^{Bat}| \quad (17)$$

The battery bank charge power is given by the equation (18) and the power absorbed by the BESS from the DC bus is represented by (19).

$$P^{Bat} = I^{Bat} \cdot V^{Bat} \quad (18)$$

$$P^{BESS} = \frac{P^{Bat}}{\eta_{BESS}} \quad (19)$$

Taking into account that P_{ref}^{BESS} stands for the power setpoint to charge the batteries sent by the MGCC to the BESS, the operating mode of the BESS is set as follows: If $P_{BEES\_ref} > 0$, the BESS will work in charge mode ('Mode = 0'), otherwise, the BESS will operate in discharge mode ('Mode = 1').

Note from Figure 8 that there is a ramp function expressed by Equation (20) that changes the value of P_{ref}^{BESS} inside the BESS, $P_{ref(k)}^{BESS}$, progressively from an initial value $P_{ref(k-1)}^{BESS}$ until it reaches the value P_{ref}^{BESS} set by the MGCC, so that soft power transitions are performed. $P_{ref(k)}^{BESS}$ can be expressed by Equation (21). In (20) and (21), the variable "t" represents the time, while "k" represents the index of the last calculated sample of the power reference. When the value of k increases from (k − 1) to k, the resulting time step is 100 ms. During the 100 ms span, 100 different intermediate values of the power reference are used to ramp between $P_{ref(k-1)}^{BESS}$ and $P_{ref(k)}^{BESS}$ each intermediate value is kept during 1 ms (Δt_{RAMP}). Other stepsize values are possible, but the chosen values have provided good practical results. Thus, the BESS avoids fluctuations in the DC bus due to abrupt bidirectional changes in the power setpoint, P_{ref}^{BESS}.

$$r(t) = \frac{t}{100 \cdot \Delta t_{RAMP}}, (0 \leq t \leq 100\, ms) \quad (20)$$

$$P_{ref(k)}^{BESS} = P_{ref(k-1)}^{BESS} + \left(P_{ref}^{BESS} - P_{ref(k-1)}^{BESS}\right) \cdot r(t) \quad (21)$$

If 'Mode = 1' (discharge mode). On the contrary, if 'Mode = 0', the BMS calculates the power required ($P_{Required}^{Bat}$) to reach the target SOC in the time interval t_{ref}. $P_{Required}^{Bat}$ is given by Equation (22).

The charging procedure DIN41773 is carried out. The batteries are charged at CC until a maximum charging voltage is reached. If $P^{Bat}_{Required} < P^{BESS}_{ref(k)}$, the batteries will be charged with current $I^{Bat}_{(Ch)}$ calculated from Equation (23) and the SOC_{ref} will be reached in the specified time t_{ref}. Otherwise, the batteries will be charged with a current $I^{Bat}_{(Ch)}$ given by Equation (24) and the SOC_{ref} will not be reached in the desired time, because the current available power is not enough.

When the maximum charging voltage $V^{Bat}_{(Ch)}$ is reached, the batteries are charged at constant voltage. The value of $V^{Bat}_{(Ch)}$ depends both on the temperature and on the charging current of batteries. The current dependence, $V^{Bat}_{(Ch)}$ $(I^{Bat}_{(Ch)})$, and the temperature dependence, $V^{Bat}_{(Ch)}$ (T^{Bat}), are shown by Equations (25) and (26), respectively. Equation (25) provides $V^{Bat}_{(Ch)}$ for charging the battery at a given current according to the charge procedure that was recommended by the manufacturer [62]. The recommended value of $V^{Bat}_{(Ch)}$ may be lower because of the battery temperature (26). Finally, the value of $V^{Bat}_{(Ch)}$ is given by Equation (27). The minimum and maximum values of the charging current suggested by the manufacturer of the chosen batteries are: I_{C20} = 5 A and I_{C5} = 20 A, being C20 and C5 the specified battery capacity (measured in A·h) for a discharge time of 20 h and 5 h, respectively.

$$P^{Bat}_{Required} = \frac{(SOC_{ref} - SOC) \cdot Q_{Rated} \cdot V^{Bat}_{Rated}}{100\% \cdot t_{ref} \cdot \eta_{Dis}} \text{ where } SOC_{ref} > SOC \quad (22)$$

$$I^{Bat}_{Ch} = MIN\left[\frac{P^{BESS}_{HB-Rated} \cdot \eta_{BESS}}{V^{Bat}_{Rated}}, \frac{P^{Bat}_{Required}}{V^{Bat}_{Rated}}\right] \quad (23)$$

$$I^{Bat}_{Ch} = MIN\left[\frac{P^{BESS}_{HB-Rated} \cdot \eta_{BESS}}{V^{Bat}_{Rated}}, \frac{P^{BESS}_{ref(k)} \cdot \eta_{BESS}}{V^{Bat}_{Rated}}\right] \quad (24)$$

$$V^{Bat}_{Ch}(I^{Bat}_{Ch}) = \frac{(V^{Bat}_{Max} - V^{Bat}_{Min}) \cdot I^{Bat}_{Ch}}{I_{C5} - I_{C20}} + 249.2\ V \quad (25)$$

$$V^{Bat}_{Ch}(T^{Bat}) = 267.7 - (0.49 \cdot T^{Bat} + 3.8 \cdot {T^{Bat}}^2 - 0.67 \cdot {T^{Bat}}^3 + 0.01 \cdot {T^{Bat}}^4) \cdot 10^{-3} \quad (26)$$

$$V^{Bat}_{Ch} = MIN[V^{Bat}_{Ch}(I^{Bat}_{Ch}), V^{Bat}_{Ch}(T^{Bat})] \quad (27)$$

Once the current that was absorbed by the batteries is lower than a pre-set tail current (I^{Bat}_{tail}) or after a certain charging time (t_{Ch}) has elapsed, the battery voltage is kept at a floating voltage value (V^{Bat}_{Float}) that is expressed by Equation (28). This Equation is obtained from the polynomial interpolation of the floating voltage curves which were provided by the manufacturer [62]. It can be observed that the value of V^{Bat}_{Float} depends on the battery temperature.

$$V_{Float}^{Bat}(T^{Bat}) = 253.5 - (0.62 \cdot T^{Bat} - 3.1 \cdot T^{Bat^2} + 0.41 \cdot T^{Bat^3}) \cdot 10^{-3} \quad (28)$$

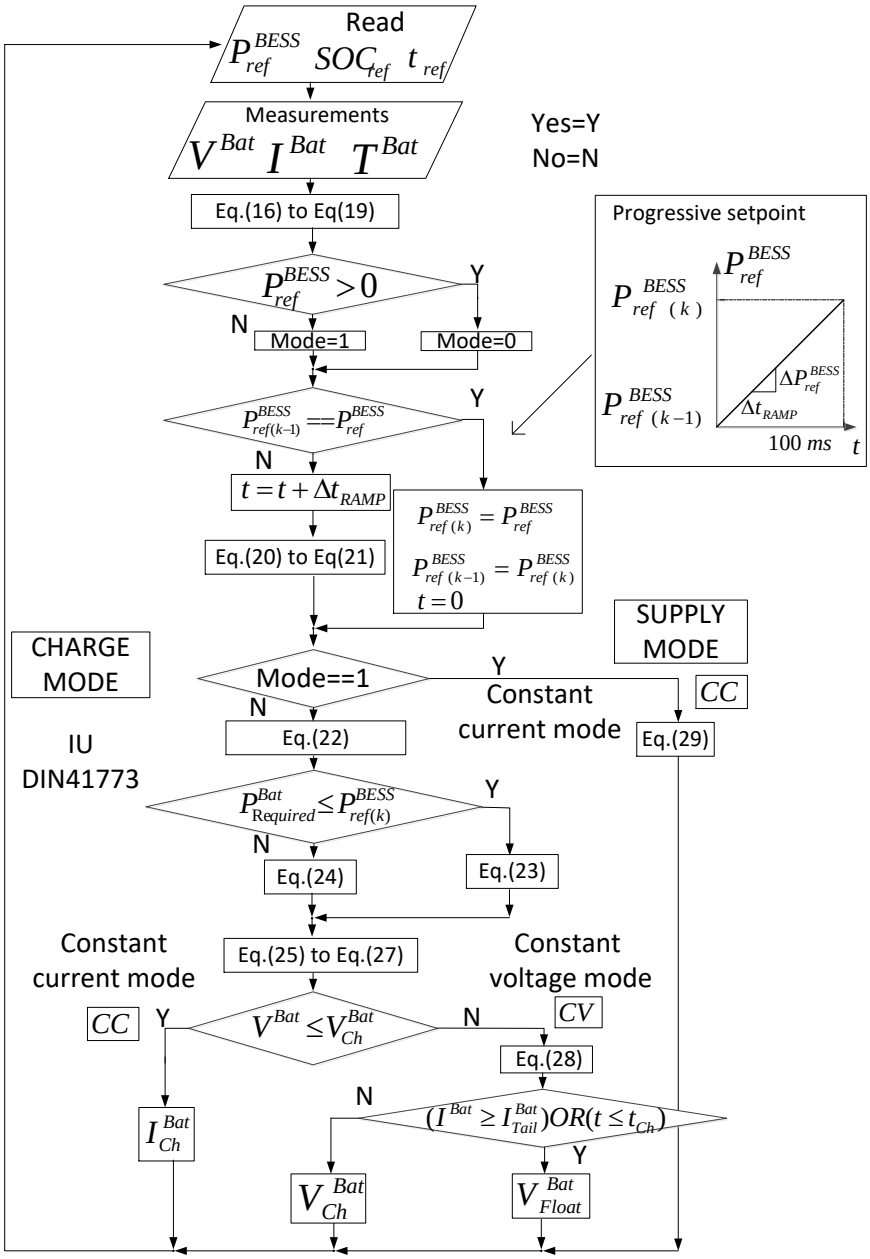

Figure 8. Battery charging algorithm.

If 'Mode = 1' (discharge mode), the BESS operation switches to discharge mode and the discharge current is calculated from equation (29).

$$I_{Dis}^{Bat} = -MIN\left[\frac{P_{HB-Rated}^{BESS}}{\eta_{BESS} \cdot V_{Rated}^{Bat}}, \frac{\left|P_{ref(k)}^{BESS}\right|}{\eta_{BESS} \cdot V_{Rated}^{Bat}}\right] \quad (29)$$

4.4. Centralized power management algorithm of the DC microgrid tied to the main grid.

In this Section a centralized power management algorithm for the grid-connected DC Microgrid is described. The DC microgrid consists of: (a) a MGCC; (b) an interlinking converter (ILC) connected to the main grid which regulates the DC bus voltage; (c) two DC/DC converters operating as controlled current sources interchanging their power with the DC bus; (d) four DC loads with their respective electronic switches; (e) an RS485 serial communication system and (f) the MG operator. Figure 9 depicts the placement of the power converters operating in the DC microgrid.

The MGCC receives the information from the MG operator about of the prices of the electricity, of the photovoltaic generation and of the load demand. The MGCC extracts the minimum possible power from the grid to the MG to reduce the electricity bill. If there is an excess of available power at the PV generation and if the SOC of the batteries is adequate, the surplus power can be injected from the MG to the grid under the limit which was determined by the MG operator. As a last resort, the MGCC depending on the SOC, can implement a load shedding functionality to decrease the power which is absorbed from the grid and avoid the batteries undercharging.

4.4.1. The power management algorithm of the MG.

The parameters broadcasted among the power converters, MG operator and the MGCC are shown in Table 5. The MGCC establishes the daily planning of the power dispatch in the MG, depending on the reference profiles sent by the MG operator to the MGCC. The evolution in time during a day of the reference profiles ($P_{Profile}^{PV}$, $P_{DC\_Profile}^{Load}$, $P_{Grid\text{-}to\text{-}MG}^{MAX}$, $P_{MG\text{-}to\text{-}Grid}^{MAX}$ and TOU) is shown in Figure 10. $P_{Profile}^{PV}$ is the PV power profile, $P_{DC\_Profile}^{Load}$ is the profile of the power consumed by the DC loads. $P_{Grid\text{-}to\text{-}MG}^{MAX}$ is the maximum power that can be imported from the grid to the MG and $P_{MG\text{-}to\text{-}Grid}^{MAX}$ is the maximum power that can be exported from the MG to the grid.

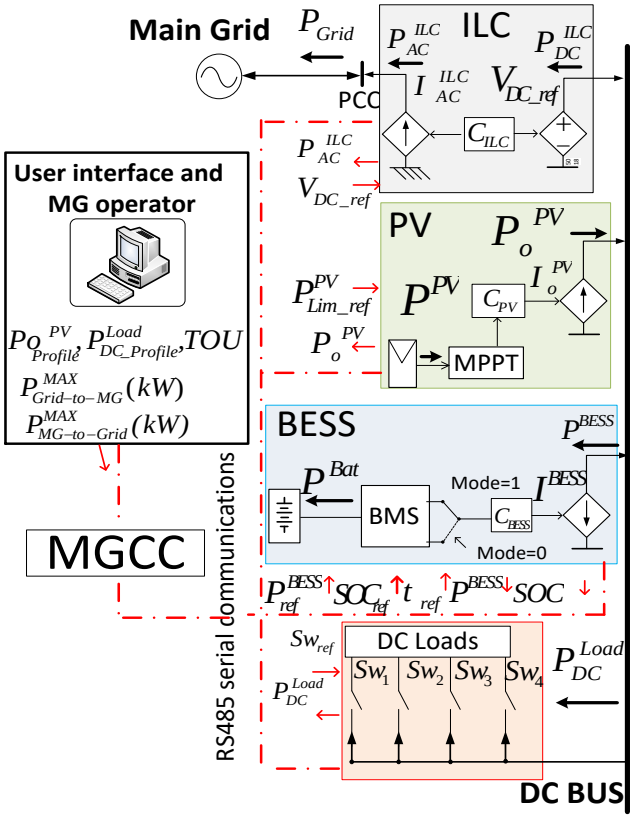

Figure 9. DC microgrid implemented. Placement of the power converters operating in the DC microgrid.

Table 5. Parameters broadcasted between the power converters of the DC microgrid and the MGCC.

MGCC	MG Operator	Power Converters			
		ILC	BESS	PV	DC Load
Output reference values (1)		V_{DC_ref}	P_{ref}^{BESS} SOC_{ref} t_{ref}	$P_{Lim\_ref}^{PV}$	$Sw_{ref} = \{Sw1_{ref}, Sw2_{ref}, Sw3_{ref}, Sw4_{ref}\}$
Input	Reference Profiles	Input measurement (2)			
	$P_{Grid-to-MG}^{MAX}$, $P_{MG-to-Grid}^{MAX}$ TOU, $P_{Profile}^{PV}$, $P_{DC\_Profile}^{Load}$	P_{Grid}	SOC P^{BESS}	$P_o{}^{PV}$	P_{Load}^{DC}

(1) Control references sent by the MGCC. (2) P_{Grid} is the power injected from the MG to Grid; $P_o{}^{PV}$ is the PV generated power and P_{Load}^{DC} is the power consumed by the DC loads.

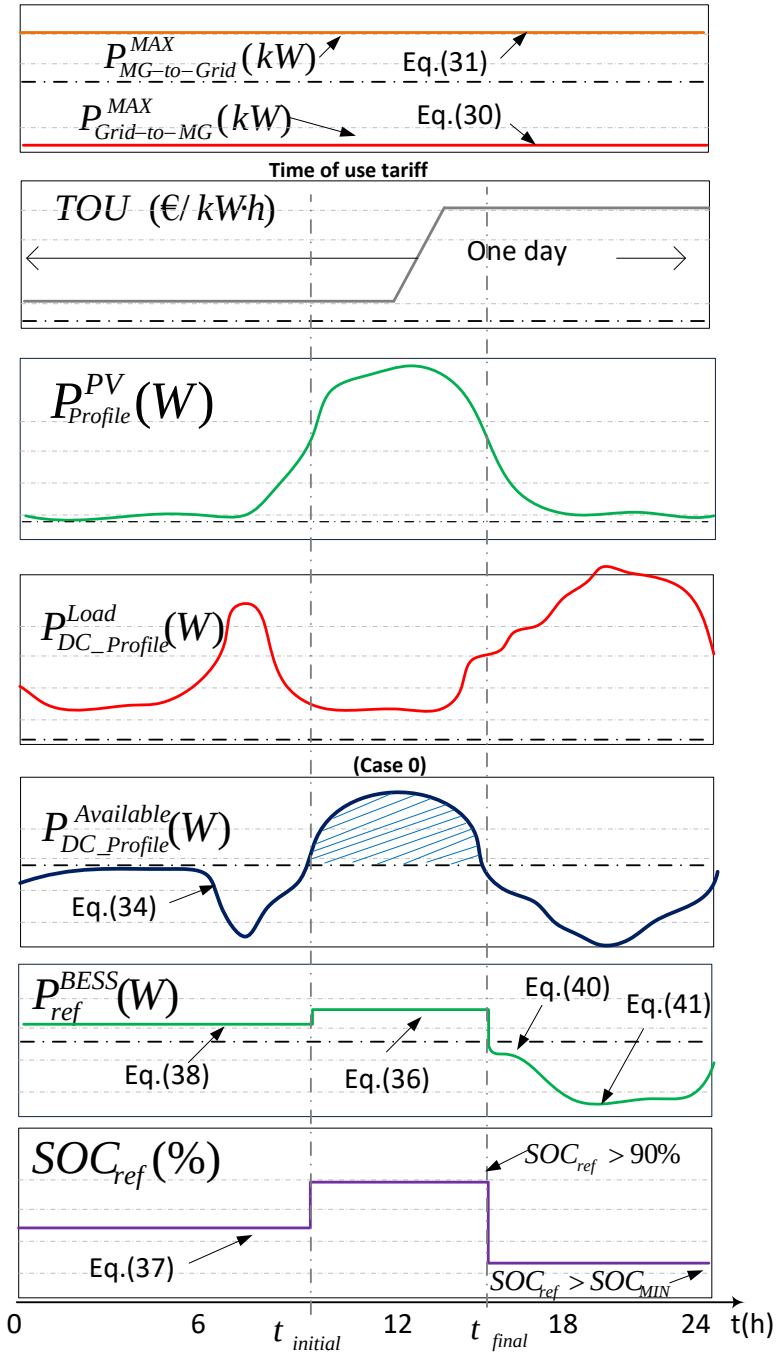

Figure 10. Graphics of the power profiles and of the charge process of the batteries (Case 0).

The power management algorithm of the MG is shown in Figure 11 and it is executed every 1 s (1 Hz), performing the request of the measurements of P^{BESS}, P^{DC}_{Load}, $P_{o}{}^{PV}$, P^{ILC}_{AC} and SOC, and transmitting the references to the MG devices. The MGCC selects one of six possible power management cases during the whole day and calculates the reference values, which are transmitted to all the power converters under operation. The cases depend on the scenarios of the MG and are summarized in Table 6. The daily power management is carried out according to the following time intervals:

0<time<0.4 h

Case 0: At the beginning of each day, case 0 is applied.

The MGCC requests to the MG operators the daily reference profiles and then they are stored in a data table. The maximum powers extracted/injected from/to the grid to/from the MG are established by equations (30) and (31), respectively. The maximum powers injected/extracted from/to the DC bus to/from the grid by the ILC are calculated by equations (32) and (33) respectively.

$$\left|\hat{P}_{Grid}\right| \leq P^{MAX}_{Grid-to-MG} \tag{30}$$

$$\hat{P}_{Grid} \leq P^{MAX}_{MG-to-Grid} \tag{31}$$

$$\hat{P}^{ILC}_{DC} \leq MIN\left(P^{ILC}_{rated}, \frac{P^{MAX}_{MG-to-Grid}}{\eta_{ILC}}\right) \tag{32}$$

$$\left|\hat{P}^{ILC}_{DC}\right| \leq MIN\left(P^{ILC}_{rated}, \frac{P^{MAX}_{Grid-to-MG}}{\eta_{ILC}}\right) \tag{33}$$

As it can be seen in Figure 10, the BESS works in charge mode during off-peak hours (TOU is off-peak), when kW·h is cheaper and when the PV power profile is enough to energize all the DC loads ($P^{Available}_{DC\_Profile} > 0$). The available power profile ($P^{Available}_{DC\_Profile}$) at the DC bus is given by Equation (34).

Table 6. Summary of the cases applied set by the MGCC.

	PV	BESS		DC Load	Output References
		Mode	Charging Procedure		
Case 0	Case 0 is applied at the beginning of each day. The MGCC performs the daily planning of the power dispatch at the MG. To perform this, it uses the data of the power profiles and TOU sent from the MG operator.				
Case 1	PV = Off	Charge mode	CC-CV based on Equation (46)	Load shedding funtionality	P_{ref}^{BESS}=Equation (46), SOC_{ref} = 100% $t_{ref} = t_{initial}$, Sw_{ref} = {0 or 1}
	Case 1 indicates that the power management profile predicted for the day has not been correctly fulfilled. This case is applied when there is not power available at the DC bus, the SOC is less than 90% or when the case 0 has failed. In this case, the MGCC complies with the power limit established by the MG operator, without taking into account the electricity tariff in the power management of the MG. The BESS will operate in charge mode, but won't be able to assure the DIN41773 charge procedure.				
Case 2	PV = Off	Charge mode	DIN41773	All Loads Connected	P_{ref}^{BESS} = Equation (38), SOC_{ref} = Equation (37) $t_{ref} = t_{initial}$, Sw_{ref} = {1, 1, 1, 1}
	Case 2 is applied when there is not PV generation, the SOC is less than 90% and the TOU is off-peak. The MGCC establishes the target SOC (SOC_{ref} = Equation (37)) at the time interval $t_{initial}$ and with a constant power to charge the batteries. In this case, the BESS can fulfill the DIN41773 charge procedure.				
Case 3	PV = On On MPPT	Charge mode	DIN41773	All Loads Connected	P_{ref}^{BESS}=Equation (36), SOC_{ref}= 100% $t_{ref} = t_{final} - t_{initial}$, Sw_{ref} = {1, 1, 1, 1}
	Case 3 is applied when the PV power is enough to energize all the DC loads, the SOC is less than 90% and the TOU is off-peak. The MGCC sets the value of SOC_{ref} at its maximum possible value (SOC_{ref} = 100%) at the time interval $t_{final} - t_{initial}$ with a constant power P_{ref}^{BESS} = Equation (36) to charge the batteries. In this case, the BESS can fulfill the DIN41773 charge procedure.				
Case 4	PV = On Off MPPT	Charge mode	CC-CV based on Equation (47)	All Loads Connected	P_{ref}^{BESS} = Equation (47), SOC_{ref} = 100% $t_{ref} = t_{final} - t_{initial}$, Sw_{ref} = {1, 1, 1, 1} $P_{Lim\_ref}^{PV}$ = Equation (43)

	In case 4 a surplus of energy is available from the PV generation and the SOC is less than 90%. The DC loads and the batteries cannot absorb the excess of power at the DC bus and the Maximum Power Point Tracking is disabled (Off-MPPT). Power is injected into the grid below the limit imposed by the MG operator. The MGCC sets the target SOC to 100% (SOC_{ref} = 100%) in the time interval $t_{final} - t_{initial}$ and the batteries are charged at a power P_{ref}^{BESS} according to Equation (47).				
Case 5	PV = Off	Discharge	-	All Loads Connected	P_{ref}^{BESS} = Equation (40), Sw_{ref} = {1, 1, 1, 1}
	Case 5 is applied when there is not PV generation, TOU is on-peak and SOC is greater than 90%. The BESS must supply power to the DC bus from the batteries. The discharge power of the batteries Equation (40) is determined to avoid a SOC lower than 35%.				
Case 6	PV = Off	Discharge	-	All Loads Connected	P_{ref}^{BESS} = Equation (41) Sw_{ref} = {1, 1, 1, 1}
	Case 6 is applied when there is not PV generation and the TOU is on-peak. This case prevents discharge the batteries to a SOC lower than SOC_{MIN}. The batteries are discharged with a maximum power P_{ref}^{BESS} given by Equation (41).				

When the value of $P_{DC\_Profile}^{Available}$ starts to be positive, the initial time is detected ($t_{initial}$). The final time (t_{final}) is detected once that $P_{DC\_Profile}^{Available}$ changes from positive to negative. With the time interval ($t_{initial}$ < time < t_{final}) the value of $P_{RES}^{Available}$ is calculated. $P_{RES}^{Available}$ is the available power from the RES for charging the batteries during the time interval ($t_{initial}$ < time < t_{final}), expressed by the Equation (35). P_{ref}^{BESS} is calculated from Equation (36) and the desired SOC (SOC_{ref}) which should be reached at $t_{initial}$ is calculated from Equation (37). When $P_{DC\_Profile}^{Available} < 0$ and the TOU is off-peak, the value of P_{ref}^{BESS} is calculated from Equation (38).

$$P_{DC\_Profile}^{Available} = P_{Profile}^{PV} - P_{DC\_Profile}^{Load} \quad (34)$$

$$P_{RES}^{Available} = \frac{1}{(t_{final} - t_{initial})} \cdot \int_{t_{initial}}^{t_{final}} P_{DC\_Profile}^{Available} \cdot dt \text{ where } P_{DC\_Profile}^{Available} > 0 \quad (35)$$

$$P_{ref}^{BESS} = MIN\left(P_{HB-rated}^{BESS}, P_{RES}^{Available}\right) \quad (36)$$

$$SOC_{ref} = SOC - \frac{P_{RES}^{Available} \cdot 100\% \cdot t_{ref} \cdot \eta_{Dis}}{C_T \cdot V_{Rated}^{Bat}} \text{ where } t_{ref} = (t_{final} - t_{initial}) \quad (37)$$

$$P_{ref}^{BESS} = MIN\left(P_{HB-rated}^{BESS}, \left|\hat{P}_{DC}^{ILC}\right| - P_{DC\_Profile}^{Load}\right) \quad (38)$$

If $P_{DC\_Profile}^{Available} < 0$ and the TOU is on-peak, the BESS must supply power to the DC bus from the batteries. The discharge power of the batteries for the time interval (t_{ref}) is calculated according to Equation (39). P_{Dis}^{BESS} determines the

maximum discharge power to avoid battery discharges leading to values of SOC lower than 35%. If $P_{Dis}^{BESS} > |P_{DC\_Profile}^{Available}|$, the P_{ref}^{BESS} is calculated by Equation (40); otherwise, it is calculated by Equation (41).

$$P_{Dis}^{BESS} = \left|\frac{(SOC_{MIN}-SOC)\cdot Q_{Rated}\cdot V_{Rated}^{Bat}}{100\%\cdot t_{ref}\cdot \eta_{Dis}}\right| \text{ where } t_{ref} = (24\ h - t_{final}) \quad (39)$$

$$P_{ref}^{BESS} = -MIN\left(P_{HB-rated}^{BESS}, \left|P_{RES}^{Available}\right|\right) \quad (40)$$

$$P_{ref}^{BESS} = -MIN(P_{HB-rated}^{BESS}, P_{Dis}^{BESS}) \quad (41)$$

0.4 h<time<t$_{initial}$

The MGCC begins to execute the strategic planning of case 0 and verifies its compliance. Thus, the MGCC calculates the power flow in the MG every second. The MGCC establishes the PV power limit ($P_{Lim\_ref}^{PV}$) by means of Equation (42). Note that in Figure 9, P_{Load}^{DC} stands for the power consumed by the DC loads. Sw_{ref} is a vector with binary variables {0, 1}, indicating which DC loads are connected {1} or disconnected {0}. P_{Load}^{DC} is calculated by Equation (43). Equation (44) stands for the available power at the DC bus ($P_{DC}^{Available}$) without taking into account the power absorbed from the main grid. $P_{DC\text{-}Total}^{Available}$ is the total available power at the DC bus and is given by Equation (45).

$$P_{Lim\_ref}^{PV} = \left|\hat{P}_{DC}^{ILC}\right| + P_{DC}^{Load} + P^{BESS} \quad (42)$$

$$P_{DC}^{Load} = V_{DC}\cdot \sum_{i=1}^{4} I_{DC}^{Load}(i)\cdot Sw(i)_{ref} \quad (43)$$

$$P_{DC}^{Available} = Po^{PV} - P_{DC}^{Load} \quad (44)$$

$$P_{DC-total}^{Available} = \left|\hat{P}_{DC}^{ILC}\right| + Po^{PV} - P_{DC}^{Load} \quad (45)$$

If SOC < SOC$_{MIN}$, the MGCC activates the fault flag and applies Case 1. Case 1 indicates that the power management profile predicted for the day has not been correctly fulfilled. In this case, if the reference profiles do not fit the power measurements, the MGCC will detect that the power generation predicted for the day is not achieved. In that case, if the SOC of the batteries is lower than 35%, the MGCC will establish that the power limit established by the MG operator is imported from the grid, no matter the value of the electricity tariff. If even in that situation the SOC tends to decrease below 35%, the MGCC will set the load shedding functionality. The BESS will operate in charge mode,

but will not be able to assure the DIN41773 charge procedure. The batteries are charged at a power according to Equation (46).

$$P_{ref}^{BESS} = MIN(P_{HB-rated}^{BESS}, P_{DC-total}^{Available}) \quad (46)$$

If SOC > SOC_{MIN} and the current time of the day is lower than $t_{initial}$, the MGCC applies case 2. Case 2 is applied at the hours of the day where there is not PV generation and the TOU is off-peak. The MGCC establishes the target SOC (SOC_{ref} = Equation (37)) at the time interval ($t_{ref} = t_{initial}$) and with a constant power (P_{ref}^{BESS} = Equation (38)) to charge the batteries. In this case, the BESS can fulfill the DIN41773 charge procedure.

$t_{initial} < time < t_{final}$

During this time interval the batteries will be charged only with the available power at the PV system ($P_{DC}^{Available}$). If $P_{DC}^{Available}$ is inside the range $P_{DC\_Profile}^{Available} \pm 10\%$, the MGCC applies case 3. The MGCC sets the value of SOC_{ref} at its maximum possible value (SOC_{ref} = 100%) at the time interval $t_{ref} = t_{final} - t_{initial}$ with a constant power P_{ref}^{BESS} = Equation (36) to charge the batteries. In this case, the BESS can fulfill the DIN41773 charge procedure.

If $P_{DC}^{Available}$ is outside the range $P_{DC\_Profile}^{Available} \pm 10\%$, it means that the MGCC cannot perform the initial planning. If $P_{DC}^{Available} > 0$, then case 4 is applied. On the contrary ($P_{DC}^{Available} < 0$), case 1 is applied.

In case 4, a surplus of energy is available from the PV generation. Power is injected to the grid below the limit imposed by the MG operator. The Maximum Power Point Tracking is off (Off-MPPT). The MGCC sets the target SOC to 100% (SOC_{ref} = 100%) in the time interval $t_{ref} = t_{final} - t_{initial}$ and the batteries are charged at a power P_{ref}^{BESS} according to Equation (47).

$t_{final} < time < 24\ h$

During this time interval the BESS should supply the necessary power to the DC bus, because the TOU is on-peak and the PV power is not enough to feed all the DC loads. If SOC < 90 %, the MGCC activates the fault flag and applies case 1.

Otherwise, if SOC >90 %, it means that MGCC can perform the initial planning.

If $P_{Dis}^{BESS} < |P_{DC}^{Available}|$, then case 5 is applied. In case 5 the batteries are discharged with a power P_{ref}^{BESS} given by Equation (40). In the opposite case, if $P_{Dis}^{BESS} > |P_{DC}^{Available}|$, case 6 is applied; because the necessary power at the DC bus is higher than the maximum available discharge power at the batteries. Case 6 avoids discharging the batteries to a SOC lower than SOC_{MIN}. The batteries are discharged with a maximum power P_{ref}^{BESS} given by Equation (41).

$$P_{ref}^{BESS} = MIN(P_{HB-rated}^{BESS}, P_{DC}^{Available}) \quad (47)$$

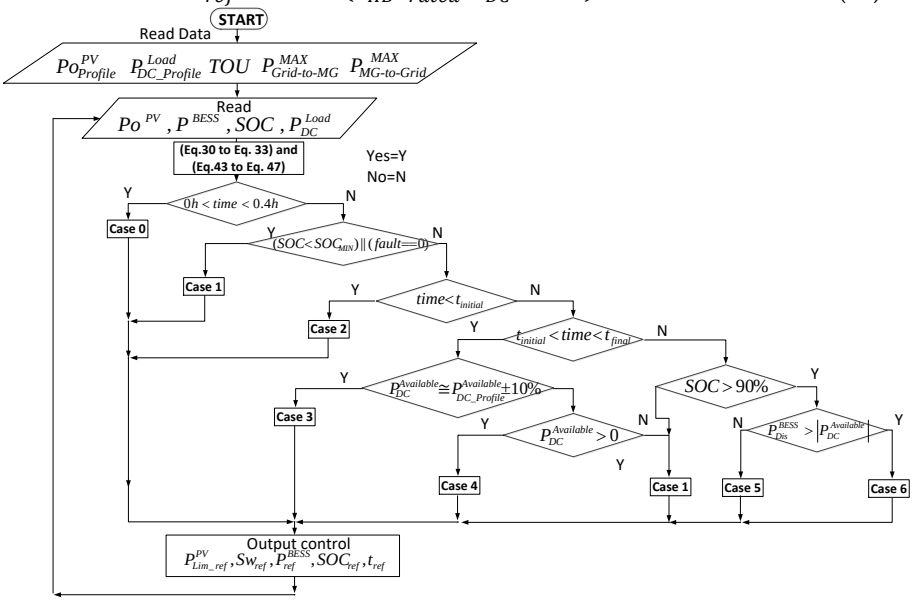

Figure 11. Power management algorithm implemented.

4.5. Experimental and simulation results

Figure 12a and b show a block diagram and a picture of the power converters operating in the experimental DC microgrid, respectively. The power converters specifications are shown in Table 7. First, several microgrid scenarios have been studied by means of the of the PSIM™ simulator [63]. After that, the proposed power management algorithm and the BESS have been tested in an experimental MG and compared with the simulated results. The proposed battery charging procedure shown in Section 3 has been verified by simulation #1 and by experiment #1. This procedure has been executed four times, each time with a different charging current: $I_{(Ch)}^{Bat}$ = 15 A, 12 A, 10 A and 5 A. The power management of the MG described in Section 4 has been validated by simulation #2 and by experiment #2. In experiment #3 the response of the MG to an abrupt change of the power flow between the MG and the main grid is studied. Finally, the communication delays between a measurement request from the MGCC and the response of the BESS are shown in experiment #4.

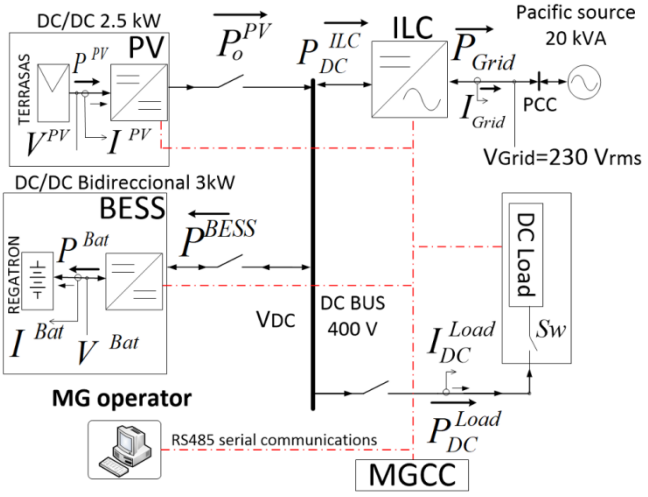

(a)

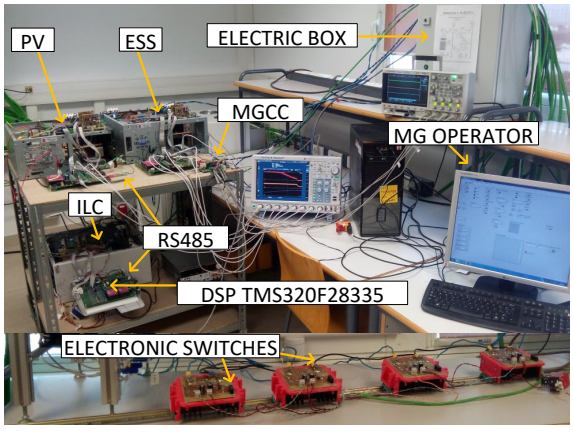

(b)

Figure 12. Experimental DC microgrid: (**a**) Block diagram of the experimental DC microgrid (**b**) Picture of the power converters operating in the experimental DC microgrid.

4.5.1. Simulation #1.

The DIN41773 compatible charging procedure has been verified by simulation #1, whose results are shown in Figure 13. It is worth pointing out that, in order to check the charging procedure with several values of the charge

current in a short simulation time, the value of Q_{Rated} was downscaled in simulations #1 and #2 to 2 A·h.

Table 7. Specifications of the power converters operating in the DC microgrid.

ILC	BESS	PV
P^{ILC}_{Rated} = 10 kW V_{Grid} = 230 V and F_{Grid} = 50 Hz V_{DC} = 400 V F_{sw_ILC} = 12.8 kHz	$P^{BESS}_{HB\_Rated}$ = 3 kW V^{Bat} = 216 V F_{sw_BESS} = 16 kHz T^{Bat} = 25 °C, Q_{Rated} = 2 A·h	P^{PV}_{Rated} = 2.5 kW V^{PV} = 306 V F_{sw_PV} = 16 kHz PV Panel: Atersa A-250P GSE

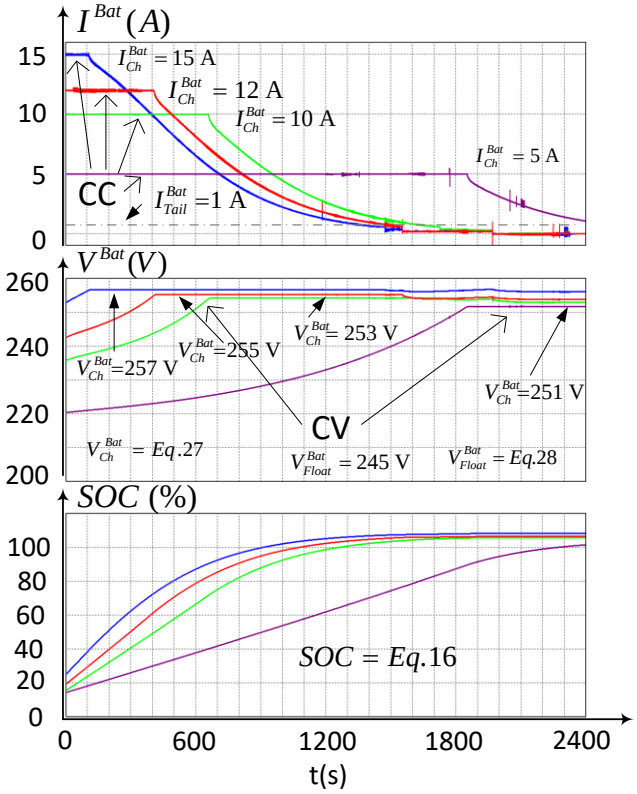

Figure 13. Simulation #1. Simulation waveforms of the charging procedure: I^{Bat}, V^{Bat} the SOC.

The batteries are initially charged at CC with several values of $I^{Bat}_{(Ch)}$ (15 A, 12 A, 10 A and 5 A) until a maximum charging voltage ($V^{Bat}_{(Ch)}$) is reached. When

$V_{(Ch)}^{Bat}$ is reached, the batteries are charged at CV at that value of $V_{(Ch)}^{Bat}$. The value of $V_{(Ch)}^{Bat}$ depends on the temperature and on the charging current value. $V_{(Ch)}^{Bat}$ is given by Equation (27). A value of T^{Bat} = 25 °C has been considered.

Finally, once the current absorbed by the batteries is lower than a pre-set tail current value (I_{tail}^{Bat} = 1 A), then the battery voltage is set at a constant floating voltage value (V_{Float}^{Bat}) that is given by Equation (28).

4.5.2. Simulation #2.

In order to check the proposed power management algorithm described in Section 4, different scenarios with a short simulation time have been analyzed. In order to avoid too long simulation times, the reference profiles were adjusted in this study to a whole equivalent 'daily' period of 2400 s, where 100 s corresponds to one hour of the day. The value of Q_{Rated} was downscaled for performing the tests #1 and #2 to 2 A·h. The reference profiles that were used to plan the power dispatch in the MG are shown in Table 8. Figure 14 shows the simulation waveforms of the power flow at the DC bus of the MG in one equivalent day. The scenarios under study are: (i) Different values of the TOU tariffs, (ii) variations of the available PV power and (iii) variations of the power consumed by the loads connected to the DC bus. Those variations can be observed in Figure 14, being labeled as TOU, P_o^{PV} and P_{Load}^{DC}, respectively. The evolution of the power flow ($P_{DC}^{Available}$, P_{DC}^{ILC}, P^{BESS}), the SOC and the batteries current (I^{Bat}), can be observed in the lower part of Figure 14.

The analysis has been performed according to the following time intervals:

Interval 1 (0 < time < 40 s)

At t = 0 s, it is assumed that the batteries have been discharged the previous day to SOC = 38%. During the duration of the time interval corresponding to case 0, the power dispatch in the MG is done. Depending on the reference profiles of Table 8, the MGCC detects the time intervals where the batteries will be charged only with the available PV power and when the TOU is off-peak. The time values are: $t_{initial}$ = 900 s, t_{final} = 1520 s.

Interval 2 (40 s < time < 900 s)

This time interval represents the hours of the night and the early hours of the day when the PV power is not enough to energize all the loads and the TOU is off-peak. The MGCC applies case 2. The MGCC sends to the BESS the target SOC, SOC_{ref} = 68% at t_{ref} = 900 s and the reference of the available power at the DC bus to charge the batteries, P_{ref}^{BESS} = Equation (38). However, the BESS only uses the power needed, P^{BESS} = 0.9 kW, to reach the target SOC, which is lower than the power available at the DC bus, $P_{ref}^{BESS} \cong$ 3 kW. In this case, the MGCC

orders the transfer of the power needed at the DC bus from the grid through the ILC, with a value below the limit imposed by Equation (33). At t = 700 s the value of the power imported from the grid by the ILC is: P_{DC}^{ILC} = −3 kW. Note that at this time interval P^{BESS} takes a constant value (0.9 kW). The BESS complies with the DIN41773 charging procedure.

Table 8. Reference profiles sent to the MGCC for the power dispatch planning in the MG.

Time(s)																	
0	500	600	700	800	900	1000	1100	1200	1300	1400	1500	1600	1700	1800	1900	2200	2300
$P_{Profile}^{PV}$ (kW)																	
0	0	0	0.05	0.5	1	2	2.5	2.5	2.5	2.5	2	1	0.5	0.3	0.1	0	0
$P_{DC\_Profile}^{Load}$ (kW)																	
0.2	0.2	0.6	2	2	1	0.5	0.5	0.5	0.5	1.2	1.8	2	2.5	2.5	3.2	3	2.8
TOU (€/kW·s)																	
0.08													0.16				
Power dispatch limits established by the electric company																	
$P_{Grid\text{-}to\text{-}MG}^{MAX}$ = 10 kW and $P_{MG-to-Grid}^{MAX}$ = 4 kW																	

Interval 3 (900 s < time < 1520 s)

This time interval represents the hours of the day when the PV power is enough to energize all the loads. The MGCC applies case 3. The MGCC sends to the BESS the target SOC, SOC_{ref} = 100%, at t_{ref} = 620 s, and the reference of the available power at the DC bus to charge the batteries calculated initially during case 0, P^{BESS} ≅ 1.56 kW (Equation (36)). In this case, the MGCC can export the excess power from the DC bus to the grid through the ILC. Note that the batteries have reached a value SOC = 97.2 % at t = 1520 s

Interval 4 (1520 s < time < 2400 s)

This time interval represents the hours of the day when the TOU is on-peak and the PV power is not enough to energize all the loads. Taking into account that the BESS is charged (SOC ≥ 80%), the MGCC transfers the needed power from the battery bank to the DC bus through the BESS. This interval is divided into three subintervals.

1520 s < time < 1800 s: The MGCC applies case 5. In this case, the MGCC sends to the BESS the power reference, P_{ref}^{BESS} = Equation (40) and the target SOC, SOC_{ref} = 35%, at t_{ref} = 880 s. The MGCC orders to import the minimum possible power from the grid.

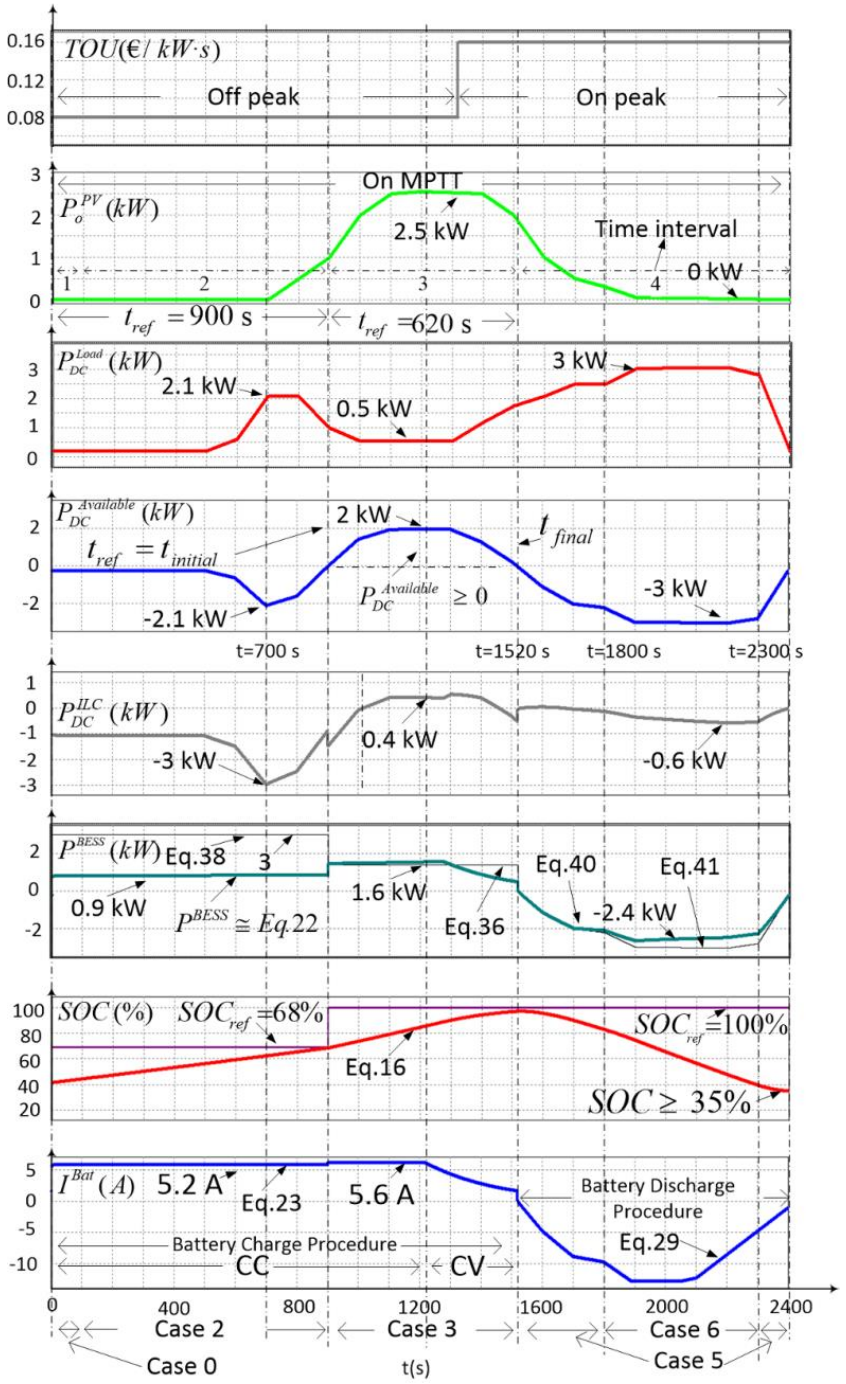

Figure 14. Simulation # 2: Simulation results of the power management in the MG. 100 seconds corresponds to 1 hour.

2000 s < time < 2300 s*:* The MGCC applies case 6. In this case, the needed power at the DC bus is higher than the maximum available discharge power at the batteries. The MGCC sends to the BESS the power reference, P_{ref}^{BESS} = Equation (41). The MGCC orders to import the minimum possible power from the grid.

2300 s < time < 2400 s: The MGCC applies case 5. In this case, the MGCC sends to the BESS the power reference, P_{ref}^{BESS} = Equation (40). The MGCC orders to import the minimum possible power from the grid.

4.5.3. Experiment #1.

A 3 kW bidirectional BESS a 2.5 kW PV system and a single-phase 10 kW ILC, have been built and connected to the experimental DC microgrid. Each power converter has its own TMS320F28335 DSP controller to perform its primary control and its serial RS485 communication system. The power converters specifications are the same as those shown in Table 7. All the experimental waveforms have been obtained by means of a Yokogawa DLM4038, 8-channel oscilloscope (Yokogawa Iberia S.A., Madrid, Spain). The batteries have been emulated by a 20 kW bidirectional DC source/battery emulator model TC.GSS-Bidirectional-DC-PSU from Regatron AG (Rorschach, Switzerland). The PV array has been emulated by means of a 10 kW PV array simulator TerraSAS ETS1000/10 from Ametek (San Diego, CA, USA). LabVIEW software (National Instruments Spain, Madrid, Spain) has been used for emulating the MG operator.

The DIN41773 compatible battery charging procedure has been verified in experiment #1. The procedure was tested with four different values of the charging current: $I_{(Ch)}^{Bat}$ = 15 A, 12 A, 10 A and 5 A, corresponding to Figure 15 a–d, respectively. As it can be observed from Figure 15, the reference value ($V_{(Ch)}^{Bat}$) of the voltage control loop is properly adjusted depending on the values of $I_{(Ch)}^{Bat}$ and of the temperature. $V_{(Ch)}^{Bat}$ is given by Equation (27). A value of T^{Bat} around 25 °C has been obtained during this experiment.

4.5.4. Experiment #2.

The evolution of the powers ($P_o{}^{PV}$, P^{BESS}, P_{Load}^{DC}, P_{DC}^{ILC}), currents (I^{Bat}, I^{PV}), SOC and voltages (V^{Bat}, V^{PV}) of the DC micrigrid can be observed in Figure 16. Initially, the MGCC applies case 0 and calculates the time intervals where the batteries will be only charged with the power available at the PV system, being the TOU is off-peak, yielding the values: $t_{initial}$ = 420 s, t_{final} = 1300 s. The analysis is performed according to the following time intervals:

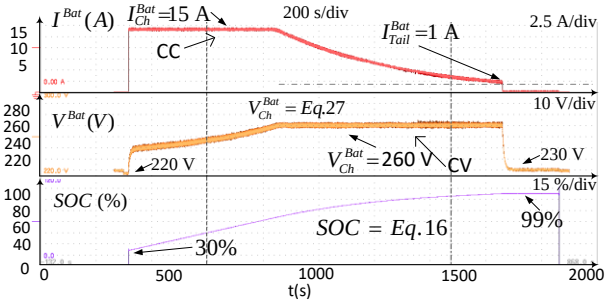

(a)

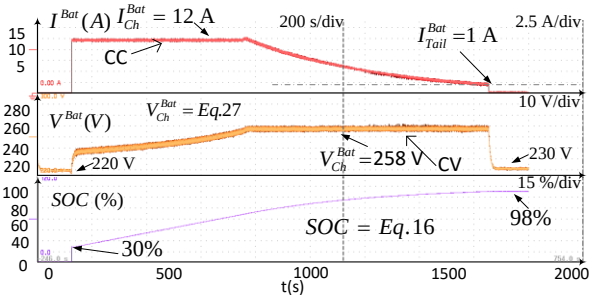

(b)

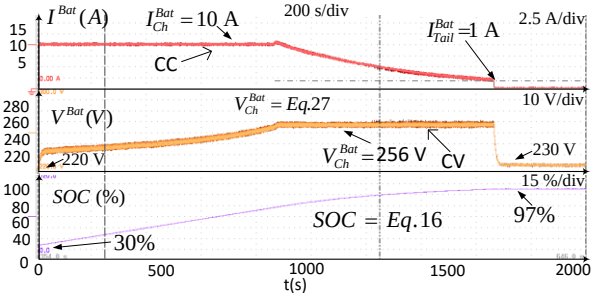

(c)

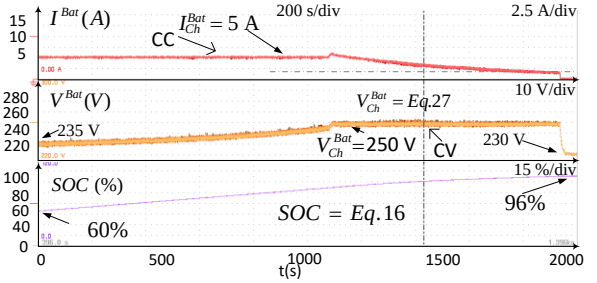

(d)

Figure 15. . Experiment #1. Waveforms of the implemented charging procedure for different values of the charging current: (a) $I_{(Ch)}^{Bat}$ = 15 A; (b) $I_{(Ch)}^{Bat}$ = 12 A; (c) $I_{(Ch)}^{Bat}$ = 10 A and (d) $I_{(Ch)}^{Bat}$ = 5 A.

Interval 1 (0 < time < 420 s)

During this time interval the PV power (P_{oPV}) is not enough to energize all the loads (P_{Load}^{DC}) and the TOU is off-peak. The MGCC applies case 2. The MGCC sends to the BESS the target SOC value, SOC_{ref} = 50%, during the time interval t_{ref} = 420 s. It also sends the reference of the available power at the DC bus to charge the batteries, P_{ref}^{BESS} = 3 kW. However, the BESS only uses the power needed (P^{BESS} = Equation (12) = 0.4 kW) to reach the target SOC, SOC_{ref} = 50 %. In this case, the MGCC orders to import the power needed at the DC bus from the grid through the ILC. At t = 100 s, the values are: $P_{oPV} > 0$, SOC = 40% and P_{DC}^{ILC} = −1.2 kW.

Interval 2 (420 s < time < 1300 s)

During this time interval, the PV power is enough to energize all the loads. At t = 420 s the MGCC applies case 3. The MGCC sends to the BESS the new power reference, P_{ref}^{BESS} = Equation (36) = 1.7 kW and the target SOC, $SOC_{ref} \cong 100$ %, during a time interval t_{ref} = 880 s. In this case, the MGCC only charges the batteries with the available power at the PV system and imports the minimum power from the grid through the ILC. At t = 420 s the power managed by the ILC is: $P_{DC}^{ILC} \cong -0.3$ kW. The DIN41773 charging procedure is verified in this time interval. At t = 800 s, the BESS changes from CC mode to CV mode with $V_{(Ch)}^{Bat}$ = 255 V. Note that the batteries have reached SOC = 94 % at t = 1300 s.

Interval 3 (1300 s < time < 2000 s)

At t = 1300 s the TOU changes from off-peak (0.08 €/kW·s) to on-peak (0.16 €/kW·s). This time interval represents the hours of the day when the TOU is on-peak and the PV power is not enough to energize all the loads. Taking into account that the BESS is charged, SOC ≥ 80% (at t = 1300 s, SOC = 94 %), the MGCC transfers the necessary power from the battery bank to the DC bus through the BESS. This interval is divided into two subintervals.

1300 s < time < 1780 s: The MGCC applies case 6. In this case, the MGCC calculates the maximum discharge power of the batteries (P_{Dis}^{BESS}) to discharge the batteries to a level which is higher than SOC_{MIN}, being $SOC_{ref} > 35\%$ at t_{ref} = 700 s. The MGCC sends the power reference to the BESS, P_{ref}^{BESS} = Equation (41), and orders to import the needed power from the grid.

1780 s < time < 2000 s: The MGCC applies case 5. In this case, the MGCC sends to the BESS the new power reference, P_{ref}^{BESS} = Equation (40), ordering to import the minimum possible power from the grid.

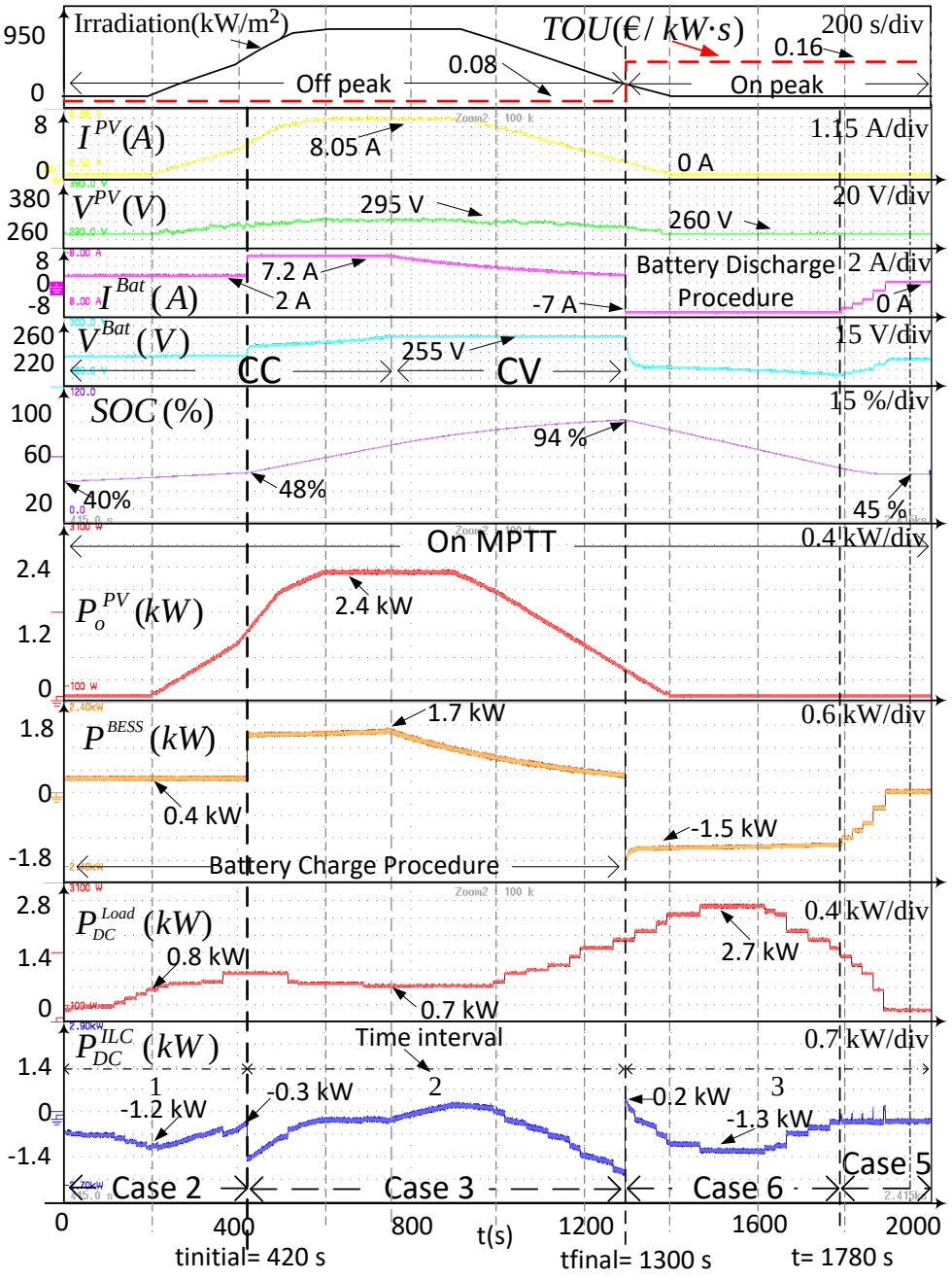

Figure 16. Experiment # 2. Experimental results of the power management in the MG.

4.5.5. Experiment #3.

The ILC regulates the voltage of the DC bus in grid connected mode, and performs the synchronization with the main grid. To verify the stability of the DC bus during heavy transients, an abrupt change from -0.8 kW to 1.9 kW (2.7 kW step at t=9.3 s) of the power flow from the DC bus to the main grid is forced. The experimental waveforms when the MG changes from exporting to importing power to/from the main grid are shown in Figure 17.

As it can be seen in ZOOM 1 of Figure 17, the DC bus voltage is stable and a small transient deviation occurs of ΔV_{DC} = 38 V, i.e., less of 10% of the DC bus voltage. A low distortion of I_{Grid} can be observed in the transition from exporting to importing power to/from the AC grid.

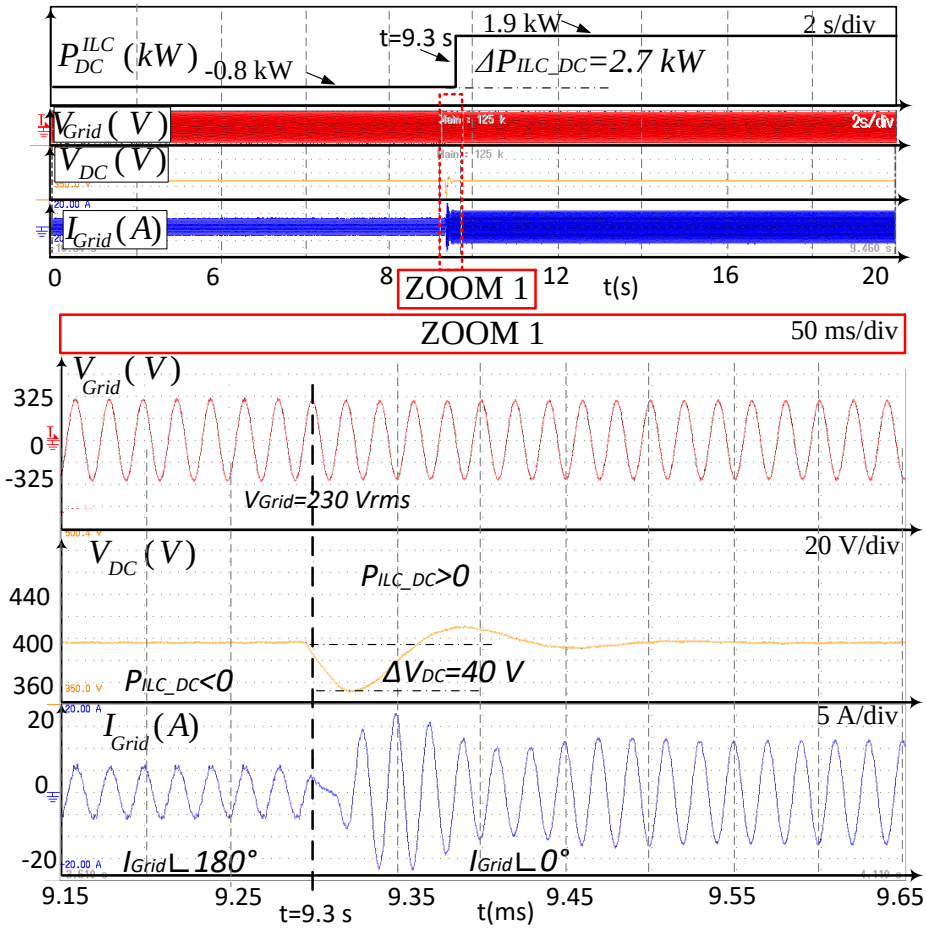

Figure 17. Experiment # 3. Experimental results of the abrupt change in power flow from the DC bus to the main grid.

4.5.6. Experiment #4.

In this work, RS485 serial communications are used with the MODBUS protocol. This protocol allows the exchange of information between the MGCC and the different devices connected to the MG with an adequate performance in MG. The implemented RS485 communications allow the calculation of the power values in several points of the microgrid quickly and accurately. The communications delay of the receiving (RX) and transmitting (TX) signals between the MGCC and the BESS can be observed in Figure 18. The RS485 communication bus baud rate is 9600 bps. The time difference between a MGCC request and the BESS response is 18 ms. The proposed power management algorithm is running every second in the microgrid under study, so that the communication delays are not critical.

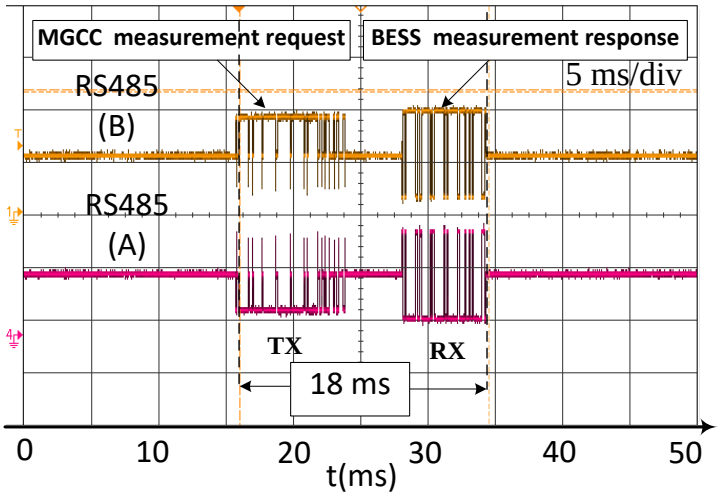

Figure 18. Experiment # 4. Communication delays between the MGCC and the BESS.

4.6. Conclusions

In this paper it has been shown the design and operation of a BESS for a grid-connected DC Microgrid with PV generation. The bidirectional power converter conforming the BESS has been modeled and verified according to any change of the battery charge/discharge currents, the SOC, the battery voltage and variations of the DC bus voltage. The BESS has a BMS that maximizes the battery life time, being compatible with a DIN41773 battery charging procedure and complying with the manufacturer specifications at the same time. The proposed procedure changes the charging parameters of the batteries depending on the MG states.

A MGCC has been used for the power management of the DC microgrid. The MGCC estimates the available power at the DC bus to charge the batteries and a target SOC in the batteries at different hours of the day. The MGCC daily plans the power dispatch in the MG and complies with two objectives: (i) to import the minimum possible power from the grid, and (ii) to charge the batteries during off-peak times and with the surplus of energy is available from the PV resources. These strategies allow for reducing the electricity bill.

The experimental and simulation results show that the implemented method allows for properly planning the power dispatch at the DC microgrid, fulfilling the battery charging procedure recommended by the manufacturer at the same time, expanding battery life.

Funding: This research was funded by the Spanish Ministry of Economy and Competitiveness (MINECO) and by the European Regional Development Fund (ERDF) under Grant ENE2015-64087-C2-2.

Acknowledgments: This work has been cofinanced by the Spanish Ministry of Economy and Competitiveness (MINECO) and by the European Regional Development Fund (ERDF) under Grant ENE2015-64087-C2-2.

Conflicts of Interest: The authors declare no conflict of interest.

4.7. Abbreviations

P_{o}^{PV}	Power supplied by the PV arrays seen from the DC bus
P_{DC}^{Load}	Overall power consumed by the DC loads
P_{Grid}	Power injected from the DC microgrid to the grid
P_{AC}^{ILC}	Power injected from the DC bus to the grid by the ILC, measured at the AC side of the ILC
P_{DC}^{ILC}	Power injected from the DC bus to the grid by the ILC, measured at the DC side of the ILC
P^{BESS}	Battery charge power seen from the DC bus
P^{Bat}	Battery charge power
$P_{DC}^{Available}$	Power available at the DC bus
I_{Grid}	RMS Current injected from the DC microgrid to the grid
V_{Grid}	RMS value of the grid voltage
V_{DC}	DC bus voltage
SOC	State of charge of the battery bank
I^{Bat}	Battery bank charge current
V^{Bat}	Battery bank voltage
I^{PV}	Current supplied by the PV array
I_{DC}^{Load}	Overall current consumed by the DC loads
$V_{(Ch)}^{Bat}$	Reference of the charging voltage
$I_{(Ch)}^{Bat}$	Reference of the charging current
$P_{Grid\text{-}to\text{-}MG}^{MAX}$	Maximum power that can be extracted from the main grid to the MG
$P_{MG\text{-}to\text{-}Grid}^{MAX}$	Maximum power that can be injected from the MG to the main grid

TOU	Time of use of electricity
$P_{Profile}^{PV}$	Reference profiles of PV generation
$P_{DC\_Profile}^{Load}$	Reference profiles of power consumed by the loads
$P_{DC\_Profile}^{Available}$	The available power profile at the DC bus
SOC_{ref}	Desired SOC in the batteries
P_{ref}^{BESS}	Reference power for charging/discharging the batteries from/to DC bus
t_{ref}	Time interval in which BESS must reach the target SOC with P_{ref}^{BESS}
V_{DC_ref}	Reference of the DC bus voltage
$P_{Lim\_ref}^{PV}$	Maximum power that should be extracted from the PV sources
Sw_{ref}	Reference of the DC load switches (load 1 to 4)

4.8. References

1. Dragičević, T.; Lu, X.; Vasquez, J.C.; Guerrero, J.M. DC Microgrids—Part I: A Review of Control Strategies and Stabilization Techniques. IEEE Trans. Power Electron. 2016, 31, 4876–4891.
2. Baek, J.; Choi, W.; Chae, S. Distributed Control Strategy for Autonomous Operation of Hybrid AC/DC Microgrid. Energies 2017, 10, 373.
3. Rahimi-Eichi, H.; Ojha, U.; Baronti, F.; Chow, M.Y. Battery Management System: An Overview of Its Application in the Smart Grid and Electric Vehicles. IEEE Ind. Electron. Mag. 2013, 7, 4–16.
4. Sujitha, N.; Krithiga, S. RES based EV battery charging system: A review. Renew. Sustain. Energy Rev. 2017, 75, 978–988.
5. Renewables 2017 Global Status Report. Available online: http://www.ren21.net/wp-content/uploads/2017/06/17-8399_GSR_2017_Full_Report_0621_Opt.pdf (accessed on 5 July 2018).
6. Chen, H.; Cong, T.N.; Yang, W.; Tan, C.; Li, Y.; Ding, Y. Progress in electrical energy storage system: A critical review. Prog. Nat. Sci. 2009, 19, 291–312.
7. May, G.J.; Davidson, A.; Monahov, B. Lead batteries for utility energy storage: A review. J. Energy Storage 2018, 15, 145–157.
8. Joseph, A.; Shahidehpour, M. Battery storage systems in electric power systems. In Proceedings of the 2006 IEEE Power Engineering Society General Meeting, Montreal, QC, Canada, 18–22 June 2006; p. 8.
9. IRENA. Available online: http://www.irena.org/eventdocs/Battery%20storage%20June%201%202017%20MICHAEL%20TAYLOR%20PDF%20version.pdf (accessed on 3 February 2018).
10. Hussein, A.A.; Fardoun, A.A. Design considerations and performance evaluation of outdoor PV battery chargers. Renew. Energy 2015, 82, 85–91.
11. Xing, Y.; Ma, E.W.M.; Tsui, K.L.; Pecht, M. Battery Management Systems in Electric and Hybrid Vehicles. Energies 2011, 4, 1840–1857.
12. Wu, D.; Tang, F.; Dragicevic, T.; Guerrero, J.M.; Vasquez, J.C. Coordinated Control Based on Bus-Signaling and Virtual Inertia for Islanded DC Microgrids. IEEE Trans. Smart Grid 2015, 6, 2627–2638.
13. Dou, C.; Zhang, Z.; Yue, D.; Zheng, Y. MAS-Based Hierarchical Distributed Coordinate Control Strategy of Virtual Power Source Voltage in Low-Voltage

Microgrid. IEEE Access 2017, 5, 11381–11390.
14. Bracale, A.; Caramia, P.; Carpinelli, G.; Mancini, E.; Mottola, F. Optimal control strategy of a DC micro grid. Int. J. Electr. Power Energy Syst. 2015, 67, 25–38.
15. Yue, J.; Hu, Z.; Li, C.; Vasquez, J.C.; Guerrero, J.M. Economic Power Schedule and Transactive Energy through an Intelligent Centralized Energy Management System for a DC Residential Distribution System. Energies 2017, 10, 916.
16. Gao, L.; Liu, Y.; Ren, H.; Guerrero, J.M. A DC Microgrid Coordinated Control Strategy Based on Integrator Current-Sharing. Energies 2017, 10, 1116.
17. Unamuno, E.; Barrena, J.A. Hybrid AC/DC microgrids—Part II: Review and classification of control strategies. Renew. Sustain. Energy Rev. 2015, 52, 1123–1134.
18. Zia, M.F.; Elbouchikhi, E.; Benbouzid, M. Microgrids energy management systems: A critical review on methods, solutions, and prospects. Appl. Energy 2018, 222, 1033–1055.
19. Feng, X.; Shekhar, A.; Yang, F.E.; Hebner, R.; Bauer, P. Comparison of Hierarchical Control and Distributed Control for Microgrid. Electr. Power Compon. Syst. 2017, 45, 1043–1056.
20. De Brabandere, K.; Bolsens, B.; van den Keybus, J.; Woyte, A.; Driesen, J.; Belmans, R. A Voltage and Frequency Droop Control Method for Parallel Inverters. IEEE Trans. Power Electron. 2007, 22, 1107–1115.
21. Kaur, A.; Kaushal, J.; Basak, P. A review on microgrid central controller. Renew. Sustain. Energy Rev. 2016, 55, 338–345.
22. Marzal, S.; González-Medina, R.; Salas-Puente, R.; Figueres, E.; Garcerá, G. A Novel Locality Algorithm and Peer-to-Peer Communication Infrastructure for Optimizing Network Performance in Smart Microgrids. Energies 2017, 10, 1275.
23. Gamarra, C.; Guerrero, J.M. Computational optimization techniques applied to microgrids planning: A review. Renew. Sustain. Energy Rev. 2015, 48, 413–424.
24. Li, W.; Logenthiran, T.; Woo, W.L.; Phan, V.T.; Srinivasan, D. Implementation of demand side management of a smart home using multi-agent system. In Proceedings of the 2016 IEEE Congress on Evolutionary Computation (CEC), Vancouver, BC, Canada, 24–29 July 2016; pp. 2028–2035.
25. Joo, I.Y.; Choi, D.H. Optimal household appliance scheduling considering consumer's electricity bill target. IEEE Trans. Consum. Electron. 2017, 63, 19–27.
26. Roozbehani, M.; Dahleh, M.A.; Mitter, S.K. Volatility of power grids under real-time pricing. IEEE Trans. Power Syst. 2012, 27, 1926–1940.
27. Carpinelli, G.; Khormali, S.; Mottola, F.; Proto, D. Optimal operation of electrical energy storage systems for industrial applications. In Proceedings of the 2013 IEEE Power & Energy Society General Meeting, Vancouver, BC, Canada, 21–25 July 2013; pp. 1–5.
28. Erol-Kantarci, M.; Hussein, T.M. Prediction-based charging of PHEVs from the smart grid with dynamic pricing. In Proceedings of the IEEE Local Computer Network Conference, Denver, CO, USA, 10–14 October 2010; pp. 1032–1039.
29. Hooppecke. Operating Instructions Valve Regulated Stationary Lead-Acid Batteries. Available online: http://www.hoppecke-us.com/tl_files/hoppecke/Documents/HO-US/Operating_Instructions_sealed_stationary_lead_acid_batteries_en1111.pdf (accessed on 13 October 2017).

30. TAB Batteries. Available online: http://www.tabspain.com/wp-content/uploads/informacion -tecnica/renovables/curvas-y-tablas/din-41773-y-din-41774-para-baterias-pzs.pdf (accessed on 13 October 2017).

31. Lu, L.; Han, X.; Li, J.; Hua, J.; Ouyang, M. A review on the key issues for lithium-ion battery management in electric vehicles. J. Power Sources 2013, 226, 272–288.

32. Hussein, A.A.; Batarseh, I. A Review of Charging Algorithms for Nickel and Lithium Battery Chargers. IEEE Trans. Veh. Technol. 2011, 60, 830–838.

33. Shen, W.; Vo, T.T.; Kapoor, A. Charging algorithms of lithium-ion batteries: An overview. In Proceedings of the 2012 7th IEEE Conference on Industrial Electronics and Applications (ICIEA), Singapore, 18–20 July 2012; pp. 1567–1572.

34. Hesse, H.C.; Schimpe, M.; Kucevic, D.; Jossen, A. Lithium-Ion Battery Storage for the Grid—A Review of Stationary Battery Storage System Design Tailored for Applications in Modern Power Grids. Energies 2017, 10, 2107.

35. Analog Devices. Available online: http://www.analog.com/media/en/technical-documentation/technical-articles/A-Closer-Look-at-State-Of-Charge-and-State-Health-Estimation-Techniques-....pdf (accessed on 1 February 2018).

36. Fathoni, G.; Widayat, S.A.; Topan, P.A.; Jalil, A.; Cahyadi, A.I.; Wahyunggoro, O. Comparison of State-of-Charge (SOC) estimation performance based on three popular methods: Coulomb counting, open circuit voltage, and Kalman filter. In Proceedings of the 2017 2nd International Conference on Automation, Cognitive Science, Optics, Micro Electro--Mechanical System, and Information Technology (ICACOMIT), Jakarta, Indonesia, 23–24 October 2017; pp. 70–74.

37. Lyu, C.; Cong, W.; Liu, H.; Zhang, L. A novel parameters acquisition method based on electrochemical impedance spectroscopy mathematical model in lithium ion cell. In Proceedings of the 2017 Prognostics and System Health Management Conference (PHM-Harbin), Harbin, China, 9–12 July 2017; pp. 1–8.

38. Hu, X.; Li, S.E.; Yang, Y. Advanced Machine Learning Approach for Lithium-Ion Battery State Estimation in Electric Vehicles. IEEE Trans. Transp. Electrification 2016, 2, 140–149.

39. Piller, S.; Perrin, M.; Jossen, A. Methods for state-of-charge determination and their applications. J. Power Sources 2001, 96, 113–120.

40. Kim, D.; Goh, T.; Park, M.; Kim, S.W. Fuzzy Sliding Mode Observer with Grey Prediction for the Estimation of the State-of-Charge of a Lithium-Ion Battery. Energies 2015, 8, 12409–12428.

41. Tian, Y.; Li, D.; Tian, J.; Xia, B. State of charge estimation of lithium-ion batteries using an optimal adaptive gain nonlinear observer. Electrochim. Acta 2017, 225, 225–234.

42. Rivera-Barrera, J.P.; Muñoz-Galeano, N.; Sarmiento-Maldonado, H.O. SoC Estimation for Lithium-ion Batteries: Review and Future Challenges. Electronics 2017, 6, 102.

43. Kozlowski, J.D. Electrochemical Cell Prognostics Using Online Impedance Measurements and Model-Based Data Fusion Techniques. In Proceedings of the IEEE Aerospace Conference, Big Sky, MT, USA, 8–15 March 2003; Volume 7, pp. 3257–3270.

44. Xiong, R.; Cao, J.; Yu, Q.; He, H.; Sun, F. Critical Review on the Battery State of

Charge Estimation Methods for Electric Vehicles. IEEE Access 2018, 6, 1832–1843.
45. Lin, C.H.; Wang, C.-M.; Lin, W.-J. A SOC-based intelligent charger with multi-charging mode. In Proceedings of the 2015 IEEE 2nd International Future Energy Electronics Conference (IFEEC), Taipei, Taiwan, 1-4 November 2015; pp. 1–6.
46. Oliveira, T.R.; Gonçalves Silva, W.W.A.; Donoso-Garcia, P.F. Distributed Secondary Level Control for Energy Storage Management in DC Microgrids. IEEE Trans. Smart Grid 2017, 8, 2597–2607.
47. Velho, R.; Beirão, M.; Calado, M.R.; Pombo, J.; Fermeiro, J.; Mariano, S. Management System for Large Li-Ion Battery Packs with a New Adaptive Multistage Charging Method. Energies 2017, 10, 605.
48. Xue, F.; Ling, Z.; Yang, Y.; Miao, X. Design and Implementation of Novel Smart Battery Management System for FPGA Based Portable Electronic Devices. Energies 2017, 10, 264.
49. Doan, V.T.; Vu, V.B.; Vu, H.N.; Tran, D.H.; Choi, W. Intelligent charger with online battery diagnosis function. In Proceedings of the 2015 9th International Conference on Power Electronics and ECCE Asia (ICPE-ECCE Asia), Seoul, South Korea, 1–5 June 2015; pp. 1644–1649.
50. Diaz, J.; Martin-Ramos, J.A.; Pernia, A.M.; Nuno, F.; Linera, F.F. Intelligent and universal fast charger for Ni-Cd and Ni-MH batteries in portable applications. IEEE Trans. Ind. Electron. 2004, 51, 857–863.
51. Mundra, T.S.; Kumar, A. An Innovative Battery Charger for Safe Charging of NiMH/NiCd Batteries. IEEE Trans. Consum. Electron. 2007, 53, 1044–1052.
52. Hu, X.; Martinez, C.M.; Yang, Y. Charging, Power management, and battery degradation mitigation in plug-in hybrid electric vehicles: A unified cost-optimal approach. Mech. Syst. Signal Process. 2017, 87, 4–16.
53. Yong, S.O.; Rahim, N.A. Development of on-off duty cycle control with zero computational algorithm for CC-CV Li ion battery charger. In Proceedings of the 2013 IEEE Conference on Clean Energy and Technology (CEAT), Lankgkawi, Malaysia, 18–20 November 2013; pp. 422–426.
54. Salas-Puente, R.; Marzal, S.; González-Medina, R.; Figueres, E.; Garcera, G. Experimental Study of a Centralized Control Strategy of a DC Microgrid Working in Grid Connected Mode. Energies 2017, 10, 1627.
55. Monteiro, V.; Ferreira, J.C.; Melendez, A.A.; Couto, C.; Afonso, J.L. Experimental Validation of a Novel Architecture Based on a Dual-Stage Converter for Off-Board Fast Battery Chargers of Electric Vehicles. IEEE Trans. Veh. Technol. 2017, 67, 1000–1011.
56. Bhatt, M.; Hurley, W.G.; Wolfle, W.H. A new approach to intermittent charging of valve-regulated lead-acid batteries in standby applications. IEEE Trans. Ind. Electron. 2005, 52, 1337–1342.
57. Hussein, A.A.H.; Pepper, M.; Harb, A.; Batarseh, I. An efficient solar charging algorithm for different battery chemistries. In Proceedings of the 2009 IEEE Vehicle Power and Propulsion Conference, Dearborn, MI, USA, 7–10 September, 2009; pp. 188–193.
58. Gallardo-Lozano, J.; Milanés-Montero, M.I.; Guerrero-Martínez, M.A.; Romero-Cadaval, E. Electric vehicle battery charger for smart grids. Electr. Power Syst. Res.

2012, 90, 18–29.
59. López, J.; Seleme, S.I.; Donoso, P.F.; Morais, L.M.F.; Cortizo, P.C.; Severo, M.A. Digital control strategy for a buck converter operating as a battery charger for stand-alone photovoltaic systems. Sol. Energy 2016, 140, 171–187.
60. Dragičević, T.; Guerrero, J.M.; Vasquez, J.C.; Škrlec, D. Supervisory Control of an Adaptive-Droop Regulated DC Microgrid with Battery Management Capability. IEEE Trans. Power Electron. 2014, 29, 695–706.
61. Chen, M.; Rincon-Mora, G.A. Accurate electrical battery model capable of predicting runtime and I-V performance. IEEE Trans. Energy Convers. 2006, 21, 504–511.
62. Support, T. Installation, Commissioning and Operation Handbook for Gel-Vrla-Batteries. 2003. Available online: http://www.sonnenschein.org/PDF%20files/GelHandbookPart2.pdf (accessed on 13 October 2017).
63. PSIM10.0; PowerSim: Rockville, Maryland, MD, USA, 2016

5

5. ANÁLISIS DE LOS RESULTADOS

En esta sección, se presenta el análisis de los resultados obtenidos en las tres publicaciones de los capítulos 2, 3 y 4. Se estudian las ventajas y desventajas de los esquemas de control y algoritmos propuestos. En las dos primeras publicaciones I y II se desarrollaron estrategias y estructuras de control preliminares, que dieron paso a la solución final presentada en la publicación III. Adicionalmente, para complementar este capítulo se ha incluido nuevos resultados relevantes que no se mostraron en las publicaciones debido a limitaciones de espacio.

5.1. Herramientas

Los convertidores electrónicos de potencia implementados en esta tesis se diseñaron utilizando principalmente dos herramientas de software: Matlab® [125] y PSIM® [126]. Matlab® fue utilizado para modelar los convertidores y diseñar los lazos de control, mientras que para simular todas sus etapas de potencia y control se utilizó el PSIM®. Este último permite además de simular el comportamiento de la microrred, la implementación de los algoritmos en código C de manera similar a como se haría en un procesador digital.

El software LabView® [127] se utilizó para: monitorizar la microrred, emular el operador de la red, ejecutar la secuencia de inicialización/detención de los convertidores de la microrred y supervisar el flujo de potencia en la microrred.

5.1.1. Equipos de laboratorio

Durante la realización de esta tesis se utilizó un osciloscopio de 8 canales, Yokogawa DLM4038, y otro de cuatro canales Agilent DSO-X 2004A para la obtención de las formas de onda experimentales. El sistema de almacenamiento de energía mediante baterías fue emulado mediante una fuente bidireccional de DC de 20 kW Regatron TC.GSS-Bidirectional-DC-PSU, con software de emulación de baterías. El generador fotovoltaico se emuló mediante un simulador de paneles fotovoltaicos de 10 kW de Ametek, el TerraSAS ETS1000/10. La red pública se emuló mediante la fuente de AC de 12 kW, Pacific Power AMX-360. Cada convertidor ha sido conectado a su correspondiente caja de distribución eléctrica, lo que permitió la conexión y desconexión de los convertidores de potencia y de los equipos de laboratorio a los buses de DC y de AC.

A continuación se enumeran los equipos utilizados y se presentan sus características más relevantes.

5.1.1.1. Equipos de medición

- Osciloscopio YOKOGAWA de ocho canales, modelo: DLM4038 con ancho de banda de 350 MHz (2.5 GSa/s)
- Osciloscopio Agilent de cuatro canales, modelo: DSO-X 2004A, con ancho de banda de 70 MHz (2 GSa/s)
- Analizador de Potencia Fluke, modelo 43B, con ancho de banda desde DC a 3.5 kHz y rango de medida de ± 1200 V

- Analizador de respuesta en frecuencia, modelo: NF FRA5097, con ancho de banda desde 0.1 mHz a 15 MHz y rango de medida de 140 dB.

- Cámara térmica Fluke, modelo: Ti25 IR *FUSION TECHNOLOGY THERMAL IMAGER*

- Sonda diferencial de alta tensión Tektronicx, modelo: p5200. Rango de tensión ±130 V / ± 1300 V.

- Sonda de corriente aislada, modelo: LEM PR30, con ancho de banda desde DC a 100 kHz y rango de medida de ± 20 A_{RMS}/± 20 A_{DC}

- Pinza Fluke amperimétrica de AC de alta seguridad, modelo: i400S AC *current clamp* y rango de medida de ± 40 A_{RMS} a ± 400 A_{RMS}

- Voltimetro Fluke, modelo: 175 *True rms*, con ancho de banda desde DC a 100 kHz y rango de medida (± 1000 V / ± 10 A)

5.1.1.2. Equipos de potencia

- Fuente de AC de 12 kW, Pacific Power, modelo: AMX-360, de tipo monofásica/trifásica con rango de tensión/frecuencia (0 V – 250 Vrms/20 Hz -5 kHz)

- Fuente de DC de 32 kW, AMREL, modelo: SPS800-40 con rango de tensión desde 0 V a 800 V

- Fuente DC/DC bidireccional de 20 kW, Regatron, Emulador de baterías, modelo: TC.GSS-Bidirectional-DC-PSU con rango de 0 V a 600 V / ± 40 A

- Fuente de DC de 10 kW, Amtek, emulador de paneles fotovoltaicos, modelo: TerraSAS ETS1000/10 con rango de tensión desde 0 V a 1000 V

- Carga Electrónica de DC de 5 kW, Chroma, modelo: 63205A-1200-200 con tensión/corriente máxima de 1200 V/ 200 A

- Cargas resistivas no-inductivas de diferentes valores

5.1.2. Descripción de la microrred

La presente tesis doctoral se ha desarrollado en la microrred experimental del Grupo de Sistemas Electrónicos Industriales del Departamento de Ingeniería Electrónica de la UPV, que se muestra en la Figura 5.1.

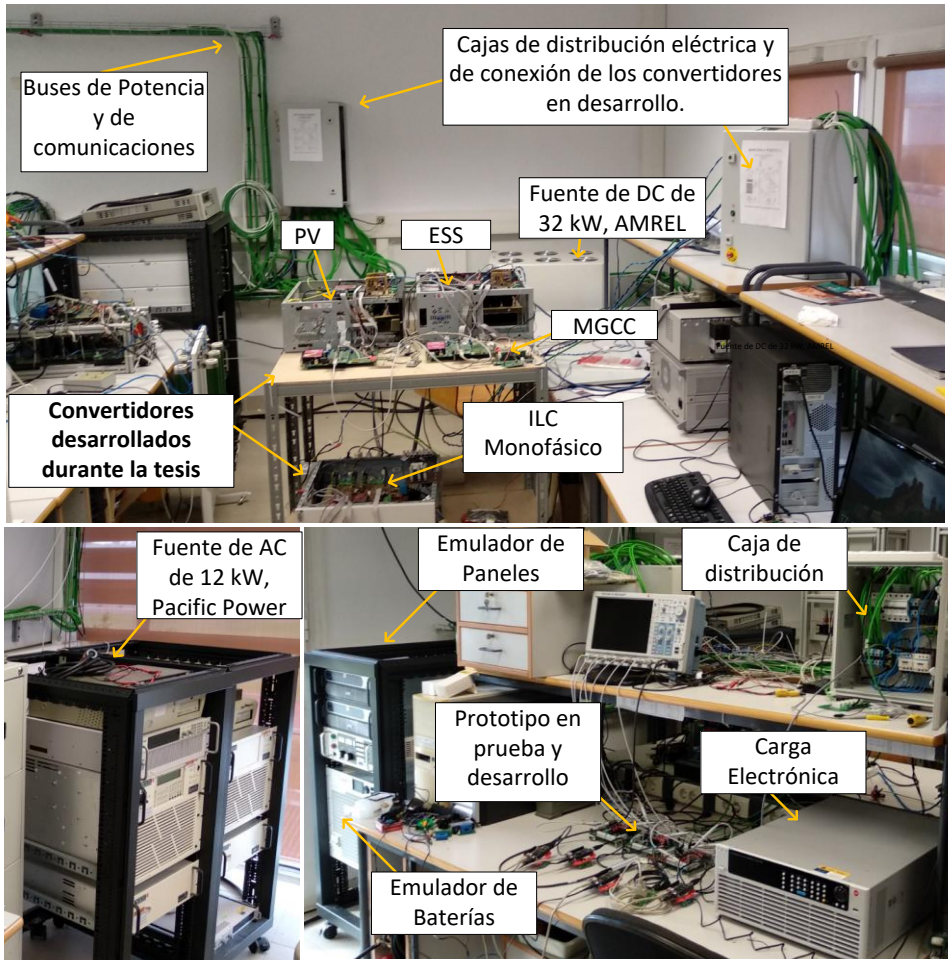

Figura 5.1. Fotografía de la microrred experimental del Grupo de Sistemas Electrónicos Industriales del Departamento de Ingeniería Electrónica de la UPV.

La Figura 5.2 muestra el esquema eléctrico de la microrred AC/DC híbrida implementada. La microrred se basa en un bus de DC y un bus de AC, este último conectado al punto de conexión común de la red pública de distribución mediante un interruptor estático. La interconexión entre los buses de DC y AC es realizada por un inversor de interconexión (ILC) monofásico de 10 kW con

topología en puente completo, lo que permite un flujo de potencia bidireccional. En el modo conectado a red, el ILC funciona como una fuente de corriente que inyecta potencia al bus de AC de manera sincronizada y regula la tensión en el bus de DC. Cuando la red pública es monofásica, el voltaje nominal del bus de DC es V_{DC} = 400 V ± 20 V, la tensión de la red vale V_{Grid} = 230 V_{rms} y su frecuencia es F_{Grid} = 50 Hz ± 1. Dos convertidores electrónicos de potencia, diseñados y construidos por el autor de esta tesis doctoral, están conectados al bus de DC de la microrred: el primero es un convertidor bidireccional de DC/DC con topología semi-puente de 3 kW conectado a las baterías y el segundo un convertidor de DC/DC de 2.5 kW con topología Boost conectado a un generador fotovoltaico. La tensión del banco de baterías (V_{Bat}) del sistema de almacenamiento puede variar de 194 V a 260 V, mientras que el voltaje en los paneles fotovoltaicos (V_{PV}) varía de 300 V a 370 V. De igual forma, se construyeron cuatro interruptores electrónicos (S_{w1} a S_{w4}) que conectan cuatro cargas en el bus de DC, de entre 650 W a 800 W cada una. Todos los dispositivos de la microrred están controlados por el controlador central. Es importante destacar que los controladores primarios de cada convertidor están diseñados para satisfacer las demandas de la microrred, manteniendo la estabilidad en la tensión del bus de DC, el banco de baterías y los paneles fotovoltaicos. Cada convertidor de potencia ejecuta sus controladores primarios internos en un DSP propio del tipo TMS320F28335 de Texas Instruments. Se ha implementado un bus de comunicación serie RS485, que permite un intercambio de información entre todos los dispositivos conectados a la microrred y la monitorización de los mismos mediante el software LabVIEW de National Instruments. En la Figura 5.3 se muestra una fotografía de los diferentes componentes de la microrred AC/DC híbrida experimental desarrollada en el laboratorio, correspondiente al esquema de la Figura 5.2.

5.1.3. Descripción general del diseño de los convertidores electrónicos de potencia de la microrred

Uno de los objetivos de este trabajo es el desarrollo e implementación de los convertidores de potencia de la microrred AC/DC híbrida para la validación realista de la gestión de potencia planteada. Durante la tesis se diseñaron e implementaron tres convertidores de potencia, los modos de funcionamiento de cada uno de ellos se observan en las Figuras 5.2b,c y d correspondientes a el PV, el ESS y el ILC, respectivamente. En la tabla 5.1, se muestra las especificaciones de los convertidores de potencia de la microrred. Algunos detalles del diseño de estos convertidores son reportados en la publicación II.

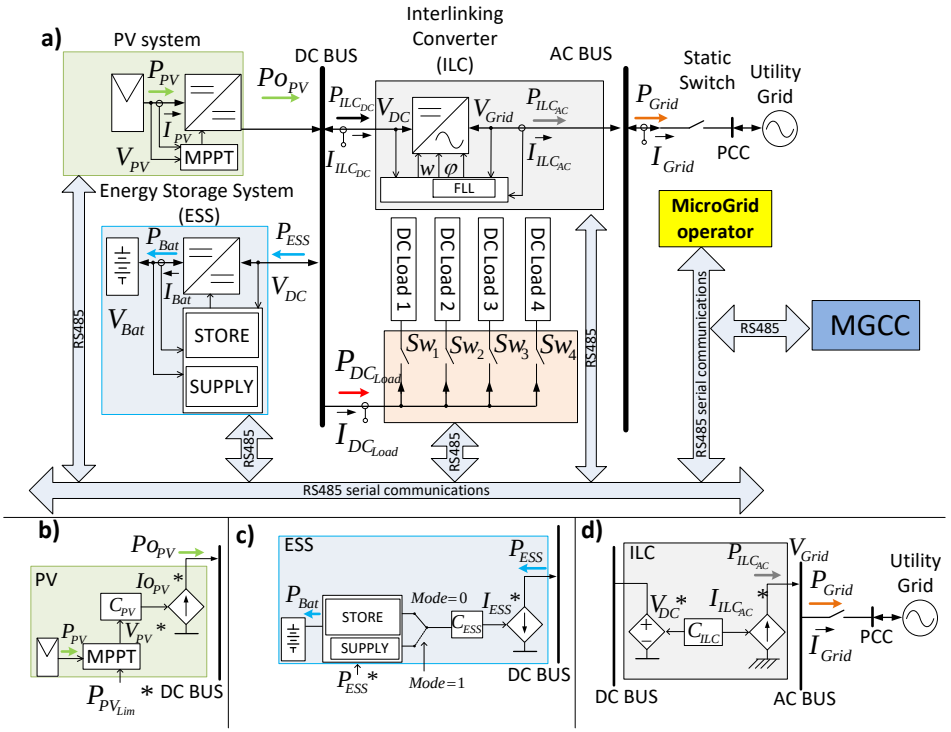

Figura 5.2. Esquemático de la microrred experimental: (a) Microrred AC/DC híbrida estudiada, (b) Sistema fotovoltaico, (c) Sistema de almacenamiento en baterías, (d) Convertidor de interconexión de los buses de AC y DC.

En el circuito electrónico de cada uno de los convertidores de potencia se introduce un tiempo muerto en los disparos y una protección contra falsos disparos de rama, que asegura que dos IGBT de la misma rama no se activen simultáneamente. Adicionalmente, tienen un circuito de detección de fallo, que envía señales al DSP mediante un pin especial de detección de interrupción, el cual detiene los disparos por fallo del sistema. Los *drivers* de los IGBT, son conectados de forma individual con tarjetas diseñadas para tal fin. Cabe mencionar que en su diseño y fabricación se tomaron en cuenta criterios de ruido electromagnético, ya que al manejar corrientes elevadas, estas se acoplan magnéticamente a las líneas de medición, protección y control. Por ello, se tuvo especial cuidado en el trazado de las pistas, sus caminos de retorno, apantallado de cables, aislamiento de fuentes de alimentación, filtros y planos de masa.

Se utilizaron sensores LEM de efecto Hall [128] en el sistema de medición de tensión y corriente. Estos son transductores que estan aislados eléctricamente y con alimentación independiente.

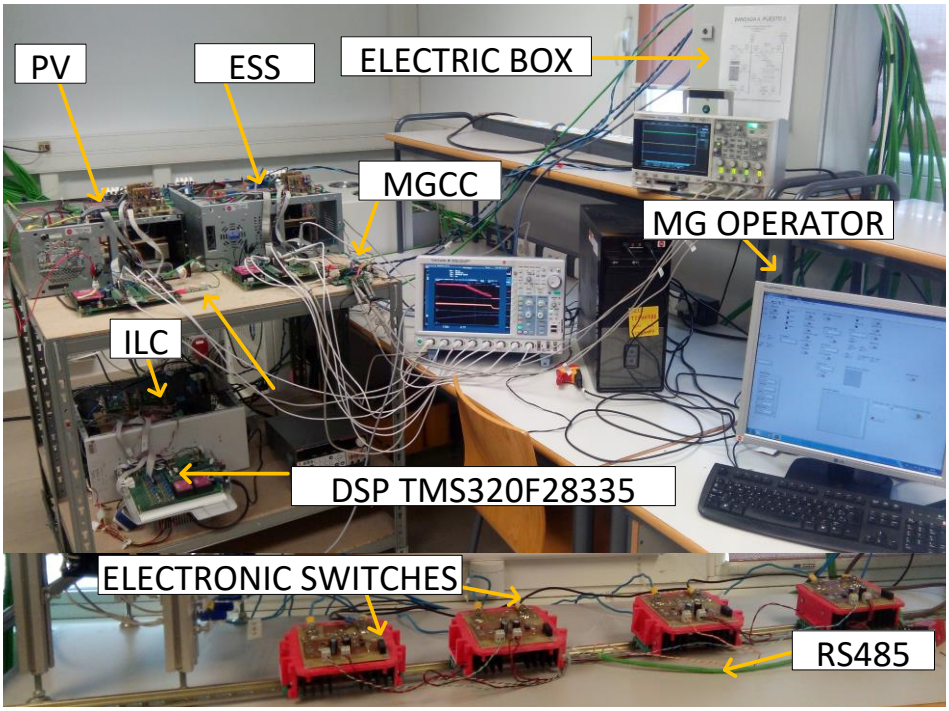

Figura 5.3. Fotografía de los componentes de la microrred AC/DC híbrida experimental desarrollada en el laboratorio.

En el diseño de los circuitos de disparo (*drivers*) de los IGBT de los convertidores de potencia, se utilizó el *driver* aislado galvánicamente ISO5500 de Texas Instruments [129]. Éste permite la activación y desactivación de los IGBT, así como la detección de fallo por sobrecorriente y reinicio del disparo de forma independiente. En la Figura 5.4, se muestra una fotografía de la tarjeta del driver implementado. En la tarjeta se utilizaron fuentes aisladas de continua de ± 15V con sus respectivos filtros, que permiten alimentar cada circuito de disparo de los IGBTs de forma independiente. Adicionalmente, se utilizó un circuito para aumentar la corriente entregada por el ISO5500, que tiene una configuración de BJT en Totem Pole, sumada a una protección con diodos Zener de salida para proteger la puerta del IGBT. El ISO5500 cuenta con un circuito de detección de fallo por desaturación, que mide durante el pulso de activación la tensión entre colector y emisor. Si dicha tensión supera un cierto valor determinado por el diseño, detecta fallo de rama o corto y apaga

el IGBT de forma automática. Esta señal también es enviada mediante la tarjeta electrónica al DSP, que detiene completamente los disparos del PWM para mayor protección.

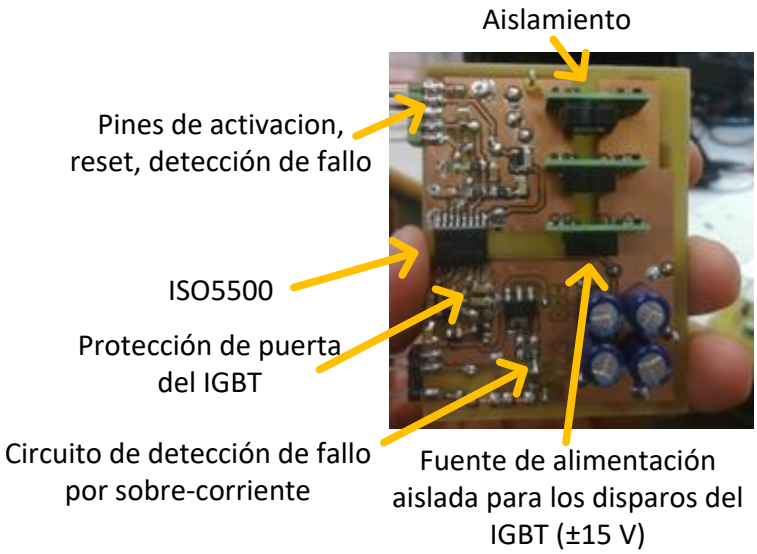

Figura 5.4. Fotografía de la tarjeta electrónica del *driver* implementado en todos los convertidores.

Tabla 5.1. Especificaciones de los convertidores de potencia de la microrred.

ILC	ESS	PV
P_{Rated}^{ILC} = 10 kW	$P_{HB\_Rated}^{BESS}$ = 3 kW	$P_{Boost\text{-}Rated}^{PV}$ = 2.5 kW
V_{Grid} = 230 V and F_{Grid} = 50 Hz	V_{Bat} = 216 V	V_{PV} = 306 V
V_{DC} = 400 V	F_{sw_BESS} = 16 kHz	F_{sw_PV} = 16 kHz
F_{sw_ILC} = 12.8 kHz	L_{BESS} = 5.4 mH	L_{PV} = 5.4 mH
L_1 = 1.2 mH	C_{iBESS} = 1 mF	C_{oPV} = 1 mF
L_2 = 0.4 mH	C_{oBESS} = 1 mF	C_{iPV} = 1 mF
C_{DC} = 3.8 mF	IGBT: VS-GT50TP60N	IGBT: VS-GT50TP60N
C = 2 µF	Baterías:	PV Panel: Atersa A-250P E
IGBT: VS-GT100TP60N	Sun Power VRM 12V105	I_{PV_MAX} = 8.18 A
	T_{Bat} = 25 °C, Q_{Rated} = 100 A·h	V_{PV_oc} = 37.01 V
		I_{PV_CC} = 8.71 A
		V_{PV_MAX} = 30.58 V

5.2. Análisis de las publicaciones

Una vez han sido descritas las herramientas utilizadas y la plataforma experimental desarrollada en este trabajo, se procede a analizar cada una de las publicaciones presentadas. Se ha dividido el análisis en algunos aspectos significativos: motivación, contribución del trabajo, metodología, análisis de resultados y conclusiones.

5.2.1. Publicación I.

En el Capítulo 1 se incluye la primera publicación denominada: "*Power management of the DC bus connected converters in a hybrid AC/DC microgrid tied to the main grid"* [116].

5.2.1.1. Motivación

Como se ha mencionado anteriormente en la introducción, un aspecto crítico en la operación de una microrred es la estrategia de control y gestión de potencia implementada. En este trabajo se presenta una estrategia adecuada que permite compensar los desequilibrios de potencia causados por la discontinuidad en la generación y demanda de energía en la microrred. El objetivo principal del trabajo reportado en la publicación I es la implementación de un algoritmo de despacho y gestión centralizada del flujo de potencia de una microrred AC/DC híbrida de generación distribuida en modo conectado a red. En la Figura 5.5, se muestra la microrred AC/DC híbrida estudiada en este trabajo. El estudio se centra en los convertidores conectados al bus de DC y su comportamiento ante la gestión centralizada implementada. El algoritmo aplica varias funciones de operación a cada uno de los dispositivos de la microrred: sistema de almacenamiento de energía en baterías, generador fotovoltaico y cargas. Este algoritmo es programado y ejecutado desde el procesador digital de control instalado en el Inversor de Interconexión de la microrred. Vale la pena destacar que el algoritmo de gestión de potencia se comprobó en simulación utilizando dos convertidores fotovoltaicos PV1 y PV2, como se muestra en el diagrama de la Figura 5.5, sin embargo experimentalmente se trabajó con un solo convertidor PV.

5.2.1.2. Contribución

Las principales contribuciones de este artículo son: (i) La definición de doce funciones de operación predefinidas que se encargan de la gestión centralizada de los convertidores conectados en el bus de DC de la microrred AC/DC híbrida; (ii) La implementación de niveles de histéresis durante el desprendimiento de las cargas de menor prioridad en los casos donde el

objetivo es mantener la energía de la batería de respaldo lo más alta posible, sin exceder un cierto límite de potencia importado de la red principal. Conjuntamente, se muestra la validación del algoritmo de gestión de potencia en una microrred AC/DC híbrida experimental. El algoritmo se ha implementado en el ILC, en un procesador central de la microrred (*Microgrid central processor*, MGCP) basado en un DSP Texas, TMS320F28335. Tanto el control como las comunicaciones de cada convertidor de potencia se han implementado por medio del mismo tipo de DSP montado individualmente en cada convertidor.

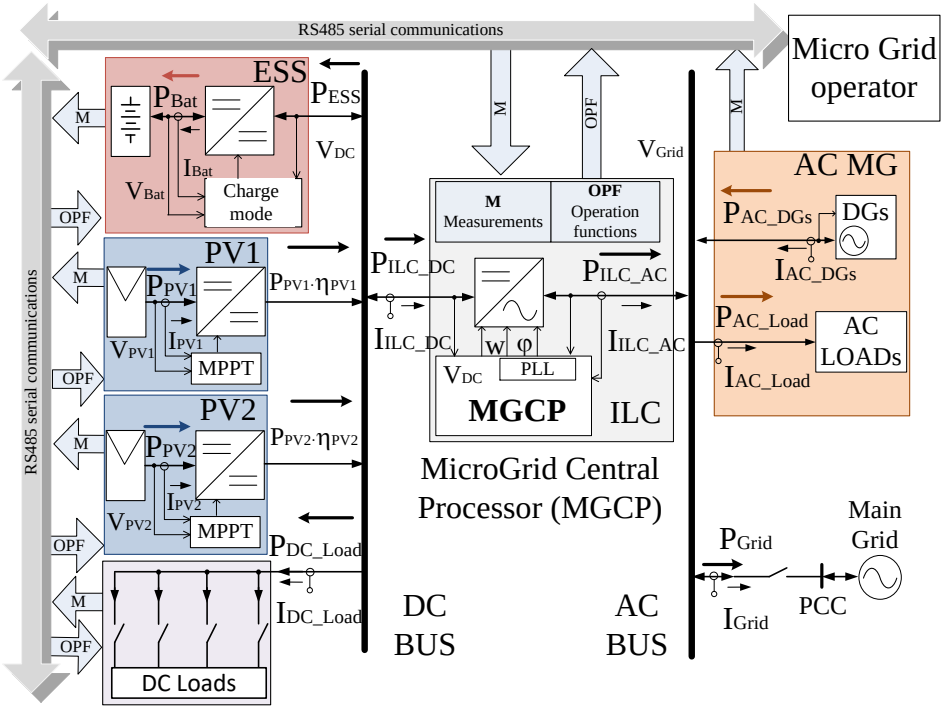

Figura 5.5. Diagrama esquemático de la microrred AC/DC híbrida estudiada en el Capítulo 2.

5.2.1.3. Metodología

La gestión de potencia en la microrred AC/DC híbrida es realizada por el MGCP mediante la aplicación de las siguientes tareas: control de los lazos internos del inversor de interconexión; sincronización con el bus de AC y la regulación del bus de DC de la microrred; comunicación con todos los dispositivos de la microrred; cálculo y envío de las funciones de operación a los convertidores de la microrred; y conexión/desconexión de la microrred con la red principal. Este estudio se basa en la microrred conectada a red. La

microrred en modo isla se encuentra fuera de los objetivos de esta tesis. Sin embargo, se ha realizado una protección anti-isla en el MGCP, basada en [29]. En ese caso, la operación de los generadores distribuidos conectados al bus de AC activaría el modo de control droop para que se pueda regular el voltaje en el bus de AC. El ILC seguiría controlando la tensión en el bus de DC. El uso de comunicaciones centralizadas entre todos los elementos de la microrred permite que esta tarea sea factible [19]. Si ocurre un fallo en las comunicaciones, cada convertidor de potencia de la microrred tiene un controlador local que actúa para mantener la estabilidad del sistema hasta que se corrija el fallo.

El MGCP aplica las funciones de operación en los convertidores de la microrred dependiendo de la información de la potencia disponible en el bus DC, la cantidad de carga conectada al bus DC, el SOC de la batería y los límites de intercambio de potencia proporcionados por el operador de la red. Estos últimos, son límites de absorción/ inyección de potencia desde /hacia la microrred hacia/desde la red. La meta de este algoritmo es importar la potencia necesaria de la red, manteniéndola por debajo del límite de absorción, alimentando las cargas y manteniendo el SOC dentro de un rango seguro. El sistema propuesto tiene una funcionalidad de desprendimiento de carga en el bus de DC, que se aplica cuando la potencia importada por la microrred desde la red tiende a superar los límites predefinidos. Si no hay suficiente energía en los generadores distribuidos y en las baterías, la funcionalidad de desprendimiento de carga se activará. Adicionalmente, para evitar la conexión o desconexión errática de las cargas, se introduce un nivel de histéresis en los umbrales de potencia.

5.2.1.4. Análisis de los resultados

Para verificar la metodología propuesta y la estabilidad de la microrred, se estudian los flujos de potencia entre los buses de DC y AC ante diferentes escenarios operativos de la microrred. Estos escenarios son cambios en la irradiación solar, en el SOC de las baterías, en la cantidad de carga conectada y en los límites impuestos por el operador de red. Según el escenario, el MGCP aplica una serie de funciones de operación a cada convertidor y carga, desde la función 1 hasta la 12. En la publicación I, se muestran tres gráficas correspondientes a los resultados de tres casos experimentales. En el experimento 1 y 2, se estudia el flujo de potencia entre los convertidores de la microrred ante cambios en la irradiación. En el experimento 1, las baterías están inicialmente cargadas con un SOC≥80%. En el experimento 2, se presenta el peor de los casos, donde las baterías están descargadas a un SOC≤ 20%. El caso donde el SOC≤20% se estudia durante el desarrollo experimental de la

tesis, con el fin de analizar la gestión de potencia en la microrred en un caso crítico de funcionamiento de las baterías. Para este tipo de baterías, el SOC mínimo recomendado de trabajo debe estar por encima del 35 %.

El MGCP realiza comparaciones y cálculos de potencia que pueden ser ejecutados en tiempo real por el DSP. No obstante, el retardo en la ejecución de las instrucciones depende del sistema de comunicaciones. Por esta razón, se realizó las medidas del experimento 3. En todas las publicaciones, la velocidad en baudios del bus de comunicación RS485 fue de 9600 bps. En el experimento 3, el algoritmo es ejecutado por el MGCP cada 1 s (1 Hz), realizando las siguientes tareas: solicitar las medidas de voltajes y corrientes a todos los dispositivos en la microrred, seleccionar la función de operación y transmitir las referencias a los dispositivos. El intervalo de tiempo, desde que el MGCP solicita información a un convertidor de la microrred hasta que se ejecuta una instrucción en dicho convertidor, es de aproximadamente 78 ms. En ese intervalo de tiempo, se ejecuta el algoritmo de control de potencia, el procesado de las comunicaciones y varios ciclos del control.

A continuación, se muestran algunos resultados experimentales correspondientes al comportamiento individual de los convertidores electrónicos de potencia de la microrred. Estos resultados no fueron incluidos por motivos de espacio y complementan la publicación I.

Estudio del comportamiento del ESS:

El ESS es el convertidor DC/DC bidireccional de 3 kW conectado entre un banco de baterías y el bus DC de la microrred. La tensión nominal del banco de baterías es de 216 V. La Figura 5.6 representa la corriente en baterías I_{Bat} y el comportamiento del flujo de potencia en las baterías P_{Bat} ante cambios repentinos negativos en la consigna de corriente por parte del MGCP ($I_{Ch_{ref}}$ cambia de 6.75 A hasta $I_{Dis_{ref}} = -6.75\ A$). En este gráfico, se puede observar el ESS trabajando con un flujo de potencia bidireccional. Como se muestra en la Figura 5.6, justo antes del cambio de corriente el ESS está cargando el banco de baterías con un valor de I_{Bat} igual a 6.75 A y absorbe desde el bus DC una potencia P_{Bat}= 1.65 kW.

La Figura 5.7 representa P_{Bat} y su comportamiento ante cambios positivos y repentinos en la corriente de referencia desde $I_{Dis_{ref}} = -6.75\ A$ hasta $I_{Ch_{ref}}$ = 6.75 A. Cuando P_{Bat} es negativo, el ESS está suministrando una potencia al bus de DC de P_{Bat}= -1.65 kW, mientras que si P_{Bat} es positivo, las baterías se cargan con una P_{Bat}=1.65 kW. En los graficos de las Figuras 5.6 y 5.7, se demuestra que cuando el ESS recibe la consigna de corriente, aplica un cambio de referencia

progresivo después de una función de rampa, evitando transitorios peligrosos de I_{Bat} que podrían afectar la estabilidad del bus de DC.

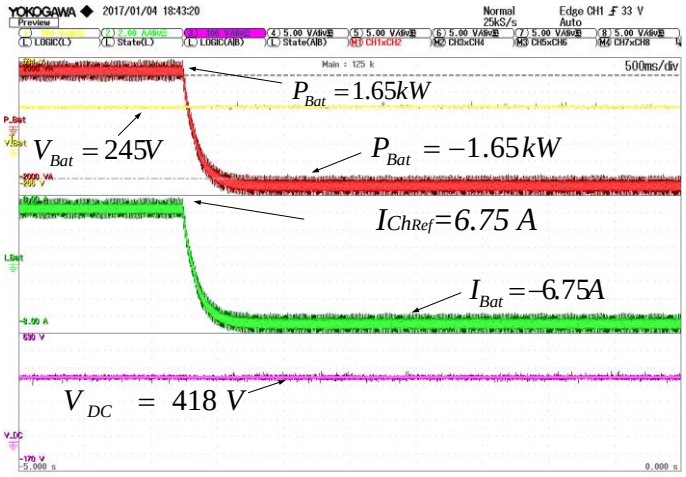

Figura 5.6. P_{Bat} y su comportamiento a cambios repentinos negativos en la corriente de referencia por parte del MGCP.

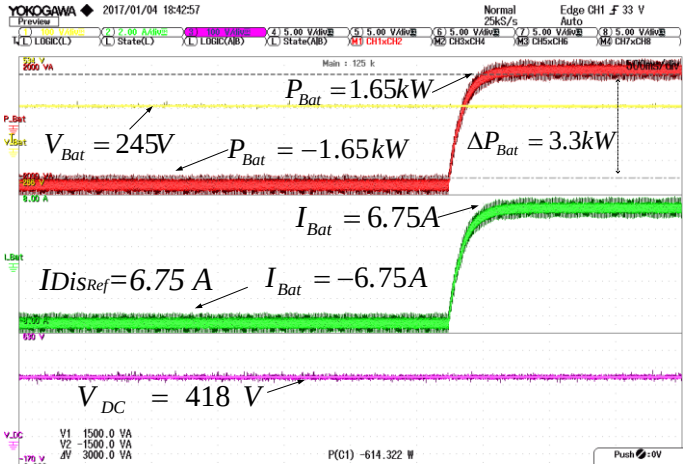

Figura 5.7. P_{Bat} y su comportamiento a cambios repentinos positivos en la corriente de referencia por parte del MGCP.

Estudio del comportamiento del sistema PV:

EL sistema PV es el convertidor DC/DC de 2.5 kW conectado a una cadena de 10 paneles fotovoltaicos conectados en serie, modelo Atersa A-250P GSE. El voltaje en los paneles fotovoltaicos varía desde 306 V a 378 V. El MGCP tiene el

control de la cantidad de potencia generada por los generadores distribuidos, enviando la consiga P_{PV_LIM} deseada al convertidor de DC/DC. Esto se hace dependiendo de las cargas conectadas, el SOC y la potencia disponible. Para verificar el funcionamiento del convertidor PV, el punto de ajuste P_{PV_Lim} se ha cambiado tres veces: P_{PV_Lim} = 3 kW, P_{PV_Lim} = 1.5 kW y P_{PV_Lim} = 1 kW.

La evolución de la potencia P_{PV} se puede observar en la Figura 5.8 y se explica a continuación.

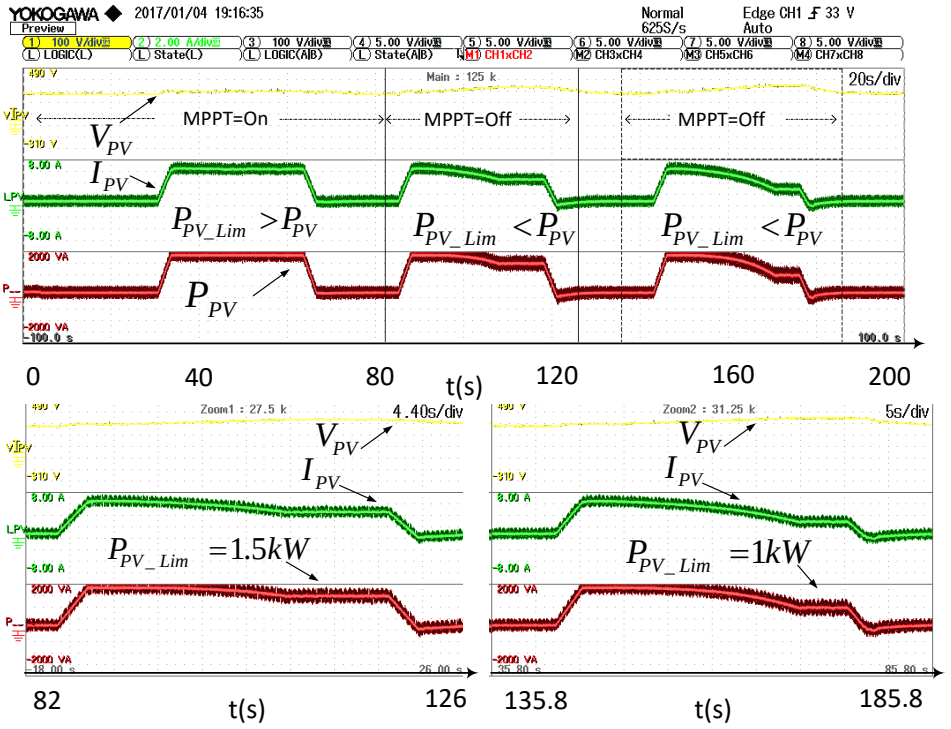

Figura 5.8. P_{PVt} y su comportamiento a cambios repentinos de la referencia P_{PV_Lim}, por parte del MGCP.

Trama superior de la Figura 5.8: en el intervalo 0 s <t <82 s, la irradiación sufre un cambio lineal es 3 s desde 200 W/m^2 a 800 W/m^2. El punto de referencia de P_{PV_Lim} es de 3 kW y el convertidor funciona en su punto máximo de potencia, MPP (MPPT = encendido), siendo P_{PV} = P_{PV_MPP} = 2.2 kW.

Gráfico inferior izquierdo de la Figura 5.8: en el intervalo 82 s <t <126 s, la irradiación sufre un cambio lineal de 200 W/m^2 a 800 W/m^2 en 3 s. La consigna de referencia P_{PV_Lim} es de 1.5 kW y el convertidor funciona fuera del MPP (MPPT = apagado). P_{PV} está limitado a 1.5 kW.

Gráfico inferior derecho de la Figura 5.8: en el intervalo de 135.8 s <t <185.80 s, la irradiación experimenta un cambio lineal de 200 W/m^2 a 800 W/m^2. El punto de referencia de P_{PV_Lim} es de 1 kW, y el convertidor funciona fuera del MPP (MPPT = Off). P_{PV} está limitado a 1 kW.

Estudio del comportamiento del ILC

El ILC es el convertidor de interconexión AC/DC de 10 kW, encargado del flujo bidireccional entre los buses de AC y DC. El estudio del comportamiento experimental del ILC se realizó ante un escenario, donde la tensión del bus AC presenta una tasa distorsión armónica del 3%. Y se realizó las mediciones del THDi correspondientes a varios niveles de inyección de potencia desde el bus DC hacia el bus de AC de la microrred. En la Figura 5.9 se muestra que la THDi de la corriente inyectada al bus AC (I_{ILC_AC}) está dentro de la norma IEEE 1547, para los diferentes niveles de intercambio de potencia. En la Figura 5.10, se observa las gráficas correspondientes a la tensión de V_{Grid}, I_{ILC_AC}, la modulación unipolar utilizada en el ILC y la variación de la tensión en el bus DC. En este caso, la variación máxima de V_{DC} es de aproximadamente 15 V_{pp} para un nivel de potencia de P_{ILC_AC}=4.14 kW.

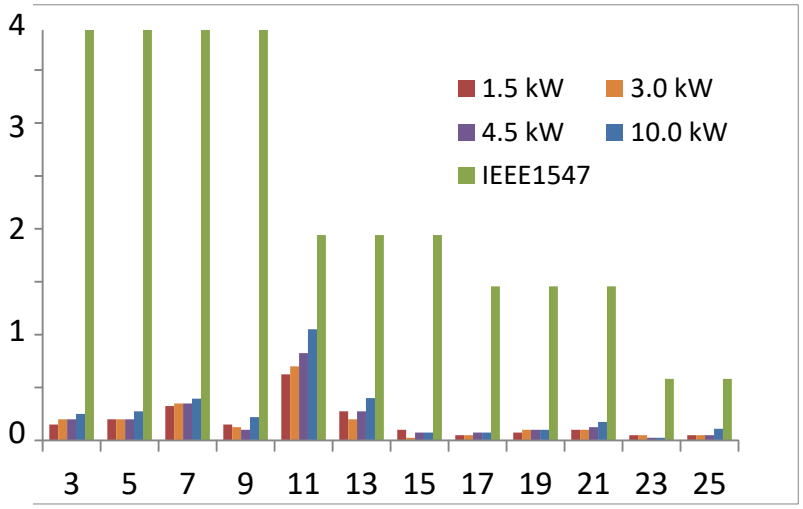

Figura 5.9. Armónicos individuales de la corriente I_{ILC_AC} vs la norma IEE1547.

5.2.1.5. Conclusiones

En la publicación I, se observó una metodología posible para realizar la gestión de potencia en una microrred experimental. Este esquema es interesante porque presenta el despacho de potencia centralizado entre los

convertidores de la microrred y demuestra que es posible implementarlo con comunicaciones de bajo ancho de banda entre ellos. La gestión centralizada del flujo de potencia es realizada mediante: (i) La sincronización con el bus de AC y la regulación del bus de DC de la microrred; (ii) La conexión y desconexión de las cargas de menor prioridad para mantener un SOC adecuado en las baterías y cumplir con los límites de absorción impuestos por la red; (iii) La distribución de la potencia disponible en los buses entre las cargas y el sistema de almacenamiento de energía; (iv) El aprovechamiento de la energía disponible cargando las baterías con el excedente de las FEERR; y (v) El establecimiento de un nivel de histéresis en los niveles de potencia de desprendimiento de la carga que permiten asegurar la estabilidad del bus DC dentro de los rangos adecuados de funcionamiento.

A partir de los resultados que se muestran en la publicación I, surgieron cuestiones relacionadas con las posibilidades existentes para cargar las baterías. El algoritmo se basa unicamente en el SOC de las baterías y ellas son cargadas a diferentes tasas de carga, sin seguir ningún procedimiento de carga que garantice niveles adecuados de tensión y corriente de carga en las baterías. Esto puede ocasionar daños permanentes en las baterías o la disminución de su vida útil.

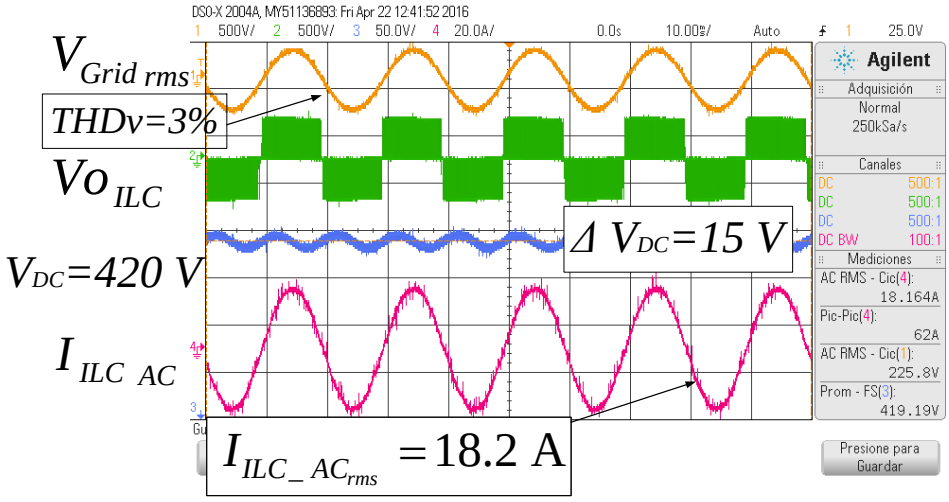

Figura 5.10. Gráficas correspondientes a la tensión de V_{Grid}, I_{ILC_AC}, la modulación unipolar utilizada en el ILC y la variación de la tensión en el bus DC.

5.2.2. Publicación II.

En el Capítulo 2, se incluye la segunda publicación denominada: "*Experimental study of a centralized control strategy of a dc microgrid working in grid connected mode"* [117].

5.2.2.1. Motivación

La publicación II surgió de la necesidad de implementar un algoritmo de gestión centralizada de la potencia en una microrred de DC que incluyera un procedimiento de carga de las baterías del ESS según lo especificado por el fabricante. La microrred de DC estudiada en las publicaciones II y III se muestra en la Figura 5.11.

Una desventaja de la metodología propuesta en la publicación I, es que el algoritmo de gestión de potencia se basa solamente en el SOC de las baterías. Estas son cargadas y descargadas a diferentes valores de corriente sin seguir ningún tipo de procedimiento que garantice valores adecuados. Por otra parte, el MGCP tiene muchas tareas de control que aumentan la complejidad del sistema, ya que se implementa en el mismo procesador del ILC de la MG. Por lo tanto, el MGCP debe ejecutar las funciones de operación que establece el estado en todos los dispositivos de la microrred, a su vez que se encarga de la sincronización con el bus de AC y de la regulación del bus de DC. Estas tareas pueden ser divididas y ejecutadas por dos dispositivos independientes sin aumentar en gran medida los costes de implementación. La publicación II fue desarrollada para cubrir esta necesidad, en la cual se ha implementado el control del ILC en un DSP y la gestión centralizada de potencia de la microrred en otro DSP, este último llamado MGCC por sus siglas en inglés "*Microgrid Central Controller*".

5.2.2.2. Contribución

La principal contribución de este documento es la integración de estrategias de control en todos los convertidores de potencia de la microrred mediante un algoritmo centralizado implementado en un MGCC, teniendo en cuenta las comunicaciones serie en tiempo real para enviar / recibir los datos necesarios. Una contribución adicional de este trabajo es la implementación de un algoritmo de carga de las baterías del ESS según el procedimiento de carga DIN 41773 [32,33]. Dependiendo del voltaje de las baterías, éstas se cargan a una corriente o tensión constante. Una vez que la corriente absorbida por las baterías es menor que un valor preestablecido por la corriente de cola, el voltaje de la batería se mantiene en un cierto voltaje de flotación. También se describe la integración de un algoritmo que aplica el procedimiento de carga,

compatible con gestión de potencia en la microrred. En este trabajo, se muestra la validación experimental del MGCC en una microrred de DC y se proporciona una evaluación realista bajo diferentes escenarios de operación de la microrred. Adicionalmente, se muestra el tiempo de ejecución del algoritmo en el MGCC, así como los retardos de comunicación determinantes para garantizar la gestión de potencia adecuada y la estabilidad del bus de DC.

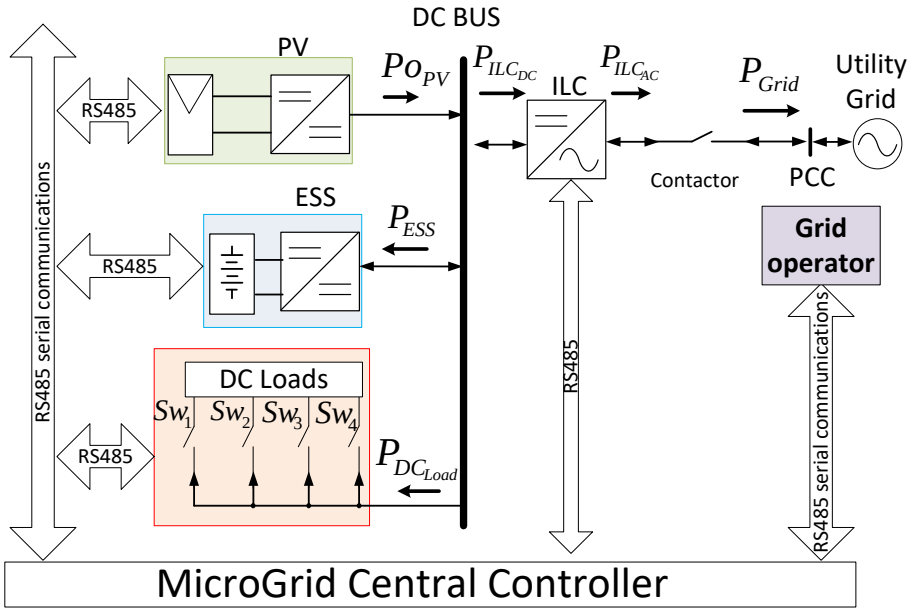

Figura 5.11. Diagrama esquemático de microrred DC estudiada en el capítulo II y III.

5.2.2.3. Metodología

La microrred de DC estudiada está conectada a la red principal a través del ILC, que se encarga del flujo bidireccional de potencia entre el bus de DC y la red principal, además de regular la tensión en el bus DC. Por su parte, el MGCC aplica las siguientes tareas: comunicación con todos los dispositivos de la microrred mediante el bus de comunicación; cómputo y envío de las consignas de potencia a los convertidores de la microrred. Estas últimas establecen el estado del flujo de potencia en la microrred. Como se muestra en la Figura 5.11, la microrred de DC está formada por: (a) un MGCC; (b) un ILC; (c) dos convertidores DC/DC que operan como una fuente de corriente que intercambia su potencia con el bus de DC; (d) cuatro cargas con sus respectivos interruptores electrónicos; (e) un sistema de comunicación serie RS-485 y (e) el operador de la red. Los bucles de control y los esquemas de los convertidores de potencia son mostrados en detalle en la publicación II. Estos bucles de

control tienen un ancho de banda alto para garantizar una respuesta rápida a los cambios en las referencias de corriente/voltaje. Asimismo, cada convertidor de potencia ejecuta sus controladores primarios internos en un DSP TMS320F28335.

Los objetivos de las estrategias de control aplicadas a la microrred de DC son los siguientes:

- Cumplir con los límites de flujo de potencia desde / hacia la microrred de DC hacia / desde la red principal. Estos límites son establecidos por el operador de la red de acuerdo con las tarifas de compra o venta de la energía generada o consumida. Este estudio tiene en cuenta el valor máximo de la absorción / inyección de potencia enviada por el operador de la red al MGCC, así como su efecto sobre el flujo de potencia en la microrred y sobre el comportamiento eléctrico en los convertidores de potencia.

- Limitar la generación de energía fotovoltaica por debajo de la potencia máxima disponible, si es necesario. Este límite depende de la potencia disponible en el bus de DC y del límite de inyección de potencia establecido por el operador de la red.

- Implementar el procedimiento de carga DIN 41773 para baterías de tipo VRLA del ESS conectado al bus de DC, a fin de garantizar el funcionamiento correcto del ESS y extender la vida útil de sus baterías.

- Gestionar la demanda de potencia de los dispositivos conectados en el bus de DC mediante una funcionalidad de desprendimiento de carga. Esta función se usa solo como último recurso y solo cuando el estado de las baterías y la potencia disponible en el bus DC está por debajo de un umbral preestablecido.

- Controlar en tiempo real el flujo de potencia dentro de la microrred a través de comunicación serie RS485. El algoritmo de gestión de potencia propuesto proporciona los valores de referencia de potencia, que se transmiten a cada convertidor para establecer el flujo de potencia deseado.

- Obtener transitorios suaves en los voltajes y las corrientes de los convertidores de potencia conectados en el bus de DC durante los cambios repentinos de las consignas de potencia en cada convertidor.

5.2.2.4. Análisis de los resultados

En la publicación II, se han realizado cuatro experimentos que describen las situaciones más comunes y críticas de la microrred ante diferentes escenarios de funcionamiento. Se han considerado los cambios en: la irradiación, en la carga de DC, el SOC y en los límites de potencia. Desde los experimentos 1 hasta el 3, se muestra el comportamiento de la microrred ante cambios en la irradiación y diferentes valores del SOC de las baterías. En el Experimento 1 las baterías del ESS están inicialmente en un SOC ≥ 50% y se puede observar que el MGCC mantiene las cargas conectadas durante todo el experimento, cumpliendo con el límite máximo de absorción de potencia desde la red hacia la microrred.

En el experimento 2, las baterías del ESS están descargadas a un SOC ≤ 20% (caso crítico). El MGCC aplica la funcionalidad de desprendimiento de carga y comienza cargar las baterías con la potencia disponible en el bus de DC, sin superar el límite de absorción de potencia desde la red. La reconexión de la carga sólo ocurre cuando existe un aumento en la generación del sistema fotovoltaico o si aumenta el límite de absorción desde la red. La funcionalidad de desprendimiento de carga se aplica cuando el banco de baterías está descargado a un valor mínimo establecido por el MGCC. La cantidad de desprendimiento de carga depende de la potencia disponible en el bus DC, teniendo en cuenta el nivel de histéresis. Este último mejora la fiabilidad de la microrred, garantizando la seguridad y la estabilidad de la tensión del bus de DC. La demanda de carga se mide en tiempo real, ya que el problema principal que se puede presentar durante el procesamiento de datos es la desconexión / conexión de una carga excesiva durante un tiempo demasiado prolongado, lo que puede ocasionar fuertes perturbaciones transitorias en el bus DC que no pueden ser asumidas por el control de tensión implementado en el ILC.

Un escenario posible de funcionamiento es que el bus DC de la microrred necesite ser alimentado temporalmente a una potencia superior a la potencia máxima de importación definida en el contrato de electricidad. Esto puede ocurrir cuando la carga conectada en el bus DC es muy alta y no hay suficiente generación fotovoltaica para cubrir la demanda. En este caso el MGCC permite que la potencia necesaria para mantener dicha carga conectada sea extraida desde las baterías. En el experimento 3 inicialmente se plantea este escenario en el que la potencia necesaria en el bus de DC es mayor que el límite de absorción permitido por el operador de red. Por lo tanto, las baterías son descargadas hasta el valor mínimo, estudiándose el caso crítico en que las baterías alcanzan un SOC≤20%. Justo en este punto, el MGCC comienza a

desprender cargas en el bus DC y las baterías pueden recargarse con el exceso de energía disponible después de la conexión / desconexión de la carga.

Los retardos de comunicación y el tiempo de ejecución del algoritmo de gestión de potencia se pueden observar en el experimento 4. En la publicación II, el algoritmo es ejecutado cuatro veces más rápido que en la publicación I y es ejecutado cada 250 ms (4 Hz). El ciclo entero de gestión de potencia en la microrred ocupa un tiempo de 70 ms, tiempo en el cual realiza las siguientes tareas: solicita las mediciones de potencia instantánea a todos los dispositivos de la microrred; cálculo, transmisión y ejecución de las referencias de potencia en todos los dispositivos.

Los algoritmos de gestión de potencia implementados en la tesis tienen un bajo coste computacional. En la publicación II el tiempo de procesamiento del algoritmo es de 200 µs. Este es el tiempo requerido desde que el MGCC recibe la información de los convertidores hasta que emite las consignas de control a cada elemento.

En la Figura 5.12, se muestran algunos resultados experimentales obtenidos durante los ensayos, que no fueron incluidos por motivos de espacio en la publicación II. La Figura 5.12 muestra las gráficas correspondientes a la tensión y corriente del ESS, PV, ILC, y carga.

En el ensayo las baterías del ESS están inicialmente en un SOC ≥ 50%, la microrred tiene una carga conectada durante todo el experimento de 0.65 kW. En t=80 s, el operador de la microrred realiza un cambio del límite de absorción de potencia hacia la microrred desde la red eléctrica, $P_{Grid\text{-}to\text{-}MG}$. Pasa de forma instantánea desde $P_{Grid\text{-}to\text{-}MG}$=4 kW a $P_{Grid\text{-}to\text{-}MG}$=0 kW. El motivo de este ensayo es verificar el cumplimiento de este límite. Esta limitación por parte del operador de la microrred se debe a la poca disponibilidad de potencia durante las horas de mayor demanda en la red o al aumento del coste de la energía durante estas horas.

En el intervalo (0 s<t<80 s) se puede observar que el MGCC mantiene la carga conectada durante todo el experimento y las baterías son cargadas a dos tasas de carga diferentes y siempre a corriente controlada. En este intervalo el MGCC mantiene la potencia absorbida de la red (P_{ILC_DC}) por debajo del límite de $P_{Grid\text{-}to\text{-}MG}$=4 kW. En t= 46 s la corriente de carga de las baterías pasa de 1.5 A hasta 6.4 A. Esto se debe a que el MGCC detecta suficiente energía proveniente de la generación fotovoltaica para cargar las baterías, de manera que se absorbe lo mínimo posible de la red. En el intervalo (46 s<t<80 s) se tiene: $P_{ILC_DC}\cong$0.2 kW.

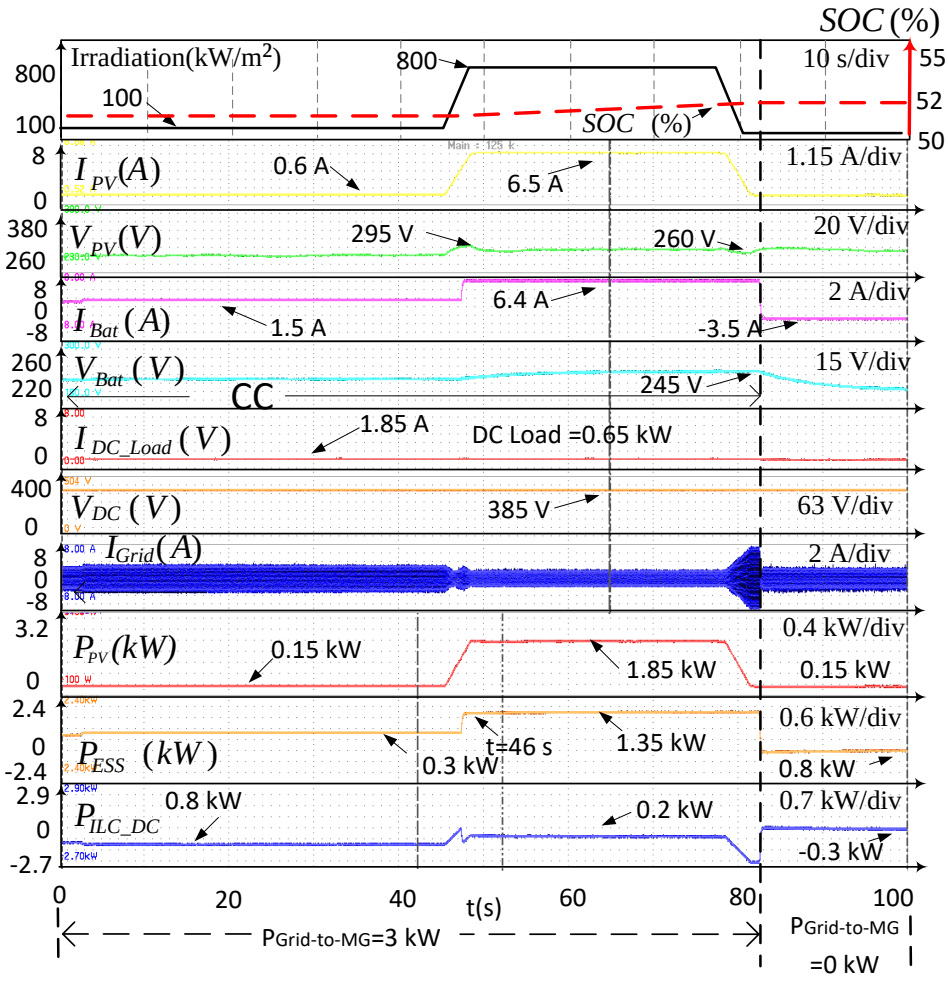

Figura 5.12. Gráficas correspondientes a la tensión y corriente del ESS, PV, ILC, y carga.

En en intervalo (80 s<t<100 s), en t=80 s, $P_{Grid\text{-}to\text{-}MG}$ pasa de forma instantánea desde $P_{Grid\text{-}to\text{-}MG}$=4 kW a $P_{Grid\text{-}to\text{-}MG}$=0 kW. Se puede observar en este instante que las baterías comienzan a inyectar potencia al bus DC, cambiando su corriente a -3.5 A. De esta manera se mantiene la carga conectada y no se sobrepasa el límite: $P_{Grid\text{-}to\text{-}MG}$=0 kW. Se absorbe 0.15 kW de la generación fotovoltaica y el restante es inyectado a la red, P_{ILC_DC}=-0.3 kW.

5.2.2.5. Conclusiones

En la publicación II se propuso una metodología simplificada y adecuada para la gestión centralizada de potencia de los convertidores de una microrred de DC. La gestión es realizada mediante un algoritmo con bajo coste

computacional. Los resultados demuestran que se mantiene la estabilidad y los valores de tensión en el bus DC dentro de los rangos adecuados de funcionamiento.

En este trabajo, se muestra un algoritmo simplificado de carga de las baterías según la norma DIN41773. En función de la tensión de las baterías, éstas son cargadas a corriente o tensión constante con dos valores de tensión. En el caso de este estudio: tensión máxima de carga de 254 V y tensión de flotación de 243 V. Asimismo, en la carga de las baterías a corriente constante se ajusta la tasa de carga en función de la potencia disponible en el bus DC. Sin embargo, en las microrredes se pueden presentar fluctuaciones inesperadas en la potencia disponible en el bus DC para cargar las baterías. Estas fluctuaciones pueden ser debidas a la naturaleza intermitente de las FEERR o a la propia estrategia de gestión de potencia aplicada en la microrred (Experimento 3), produciendo variaciones bruscas en las corrientes de carga/descarga de las baterías que limitan la aplicación adecuada del procedimiento de carga recomendado por el fabricante. Una solución a esta problemática es realizar una planificación preliminar de la potencia disponible para cargar las baterías. Es decir, que el ESS disponga de la energía necesaria durante el proceso de carga de las baterías para garantizar el cumplimiento del procedimiento de carga. Esta problemática se cubre con la estrategia de gestión de potencia aplicada en la publicación III.

5.2.3. Publicación III.

En el Capítulo 3, se incluye la tercera publicación denominada: *"Practical Analysis and Design of a Battery Management System for a Grid-Connected DC Microgrid for the Reduction of the Tariff Cost and Battery Life Maximization"* [118].

5.2.3.1. Motivación

Los algoritmos implementados en la publicación I y II no toman en cuenta en la gestión de potencia de la microrred los costes de la tarifa eléctrica según el tiempo de uso (*time of use*, TOU) de la electricidad, que es un factor determinante del precio total de la energía absorbida hacia la microrred desde la red eléctrica. La publicación III cubre esta necesidad, ya que implementa un nuevo algoritmo en el MGCC, que realiza la planificación diaria del despacho de potencia en la microrred DC tomando en cuenta los costos de la tarifa eléctrica según el TOU. Adicionalmente, en la publicación III, se diseñó un sistema de almacenamiento de energía en baterías (*Battery Energy Storage System*, BESS), que permite alcanzar los siguientes objetivos de gestión: (i) las baterías suministran la potencia necesaria en la microrred cuando existe poca

disponibilidad de potencia en las FEERR y durante las horas donde la tarifa eléctrica es alta; (ii) las baterías se cargan con el excedente de potencia de las FEERR y preferiblemente cuando la tarifa eléctrica es baja.

5.2.3.2. Contribución

La principal contribución de este trabajo es la estrategia de gestión implementada por el MGCC. Esta utiliza un algoritmo que minimiza la tarifa de la energía importada de la red principal hacia la microrred, estableciendo el SOC objetivo en el BESS en un tiempo determinado del día y cambiando las tasas de carga de las baterías en función del estado de la microrred. Esto permite aprovechar las FEERR presentes en la microrred y gestionar la energía almacenada en las baterías. Es decir, las baterías serán cargadas de forma planificada cuando el precio de la tarifa eléctrica sea bajo, y aprovechando el excedente de generación de renovables.

Una contribución adicional de la Publicación III es la presentación de la metodología de diseño completo de un BESS para el entorno de la microrred DC. Se presenta el modelado del sistema de potencia del BESS, tomando en cuenta un modelo eléctrico RC de segundo orden de las baterías. En la Publicación II y III, el BESS contiene un BMS que implementa el procedimiento de carga DIN 41773. Se realiza la carga/descarga adecuada de las baterías, aumentando su vida útil y por ende disminuyendo los costos por reemplazo de las mismas. No obstante, en la publicación III a diferencia de la II, se garantiza que el procedimiento de carga se ha cumplido, mediante la planificación por parte del MGCC del proceso de carga de las baterías durante el día. En este caso, las tasas de carga de dicho procedimiento son ajustadas por el BMS en función del SOC objetivo que se desea alcanzar y de la potencia disponible en el bus DC en cierto momento del día. Asimismo, el BMS realiza: la compensación térmica de la tensión de carga y de flotación; la determinación de las corrientes máximas/mínimas de carga y, finalmente, las protecciones térmicas, contra sobrecorrientes, contra sobretensiones, contra sobrecargas, etc...

5.2.3.3. Metodología

El despacho de potencia es realizado entre el MGCC y el BESS de la microrred. El objetivo es minimizar el costo de la energía importada desde la red principal y gestionar adecuadamente el despacho entre los convertidores y el bus DC. El MGCC envía/recibe los datos necesarios utilizando comunicaciones serie en tiempo real. El MGCC recibe desde el operador de la microrred la información del pronóstico diario de la generación fotovoltaica, del consumo habitual de la microrred y de los precios de la tarifa eléctrica. Con

esta información realiza la planificación del intercambio de potencia en la microrred diariamente, estableciendo en determinados momentos del día el estado de carga deseado en las baterías del BESS y la potencia en los convertidores.

El BMS del BESS recibe desde el MGCC la información de la potencia disponible en la microrred para cargar baterías, el tiempo en que dispondrá de esa potencia y el SOC deseado durante ese tiempo. Inicialmente las baterías son cargadas a corriente constante (CC) hasta alcanzar un valor de tensión máximo de carga, en este punto se cambia a voltaje constante (CV). El BMS se encarga de ajustar los parámetros de corriente y tensión para cumplir con el procedimiento DIN 41773. Para ello, las ecuaciones que calculan las consignas de referencia de tensión y corriente de carga de las baterías se obtienen mediante la interpolación lineal y polinómica de las curvas presentadas en las especificaciones técnicas proporcionadas por el fabricante de baterías. De igual forma, el BMS realiza la compensación térmica ajustando los parámetros de carga en función de la temperatura de las baterías.

5.2.3.4. Análisis de los resultados

En la publicación III, se ha realizado cuatro experimentos. En el experimento 1 se comprueba la metodología de diseño del BESS y el procedimiento de carga implementado en la sección 3 de dicha publicación. En el experimento 2, se muestra el flujo de potencia de los convertidores presentes en la microrred ante diferentes escenarios de funcionamiento, que describen las situaciones más comunes de la microrred. En los escenarios bajo estudio se han considerado los cambios estimados durante un día en la irradiación, la carga, el SOC, el TOU y los límites de potencia. En el experimento 3, se observa el comportamiento del ILC ante un cambio bidireccional del flujo de potencia entre la microrred y la red eléctrica. Finalmente, en el experimento 4 se representa los retardos de la comunicación implementada.

En el experimento 1, se muestra la comprobación del funcionamiento del algoritmo de despacho de potencia descrito en la sección 4 de la publicación III. Para acortar el tiempo total de los experimentos los perfiles de generación fotovoltaica, demanda, discriminación diaria del costo unitario de la electricidad y la capacidad de las baterías se ajustaron a un periodo de 2400 s, que representa un día entero (100 s corresponde a 1 h). Los perfiles de referencia son utilizados por el MGCC para la planificación del despacho de potencia en la microrred durante el día. Obsérvese que para este estudio el coste unitario de la tarifa eléctrica aumenta a partir de los 1300 s (las 13 h).

En la Figura 5.13, se puede observar los resultados experimentales equivalentes al despacho de potencia en la microrred del experimento 2. Al comienzo de cada día en t=0 s el MGCC aplica el caso 0. El caso 0 se refiere a un algoritmo que estima la planificación y gestión de la potencia de los convertidores de potencia que conforman la microrred. Este algoritmo realiza la planificación según la información diaria de los perfiles de referencia enviados desde el operador de la microrred. Estos perfiles son: (i) el perfil diario de generación fotovoltaica $P_{Profile}^{PV}$ estimado según la predicción del tiempo; (ii) el perfil diario habitual de consumo en la microrred; (iii) la tarifa eléctrica según su discriminación diaria (TOU) y (iv) los límites de la potencia absorbida/inyectada desde/hacia la red hacia/desde la microrred establecidos por la compañía eléctrica ($P_{Grid\text{-}to\text{-}MG}^{MAX} = 10$ kW y $P_{MG\text{-}to\text{-}Grid}^{MAX} = 4$ kW). $P_{Grid\text{-}to\text{-}MG}^{MAX}$ se refiere a la potencia contratada, la cual es la máxima potencia que puede ser absorbida desde la red hacia la microrred. $P_{MG\text{-}to\text{-}Grid}^{MAX}$ se refiere a la potencia máxima que se puede exportar a la red desde la microrred.

La evolución de las potencias (P_o^{PV}, P^{BESS}, P_{Load}^{DC}, P_{DC}^{ILC}), corrientes (I^{Bat}, I^{PV}), SOC y voltajes (V^{Bat}, V^{PV}) de la microrred se pueden observar en la Figura 5.13. Después de la aplicación del algoritmo de planificación de potencia en la microrred, el MGCC guarda la información de la potencia estimada para cargar las baterías P_{ref}^{BESS}, el SOC objetivo SOC_{ref} y los intervalos de tiempo t_{ref} ($t_{initial}$ = 420 s, t_{final} = 1300 s). En t=0 s, se observa en que el MGCC descargó las baterías en el día anterior hasta un $SOC>SOC_{MIN}$. Esto indica el cumplimento de la planificación del despacho de potencia del día anterior. Por ello, el MGCC comienza a ejecutar la planificación estimada para el día actual en los intervalos de tiempo presentados en la Figura 5.13 y explicados a continuación:

Intervalo 1 (0 s < t < 420 s):

$t_{initial}$ es el tiempo calculado cuando $P_{DC}^{Available}$ comienza a ser mayor que cero, para este caso $t_{initial}$ = 420 s. En este intervalo, se aplica el caso 2 que se emplea cuando no existe generación por parte de las FEERR y la tarifa eléctrica es baja (horas de la madrugada). En la gráfica de la Figura 5.13, el MGCC calculó el SOC objetivo en las baterías SOC_{ref} =50%, que debe ser alcanzado en un tiempo $t_{initial}$ = 420 s, el SOC debe partir desde su valor a principios del día de SOC=40 %. P_{ref}^{BESS} sigue la ecuación (38) y es de aproximadamente 3 kW. Sin embargo, con el objetivo de disminuir la potencia absorbida de la red, el BESS estima con la ecuación (22) la potencia requerida por las baterías para alcanzar el SOC objetivo (SOC_{ref} = 50 %) en el intervalo de tiempo (t_{ref} = $t_{initial}$) indicado

por el MGCC. Por ello, la potencia requerida para alcanzar el SOC objetivo de 50 % en el tiempo de referencia de 420 s es de 0.4 kW, siendo este valor mucho menor que la potencia disponible en el bus DC para cargar baterías, ahorrando costes de la factura eléctrica durante el proceso de carga. En la parte superior de la Figura 5.13, se observa que el BESS carga las baterías en este intervalo a corriente constante, I^{Bat}=2 A.

Intervalo 2 (420 s< t < 1300 s):

En este intervalo, la generación fotovoltaica es suficiente para alimentar todas las cargas. t_{final} es el tiempo calculado cuando $P_{DC}^{Available}$ comienza a ser menor que cero, en este caso t_{final} = 1300 s. En intervalo 2, se verifica que las potencias medidas están dentro del rango de las potencias estimadas inicialmente en la planificación. Por lo tanto, el MGCC aplica el caso 3, donde la potencia estimada para cargar las baterías aprovecha al máximo las FEERR de la microrred y no absorbe potencia desde la red eléctrica hacia la microrred (Ver P_{DC}^{ILC} en este intervalo). Los valores enviados por el MGCC al BESS son t_{ref}= 880 s, el SOC objetivo es de SOC_{ref} =100% partiendo desde su valor en t=420 s de SOC=50 %. P_{ref}^{BESS} sigue la ecuación (36) y P^{BESS} es de aproximadamente 1.7 kW. En t = 420 s la potencia gestionada por el ILC es: $P_{DC}^{ILC} \cong -0.3$ kW. El procedimiento de carga DIN41773 aplicado por el BESS es verificado en este intervalo. En t = 800 s, el BESS cambia desde modo CC a modo CV con $V_{(Ch)}^{Bat}$=255 V. En t= 1300 s se observa que las baterías han alcanzado un SOC=94 %.

Intervalo 3 (1300 s < t <2000 s):

En este intervalo la potencia generada proveniente de las FEERR no es suficiente para alimentar las cargas y el coste unitario de la tarifa eléctrica es alto, por lo tanto el BESS debe comenzar a suministrar potencia al bus DC de la microrred. En t = 1300 s, el TOU cambia desde (0.08 €/kW·s) a (0.16 €/kW·s). El MGCC envía al BESS la potencia estimada para descargar las baterías hasta alcanzar un SOC > SOC_{MIN}. En este intervalo, el MGCC disminuye el coste de la factura eléctrica absorbiendo la mínima potencia posible desde la red eléctrica hacia la microrred.

En la gráfica de la Figura 5.13, se observa que el SOC objetivo fue alcanzado en t_{final} = 1300 s y en ese punto se calcula la máxima potencia de descarga de baterías P_{Dis}^{BESS} según la ecuación (39) para el intervalo (1300 s < t <2000 s), con el fin de garantizar un estado de carga de las baterías mínimo (SOC>SOC_{MIN}) al finalizar el día. En el intervalo (1300 s<t<1780 s), se cumple que P_{Dis}^{BESS} <

$|P_{DC}^{Available}|$, y se aplica el caso 5. La potencia para descargar baterías P_{ref}^{BESS} sigue la ecuación (40). En el intervalo (1780 s<t<2000 s), ocurre el caso contrario $P_{Dis}^{BESS} > |P_{DC}^{Available}|$, se aplica el caso 6 y P_{ref}^{BESS} sigue la ecuación (41). En ambos casos se absorbe lo minimo posible de la red eléctrica.

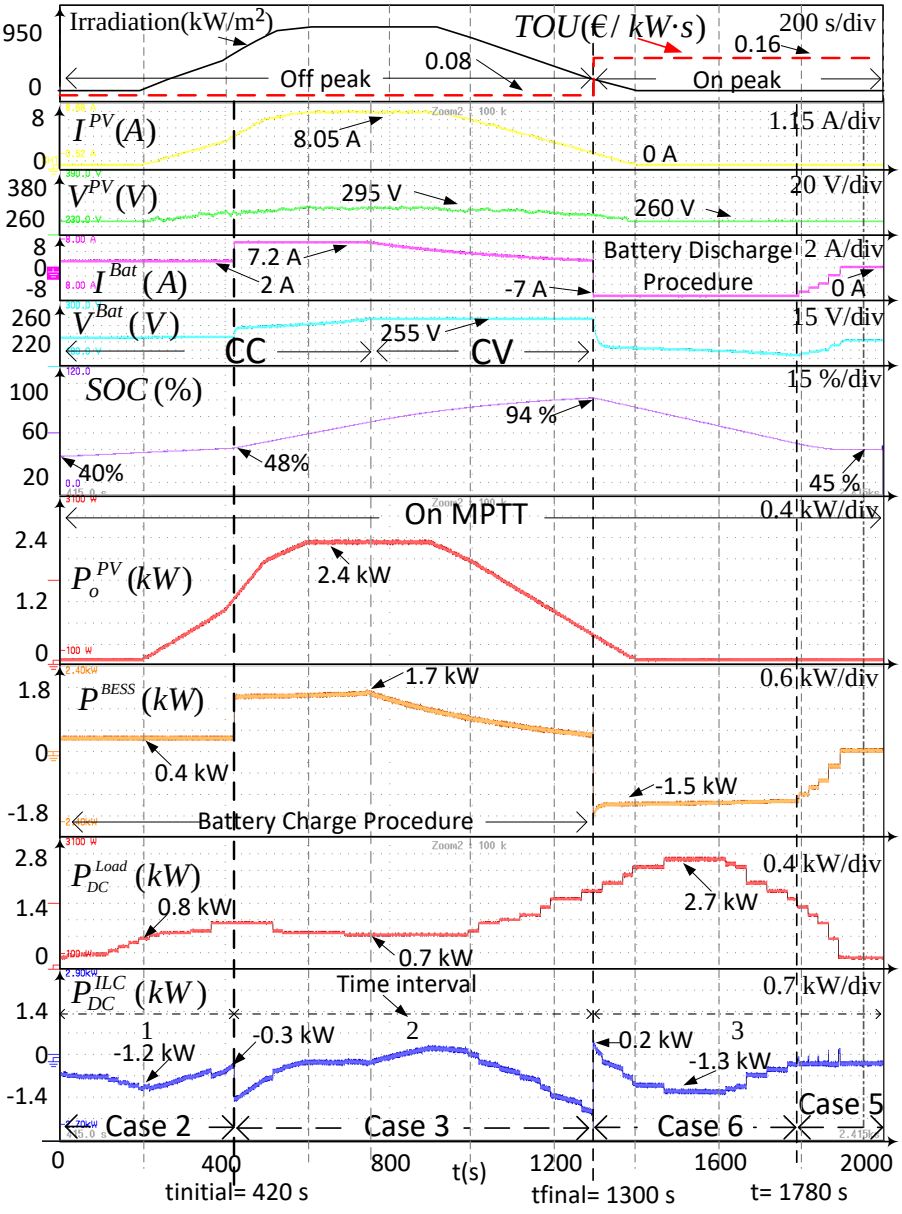

Figura 5.13. Gráficas correspondientes a la evolución de las potencias (P_o^{PV}, P^{BESS}, P_{Load}^{DC}, P_{DC}^{ILC}), corrientes (I^{Bat}, I^{PV}), SOC y voltajes (V^{Bat}, V^{PV}) de la microrred

5.2.3.5. Conclusiones

La estrategia utilizada en este trabajo para reducir el coste de la factura eléctrica en la microrred, es principalmente gestionar el funcionamiento del sistema de almacenamiento, cambiando el horario de aprovechamiento de la energía almacenada en las baterías a partir de las opciones de generación que contenga la microrred y de los datos del precio del tiempo de uso (TOU) de la electricidad. Esto permite cargar las baterías con el excedente de las FEERR y en los momentos donde la demanda y el precio de la tarifa eléctrica son bajos. Y luego cuando estos son altos descargar las baterías, en lugar de comprar la electricidad a un alto precio.

6

6. CONCLUSIONES Y TRABAJOS FUTUROS

En este capítulo se muestra un resumen de las conclusiones más relevantes obtenidas durante el desarrollo de la tesis. Así como también, se presentan algunas líneas de investigación que pueden ser derivadas de este trabajo.

Esta tesis se ha enmarcado en el contexto de la presentación de algoritmos de gestión centralizada de potencia de una microrred de generación distribuida en modo conectado a red. Los algoritmos presentados se pueden aplicar a los convertidores electrónicos conectados en una microrred AC/DC híbrida o en una microrred de DC. Los algoritmos implementan las estrategias de control en función de los objetivos planteados inicialmente para la microrred. Las estrategias que se aplican para alcanzar los objetivos planteados en cada uno de los trabajos de investigación se resumen en la tabla 6.1. Los objetivos y las estrategias aplicadas se enumeran a continuación:

Objetivos de gestión de potencia alcanzados durante la tesis

(i) Integración de estrategias de control en todos los convertidores de potencia de la microrred mediante un sistema de gestión de potencia centralizado.

(ii) Importación de la potencia necesaria desde la red principal hasta la microrred, manteniéndola por debajo del límite de absorción establecido por el operador de la microrred.

(iii) Inyección desde la microrred hacia la red principal del exceso de potencia generado en el bus DC de la microrred, manteniendo la potencia por debajo del límite de inyección impuesto por el operador de la microrred.

(iv) Estabilidad del bus DC y del bus AC ante la gestión de potencia planteada para la microrred.

(v) Cumplimiento de la norma IEEE 1547 (la THDi de la corriente inyectada/absorbida en el bus AC debe estar por debajo del 5 %).

(vi) Desarrollo de algoritmos de gestión con bajo coste computacional.

(vii) Preservación del SOC de las baterías dentro de un rango seguro establecido por el operador de la microrred.

(viii) Implementación del procedimiento de carga DIN 41773 para baterías de tipo VRLA, a fin de garantizar el funcionamiento correcto del sistema de almacenamiento de energía y de extender la vida útil de sus baterías.

(ix) Implementación de un BMS que realiza funciones adicionales de protección y gestión eficiente de la carga en las baterías en función del escenario de la microrred y del precio de la tarifa eléctrica. Adicionalmente, se realiza la gestión de potencia de forma conjunta entre el controlador central y el sistema de almacenamiento de energía en baterías.

(x) Minimización de la potencia importada desde la red principal hacia la microrred, para disminuir el importe de la factura eléctrica.

Estrategias aplicadas por los dispositivos de la microrred.

(a) Gestión centralizada de potencia en los convertidores de la microrred.

(b) Sincronización con la red eléctrica y regulación del bus DC.

(c) Conexión y desconexión de las cargas prioritarias dentro de la microrred, en función de la disponibilidad de potencia en el bus DC y para mantener un SOC adecuado en las baterías. Esta función se usa solo como último recurso y cuando el estado de las baterías y la potencia disponible en el bus DC están por debajo de un umbral preestablecido.

(d) Cambios progresivos de las consignas de control recibidas por cada controlador local desde el controlador central. De esta manera se obtiene transitorios suaves en los voltajes y las corrientes de los convertidores de potencia conectados al bus de DC.

(e) Intercambio de información entre el controlador central y todos los dispositivos electrónicos de la microrred mediante un sistema de comunicación serie de bajo ancho de banda y de bajo coste de implementación.

(f) Implementación de un nivel de histéresis en los umbrales de comparación de los niveles de potencia que permiten asegurar la estabilidad del bus DC dentro de los rangos adecuados de funcionamiento.

(g) Generación de energía fotovoltaica en el punto de máxima potencia (MPPT) o, si es necesario, por debajo de este punto.

(h) Implementacion de un procedimiento de carga de baterías según lo establecido por el fabricante, que evite descargas profundas y maximice su vida útil.

(i) Gestión de potencia en la microrred mediante la utilización de la información diaria de los perfiles de referencia enviados desde el operador de la microrred. Estos perfiles son: el perfil diario de generación fotovoltaica estimado según la predicción del tiempo; el perfil diario habitual de consumo en la microrred y la tarifa eléctrica según su discriminación diaria (TOU). Con esta información se realiza la planificación del intercambio de potencia en la

microrred diariamente, estableciendo en determinados momentos del día el estado de carga deseado en las baterías y la potencia en los convertidores.

(j) Planificación de los momentos adecuados para la carga de las baterías, coincidiendo con franjas horarias de baja tarifa eléctrica y aprovechando el excedente de generación de renovables. Se gestiona en tiempo real el sistema de almacenamiento, cambiando el horario de aprovechamiento de la energía almacenada en las baterías a partir de las opciones de generación que contenga la microrred y de los precios del tiempo de uso de la electricidad.

Tabla 6.1. Resumen de las estrategias aplicadas en cada artículo del compendio y de los objetivos alcanzados.

Pub.	Estrategias implementadas en los dispositivos de la microrred					Objetivos alcanzados mediante la implementación de las estrategias									
	ILC	BESS	PV	DC load	MGCC	i	ii	iii	iv	v	vi	vii	viii	ix	x
I	a,b,c, d,e,f	d,e	d, e,g	e,f	–	•[1]	•	•	•	•	•	•	–	–	–
II	b,d,e	d,e,h	d, e,g	e,f	a,c,e,f	•	•	•	•	•	•	•	•	–	–
III	b,d,e	d,e,h,j	d, e,g	e,f	a,c,d,e,f,i,j	•	•	•	•	•	•	•	•	•	•

[1] Un (•) indica el objetivo cumplido de la columna, correspondiente al artículo que indica la fila; el (–) indica que no se cumple el objetivo para esa publicación.

A partir del estudio realizado en la presente tesis doctoral, se abren nuevas posibilidades en la selección de otros objetivos de gestión de potencia que no han sido contemplados en esta tesis y, en consecuencia, surgen futuras líneas de investigación. En línea general, los objetivos de gestión en las microrredes dependen de diferentes factores, como son: el modo de operación de la microrred, el tipo de operación (centralizada, distribuida y descentralizada); los aspectos económicos del sistema (tarifa eléctrica, costes de las penalizaciones de conexión o por las emisiones de los generadores convencionales, aumento de costes por el uso de comunicaciones o por la complejidad del control, etc.); la naturaleza intermitente de las fuentes de energía renovables y los problemas ambientales de los generadores convencionales; el estado de carga de las baterías; la inclusión de vehículos eléctricos en la gestion; las pérdidas, la estabilidad y la confiabilidad del sistema; la privacidad del cliente; los costes computacionales de los algoritmos de gestión, etc… Vale la pena señalar, que en la actualidad se han realizado estudios de investigación que abordan de manera particular algunos de los factores nombrados anteriormente. No obstante, se requiere un estudio exhaustivo tanto de los problemas de la privacidad del cliente como de la gestión segura y fiable del sistema de comunicación en microrredes. El análisis de la fiabilidad de la microrred AC/DC

híbrida en modo isla no se aborda en la presente tesis y queda abierto para el futuro.

Por otra parte, los objetivos de gestión también pueden variar en función de la aplicación de la microrred. Por ejemplo, en el caso de una microrred residencial, un trabajo futuro puede ser enfocado a alcanzar los siguientes objetivos de gestión: la comodidad del usuario; la participación del sistema de almacenamiento de energía de vehículos eléctricos u otros; la participación de las microrredes vecinas y el estudio de los posibles beneficios de la comunidad ante dicha gestión; la optimización del consumo de energía en la microrred mediante la participación y programación de las cargas en función de su prioridad (luminarias, refrigeración, calefacción, agua caliente, etc.). En este sentido, las cargas pueden ser gestionadas de forma inteligente mediante un pronóstico semanal o mensual de la demanda de potencia en la microrred. Este pronóstico puede ser realizado en función de la variabilidad de los perfiles de demanda, que dependen de los hábitos de consumo del usuario, la estación del año y las preferencias del usuario según su nivel de comodidad.

Respecto a los esquemas de gestión de potencia utilizados en este trabajo, se utiliza un diagrama de control jerárquico donde el controlador central se encarga del control segundario de la microrred mediante la comunicación con todos los demas dispositivos a través de DSPs dedicados. El control centralizado aplicado ofrece el más alto nivel de flexibilidad para lograr funcionalidades avanzadas en la microrred con un bajo coste computacional. Su desventaja principal es que es un sistema con un único punto de fallo, debido a su dependencia de las comunicaciones. Una solución a esta problemática es utilizar los métodos de control distribuido, que se asemejan estructuralmente a los descentralizados, pero pueden lograr funciones similares a los métodos centralizados, ya que también implican la comunicación digital. El control distribuido reúne datos entre todos los actores de la microrred, que son procesados colectivamente a través de algoritmos de gestión basados en el consenso [130-131]. Por el principio de consenso, cada controlador local puede obtener información sobre la microrred comparable a la del control centralizado, pero con un retraso en el tiempo de cómputo, el cual es requerido para la convergencia de sus controles. Según la literatura [11],[18-25],[132], el control distribuido ha mejorado la confiabilidad en comparación con el control centralizado, ya que no existe un solo punto de fallo. Sin embargo, el riguroso análisis matemático de las estrategias de control distribuido sigue siendo un tema de investigación abierto, especialmente en entornos no ideales que aumentan la complejidad de implementación de este control. Los fenómenos que se producen en estos entornos son: los diferentes

retrasos en los tiempos de comunicación entre dispositivos, ruido en la medición de las variables, tiempos de cómputo de los algoritmos muy elevados y sistemas de control imperfectos.

Finalmente, existe un amplio abanico de funcionalidades técnicas que han sido superadas y que agregan inteligencia a la microrred, las cuales permiten aplicar técnicas de control, gestión, pronóstico, transmisión, procesado y monitorización de datos en la microrred. Sin embargo, estas funcionalidades aún no pueden resolver todos los problemas existentes en las microrredes. Por ello, se requiere más estudios de implementación que agregen soluciones sobre las barreras técnicas en el aprovechamiento de la energía y comunicaciones seguras en microrredes.

7

7. REFERENCIAS BIBLIOGRÁFICAS

1. Renewables 2017 Global Status Report. Disponible en linea en Julio 2018: http://www.ren21.net/wp-content/uploads/2017/06/17-8399_GSR_2017_Full_Report_0621_Opt.pdf.
2. Lasseter R, Akhil A, Marnay C, Stephens J, Dagle J, Guttromson R, Meliopoulos A, Yinger R, Eto J. White paper on integration of distributed energy resources. The CERTS microgrid concept. Consortium for Electric Reliability Technology Solutions CERTS. CA, Tech. Rep. LBNL-50829, Apr. 2002.
3. R. H. Lasseter, "Microgrid," in Proc. IEEE Power Eng. Soc. Winter Meeting, New York, 2002, vol. 1, pp. 305–308.
4. Hossain Eklas, Kabalci Ersan, Bayindir Ramazan A Comprehensive Study on Microgrid Technology Int J Renew Energy Res, 4 (4) (2014), pp. 1094-1107.
5. P. Basak, S. Chowdhury, S.P. Chowdhury, S. Halder. A literature review on integration of distributed energy resources in the perspective of control, protection and stability of microgrid. Renew Sustain Energy Rev, vol.16 (8) (2012).
6. Unamuno, E.; Barrena, J.A. Hybrid AC/DC microgrids—Part II: Review and classification of control strategies. Renew. Sustain. Energy Rev. 2015, 52, 1123–1134.
7. Patrao, I.; Figueres, E.; Garcerá, G. González-Medina, Microgrid architectures for low voltage distributed generation. Renew. Sustain. Energy Rev. 2015, 43, 415–424.
8. Patrao, I.; González-Medina, R.; Marzal, S.; Garcerá, G.; Figueres, E. Synchronization of Power Inverters in Islanded Microgrids Using an FM-Modulated Signal. IEEE Trans. Smart Grid 2017, 8, 503–510.
9. J. Rocabert, A. Luna, F. Blaabjerg, P. Rodríguez Control of power converters in AC microgrids. IEEE Trans Power Electron, 27 (11) (2012), pp. 4734-4749.
10. A. Das, V. Balakrishnan. Sustainable energy future via grid interactive operation of spv system at isolated remote island. Renew Sustain Energy Rev, 16 (7) (2012), pp. 5430-5442.
11. Dragičević, T.; Lu, X.; Vasquez, J.C.; Guerrero, J.M. DC Microgrids—Part I: A Review of Control Strategies and Stabilization Techniques. IEEE Trans. Power Electron. 2016, 31, 4876–4891.

12. R. Noroozian, M. Abedi, G.B. Gharehpetian, S.H. Hosseini. Distribution resources and DC distribution system combination for high power quality. Electrical Power and Energy System, 32 (2010), pp. 769-781.
13. L. Xu, D. Chen. Control and operation of a DC microgrid with variable generation and energy storage. IEEE Transactions on Power Delivery, 26 (4) (2011), pp. 2513-2522.
14. A. Kwasinski Quantitative evaluation of DC microgrids availability: effects of system architecture and converter topology design choices. IEEE Transactions on Power Electronics, 26 (3) (2011), pp. 835-851.
15. J.J. Justo, F. Mwasilu, J. Lee, J.W. Jung. AC-microgrids versus DC-microgrids with distributed energy resources: a review. Renew Sustain Energy Rev, 24 (0) (2013), pp. 387-405.
16. Baek, J.; Choi, W.; Chae, S. Distributed Control Strategy for Autonomous Operation of Hybrid AC/DC Microgrid. Energies 2017, 10, 373.
17. Liu, X.; Wang, P.; Loh, P.C. A hybrid AC/DC micro-grid. In Proceedings of the 2010 Conference IPEC, Singapore, 27–29 October 2010; pp. 746–751.
18. Muhammad Fahad Zia, Elhoussin Elbouchikhi, Mohamed Benbouzid,Microgrids energy management systems: A critical review on methods, solutions, and prospects, Applied Energy, Volume 222, 2018, Pages 1033-1055.
19. Depuru SSSR, L.F. Wang, V. Devabhaktuni. Smart meters for power grid: challenges, issues, Advantages and status.Renew Sust Energ Rev, 15 (2011), pp. 2736-2742
20. Yeliz Yoldaş, Ahmet Önen, S.M. Muyeen, Athanasios V. Vasilakos, İrfan Alan, Enhancing smart grid with microgrids: Challenges and opportunities, Renewable and Sustainable Energy Reviews, Volume 72, 2017, Pages 205-214.
21. Salam AA, Mohamed A, Hannan MA. Technical challenges on microgrids. ARPN-J Eng Appl Sci 2008;3:64–9
22. Stadler M, Cardoso G, Mashayekh S, Forget T, DeForest N, Agarwal A, et al. Value streams in microgrids: a literature review. Appl Energy 2016; 162:980–9.
23. Mirsaeidi S, Said DM, Mustafa MW, Habibuddin MH, Ghaffari K. Progress and problems in microgrid protection schemes. Renew Sust Energ Rev 2014; 37:834–9.
24. Basak P, Chowdhury S, Dey SHN, Chowdhury SP. A literature review on integration of distributed energy resources in the perspective of control, protection and stability of microgrid. Renew Sust Energ Rev 2012; 16:5545–56.
25. Soshinskaya M, Crijns-Graus WHJ, Guerrero JM, Vasquez JC. Microgrids: experiences, barriers and success factors. Renew Sust Energ Rev 2014; 40:659–72.
26. Standard for interconnecting distributed resources with electric power systems 1547. In: IEEE Standards Coordinating Committee 21; 2003.
27. Moschakis M, Karfopoulos E, Zountouridou E, Papathanassiou S. Adapting ev-microgrid concepts to European grid standards related to power quality. In: International conference on intelligent system applications to power systems; 2011. p. 1–6.

28. Vasquez, J.C.; Guerrero, J.M.; Miret, J.; Castilla, M.; de Vicuna, L.G. Hierarchical Control of Intelligent Microgrids. IEEE Ind. Electron. Mag. 2010, 4, 23–29.
29. Kaur, A.; Kaushal, J.; Basak, P. A review on microgrid central controller. Renew. Sustain. Energy Rev. 2016, 55, 338–345.
30. Hatziargyriou ND, Dimeas A, Tsikalakis A., Lopes JAP, Karniotakis G, Oyarzabal J. Management of microgrids in market environment. In: Proceedings of the 2005 international conference on future power systems; 18 Nov. 2005. p. 7.
31. M. C. Chandorkar, D. M. Divan and R. Adapa, "Control of parallel connected inverters in standalone AC supply systems," in IEEE Transactions on Industry Applications, vol. 29, no. 1, pp. 136-143, Jan/Feb 1993.
32. A. Mehrizi-Sani and R. Iravani, "Potential-function based control of a microgrid in islanded and grid-connected models," IEEE Trans. Power Syst., vol. 25, pp. 1883–1891, Nov. 2010.
33. C. Yuen, A. Oudalov, and A. Timbus, "The provision of frequency control reserves from multiple microgrids," IEEE Trans. Ind. Electron., vol. 58, pp. 173–183, Jan. 2011.
34. K. D. Brabandere, K. Vanthournout, J. Driesen, G. Deconinck, and R. Belmans, "Control of microgrids," in Proc. IEEE Power & Energy Society General Meeting, 2007, pp. 1–7.
35. Guerrero JM, Vasquez JC, Matas J, de Vicuna LG, Castilla M. Hierarchical control of droop-controlled AC and DC microgrids – a general approach toward standardization. IEEE Trans Ind Electron 2011; 58(1):158–72.
36. F. Blaabjerg, R. Teodorescu, M. Liserre and A. V. Timbus, "Overview of Control and Grid Synchronization for Distributed Power Generation Systems," in IEEE Transactions on Industrial Electronics, vol. 53, no. 5, pp. 1398-1409, Oct. 2006.
37. De Brabandere, K.; Bolsens, B.; van den Keybus, J.; Woyte, A.; Driesen, J.; Belmans, R. A Voltage and Frequency Droop Control Method for Parallel Inverters. *IEEE Trans. Power Electron.* **2007**, *22*, 1107–1115.
38. J. Kim, J. M. Guerrero, P. Rodriguez, R. Teodorescu and K. Nam, "Mode Adaptive Droop Control With Virtual Output Impedances for an Inverter-Based Flexible AC Microgrid," in IEEE Transactions on Power Electronics, vol. 26, no. 3, pp. 689-701, March 2011.
39. Shivashankar Sukumar, Hazlie Mokhlis, Saad Mekhilef, Kanendra Naidu, Mazaher Karimi, Mix-mode energy management strategy and battery sizing for economic operation of grid-tied microgrid, Energy, Volume 118, 2017, Pages 1322-1333.
40. L. Igualada, C. Corchero, M. Cruz-Zambrano and F. -. Heredia, "Optimal Energy Management for a Residential Microgrid Including a Vehicle-to-Grid System," in IEEE Transactions on Smart Grid, vol. 5, no. 4, pp. 2163-2172, July 2014.
41. Tsikalakis AG, Hatziargyriou ND. Centralized control for optimizing microgrids operation. Power and energy society general meeting, 2011 IEEE. IEEE; 2011. p. 1–8.

42. An LN, Quoc-Tuan T. Optimal energy management for grid connected microgrid by using dynamic programming method. Power & energy society general meeting, 2015 IEEE. IEEE; 2015. p. 1–5.
43. Kanchev H, Lu D, Colas F, Lazarov V, Francois B. Energy management and operational planning of a microgrid with a PV-based active generator for smart grid applications. IEEE Trans Industr Electron 2011; 58(10):4583–92.
44. Elsied M, Oukaour A, Youssef T, Gualous H, Mohammed O. An advanced real time energy management system for microgrids. Energy 2016; 114:742–52.
45. Marzband M, Yousefnejad E, Sumper A, Domínguez-García JL. Real time experimental implementation of optimum energy management system in standalone microgrid by using multi-layer ant colony optimization. Int J Electr Power Energy Syst 2016; 75:265–74.
46. Kyriakarakos G, Dounis AI, Arvanitis KG, Papadakis G. A fuzzy logic energy management system for polygeneration microgrids. Renew Energy 2012;41:315–27.
47. Arcos-Aviles D, Pascual J, Guinjoan F, Marroyo L, Sanchis P, Marietta MP. Low complexity energy management strategy for grid profile smoothing of a residential grid-connected microgrid using generation and demand forecasting. Appl Energy 2017; 205:69–84.
48. Dou C-X, Liu B. Multi-agent based hierarchical hybrid control for smart microgrid. IEEE Trans Smart Grid 2013; 4(2):771–8.
49. Liu N, Yu X, Wang C, Wang J. Energy sharing management for microgrids with PV prosumers: a stackelberg game approach. IEEE Trans Industr Inf 2017;13(3):1088–98
50. Kuznetsova E, Li Y-F, Ruiz C, Zio E. An integrated framework of agent-based modelling and robust optimization for microgrid energy management. Appl Energy 2014; 129:70–88.
51. Milczarek A, Malinowski M, Guerrero JM. Reactive power management in islanded microgrid – proportional power sharing in hierarchical droop control. IEEE Trans Smart Grid 2015;6(4):1631–8.
52. Helal S, Najee R, Hanna M, Shaaban M, Osman A, Hassan M. An energy management system for hybrid microgrids in remote communities. Electrical and computer engineering (CCECE), 2017 IEEE 30th Canadian conference on. IEEE; 2017. p. 1–4.
53. Panwar LK, Konda SR, Verma A, Panigrahi BK, Kumar R. Operation window constrained strategic energy management of microgrid with electric vehicle and distributed resources. IET Gener Transmiss Distrib 2017;11(3):615–26
54. Almada J, Leão R, Sampaio R, Barroso G. A centralized and heuristic approach for energy management of an ac microgrid. Renew Sustain Energy Rev 2016;60: 1396–404
55. Choudar A, Boukhetala D, Barkat S, Brucker J-M. A local energy management of a hybrid PV-storage based distributed generation for microgrids. Energy Convers Manage 2015; 90:21–33.

56. Pascual J, Barricarte J, Sanchis P, Marroyo L. Energy management strategy for a renewable-based residential microgrid with generation and demand forecasting. Appl Energy 2015;158: 12–25
57. Arcos-Aviles D, Pascual J, Guinjoan F, Marroyo L, Sanchis P, Marietta MP. Low complexity energy management strategy for grid profile smoothing of a residential grid-connected microgrid using generation and demand forecasting. Appl Energy 2017;205:69–84.
58. Rezaei N, Kalantar M. Stochastic frequency-security constrained energy and reserve management of an inverter interfaced islanded microgrid considering demand response programs. Int J Electr Power Energy Syst 2015;69: 273–86
59. Ghorbani S, Rahmani R, Unland R. Multi-agent autonomous decision making in smart micro-grids energy management: a decentralized approach. German conference on multiagent system technologies. Springer; 2017. p. 223–37.
60. Diaz NL, Dragicevic T, Vasquez JC, Guerrero JM. Intelligent distributed generation and storage units for DC microgrids – a new concept on cooperative control without communications beyond droop control. IEEE Trans Smart Grid 2014; 5(5):2476–85.
61. Katiraei F, Iravani MR. Power management strategies for a microgrid with multiple distributed generation units. IEEE Trans Power Syst 2006;21 (4):1821–31.
62. Shi H, Fang Z, Yi H, Wang F, Zhang D, Geng Z. A novel real-time voltage and frequency compensation strategy for photovoltaic-based microgrid. IEEE Trans Ind Electron 2014; 0046(no. c) (1–1).
63. Gao, L.; Liu, Y.; Ren, H.; Guerrero, J.M. A DC Microgrid Coordinated Control Strategy Based on Integrator Current-Sharing. Energies 2017, 10, 1116.
64. Zia, M.F.; Elbouchikhi, E.; Benbouzid, M. Microgrids energy management systems: A critical review on methods, solutions, and prospects. Appl. Energy 2018, 222, 1033–1055.
65. Feng, X.; Shekhar, A.; Yang, F.E.; Hebner, R.; Bauer, P. Comparison of Hierarchical Control and Distributed Control for Microgrid. Electr. Power Compon. Syst. 2017, 45, 1043–1056.
66. Gamarra, C.; Guerrero, J.M. Computational optimization techniques applied to microgrids planning: A review. Renew. Sustain. Energy Rev. 2015, 48, 413–424.
67. Li, W.; Logenthiran, T.; Woo, W.L.; Phan, V.T.; Srinivasan, D. Implementation of demand side management of a smart home using multi-agent system. In Proceedings of the 2016 IEEE Congress on Evolutionary Computation (CEC), Vancouver, BC, Canada, 24–29 July 2016; pp. 2028–2035.
68. Joo, I.Y.; Choi, D.H. Optimal household appliance scheduling considering consumer's electricity bill target. IEEE Trans. Consum. Electron. 2017, 63, 19–27.
69. Roozbehani, M.; Dahleh, M.A.; Mitter, S.K. Volatility of power grids under real-time pricing. IEEE Trans. Power Syst. 2012, 27, 1926–1940.
70. Carpinelli, G.; Khormali, S.; Mottola, F.; Proto, D. Optimal operation of electrical energy storage systems for industrial applications. In Proceedings of the 2013 IEEE

Power & Energy Society General Meeting, Vancouver, BC, Canada, 21–25 July 2013; pp. 1–5.
71. Erol-Kantarci, M.; Hussein, T.M. Prediction-based charging of PHEVs from the smart grid with dynamic pricing. In Proceedings of the IEEE Local Computer Network Conference, Denver, CO, USA, 10–14 October 2010; pp. 1032–1039.
72. Petr Vanýsek, Vítězslav Novák,Redox flow batteries as the means for energy storage, Journal of Energy Storage,Volume 13,2017,Pages 435-441
73. . G. Bitterly, "Flywheel technology: past, present, and 21st century projections," in IEEE Aerospace and Electronic Systems Magazine, vol. 13, no. 8, pp. 13-16, Aug. 1998.
74. W. F. Pickard, "The History, Present State, and Future Prospects of Underground Pumped Hydro for Massive Energy Storage," in Proceedings of the IEEE, vol. 100, no. 2, pp. 473-483, Feb. 2012.
75. Cong Guo, Yujie Xu, Xinjing Zhang, Huan Guo, Xuezhi Zhou, Chang Liu, Wei Qin, Wen Li, Binlin Dou, Haisheng Chen, Performance analysis of compressed air energy storage systems considering dynamic characteristics of compressed air storage, Energy, Volume 135,2017.
76. Sujitha, N.; Krithiga, S. RES based EV battery charging system: A review. Renew. Sustain. Energy Rev. 2017, 75, 978–988.
77. Chen, H.; Cong, T.N.; Yang, W.; Tan, C.; Li, Y.; Ding, Y. Progress in electrical energy storage system: A critical review. Prog. Nat. Sci. 2009, 19, 291–312.
78. May, G.J.; Davidson, A.; Monahov, B. Lead batteries for utility energy storage: A review. J. Energy Storage 2018, 15, 145–157.
79. Joseph, A.; Shahidehpour, M. Battery storage systems in electric power systems. In Proceedings of the 2006 IEEE Power Engineering Society General Meeting, Montreal, QC, Canada, 18–22 June 2006; p. 8.
80. IRENA. Disponible en linea en Febrero 2018: http://www.irena.org/eventdocs/Battery%20storage%20June%201%202017%20MICHAEL%20TAYLOR%20PDF%20version.pdf.
81. Hussein, A.A.; Fardoun, A.A. Design considerations and performance evaluation of outdoor PV battery chargers. Renew. Energy 2015, 82, 85–91.
82. Xing, Y.; Ma, E.W.M.; Tsui, K.L.; Pecht, M. Battery Management Systems in Electric and Hybrid Vehicles. Energies 2011, 4, 1840–1857.
83. Rahimi-Eichi, H.; Ojha, U.; Baronti, F.; Chow, M.Y. Battery Management System: An Overview of Its Application in the Smart Grid and Electric Vehicles. IEEE Ind. Electron. Mag. 2013, 7, 4–16.
84. Sujitha, N.; Krithiga, S. RES based EV battery charging system: A review. Renew. Sustain. Energy Rev. 2017, 75, 978–988.
85. Lu, L.; Han, X.; Li, J.; Hua, J.; Ouyang, M. A review on the key issues for lithium-ion battery management in electric vehicles. J. Power Sources 2013, 226, 272–288.
86. Hussein, A.A.; Batarseh, I. A Review of Charging Algorithms for Nickel and Lithium Battery Chargers. IEEE Trans. Veh. Technol. 2011, 60, 830–838.

87. Shen, W.; Vo, T.T.; Kapoor, A. Charging algorithms of lithium-ion batteries: An overview. In Proceedings of the 2012 7th IEEE Conference on Industrial Electronics and Applications (ICIEA), Singapore, 18–20 July 2012; pp. 1567–1572.
88. Kozlowski, J.D. Electrochemical Cell Prognostics Using Online Impedance Measurements and Model-Based Data Fusion Techniques. In Proceedings of the IEEE Aerospace Conference, Big Sky, MT, USA, 8–15 March 2003; Volume 7, pp. 3257–3270.
89. Analog Devices. Disponible en linea en Febrero 2018: http://www.analog.com/media/en/technical-documentation/technical-articles/A-Closer-Look-at-State-Of-Charge-and-State-Health-Estimation-Techniques-....pdf.
90. Fathoni, G.; Widayat, S.A.; Topan, P.A.; Jalil, A.; Cahyadi, A.I.; Wahyunggoro, O. Comparison of State-of-Charge (SOC) estimation performance based on three popular methods: Coulomb counting, open circuit voltage, and Kalman filter. In Proceedings of the 2017 2nd International Conference on Automation, Cognitive Science, Optics, Micro Electro--Mechanical System, and Information Technology (ICACOMIT), Jakarta, Indonesia, 23–24 October 2017; pp. 70–74.
91. Lyu, C.; Cong, W.; Liu, H.; Zhang, L. A novel parameters acquisition method based on electrochemical impedance spectroscopy mathematical model in lithium ion cell. In Proceedings of the 2017 Prognostics and System Health Management Conference (PHM-Harbin), Harbin, China, 9–12 July 2017; pp. 1–8.
92. Hu, X.; Li, S.E.; Yang, Y. Advanced Machine Learning Approach for Lithium-Ion Battery State Estimation in Electric Vehicles. IEEE Trans. Transp. Electrification 2016, 2, 140–149.
93. Piller, S.; Perrin, M.; Jossen, A. Methods for state-of-charge determination and their applications. J. Power Sources 2001, 96, 113–120.
94. Kim, D.; Goh, T.; Park, M.; Kim, S.W. Fuzzy Sliding Mode Observer with Grey Prediction for the Estimation of the State-of-Charge of a Lithium-Ion Battery. Energies 2015, 8, 12409–12428.
95. Tian, Y.; Li, D.; Tian, J.; Xia, B. State of charge estimation of lithium-ion batteries using an optimal adaptive gain nonlinear observer. Electrochim. Acta 2017, 225, 225–234.
96. Rivera-Barrera, J.P.; Muñoz-Galeano, N.; Sarmiento-Maldonado, H.O. SoC Estimation for Lithium-ion Batteries: Review and Future Challenges. Electronics 2017, 6, 102.
97. Xiong, R.; Cao, J.; Yu, Q.; He, H.; Sun, F. Critical Review on the Battery State of Charge Estimation Methods for Electric Vehicles. IEEE Access 2018, 6, 1832–1843.
98. Lin, C.H.; Wang, C.-M.; Lin, W.-J. A SOC-based intelligent charger with multi-charging mode. In Proceedings of the 2015 IEEE 2nd International Future Energy Electronics Conference (IFEEC), Taipei, Taiwan, 1-4 November 2015; pp. 1–6.
99. Oliveira, T.R.; Gonçalves Silva, W.W.A.; Donoso-Garcia, P.F. Distributed Secondary Level Control for Energy Storage Management in DC Microgrids. IEEE Trans. Smart Grid 2017, 8, 2597–2607.

100. Velho, R.; Beirão, M.; Calado, M.R.; Pombo, J.; Fermeiro, J.; Mariano, S. Management System for Large Li-Ion Battery Packs with a New Adaptive Multistage Charging Method. Energies 2017, 10, 605.
101. Xue, F.; Ling, Z.; Yang, Y.; Miao, X. Design and Implementation of Novel Smart Battery Management System for FPGA Based Portable Electronic Devices. Energies 2017, 10, 264.
102. Doan, V.T.; Vu, V.B.; Vu, H.N.; Tran, D.H.; Choi, W. Intelligent charger with online battery diagnosis function. In Proceedings of the 2015 9th International Conference on Power Electronics and ECCE Asia (ICPE-ECCE Asia), Seoul, South Korea, 1–5 June 2015; pp. 1644–1649.
103. Diaz, J.; Martin-Ramos, J.A.; Pernia, A.M.; Nuno, F.; Linera, F.F. Intelligent and universal fast charger for Ni-Cd and Ni-MH batteries in portable applications. IEEE Trans. Ind. Electron. 2004, 51, 857–863.
104. Mundra, T.S.; Kumar, A. An Innovative Battery Charger for Safe Charging of NiMH/NiCd Batteries. IEEE Trans. Consum. Electron. 2007, 53, 1044–1052.
105. Hu, X.; Martinez, C.M.; Yang, Y. Charging, Power management, and battery degradation mitigation in plug-in hybrid electric vehicles: A unified cost-optimal approach. Mech. Syst. Signal Process. 2017, 87, 4–16.
106. Yong, S.O.; Rahim, N.A. Development of on-off duty cycle control with zero computational algorithm for CC-CV Li ion battery charger. In Proceedings of the 2013 IEEE Conference on Clean Energy and Technology (CEAT), Lankgkawi, Malaysia, 18–20 November 2013; pp. 422–426.
107. Monteiro, V.; Ferreira, J.C.; Melendez, A.A.; Couto, C.; Afonso, J.L. Experimental Validation of a Novel Architecture Based on a Dual-Stage Converter for Off-Board Fast Battery Chargers of Electric Vehicles. IEEE Trans. Veh. Technol. 2017, 67, 1000–1011.
108. Bhatt, M.; Hurley, W.G.; Wolfle, W.H. A new approach to intermittent charging of valve-regulated lead-acid batteries in standby applications. IEEE Trans. Ind. Electron. 2005, 52, 1337–1342.
109. Hussein, A.A.H.; Pepper, M.; Harb, A.; Batarseh, I. An efficient solar charging algorithm for different battery chemistries. In Proceedings of the 2009 IEEE Vehicle Power and Propulsion Conference, Dearborn, MI, USA, 7–10 September, 2009; pp. 188–193.
110. Gallardo-Lozano, J.; Milanés-Montero, M.I.; Guerrero-Martínez, M.A.; Romero-Cadaval, E. Electric vehicle battery charger for smart grids. Electr. Power Syst. Res. 2012, 90, 18–29.
111. López, J.; Seleme, S.I.; Donoso, P.F.; Morais, L.M.F.; Cortizo, P.C.; Severo, M.A. Digital control strategy for a buck converter operating as a battery charger for stand-alone photovoltaic systems. Sol. Energy 2016, 140, 171–187.
112. I. Joo and D. Choi, "Optimal household appliance scheduling considering consumer's electricity bill target," in IEEE Transactions on Consumer Electronics, vol. 63, no. 1, pp. 19-27, February 2017.

113. Support, T. Installation, Commissioning and Operation Handbook for Gel-Vrla-Batteries. 2003. Disponible en linea en octubre de 2017: http://www.sonnenschein.org/PDF%20files/GelHandbookPart2.pdf.
114. Hooppecke. Operating Instructions Valve Regulated Stationary Lead-Acid Batteries. Disponible en linea en octubre de 2017: http://www.hoppecke-us.com/tl_files/hoppecke/Documents/HO-US/Operating_Instructions_sealed_stationary_lead_acid_batteries_en1111.pdf.
115. TAB Batteries. Disponible en linea en Octubre 2017: http://www.tabspain.com/wp-content/uploads/informacion -tecnica/renovables/curvas-y-tablas/din-41773-y-din-41774-para-baterías-pzs.pdf .
116. Salas-Puente, Robert; Marzal, Silvia; González-Medina, Raúl; Figueres, Emilio; Garcera, Gabriel. 2018. "Power Management of the DC Bus Connected Converters in a Hybrid AC/DC Microgrid Tied to the Main Grid." Energies 11, no. 4: 794. https://doi.org/10.3390/en11040794
117. Salas-Puente, Robert; Marzal, Silvia; González-Medina, Raúl; Figueres, Emilio; Garcera, Gabriel. 2017. "Experimental Study of a Centralized Control Strategy of a DC Microgrid Working in Grid Connected Mode." Energies 10, no. 10: 1627. https://doi.org/10.3390/en10101627
118. Salas-Puente, Robert; Marzal, Silvia; Gonzalez-Medina, Raul; Figueres, Emilio; Garcera, Gabriel. 2018. "Practical Analysis and Design of a Battery Management System for a Grid-Connected DC Microgrid for the Reduction of the Tariff Cost and Battery Life Maximization." Energies 11, no. 7: 1889. https://doi.org/10.3390/en11071889
119. Robert Salas-Puente, Silvia Marzal, Raúl González-Medina, Emilio Figueres & Gabriel Garcerá. 2018. "An Algorithm for the Efficient Management of the Power Converters Connected to the DC Bus of a Hybrid Microgrid Operating in Grid-connection Mode", Electric Power Components and Systems, DOI: 10.1080/15325008.2018.1469177
120. R. Salas-Puente, S. Marzal, R. González-Medina, E. Figueres and G. Garcerá, "Efficient management strategy of the power converters connected to the DC bus in a hybrid microgrid of Distributed Generation," 2017 19th European Conference on Power Electronics and Applications (EPE'17 ECCE Europe), Warsaw, 2017, pp. P.1-P.10. DOI: 10.23919/EPE17ECCEEurope.2017.8098994
121. Silvia Marzal, Robert Salas, Raúl González-Medina, Gabriel Garcerá, Emilio Figueres, "Current challenges and future trends in the field of communication architectures for microgrids," Renewable and Sustainable Energy Reviews, Volume 82, Part 3, 2018, Pages 3610-3622, ISSN 1364-0321, https://doi.org/10.1016/j.rser.2017.10.101
122. S. Marzal, R. Salas-Puente, R. González-Medina, G. Garcerá and E. Figueres, "Efficient Event Notification Middleware for Smart Microgrids over P2P Networks," in IEEE Transactions on Smart Grid.doi: 10.1109/TSG.2018.2865432

123. Marzal, Silvia; González-Medina, Raul; Salas-Puente, Robert; Figueres, Emilio; Garcerá, Gabriel.2017. "A Novel Locality Algorithm and Peer-to-Peer Communication Infrastructure for Optimizing Network Performance in Smart Microgrids." Energies 10, no. 9: 1275. https://doi.org/10.3390/en10091275
124. S. Marzal, R. Salas-Puente, R. González-Medina, E. Figueres and G. Garcerá, "Peer-to-peer decentralized control structure for real time monitoring and control of microgrids," 2017 IEEE 26th International Symposium on Industrial Electronics (ISIE), Edinburgh, 2017, pp. 140-145. DOI: 10.1109/ISIE.2017.8001237
125. Matlab. The MathWorks; (Natick, MA, USA) Matlab 2015.
126. PowerSim. PSIM10.0; (Rockville, MD, USA) PowerSim 2016.
127. LabView software; (National Instruments Spain, Madrid, Spain) LabView 2015.
128. LEM. Disponible en linea en Julio 2018. https://www.lem.com/en.
129. Texas Instruments. Disponible en linea en Julio 2018. http://www.ti.com/product/iso5500.
130. Q. Shafiee, T. Dragicevic, F. Andrade, J. C. Vasquez, and J. M. Guerrero, "Distributed consensus-based control of multiple DC-microgrids clusters," in Proc. IEEE Annu. Conf. Ind. Electron. Soc., 2014, pp. 2056–2062.
131. V. Nasirian, S. Moayedi, A. Davoudi, and F. Lewis, "Distributed cooperative control of DC Microgrids," IEEE Trans. Power Electron., vol. 30, no. 4, pp. 2288–2303, Apr. 2015.
132. Dragičević, T.; Guerrero, J.M.; Vasquez, J.C.; Škrlec, D. Supervisory Control of an Adaptive-Droop Regulated DC Microgrid with Battery Management Capability. IEEE Trans. Power Electron. 2014, 29, 695–706.